Metal-Oxygen Batteries

Redox mediators and electrode characterization

Dissertation

zur
Erlangung des Doktorgrades (Dr. rer. nat.)
der
Mathematisch-Naturwissenschaftlichen Fakultät
der
Rheinischen Friedrich-Wilhelms-Universität Bonn

vorgelegt von
Pawel Peter Bawol
aus Oppeln, Polen

Bonn 2020

Angefertigt mit Genehmigung der Mathematisch-Naturwissenschaftlichen Fakultät
der
Rheinischen Friedrich-Wilhelms-Universität Bonn

Promotionskommission

Betreuer/Erstgutachter: Prof. Dr. Helmut Baltruschat

Zweitgutachterin: Prof. Dr. Barbara Kirchner

Tag der mündlichen Prüfung: 03.12.2020

Erscheinungsjahr: 2021

Lashing out the action, returning the reaction
Weak are ripped and torn away
Hypnotizing power, crushing all that cower
Battery is here to stay
Smashing through the boundaries
Lunacy has found me
Cannot kill the battery [...]

Metallica
Battery - Master Of Puppets

Selbstständigkeitserklärung gemäß Promotionsordnung der Mathematisch-Naturwissenschaftlichen Fakultät (§6, Absatz 2)

Ich versichere, dass ich die vorliegende Arbeit unter Einhaltung der Regeln guter wissenschaftlicher Praxis selbstständig verfasst, keine anderen als die angegebenen Quellen und Hilfsmittel benutzt und die Zitate kenntlich gemacht habe. Ich habe weder vor noch während meiner Promotion oder bei der Anfertigung dieser Dissertation entgeltliche oder nichtentgeltliche Beratungs- oder Vermittlungsdienstleistungen in Anspruch genommen.

Bonn, den

Publications

Parts of this thesis have already been published in international, peer-reviewed journals or as preprints:

[4] P. P. Bawol, P. H. Reinsberg, A. Koellisch-Mirbach, C. J. Bondue, Helmut Baltruschat; *The ORR in Ca^{2+} Containing DMSO: Reaction Mechanism, Electrode Surface Characterization and Redox Mediation*, ChemRxiv. Preprint, **2020**, DOI: 10.26434/chemrxiv.12480974.v1

[3] P. P. Bawol, J. H. Thimm and H. Baltruschat; *Unraveling the mechanism of the solution mediated ORR in metal-O_2 batteries: The importance of ion association*, ChemElectroChem, **2019**, 6, 6038-6049.

[2] P. P. Bawol, P. H. Reinsberg and H. Baltruschat; *Fast and Simultaneous Determination of Gas Diffusivities and Solubilities in Liquids Employing a Thin-Layer Cell Coupled to a Mass Spectrometer, Part I: Setup and Methodology*, Analytical chemistry, **2018**, 90, 14145-14149.

[1] P. P. Bawol, P. H. Reinsberg, A. A. Abd-El-Latif, P. Königshoven and H. Baltruschat; *A new thin layer cell for battery related DEMS-experiments: the activity of redox mediators in the Li–O_2 cell*, Physical Chemistry Chemical Physics, **2018**, 20, 21447-21456.

Additionally, chapter 8 is a part of a manuscript which is also prepared for submission to a journal.

Complete list of publications

[10] P. P. Bawol, P. H. Reinsberg, A. Koellisch-Mirbach, C. J. Bondue, Helmut Baltruschat; *The ORR in Ca^{2+} Containing DMSO: Reaction Mechanism, Electrode Surface Characterization and Redox Mediation*, ChemRxiv. Preprint, **2020**,
DOI: 10.26434/chemrxiv.12480974.v1

[9] N. Fleck, C. A. Heubach, T. Hett. F. R. Haege, P. P. Bawol, H. Baltruschat and O. Schiemann; *SLIM: A short-linked, highly redox-stable trityl label for high sensitivity in cell EPR distance measurements*, Angewandte Chemie, 132(24), **2020**, 9854-9859.

[8] P. P. Bawol, J. H. Thimm and H. Baltruschat; *Unraveling the mechanism of the solution mediated ORR in metal-O_2 batteries: The importance of ion association*, ChemElectroChem, **2019**, 6, 6038-6049.

[7] P. H. Reinsberg, A. Koellisch, P. P. Bawol and H. Baltruschat; *K–O_2 electrochemistry: achieving highly reversible peroxide formation*, Physical Chemistry Chemical Physics , **2019**, 21, 4286-4294.

[6] P. H. Reinsberg, P. P. Bawol, E. Thome and H. Baltruschat; *Fast and simultaneous determination of gas diffusivities and solubilities in liquids employing a thin-layer cell coupled to a mass spectrometer, Part II: proof of concept and Experimental Results*, Analytical chemistry, **2018**, 90, 14150-14155.

[5] P. P. Bawol, P. H. Reinsberg and H. Baltruschat; *Fast and Simultaneous Determination of Gas Diffusivities and Solubilities in Liquids Employing a Thin-Layer Cell Coupled to a Mass Spectrometer, Part I: Setup and Methodology*, Analytical chemistry, **2018**, 90, 14145-14149.

[4] P. P. Bawol, P. H. Reinsberg, A. A. Abd-El-Latif, P. Königshoven and H. Baltruschat; *A new thin layer cell for battery related DEMS-experiments: the activity of redox mediators in the Li–O_2 cell*, Physical Chemistry Chemical Physics, **2018**, 20, 21447-21456.

[3] H. M. A. Amin, C. Molls, P. P. Bawol and H. Baltruschat; *The impact of solvent properties on the performance of oxygen reduction and evolution in mixed tetraglyme-dimethyl sulfoxide electrolytes for Li-O_2 batteries: Mechanism and stability*, Electrochimica Acta, **2017**, 245, 967-980.

[2] C. J. Bondue, P. P. Bawol, A. A. Abd-El-Latif, P. Reinsberg and H. Baltruschat; *Gaining control over the mechanism of oxygen reduction in organic electrolytes: the effect of solvent properties*, The Journal of Physical Chemistry C, **2017**, 121, 8864-8872.

[1] P. H. Reinsberg, A. Weiß, P. P. Bawol and H. Baltruschat; *Electrochemical Reaction Order of the Oxygen Reduction Reaction in Li^+-Containing DMSO*, The Journal of Physical Chemistry C, **2017**, 121, 7677-7688.

Selection of conference contributions

[7] **Talk**: P. P. Bawol, C. Merdon, H. Baltruschat und J. Fuhrmann; *Rotating Ring Disc Electrode simulations: A comparison of a classical finite diffrences to fully implicit finite volume scheme*, 70th Annual Meeting of the International Society of Electrochemistry, 04.08.2019 – 09.08.2019, Durban, Southafrica.

[6] **Poster**: P. P. Bawol, P. H. Reinsberg J. H. Thimm und H. Baltruschat; *Towards the mechanism of solution mediated ORR by benzoquinones in metal-O_2 batteries*, 70th Annual Meeting of the International Society of Electrochemistry, 04.08.2019 – 09.08.2019, Durban, Southafrica.

[5] **Poster**: P. P. Bawol, C. Merdon , H. Baltruschat und J. Fuhrmann; *Rotating Ring Disc Electrode simulations: A comparison of a classical finite differences to fully implicit finite volume scheme.*, 16th Symposium on Modeling and Experimental Validation of Electrochemical Energy Technologies, 12.03.2019 – 13.03.2019, Braunschweig, Germany.

[4] **Poster**: P. P. Bawol, A. Köllisch, P. H. Reinsberg, J. H. Thimm und H. Baltruschat; *Understanding the shape of ring current transients in RRDE experiments: From simulations to more detailed insights*, Electrochemistry 2018, 24.09.2019 – 26.09.2018, Ulm, Germany.

[3] **Talk**: P. P. Bawol, P. H. Reinsberg, J. H. Thimm, T. Lohrmann und H. Baltruschat; *Kinetics of O_2 reduction in metal-O_2 batteries by a redox mediator: A DEMS and RRDE study*, 69th Annual Meeting of the International Society of Electrochemistry, 02.09.2019 – 07.09.2018, Bologna, Italy.

[2] **Poster (Posterprize)**: P. P. Bawol, J. H. Thimm, und H. Baltruschat; *Insights into the kinetics of redox mediation in Li-O_2 batteries: A DEMS and RRDE study*, Bunsentagung 2018 - Kinetics in the Real World, 10.05.2018 – 12.05.2018, Hannover, Germany.

[1] **Poster**: P. P. Bawol, P. Königshoven und H. Baltruschat; *Observing the activity of redox mediators in the OER for Li-O_2 systems with a new thin layer cell for DEMS-experiments*, Electrochemistry 2016, 26.09.2016 – 28.09.2016, Goslar, Germany.

Patents

[1] H. Baltruschat, P. P. Bawol, P. Königshoven und P. H. Reinsberg; *Messzelle zur Bestimmung von Diffusionskoeffizienten und Löslichkeiten von Gasen*, Patentanmeldung DE102017128269A1, 11. September **2017**.

Danksagung

An dieser Stelle möchte ich mich bei allen Personen in meinem Umfeld bedanken, die mich in der Zeit meiner Promotion unterstützt haben. Zuallererst will ich meinen Dank Prof. Dr. Helmut Baltruschat aussprechen. Durch Ihn habe ich eine exzellente Betreuung erfahren. Es ist oft vorgekommen, dass Helmut Baltruschat seine Arbeit unterbrochen hat um über aktuelle Probleme in der Auswertung/Interpretation der Messdaten zu diskutieren oder um mir mit seiner Expertise im Labor zu helfen. Ich habe es sehr genossen, dass ich meine eigenen Interessen in der Forschung ausleben durfte. Außerdem bin ich dafür dankbar, dass er mir die Möglichkeit gegeben hat meine Ergebnisse auf einer Vielzahl von Konferenzen zu präsentieren.

Bei Frau Prof. Dr. Barbara Kirchner möchte ich mich für die freundliche Übernahme des Vorsitzes der Promotionskommission bedanken. Ebenso danke ich den weiteren Mitgliedern der Promotionskommission Frau Priv.-Doz. Dr. Elisabeth Soergel und Herrn Prof. Dr. Werner Mader.

Ich möchte mich bei allen Mitgliedern der Abteilung Elektrochemie für die wissenschaftliche Zusammenarbeit sowie die persönlichen Bereicherungen bedanken. Mein besonderer Dank gilt hierbei Dr. Philip H. Reinsberg und Andreas Köllisch-Mirbach, für die Gespräche rund um elektrochemische Fragestellungen und der guten Gesellschaft außerhalb der Arbeit. Bei Dr. Jan K. Kaul und Dr. Chistoph J. Bondü möchte ich mich für die Zeit während meiner Bachelor- und Masterarbeit bedanken, die sicherlich dazu beigetragen hat, dass ich der Elektrochemie treu geblieben bin. Bei Dr. Siegfried Ernst will ich mich für die produktiven Gespräche und Diskussionen um wissenschaftliche Fragestellungen bedanken. Mein Dank gilt auch Carole Rossignole für ihre tolle Unterstützung bei Büroarbeiten und an Elke Thome für die Unterstützung im Labor. Auch möchte ich mich bei Cara Tabea Lohrmann und Jan Hendrik Thimm für die Unterstützung bei einigen Messungen bedanken, die im Rahmen ihrer Bachelor- und Masterarbeiten entstanden sind und Einzug in diese Arbeit gefunden haben. Bei den Werkstätten des Instituts für Physikalische und Theoretische Chemie bedanke ich mich für die gute Zusammenarbeit und die schnelle Hilfe bei der Konstruktion von neuen Experimenten oder Reparatur von defekten Messapparaturen.

Genauso wichtig für den Erfolg dieser Arbeit war allerdings mein soziales Umfeld, welches mir oft eine gute Abwechslung zum alltäglichen Laborstress anbieten konnte. Hier ist die "Rock am Ring-Gruppe" zu nennen. Immer wieder freuen mich die Treffen mit meinen langjährigen Freund/innen Svenja, Marco und Tim, die aufgrund der Distanz zwischen uns leider seltener geworden sind. Tim und Laura-Luise danke für das Korrekturlesen der Arbeit.

Meiner Mutter Weronika, meinem Vater Janusz und meiner Schwester Laura danke ich für die unermüdliche Unterstützung in jeder Lebensituation.

Bei meiner Freundin Laura-Luise Maibaum bedanke ich mich für den emotionalen Rückhalt. Meine Promotionszeit wäre um einiges trister gewesen, wenn ich nicht gewusst hätte, dass ich Abends zu dir nach Hause komme. Ich freue mich sehr auf die weitere gemeinsame Zeit!

Abstract

In this study some new findings on metal-oxygen batteries are presented. Tackling climate change requires a transition from the use of fossil fuels as energy sources to renewable energies. This is associated with the need to store electricity for different applications. Especially for the use in cars the current Li-ion technology cannot guarantee comparable ranges of the car as fossil fuels allow. In addition, the circumstances surrounding the mining of cobalt and lithium for Li-ion technology are questionable. Therefore, research on new battery technologies is necessary and metal-oxygen batteries appear to be the most promising candidate with respect to the higher energy densities compared to Li-ion technology.

The results published prior to this study have shown some difficulties in Li-O_2 technology regarding the storage of the discharge product Li_2O_2 on the cathode surface, the stability of the electrolyte against reactive oxygen species and the kinetics during battery charging. Redox mediators for the oxygen reduction reaction (ORR) and oxygen evolution reaction (OER) as an additive to the electrolyte can help to solve these problems. Nevertheless, the redox mediators, mostly organic molecules, are also exposed to the reactive oxygen species and it has to be checked if the redox mediators are stable. Therefore, a new electrochemical cell for differential electrochemical mass spectrometry (DEMS) was developed. This cell has a high electrode surface to the electrolyte volume and is therefore comparable to battery architectures. Additionally, high sensitivities for the O_2 signal in the mass spectrometer could be achieved. Thus it was possible to demonstrate that the redox mediators for the OER N,N,N′,N′-tetramethyl-p-phenylenediamine (TMPD) and tetrathiafulvalene (TTF) known from the Li-O_2 literature also undergo side reactions in the OER. Furthermore, the kinetics of the oxidation of Li_2O_2 by a redox mediator was investigated and a model was derived. It was shown that the electron transfer from Li_2O_2 to the oxidized redox mediator can be understood by an outer sphere mechanism. Furthermore, it could be shown that an increase of the mediator concentration in the electrolyte leads to a shift of the potential of the OER through the mediator to more negative potentials. This finding is especially interesting for practical purpose as it shows that the charging voltage of the Li-O_2 battery could be lowered by increasing the redox mediator concentration.

The kinetics of ORR by the redox mediator 2,5-di-tert-butyl-1,4-benzoquinone (DBBQ) was extensively studied using DEMS and rotating ring disc electrode (RRDE). For this purpose a variation of the solvent (dimethyl sulfoxide and tetraglyme) as well as variations of the conducting salt concentration and the cation of the conducting salt were performed. It was shown that the ORR mediated by DBBQ is faster if the interaction of the cation of the electrolyte and the reduced DBBQ increases. These investigations were supported by kinetic modelling of the experiments with a finite difference algorithm. Additionally, by increasing this interaction, the ORR potential can be shifted to higher electrode potentials. This was explained by the thermodynamic potential shift of the DBBQ reduction due to a higher ion pair formation with increasing cation concentration. In general this finding could help to increase the discharge voltage of the metal-O_2 battery. Further experiments

also showed the effectiveness of DBBQ as a redox mediator in Ca^{2+} and Mg^{2+} containing DMSO.

Special attention was paid to the investigation of ORR and OER in Ca^{2+} containing DMSO. There are almost no fundamental investigations published and only one first study has revealed a high reversibility of the OER charge to the ORR charge compared to other metal O_2 systems. Thus, we were able to prove by mass spectrometry that the superoxide formed in the ORR disproportionates to peroxide and oxygen in the presence of Ca^{2+} in the electrolyte. Carbonates as well as volatile organic compounds were detected as by-products. This observation is consistent with the recently reported proportionate formation of singlet oxygen during the disproportionation of superoxide. Due to its reactivity, the formed singlet oxygen is considered responsible for a large part of the side reactions in metal-O_2 batteries. Furthermore, the electrocatalysts Au and Pt were investigated after ORR using photoelectron spectroscopy (XPS). It was found that although a large part of the ORR products are soluble in the Ca^{2+} containing electrolyte, a thin layer is deposited on the electrode surface. This consists of decomposition products of the electrolyte on the surface, Ca-peroxide and Ca-superoxide in deeper layers and a thin layer of Ca-oxide directly in front of the electrode. If the potential of the electrode is cycled into the OER, this layer can be oxidized again to O_2 and Ca^{2+}. Based on further investigations with the RRDE, a model of the ORR in the Ca^{2+} containing DMSO can be discussed. In this model, a transition from peroxide formation to superoxide formation during ORR is attributed to a poisoning of the electrocatalyst by calcium oxide or strongly adsorbed calcium peroxide.

Furthermore, the Mg deposition on Pt and the Mg insertion into a Sb electrode is investigated using XPS. As electrolyte system a mixture of $MgCl_2$ and $AlCl_3$ in tetraglyme was used (MACC electrolyte). It could be shown that an irreversible Al deposition occurs both during the deposition of Mg and during the insertion of Mg. In addition, the surfaces accumulate with Cl-containing species. The importance of Cl in metal deposition is discussed. The electrochemical fabrication of Sb electrodes is also investigated with XPS. It has been shown that these electrodes oxidize to Sb_2O_3 by air contact. In the insertion process, a reduction of Sb_2O_3 takes place which proves that the insertion material is Sb and not Sb_2O_3.

This study also describes the construction of new electrochemical cells and the design of a sample transfer system between the electrochemical experiment and the XPS apparatus. Furthermore, this study provides a new experimental technique for the determination of diffusion coefficients and solubility of gases in liquids by time-resolved tracking of the mass signal of the gas through a thin liquid film by a mass spectrometer. The collection of these data is essential for the optimization of metal-O_2 batteries in the case of oxygen, as well as for kinetic studies of the ORR.

Contents

List of Figures

List of Tables

List of Abbreviations

CE Counter Electrode
CV Cyclic Voltammetry
DBBQ 2,5-Di-tert-butyl-1,4-benzoquinone
DMSO Dimethyl sulfoxide
EC Ethylen carbonat
EPR Electron paramagnetic resonance
Fc Ferrocene
LEED Low Energy Electron Diffraction
MACC Magnesium aluminium chloro complex
MS Mass Spectrometer
NMP N-methyl-2-pyrrolidone
OER Oxygen Evolution Reaction
ORR Oxygen Reduction Reaction
PC Propylen Carbonat
PTFE Polytetrafluoroethylene
PVDF Polyvinylidene fluoride
RDE Rotating Disk Elektrode
RE Reference Electrode
RRDE Rotating Ring Disk Elektrode
SEI Solid Electrolyte Interphase
SEM Secondary Electron Multiplier
SHE Standard Hydrogen Electrode
TBA Tetrabutylammonium

TEGDME	Tetraglyme
TEMPO	(2,2,6,6-Tetramethylpiperidin-1-yl)oxyl
TFSI	Trifluoromethanesulfonimide
THF	Tetrahydrofuran
TMPD	N,N,N′,N′-tetramethyl-p-phenylenediamine
TTF	Tetrathiafulvalene
TPU	Turbo pump unit
UHV	Ultra High Vacuum
UPD	Under Potential Deposition
WE	Working Electrode
XPS	X-Ray Photoelectron Spectroscopy

1

Introduction

This thesis addresses different questions from the research on metal-O_2 batteries. Therefore, this chapter shall give a short motivation for the relevance of research on new battery technologies. The technology of non-aqueous metal-air-batteries is explained. Furthermore, challenges for the development of this technology caused by side reactions of reactive oxygen species are explained. Since a large part of this thesis deals with the use of redox mediators for the oxygen reduction reaction (ORR) and the oxygen evolution reaction (OER), a short literature review on this topic was also written. At the end of this chapter the objectives for this thesis are formulated.

This is followed by a short introduction to the used experimental methods and finite difference simulation of electrochemical experiments.

The main part of this thesis consists of manuscripts, most of them published in peer reviewed journals. Each manuscript is a separate chapter. At the beginning of each manuscript, a short introduction to the topic under investigation is given.

1.1 | Motivation

Climate change is nowadays a topic of public interest. The "Fridays for Future" initiative [1], launched by Greta Thunberg, has attracted a lot of media attention in recent years. The European elections in 2019 have shown that climate policy is an important issue for German voters at the European level, as the party "Die Grünen", which focuses on climate policy issues, achieved the second best result. Looking at German climate policy, the reactor catastrophe in Fukushima in 2011 is probably responsible for the fact that climate policy issues became the focus of political attention. As a result, chancellor Merkel announced the exit from nuclear energy. The Paris Climate Agreement of December 2015 [2] also shows that climate policy is becoming global policy. As an outcome it declares that the global temperature rise in this century should be well below two degrees Celsius. Nowadays a correlation between the mean temperature on earth and the CO_2 content in the atmosphere is regarded as proven [3–5]. Therefore, an "Energiewende"[1] is necessary to meet the Paris climate goals of 2015. This means in particular that fossil fuels, such as coal, petrol or oil, must be dispensed within energy generation and vehicles in the long term, as this will save CO_2 emissions. Furthermore, the Paris Climate Conference decided on a complete abandonment of fossil fuels until 2050. Looking at the CO_2 savings for Germany, it has been shown that a significant reduction in CO_2 emissions was not observed until 2018. Recent evaluations show that the emission values aimed at by the German government for the year 2020 will probably be reached [6]. The reason for this is the corona crisis prevailing at the time of writing this thesis and the mild winter 2019/2020.

The achievement of the climate targets is linked to the necessity of storing electrical power. Electrochemistry can make a considerable contribution to the development of new electrochemical energy storage systems. Electrochemical energy storage devices have long since become part of our everyday life. The Li-ion battery is present in mobile phones, laptops and electric cars. It was first sold commercially in 1991 by Sony [7]. However, a lot of research was necessary until the market launch. In this context, the work of John B. Goodenough, M. Stanley Whittingham and Akira Yoshino, who were awarded the Nobel Prize in Chemistry in 2019 for the development of the lithium-ion battery, deserves special mention. In 1976 M. Stanley Whittingham succeeded in designing the first rechargeable Li-ion battery based with a Li anode and a TiS_2 cathode [8]. John B. Goodenough recognized the superiority of CoO_2 over TiS_2 as a cathode material, since higher voltages (4-5 V vs. $Li^+ | Li$) could be achieved and was able to publish the first electrochemical studies on this in 1980 [9]. Both CoO_2 and TiS_2 act as carriers for Li ions, which are incorporated into the material when the battery is discharged. One obstacle still had to be overcome before the product could be launched on the market: The use of metallic lithium as an anode had to be prevented, as the safety issues arising from the reactivity of Li metal were not acceptable. Akira Yoshino was able to avoid this safety risk by using carbon-based anode materials. In the following years, the energy density of Li-ion batteries could be increased by optimizing the individual battery components (electrolyte, electrodes, structure of the battery, ...). Nevertheless, even newer battery technologies use cobalt compounds as cathode material. Cobalt is mainly mined in the Congo, where child labor and generally inhumane mining conditions occur [10]. In addition, cobalt mining can lead to acidic mine water in the mines, according to a report by the United Nations Human Settlements Programme [11]. Li mining can also cause damage to the environment, as it is mainly mined from salt lakes in Chile, Argentina and Bolivia. The mining is connected with a large water consumption, which results in a sinking of the groundwater level in these dry regions [12]. The necessity of a cobalt-

---

[1] "Energiewende" is a german word, whose direct translation is "energy turnaround". It refers to the shift from fossil fuels as energy source to renewable energies and the associated infrastructural changes.

containing cathode is no longer given if oxygen reduction or sulfur reduction is introduced as the cathode reaction. This approach can be used to motivate Li-O_2 battery or Li-S battery. A further advantage is the higher theoretical energy density compared to Li-ion technology. Battery systems with higher energy densities than the Li-ion battery are indispensable for the development of new electric cars in order to achieve travel distances comparable to those of cars powered by fossil fuels. Furthermore, the substitution of Li by other alkali metals and alkaline earth metals is still conceivable. This would have the advantage of opening up different mining areas - also in Germany.

In general, it is advantageous to develop different energy storage technologies (not only chemical ones) in order to make optimum use of the different energy storage requirements that the "Energiewende" brings with it.

1.2 | Non-Aqueous Metal-Air-Batteries

Combining a metal anode with an oxygen cathode to obtain an electrochemical energy storage device is not a new concept. In 1878 the previously developed Zn battery (Leclanché cell) could be modified by a porous Pt/C cathode [13, 14]. This is the birth of the primary Zn-air battery. Commercialization did not occur until 1933 due to technical difficulties [15]. In general, primary metal-air cells based on aqueous electrolytes are nowadays used in hearing aids and for military and maritime purposes [14]. The representatives are Zn-air, Mg-air and Al-air cells. Since elements with a significantly lower standard electrode potential than the Standard Hydrogen Electrode (SHE) are used as anode materials, corrosion of the anode occurs in the aqueous electrolyte. Organic chemistry has produced a large number of molecules whose reductive stability is higher than that of water. Therefore, secondary Li-ion batteries are based on organic electrolytes. Nevertheless, it turns out that even these electrolytes do not withstand the strong reductive environment of a Li-ion battery. The electrolytes decompose. However, a layer of decomposition products can be formed on the electrodes by a suitable choice of electrolyte or by the use of additives. This solid electrolyte interphase (SEI) is Li^+ permeable, allowing the electrochemical reactions at the anode and cathode to be maintained [16, 17]. The development of metal-air batteries is mainly driven by the need to develop battery systems with energy densities greater than those of Li-ion batteries. In a first simple analysis there are two main reasons for the choice of chemical properties to design a high energy density battery:

1. A high charge carrier capacity of the anode and cathode materials, which is resulting in a high charge density of the battery.

2. A high voltage difference between the anode and cathode reaction

For the first issue, the density of the charge carriers of the anode and cathode materials is crucial. If one takes the metals as a starting point, the choice are Li, Na, Mg, K, Ca or Al. On the basis of these elements, the second point must now be considered. Thus fluorine would be the most attractive candidate. Due to the complications resulting from the high reactivity of fluorine, this idea can be rejected. The next two elements would then be oxygen and sulphur, which explains the interest in metal-O_2 and metal-S batteries.

The discussion will continue with metal-O_2 batteries. If one wants to calculate the theoretical energy density, the cathode reaction and the anode reaction must be taken into account. For the anode it is assumed in the first step that it consists of the pure metal. Thus the following reaction can be formulated for the metal anode consisting out of the metal M:[2]

$$\mathrm{M} \longrightarrow \mathrm{M}^{n+} + n\mathrm{e}^- \tag{1.1}$$

The oxygen reaction in the presence of the different cations was studied in a variety of non-aqueous electrolytes. It was shown that in contrast to the aqueous electrolyte, the ORR stops after the second reduction step. Thus the main products are superoxide and peroxide:

$$\mathrm{O_2} + \mathrm{e}^- \longrightarrow \mathrm{O_2}^{\cdot -} \tag{1.2}$$

$$\mathrm{O_2}^{\cdot -} + \mathrm{e}^- \longrightarrow \mathrm{O_2}^{2-} \tag{1.3}$$

Another reaction pathway that can result in the formation of peroxide is the disproportionate of the formed superoxide:

$$2\,\mathrm{O_2}^{\cdot -} \longrightarrow \mathrm{O_2}^{2-} + \mathrm{O_2} \tag{1.4}$$

With the help of the standard enthalpies of formation of the different superoxides and peroxides, the theoretical specific energy can be calculated. The values are shown in Wh/kg in Figure 1.1. Also shown is the theoretical operating voltage of the battery in respect to the a metal anode. This shows that if it is assumed that peroxide is the main product of battery discharge, the Li-O_2, Mg-O_2 and Ca-O_2 batteries achieve the highest theoretical specific energy densities. But what specific energy is currently achieved by the Li-ion technology? The current batteries installed in Tesla electric cars have a specific energy of 250-270 Wh/kg [18, 19]. Therefore a comparison with commercial batteries shows that metal-air batteries can achieve significantly higher energy densities, which is essential for the driving range of the car. However, to calculate a realistic specific energy, the other components of the battery that contribute to the weight of the battery must be taken into account. These are for example the electrolyte, separators, current collectors, the battery housing etc. If, for example, the theoretical specific energy of the

---

[2] The following reactions are formulated for the discharge of the battery. For the construction of a secondary battery it is necessary that the back reactions in the charging cycle are also possible.

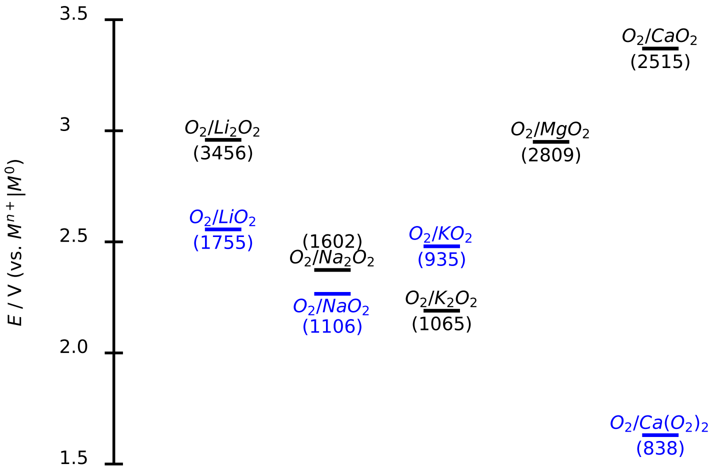

Figure 1.1: Theoretical specific energy of different metal-O_2 batteries based on superoxides and peroxides as discharge products. The standard potentials are given with respect to the corresponding metal of the superoxide/peroxide. Based on these potentials the theoretical specific energy (in Wh/kg) with respect to the mass of the product is displayed in brackets. To our knowledge no thermodynamic data is available for the $O_2/Mg(O_2)_2$ system.

battery installed by Tesla is calculated in analogy to the values shown in Figure 1.1, a value of $\approx$ 1032 Wh/kg is otained.[3] This example shows that the technical implementation of the battery results in a reduction of the theoretical specific energy density.

To illustrate which components in a metal-O_2 battery can contribute to its weight, this is to be explained by using an example from Li-O_2 cells. Figure 1.2 shows a schematic structure of the individual components. This structure was was developed in the "LiBaLu"-project supported by the German Federal Ministry of Education and Research [22]. Parts of this thesis were supported by this project. In general, different architectures of a Li-O_2 battery have been proposed [23, 24].

The structure in Figure 1.2 consists of the following components (from top to bottom): The gas diffusion layer is used to ensure a barrier-free transport of O_2 to the cathode. It can for example consist of a textile fleece. In addition, electrolyte leakage must be prevented here (for example by a porous PTFE membrane). The cathode itself needs to have a porous structure as well, since the transport of oxygen through the electrolyte to the cathode surface has to take place here. In general, the pores of the cathode are partly filled with the electrolyte. If a special

---

[3] This value was calculated based on the used cathode material $LiNi_{0.8}Co_{0.15}Al_{0.05}O_2$. For this material a theoretical capacity of 279 mAh/g at an average discharge voltage of 3.7 V vs. $Li^+ \mid Li$ [20, 21] is achieved.

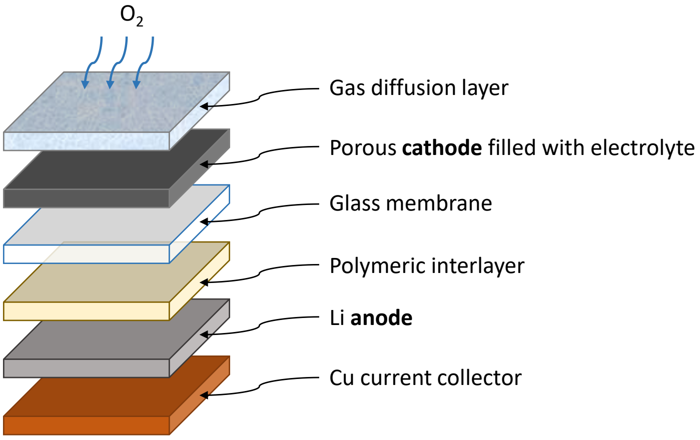

Figure 1.2: Schematic respresentation of the components of the Li-O_2 battery. This design was developed in the "LiBaLu"-project funded by the German Federal Ministry of Education and Research [22].

electrocatalyst is needed to catalyze the ORR and OER, it can be attached as particles to the porous cathode (usually fabricated out of carbon). In general, a large electrode surface area, as achieved by the porous cathode structure, is desirable. This is because the ORR product (Li_2O_2) is an electrical insulator and is deposited on the electrode surface [25–30]. The surface covered with Li_2O_2 can therefore no longer contribute to ORR, which means that the high surface area of the cathode can prevent the electrode surface from being completely deactivated. Furthermore, a separation of the Li anode by a glass membrane and a polymeric interlayer is necessary. The necessity is that a diffusion of O_2 to the Li anode must be avoided, otherwise the Li anode will decompose. The polymeric interlayer can prevent dendrite formation during Li plating while charging the battery. This phenomenon is a safety risk as it can lead to internal short circuits in the battery [31].[4] In addition, a glass membrane was found to be necessary because the electrolyte used in the LiBaLu framework is based on dimethyl sulfoxide (DMSO) which dissolves the common polymeric interlayers. Both the polymeric interlayer and the glass membrane must have a good Li^+ conductivity to be able to handle high current densities output from the battery. The Li anode is additionally contacted with a Cu current collector. Additional weight would also be generated by the battery housing. Furthermore, previous studies have shown that CO_2 must be removed from the air before it can be fed into the Li-O_2 battery as otherwise Li_2CO_3 is forming between CO_2 and Li_2O_2 [33]. This would require additional equipment to process the air, which must be considered in the calculation of the energy density of the battery system.

---

[4] The Samsung Galaxy Note 7 mobile phone is a prominent example for this. In 2016, pictures were broadcast in the media in which this mobile phone "exploded". One possible cause is the dendrite formation and the resulting short circuit in the battery [32].

1.3 | Redox Mediators

A popular additive for the electrolyte in metal-O_2 batteries are redox mediators. Redox mediators are organic molecules, halides or transition metal complexes that are dissolved in the electrolyte. They are electrochemically active in the potential window of the ORR or OER and support the product formation in the ORR or the dissolution of the ORR products in the OER. Since most studies with redox mediators have been performed on the Li-O_2 system, the concepts and functioning principle of redox mediators will be explained based on Li-O_2 cells.

In the absence of a redox mediator in the electrolyte, the oxygen dissolved in the electrolyte must be transported to the electrode surface. There it is reduced to Li_2O_2, the main product of ORR in the Li-O_2 battery (see Figure 1.3). Since Li_2O_2 is insoluble, it is deposited on the electrode surface. A disadvantage is that Li_2O_2 is a wide band gap insulator [25–30]. Thus, the cathode surface of the Li-O_2 cell becomes electronically passivated, causing the ORR to cease. Investigations on model electrodes of Bondue *et al.* showed that the 1-2 monolayers of Li_2O_2 on the electrode surface are sufficient to force a complete blockage of the electrode [26]. However, to meet the energy density requirements of the Li-O_2 technology, a larger storage of Li_2O_2 within the battery is necessary. A more effective storage of Li_2O_2 has been achieved by the addition of trace amounts of H_2O, acids or by using solvents as DMSO [34–36]. There the growth of Li_2O_2 often occurs in toroidal structures [36–40]. The greatest effect on the discharge capacity of the Li-O_2 has been observed when a redox mediator is added to the electrolyte. Thus ethylviologen [41, 42], phthalocyanines [43], polyoxometalates [44] and benzoquinones [45–48] have been proposed as redox mediators in Li-O_2 cells. The redox mediator RM_R is reduced to RM_R^- at the electrode (see Figure 1.3 (b)). RM_R^- diffuses into the electrolyte where it can reduce O_2 to Li_2O_2 which can grow on crystallization centers in the battery. This regenerates RM_R and can initiate again an ORR cycle. The molecule 2,5-di-tert-butyl-1,4-benzoquinone DBBQ showed an additional catalytic effect, whereby the ORR potential could be shifted positively [46]. Especially the mechanism of this molecule is discussed in detail in chapter 6. It has been shown that the use of a redox mediator for the ORR increases the discharge capacity by a factor of 100 compared to the same cell without mediator [46].

High overvoltages and slow kinetics were observed for the oxidation of Li_2O_2 [49]. Additionally, the ratio of the OER charge to the ORR charge is low. One reason for this is probably the poor electrical contact between the Li_2O_2 particles and the electrode surface. The heterogeneous oxidation of Li_2O_2 can only occur at the contact areas between the Li_2O_2 and the electrode. Therefore, some of the Li_2O_2 can remain unoxidized in the electrolyte volume in front of the cathode after the OER potential has been applied to the cathode. This process is shown in Figure 1.4 (a). The contact between the Li_2O_2 particles and the electrode surface is particularly poor if a mediator for ORR was previously used, because the Li_2O_2 deposition can take place

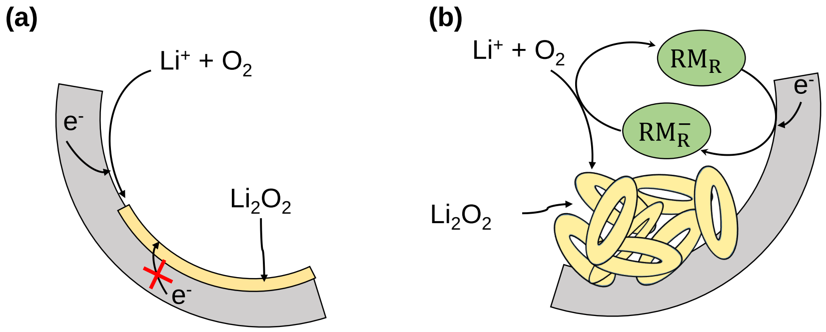

Figure 1.3: Illustration of the ORR mediated by a redox mediator RM_R (b) in comparison without a redox mediator (a). The impact on the Li_2O_2-growth is shown.

on nucleation centers within the battery and the Li_2O_2 particles formed have thus poor or no electrical contact with the electrode.[5] To overcome this problem, mobile redox mediators RM_O are also used for the OER. Among others tetrathiafulvalen [50, 51] , TEMPO [52] and halides [53–57] have been suggested as redox mediators for the OER. These are oxidized to RM_O^+ at the electrode surface and then diffuse to the Li_2O_2 particles to oxidize them. This regenerates RM_O and can initiate an OER cycle. As a result more Li_2O_2 can be oxidized than without RM_O. The mechanism of the electron transfer from Li_2O_2 to RM_O^+ (inner sphere vs. outer sphere) is the subject of current research [58–60].

Most controversial are the results concerning the OER redox mediator LiI. It could be shown that it is possible to have more than 900 cycles with a Li-O_2 battery when LiI is used as OER mediator with a lower overvoltage during charging than without LiI [53]. This result is supported by other publications where similar observations have been made [61, 62]. However, further studies have shown that in a LiI containing Li-O_2 cell with residual water in the electrolyte LiOH can form [54, 55]. Therefore the relevance of the use of LiI as a redox mediator depends on whether LiOH can be reversibly oxidized or not. In recent studies it is noted that the oxidation of LiOH is possible [63].

In the meantime, the first studies on the simultaneous use of an ORR and OER redox mediator have been published [64–66]. It was shown that the principle of using two mediators compared to a cell without mediators increases the cycling stability.

In the many studies published on redox mediators and their use in metal-O_2 batteries, the desired effects could be observed in the first cycles of the battery. Only a few long-term experiments have been published on this topic. In general, the use of redox mediators depends on their chemical stability in the metal-O_2 cell. This is also one subject of research in this thesis

---

[5] The same effect is resulting if Li_2O_2 is mainly generated by the disproportionation of the superoxide anions (see reaction 1.4)

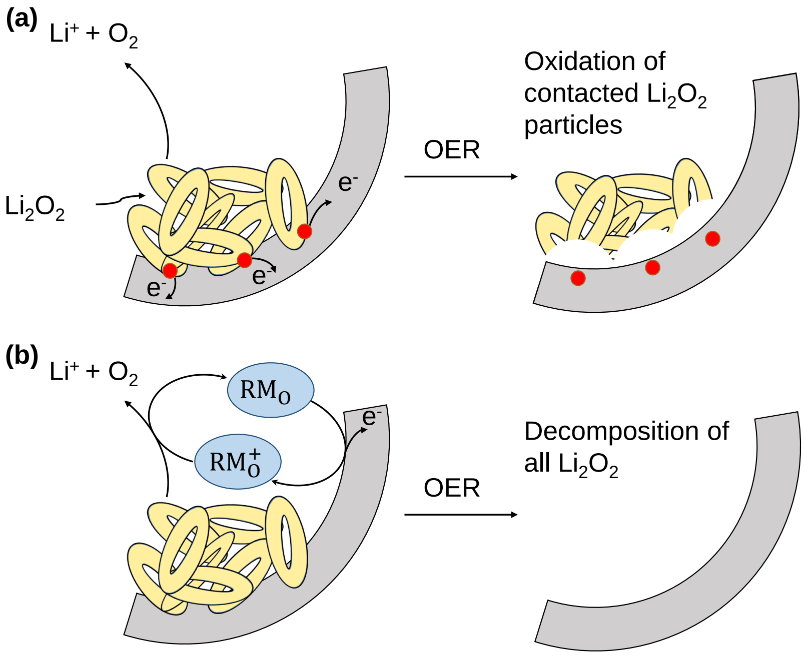

Figure 1.4: Illustration of the ORR mediated by a redox mediator RM_O (b) in comparison without a redox mediator (a). The red circles in (a) are representing the contact areas between the electrode and the Li_2O_2 particles. The impact on the dissolution of Li_2O_2 is shown.

(see chapter 4). Therefore the reactive oxygen species of the metal O_2 cell will be discussed in the following chapter.

1.4 | Reactive Oxygen Species

Reactive oxygen species in metal-O_2 batteries are mainly superoxide and singlet oxygen. A historical overview of research on metal-O_2 batteries is at this point interesting, which shows that the discovery of these problems took more than 20 years of research.

The first work of Abraham and Jinang in 1996 on Li-O_2 batteries was done in ethylene carbonate (EC) based electrolytes [67]. Carbonate based electrolytes were probably chosen because they have been used in many applications on Li-ion batteries and have good formation properties of an SEI [68, 69]. This would ensure the reversibility of lithium plating stripping on the anode side of the Li-O_2 cell. After this publication it was very long silent around the Li-O_2 battery. Again the interest in the Li-O_2 batteries increased around the year 2010. It is conceivable that, on the one hand, publications from the well known Bruce group [70–72] attracted attention to the topic, on the other hand, interest in battery research increased due to its importance for climate policy issues (as described in chapter 1.1). In addition IBM started the Battery

500 project in 2009 focusing on the development of the Li-O_2 battery for the use in electric vehicles [73]. Thus, a large number of publications appeared dealing with the Li-O_2 battery - all on carbonate-based electrolytes [70, 71, 74–81]. These studies have shown that the Li-O_2 technology can provide higher energy densities than Li-ion batteries. However, these studies have widely shown that the Li-O_2 cells have a worse long-term performance as well as higher voltage difference between the charge and discharge cycle. At this point, there was a shift in the approach of research on metal-air batteries. Thus, fundamental electrochemical research approaches (in situ analytical methods combined with electrochemical experiments) found their way into metal-air battery research in order to characterize the reaction and especially the side reactions and thus optimize this battery technology. This approach has been the subject of a series of publications in 2011, dealing with the characterization of the decomposition products of carbonate-based electrolytes. For example, Li_2CO_3, $C_3H_6(OCO_2Li)_2$, CH_3CO_2Li, HCO_2Li, CO_2 and H_2O were characterized using DEMS [82], XPS [83], Raman spectroscopy [82, 83], FTIR spectroscopy [83–86], NMR [84, 85], SERS [84] and XRD [85–87]. The origin of these decomposition products was traced back to the nucleophilicity of $O_2^{\cdot -}$. Freunberger *et al.* then postulated a reaction mechanism for the decomposition of propylene carbonate (PC) by $O_2^{\cdot -}$ as shown in Figure 1.5 [84].

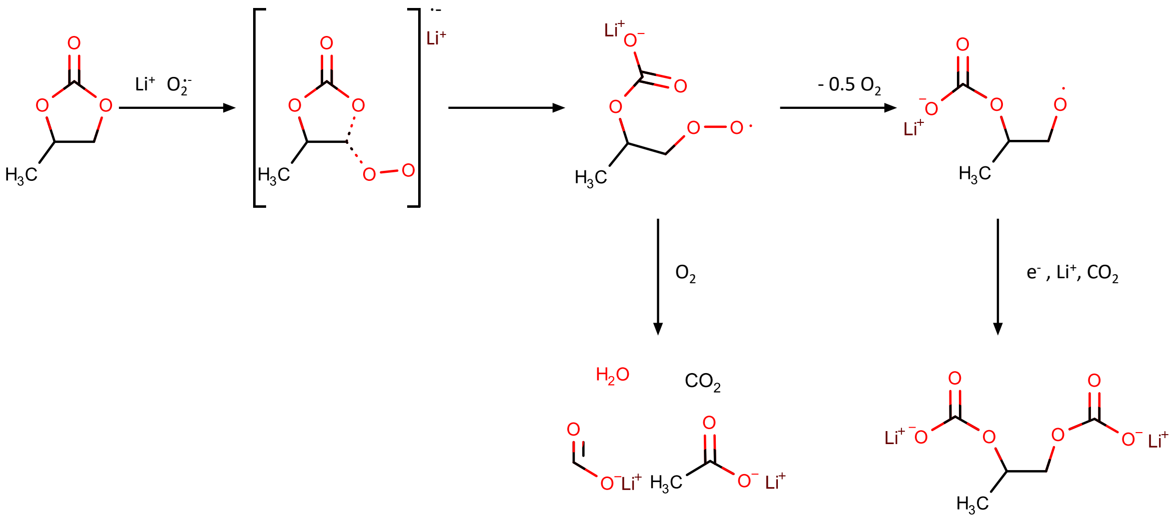

Figure 1.5: Decomposition mechanism of PC by $O_2^{\cdot -}$ as pusblished by Freunberger *et al.* [84].

At this point it is worth mentioning that already in 1991 Aurbach *et al.* were able to show with the help of cyclic voltammetry that the redox-couple ($O_2/O_2^{\cdot -}$) is irreversible in an electrolyte based on PC [88]. Furthermore, in this work the problem of a nucleophilic attack of $O_2^{\cdot -}$ on PC has already been mentioned.

After it was discovered that the carbonate based electrolytes are not suitable for use in a Li-O_2 battery, research on more suitable solvents started. Ethers, DMSO, acetonitrile, ionic liquids and hydrate melt were investigated for their properties as electrolyte in Li-O_2 batteries [89–95]. In parallel, the oxygen reduction in the presence of different cations was investigated [96–102]. In addition, extensive quantum chemical screenings were performed on the activation barrier of a nucleophilic attack by $O_2^{\cdot -}$ on the solvent [103–108]. Experimentally, decomposition products of the numerous electrolytes under investigation were also discovered. However, the experimental observations did not yield a consistent picture with the quantum chemical calculations. Electrolytes which showed a high activation barrier for a nucleophilic attack of $O_2^{\cdot -}$ in the quantum mechanical calculation, showed a poor performance in the experiment. A further contradiction concerning the reactivity of $O_2^{\cdot -}$ becomes apparent when the reversibility of the redox pair ($O_2/O_2^{\cdot -}$) in K^+ and TBA^+ (tetrabutylammonium) containing DMSO is considered. Here a reversible redox pair is observed [109, 110]. In the presence of Li^+, however, DEMS measurements showed that the reversibility is only 50% [26, 58, 111]. Thus, an explanation regarding reactivity of $O_2^{\cdot -}$, as in the case of carbonate based electrolyte, is not valid for all solvent classes. Already in 2011 Hassoun *et al.* postulated the possibility that during the oxidation of Li_2O_2 the electronically excited singlet O_2 can be formed [112].

With the help of molecular orbital theory the electronic structures of O_2 can be clarified. The molecular orbital diagrams are shown in Figure 1.6.

If one follows *Pauli's* exclusion principle and *Hunds's* rules when filling up the molecular orbitals, the ground state of O_2 is the tripplet state $^3\Sigma_g^-$. This also illustrates the diradical character of the ground state of O_2. Thus the singlet states $^1\Delta_g$ and $^1\Sigma_g^+$ of O_2 are electronic excitation of $^3\Sigma_g^-$. The excitation energies are $\Delta H(^3\Sigma_g^- \rightarrow {}^1\Delta_g) = 94\ \mathrm{kJ\,mol^{-1}}$ and $\Delta H(^3\Sigma_g^- \rightarrow {}^1\Sigma_g^+) = 157\ \mathrm{kJ\,mol^{-1}}$ [114]. In an electrochemical experiment one would thus observe the formation of $^1\Delta_g$ O_2 0.5 V above the formation of $^3\Sigma_g^-$ O_2 during the oxidation of peroxides. With the help of electron paramagnetic resonance spectrocopy (EPR), this could also be confirmed experimentally in 2016 by Wandt *et al.* [115].[6] The term symbol $^1\Delta_g$ O_2 is written as $^1O_2$ in the following.

The findings of Wandt *et al.* were followed by a series of further investigations on the $^1O_2$ evolution in metal-O_2 [116–122]. For instance $^1O_2$ could be detected directly in the battery by the 1270 nm emission during decay into the tripplet state [116]. Furthermore, the formation of $^1O_2$ in Na-O_2 cells could be observed during the oxidation of NaO_2 [119]. One of the most important findings has only recently been made. Freunberger and coworkers have identified the disproportionation of $O_2^{\cdot -}$ as a new reaction pathway for the formation of $^1O_2$ [118]. In

---

[6] The detection was carried out with the spin-trap approach: The molecule 4-oxo-TEMP (2,2,6,6-tetramethyl-4-piperidone) is transformed by $^1O_2$ into the stable radical TEMPO (4- oxo-2,2,6,6-tetramethyl-1-piperidinyloxy) which has a characteristic EPR spectrum.

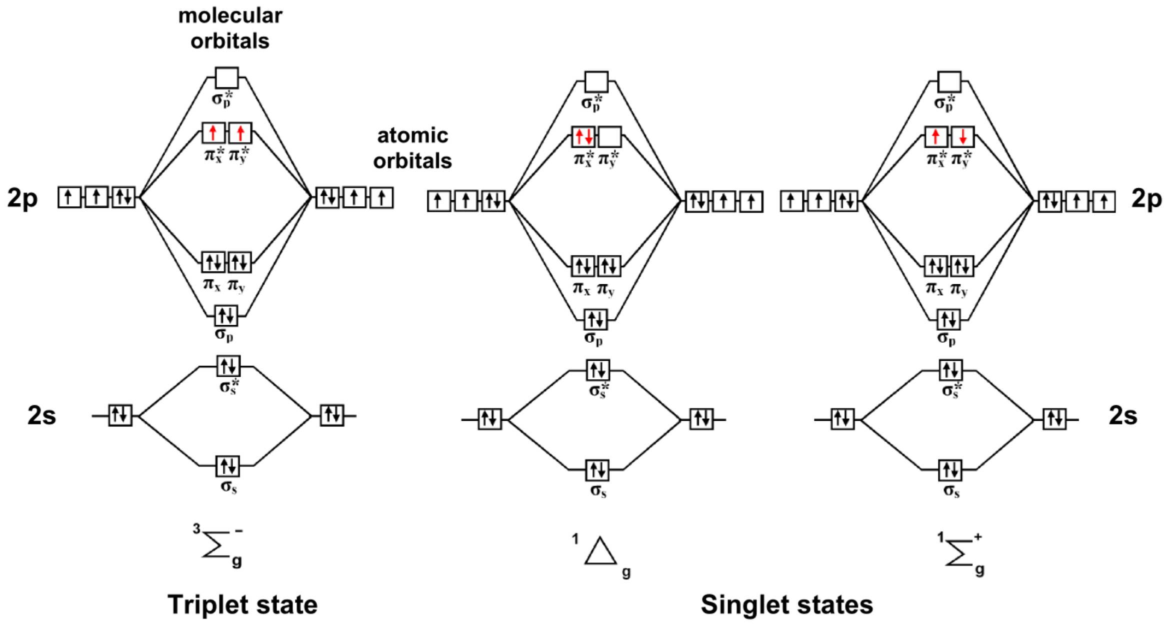

Figure 1.6: Molecular orbital digramms of the triplet ground state $^3\Sigma_g^-$ of O_2 and its excites singlet states $^1\Delta_g$ and $^1\Sigma_g^+$. Taken from [113].

this case $^1O_2$ is formed as a proportion of the overall O_2 evolution as described in the following reaction equation:

$$2\,O_2^{\cdot-} \longrightarrow O_2^{2-} + x \cdot {}^3O_2 + (1-x) \cdot {}^1O_2 \tag{1.5}$$

It was observed that the amount of $^1O_2$ increases with decreasing Lewis acidity of the cation. At the same time the tendency of the superoxide to disproportionate decreases. Thus, especially high $^1O_2$ contents($\approx$ 10-20%) were observed with mixtures of Li^+ and a soft cation like TBA^+. The authors of [118] were able to explain this observation by quantum chemical calculations of the reaction free energy profiles. Furthermore, a correlation between the formed CO_3^{2-}, a well-known side product in metal O_2 batteries, and the formed $^1O_2$ could be found. In general, these studies have shown why $^1O_2$ is also formed during the ORR, since the disproportionation of superoxide plays an important role here [103, 123, 124].

$^1O_2$ undergoes completely different chemical reactions than $^3O_2$. For example, in organic chemistry [4+2]-cycloadditions, [2+2]-cycloadditions, ene-reactions, the oxidation of thioethers to sulfoxides and the formation of organometallic dioxygen complexes are known [125]. The [2+2]-cycloaddition is responsible for the deactivation of the redox mediator TTF, as was also postulated in the publication in chapter 4 and which could be proven in 2019 by Kwak et al. [120]. The product is a cyclic TTF peroxide which fragments into two 1,3-dithiol-2-one molecules (as shown in 1.7) [126].

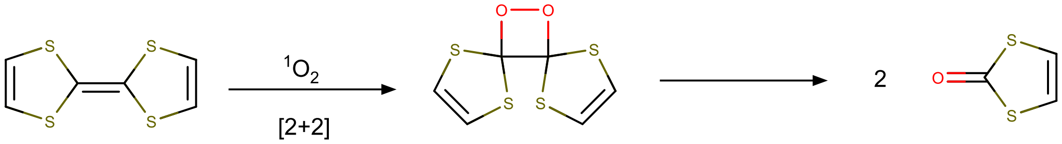

Figure 1.7: Deactivation of TTF by singlet oxygen.

In summary it can be said that one of the key steps in the development of a nonaqueous metal-O_2 battery is to increase the reversibility of cathode reactions. Thus, side reactions triggered by reactive oxygen species must be reduced. The current state of research shows that this can be achieved mainly by suppressing the $^1O_2$ production. For this purpose, first concepts, such as the introduction of $^1O_2$ quenchers have already been outlined [116, 121]. However, this is the current state of research and the long-term stability of the cells has to be proven.

1.5 | Objectives for this thesis

This thesis deals with questions from the field of metal-O_2 battery research. For some of these projects it was necessary to develop new electrochemical cells or to modify experimental setups with the workshops of the Institute of Physical and Theoretical Chemistry of the University of Bonn:

- The Thin-Layer DEMS cell already constructed in my master thesis [127] has to be optimized regarding the current distribution, because in the CVs with redox systems with two successive electron transfers, the peak heights in the CVs did not meet the expectation. The modified cell can be seen in chapter 4.
- To determine the solubility of O_2 and the diffusion coefficient of O_2 in the electrolyte we developed a measuring cell for combination with mass spectrometry (see chapter 5). The collection of these data is essential for the understanding of the ORR in different electrolytes and a series of data on DMSO based electrolytes has been published [128].
- For the characterization of electrode surfaces after the electrochemical experiments using XPS a transfer system for the samples between the glovebox and the UHV chamber is necessary. This system should protect especially sensitive samples from contact with air. The experimental setup and modifications are described in chapter 2.4.2.

Furthermore, the following questions from the metal-O_2 battery research were investigated:

- The stability of OER redox mediators against reactive oxygen species in the Li-O_2 cell should be analyzed (see chapter 4)
- A mechanistic analysis of the kinetics of Li_2O_2 oxidation by the redox mediator should be carried out (see chapter 4)
- A mechanistic analysis of the ORR by the redox mediator DBBQ is carried out. The focus of this research was on the dependence of the conducting salt concentration, the used solvent and the influence of different cations on the redox mediator and the ORR (see chapter 6 and chapter 7).
- The electrode surfaces of Au and Pt are examined by XPS after the ORR in Ca^{2+} containing DMSO. Furthermore, the reaction mechanism of the ORR in Ca^{2+} containing DMSO shall be further investigated. The presence of possible reaction paths such as the disproportionation of $O_2^{\cdot-}$ in the presence of Ca^{2+} has to be checked. These studies are summarized in chapter 7.

- Sb electrodes should be characterized by XPS after the insertion of Mg into Sb from MACC/TEGDME. XPS characterization of the electrochemically deposited Sb layers will also be performed (see chapter 8).

2

Experimental methods

2.1 | The Three Electrode Arrangement

In most electrochemical experiments a three electrode arrangement is chosen. The reaction, which is the subject of the investigation, is examined at the working electrode (WE). In addition a counter electrode (CE) and a reference electrode (RE) are inserted into the electrolyte solution. Using a potentiostat, the three electrodes can be connected to the WE in such a way that the current flow is adjusted between the WE and CE and no current flows between WE and RE. Descriptions to the working principle of a potentiostat can be found in common electrochemistry books [129, 130]. A sketch of a common glass cell for electrochemical experiments, as it was used in this study, is shown in Figure 2.1. This figure shows that there is a separate

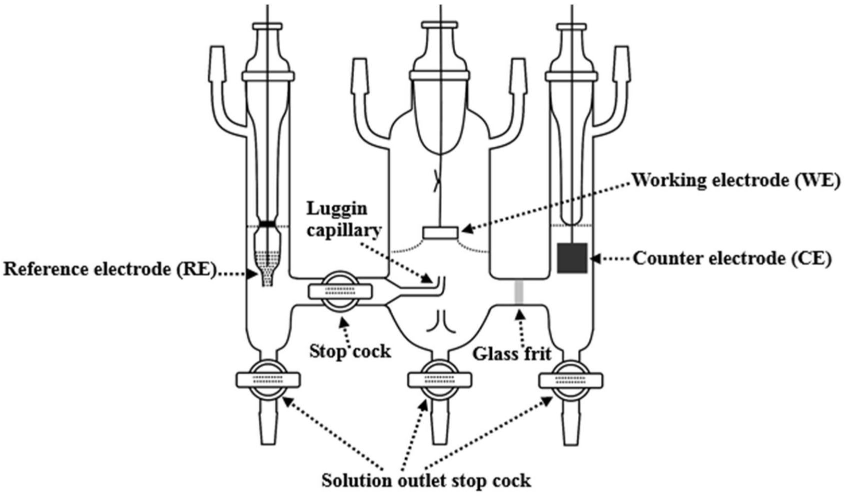

Figure 2.1: Sketch of an electrochemical glass cell as it was used in this study. This cell has separate compartments for the reference electrode, working electrode and counter electrode. Taken form [131].

electrode compartment for each of the three electrodes. In addition, the glass cell is purged with highly pure Ar or Ar/O_2 gas during the measurement. The individual electrodes make special demands on the success of the experiment, which will be briefly summarized:

> The **working electrode** (RE) is made out of the electrocatalyst that will be investigated for its activity in this study. Due to the catalytic reactivity of the electrode material, the working electrode defines the potential window in which the electrochemical experiment can be performed. Classically, for an aqueous electrolyte, the potential limits between hydrogen and oxygen evolution are selected. In an organic electrolyte the stability window of the electrolyte determines the potential limits. In this study, disc electrodes of Au and Pt were chosen as WE for the XPS experiments (see chapter 2.4.2). For the RRDE experiments Au and Pt disk electrodes embedded in PTFE and surrounded by a concentric Au or Pt ring electrode (see chapter 2.2) and for the DEMS measurements a porous PTFE membrane with a 50 nm thick evaporated Au layer (see chapter 2.3) are used. The XPS electrodes and the RRDE electrodes were checked for cleanliness before starting the experiment. This was done by cycling in a sulfuric acid electrolyte until the characteristic adsorption charges for oxide formation on Pt and Au and for hydrogen adsorption on Pt were observed. Typical CVs obtained for Pt and Au are shown in Figure 2.2.

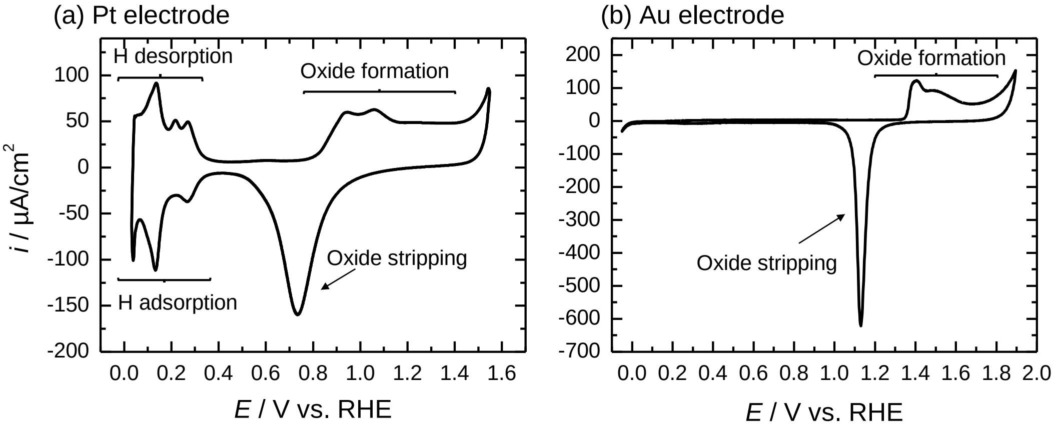

Figure 2.2: Typical CVs recorded for a Pt (a) and Au (b) electrode in 0.5 M H_2SO_4 wit a sweep rate of 50 mV s^{-1}. The electrolyte was purged wit Ar. The adsorption regions of H and O are indicated in the figures.

> The **counter electrode** (CE) used in this study is always made out of the same electrode material as the WE to avoid cross-contamination of different electrocatalysts. The task of this electrode is to provide the current necessary to set the desired potential at the WE. Therefore, it is advisable to ensure that the electrode surface of the CE is always larger

than that of the WE. Products that are formed at the CE should not reach the WE, so that the measurement is not disturbed by contamination or side reactions. Therefore, if possible, the WE and CE are separated by a porous glass frit (as shown in Figure 2.1).

The **reference electrode** (RE) should provide a stable potential over the duration of the experiment. Three different reference electrodes were used in this study. For the measurements in the aqueous electrolyte a reversible hydrogen electrode (RHE) was used. This consists of a Pt-wire around which a hydrogen atmosphere is arranged (see sketch of the RHE in Figure 2.1). For this purpose, the hydrogen atmosphere is generated electrochemically at the beginning of each new measurement day. For the measurements in the organic electrolyte an Ag-wire immersed in an electrolyte containing Ag^+ is used. The standard potentials of this reference electrode are tabulated in [132]. For the investigations concerning the Mg deposition, a Mg wire immersed in a Mg^{2+} containing electrolyte is used. If the electrolyte in the WE compartment and in the RE compartment are different, it is important to ensure that they are not mixed. This was achieved in the glass cell by means of a closed, but electrolyte wetted glass stop cock. In DEMS measurements, the reference electrode was introduced into the electrochemical cell with a tube sealed with a small glass ball. A detailed description of this reference electrode can be found in [90]. In both cases the electrical contact between the WE and RE is ensured by the electrolyte wetted glass surfaces. In order not to disturb the chemical equilibrium between the reference electrode and the reference electrolyte, a current-less potential measurement is also required.

With this three electrode arrangement, a wide variety of experiments can now be carried out. The experiments in this study were performed with different potential programs. The most common method of analysis is cyclic votammetry (CV) where the potential varies periodically between a lower limit and an upper limit. The variation is linear and the potential change is called sweep rate. In chapter 3.2 some more details concerning CV are given. In general, the potential programs were adjusted on a computer and transferred via an analog/digital converter to the potentiostat. The data acquisition was also done by the analog/digital converter and the corresponding programs were written in LabView. These programs were developed by Dr. Philip Reinsberg and details about the data acquisition can be found in his PhD thesis [96].

2.2 | Rotating Ring Disk Electrode

The current response due to oxidation/reduction of a species at the electrode is a combination of the electron transfer kinetics and the transport of the species to the electrode. These electroactive species can move towards the electrode in different ways. The movement is realized via diffusion along the concentration gradient in front of the electrode, migration of charged species in the electric field and the forced movement due to convection. Migration can often be neglected if the supporting salt concentration of the electrolyte is high. Convection is the movement of matter in its respective physical state variables in a flowing fluid. Convection is a phenomenon that appears in every electrochemical experiment, as Veniamin Levich, one of the pioneers of RRDE, appropriately formulated [133]:

> *"Motion of the solution in natural convection is spontaneous and arises due to forces originating from heterogeneous reactions. Such forces usually follow the change in the density of the solution which accompany the reaction."* (p.127 taken from [133])

Since natural convection is a spontaneous process, it cannot be controlled and leads to inaccuracies in the determination of kinetic data of the electron transfer out of the flowwing current. Therefore it is important to control the mass transport of electroactive species towards the electrode by forced convection methods. One approach are rotating electrode methods as the Rotating Disk Electrode (RDE) and the Rotating Ring Disk Electrode (RRDE). A sketch of the RRDE electrode is shown in Figure 2.3. This illustration shows, that the RRDE consists out of a disk electrode with a radius of r_1. The disk electrode is surrounded by a concentric ring electrode with an inner radius of r_2 and an outer radius of r_3. The disk electrode and the ring electrode are immersed into an electrically insulating material, for example PTFE, to electrically isolate the disk and ring electrode. A Bipotentiostat [1] has to be used to control the potential of both electrodes separately.

---

[1] A Bipotentiostat is a potentiostat which is capable of controlling two working electrodes at the same time. In total 4 electrode are used and the potentials of the two working electrodes are adjusted against the same reference. Both working electrodes are connected to the same counter electrode.

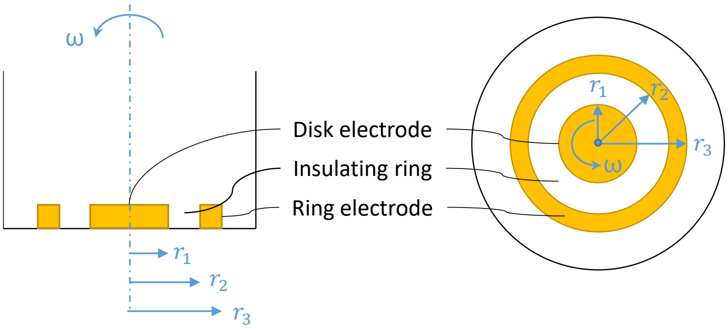

Figure 2.3: Sketch of the Rotating Ring Disk Electrode as a cross section (left figure) and as top view on the electrode surface (right figure).

In a RRDE setup the convection of the electrolyte is forced by rotating the electrode around its own axis (see axis of rotation in Figure 2.3). The underlying mathematical description of the velocity field of a liquid in front of a rotating cylinder was carried out by Von Karman [134] and Cochran [135]. For the speed components in the direction perpendicular to the electrode (z-direction, v_z), radial to the electrode (r-direction, v_r) and azimuthal v_ϕ series expansions were derived:

$$v_z = \sqrt{\omega\nu}\left(-a\gamma^2 + \frac{\gamma^3}{3} + \frac{b\gamma^4}{6} + \dots\right) \tag{2.1}$$

$$v_r = r\omega\left(a\gamma - \frac{\gamma^2}{2} - \frac{1}{3}b\gamma^3 + \dots\right) \tag{2.2}$$

$$v_\phi = r\omega\left(1 + b\gamma + \frac{1}{3}a\gamma^3 + \dots\right) \tag{2.3}$$

in which $a = 0.51023$ and $b = -0.6159$. In equation 2.1 and 2.2 is z the distance perpendicular from the electrode surface. r is the radial distance from the center of the RRDE and ν is the kinematic viscosity of the electrolyte. ω is the angular velocity of the RRDE electrode and is dependent on the rotation frequency f of the RRDE electrode as follows:

$$\omega = 2\pi f \tag{2.4}$$

Furthermore, γ is defined as:

$$\gamma = \sqrt{\frac{\omega}{\nu}}z \tag{2.5}$$

A common approximation made for the derivation of the equations describing phenomena of the RRDE is to stop the series expansions in 2.1 and 2.2 after the first term. This approach is chosen because the transport phenomena relevant for RRDE have to be described in the diffusion boundary layer and thus $z \to 0$. Thus $\gamma \to 0$ also applies and only $a = 0.51023$

is needed for further consideration. Further remarks to this approximation are discussed in appendix D. With the help of equations 2.1-2.3 the velocity field in front of the electrode can be calculated. The velocity profiles from two different viewpoints are shown in Figure 2.4 as a stream line profile.

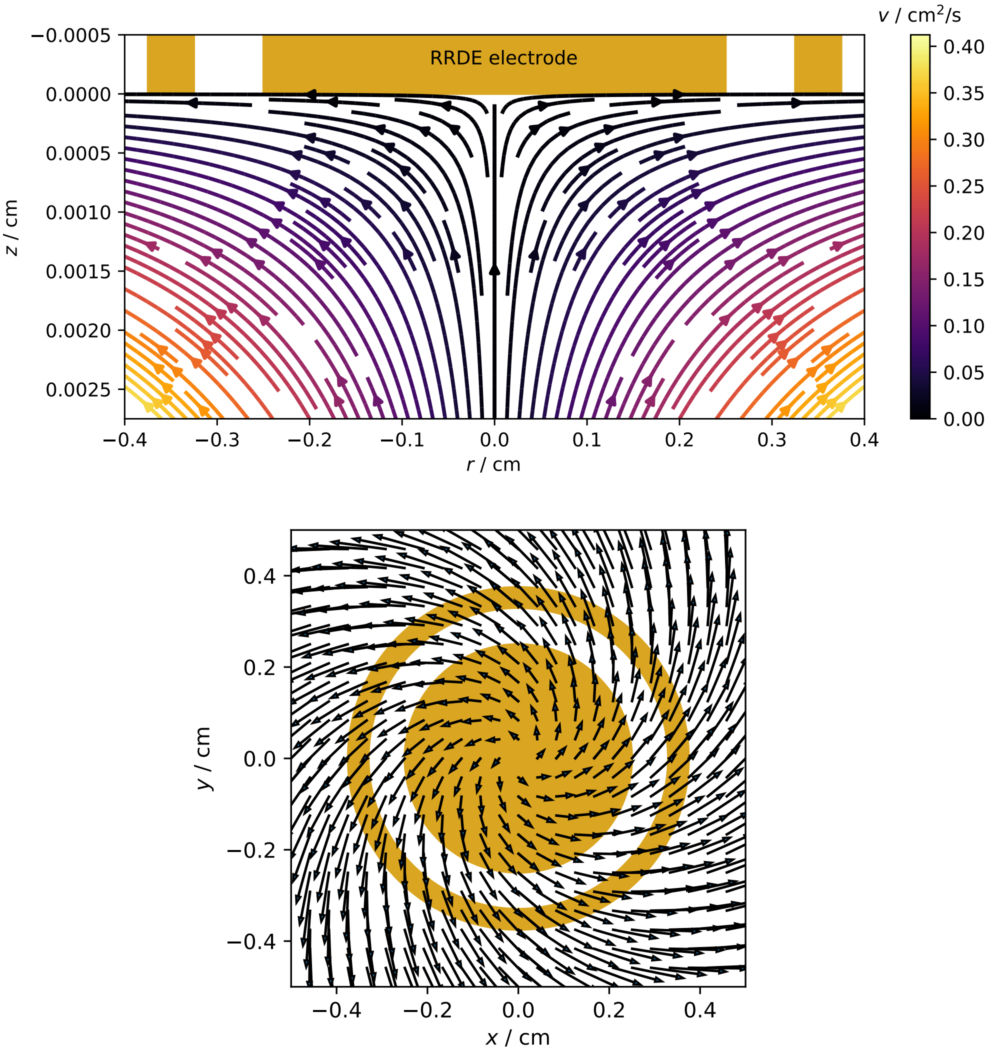

Figure 2.4: **Top:** Stream line profile calculated according to equations 2.1 and 2.2 (side view). The colour code of the stream lines is indicating the respective speed of the electrolyte ($\sqrt{v_z^2 + v_r^2}$). **Bottom:** stream line profile calculated according to equations 2.2 and 2.3 (top view). The vector length is an measure for the speed of the electrolyte ($\sqrt{v_z^2 + v_\phi^2}$). The following parameters were chosen: $f = 4$ Hz, $\nu = 2.942 \cdot 10^{-2}$ cm^2 s^{-1}. A sketch of one of the RRDE geometries used in this study ($r_1 = 0.250$ cm, $r_1 = 0.325$ cm and $r_1 = 0.375$ cm) was also included in the figure.

The top stream line profile in Figure 2.4 shows the movement of the electrolyte caused by the rotation of the electrode. The electrolyte is sucked to the electrode along the axis of rotation. It is then thrown away in a radial direction. Furthermore, Figure 2.4 shows the speed of the electrolyte via a colour code. It can be seen that the electrolyte speed approaches $0\,\mathrm{cm^2\,s^{-1}}$ at the electrode (z=0). Therefore, the mass transport close to the electrode is mainly determined by diffusion. The speed of the electrolyte increases with increasing distance perpendicular to the electrode and radially from the axis of rotation.[2] For the upper velocity field shown in Figure 2.4, the scale of the z-axis is in the order of magnitude of the diffusion boundary layer as expected for a diffusion coefficient of $10^{-6}\ \mathrm{cm^2\,s^{-1}}$ $f = 4$ Hz and $\nu = 2.942 \cdot 10^{-2}\ \mathrm{cm^2\,s^{-1}}$. In addition, the current field is calculated from a top view of the electrode (see Figure 2.4). Here the vector lengths are a measure for the velocity of the electrolyte. It can be seen that the electrolyte in the centre of the disc electrode comes to stagnation. The speed of the electrolyte increases with increasing radius from the center of the disc electrode. Furthermore, the angular velocity component (equation 2.3) causes a rotation of the flow field in the direction of rotation of the electrode. The angular velocity component is not important for the derivation of the Farday current of an RRDE experiment. This is due to the fact that the RRDE electrode is symmetrical around the centre of the disc electrode. Thus a concentration gradient $\frac{\partial c}{\partial \theta} = 0$ and does not contribute to the current [133].

Due to the forced convection caused by the rotation of the electrode, a stationary state in the concentration profile of the reactants and products in front of the electrode is quickly established compared to a system without convection. The steepness of this concentration profile depends on the selected rotation frequency of the electrode. As the rotation frequency increases, the concentration profile becomes steeper and thus the disk current increases. If the disk electrode potential is chosen such that the concentration of reactants at the surface is zero, a mass transport controlled limiting current I_L is obtained. This can be calculated using the Levich equation:

$$I_L = 0.62nFD^{2/3}\nu^{-1/6}c_0\omega^{1/2} \tag{2.6}$$

In equation 2.6 n is the number of transferred electrons in the reaction, F is the Faraday constant, D is the diffusion coefficient of the reactant and c_0 describes the concentration of the reactant in the electrolyte. For the calculation of I_L there are also more complex expressions [136]:

$$I_L = zF\omega^{1/2}c_0 \frac{0.62048\left(\frac{\nu}{D}\right)^{-2/3}}{1 + 0.2980\left(\frac{\nu}{D}\right)^{-1/3} + 0.14514\left(\frac{\nu}{D}\right)^{-2/3}} \tag{2.7}$$

There the authors did not terminate the velocity field in 2.1 and 2.2 after the first term in the derivation of their expression. The error of the limiting current compared to the Levich equa-

---

[2] It must be noted, that the displayed velocity in the upper figure of Figure 2.4 was calculated only by v_z and v_r and the angular component was neglected. Thus, the underlying angular electrolyte velocity is the observational frame of reference for the shown velocity profile.

tion for a relevant system in this study (O_2 in DMSO) is in the range of 3% [96]. Even more accurate results can be achieved with numerical simulations (see Appendix D). However, due to their complexity, equation 2.7 is not practical for the evaluation of the RRDE data.

In 1957, Levich and Koutecký succeeded in deriving an expression which expresses the fraction of the disk current I_D caused by the transport of the reactants to the electrode as well as the fraction caused by the kinetics of the electron transfer I_k [137]:

$$\frac{1}{I_D} = \frac{1}{I_k} + \frac{1}{0.62nFD^{2/3}\nu^{-1/6}c_0}\omega^{-1/2} \tag{2.8}$$

Equation 2.8 is known as Levich- Koutecký equation. With the help of this equation the disk current can be extrapolated to an infinite rotation. The resulting value is free of the part of the reactants' transport to the electrode and thus reflects the kinetic current.

By introducing a ring electrode to the RDE, the RRDE allows the investigation of intermediates of the disc reaction. This is due to the fact, that the ring is located downstream of the electrolyte velocity field (see Figure 2.4). Therefore intermediates and products of the disc reaction are swept towards the ring electrode. If these products or intermediates are electrochemically active, the ring potential can be selected so that a current response occurs. In the following, the transport of the species to the ring will be illustrated by using simulated concentration profiles (for details on the simulation see chapter 3.3). For this purpose a sudden transformation of species A at the disk to B is chosen (disk: $\mathrm{A} \longrightarrow \mathrm{B} + \mathrm{e}^-$). In the experiment this would be realized by a potential jump with a sufficiently strong offset from the equilibrium potential of the reaction $\mathrm{A} \longrightarrow \mathrm{B} + \mathrm{e}^-$. For this reason, the following also refers to a potential jump experiment. The back reaction takes place at the ring electrode (ring: $\mathrm{B} + \mathrm{e}^- \longrightarrow \mathrm{A}$). Both reactions are mass transport controlled, i.e. the concentration of A at the disc electrode is 0 and the concentration B at the ring electrode is 0. The resulting current transients are shown in Figure 2.5. Figure 2.6 shows the concentration profiles of species B between the disc electrode and the ring electrode as a contour line profile. A total of 6 concentration profiles are shown at different points in time after the start of the experiment. The respective times are also shown as circles in the transients in Figure 2.5. The underlying velocity profile is the already shown profile in Figure 2.4.

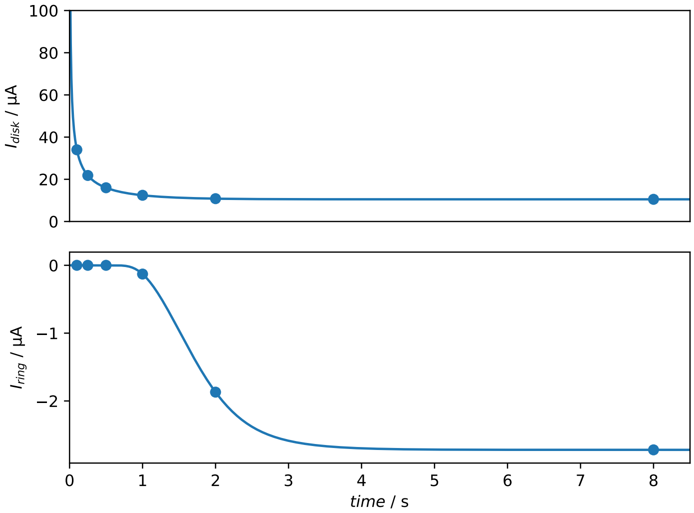

Figure 2.5: Simulated current transients in a RRDE experiment after a potential jump. Top figure: Disk current after a sudden oxidation of species A to species B. Bottom figure: Resulting ring current transients due to the mass transport limited reduction of species B to A. For this simulation a RRDE, which was also used in this study, with ($r_1 = 0.250\,\mathrm{cm}$, $r_2 = 0.325\,\mathrm{cm}$ and $r_3 = 0.375\,\mathrm{cm}$) was used. The diffusion coefficients are: $D(\mathrm{A}) = D(\mathrm{B}) = 1 \cdot 10^{-6}\,\mathrm{cm}^2\,\mathrm{s}^{-1}$. The chosen kinematic viscosity is: $\nu = 2.942 \cdot 10^{-2}\,\mathrm{cm}^2\,\mathrm{s}^{-1}$ and the rotation frequency is 4 Hz. Details about the algorithm are discussed in chapter 3.3

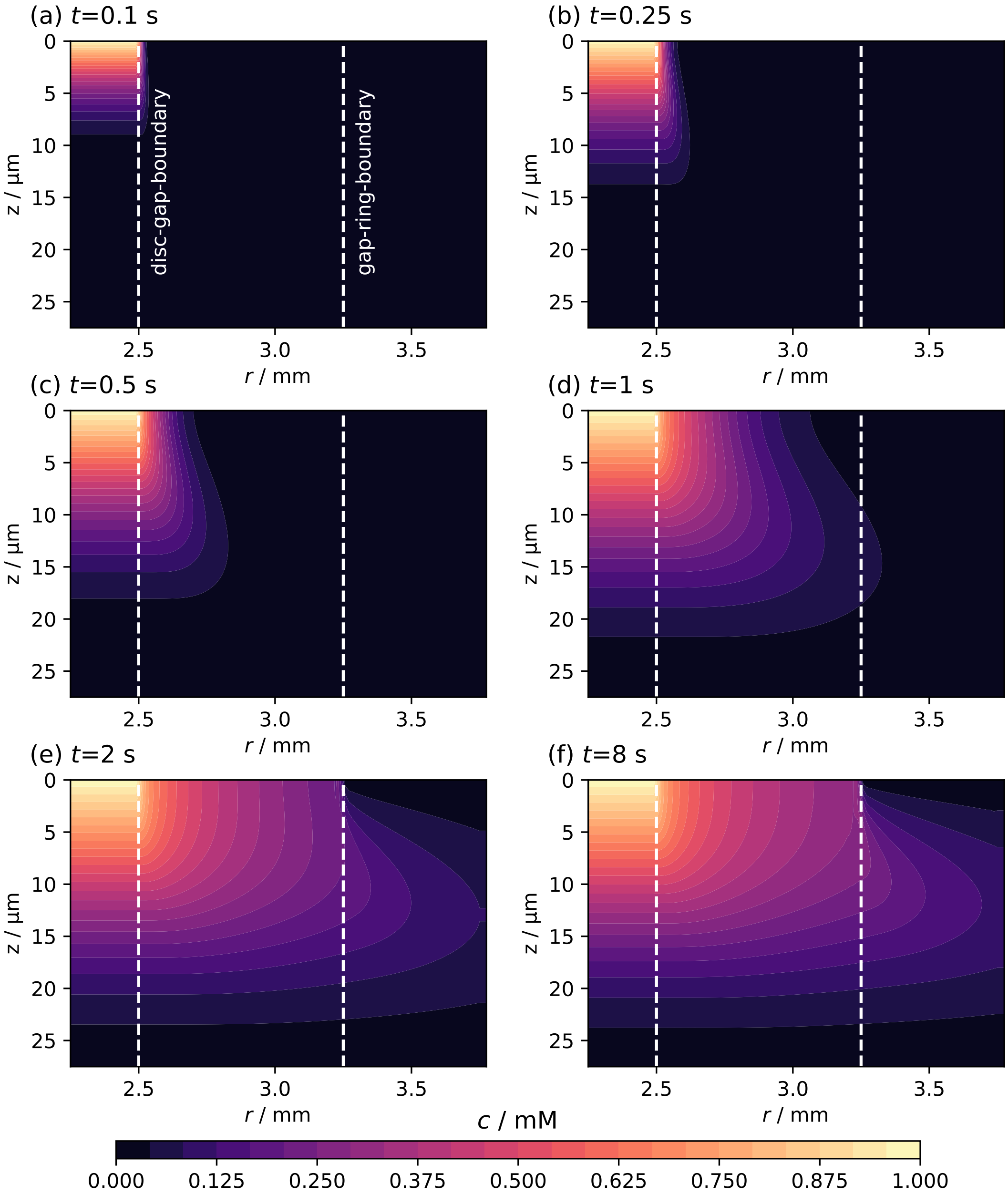

Figure 2.6: Simulated concentration profiles of species B in front of an RRDE electrode after a potential jump. The concentration profile is plotted as contour plot for different times after the potential jump shown in Figure 2.5. The x-axis is showing the radial distance from the center of the disk electrode. The disk-gap and gap-ring boundaries are indicated as dashed white lines. The y-axis is showing the distance perpendicular from the electrode surface.

As Figure 2.5 shows, the disc current increases rapidly after the potential jump. This is due to the steep concentration profile perpendicular to the disc electrode (z-direction) (see Figure 2.6 (a)). As the experiment progresses, the concentration profile flattens in the z-direction (see Figure 2.6 (b)-(e)), resulting in a decrease of the disk current. A stationary concentration profile in front of the disc electrode and thus a diffusion limit current is established (see Figure 2.6 (f)). For the propagation of the concentration profile in the z-direction, equation 2.9 describes a relationship for the RRDE experiment, similar to the Nernst diffusion boundary layer, with a dependence of ω.

$$\delta = 1.61 \nu^{1/6} D^{1/3} \omega^{-1/2} \tag{2.9}$$

For the underlying parameters of the simulation $\delta = 26.19\,\mu\text{m}$ is obtained, which is in good agreement to the propagation of the concentration profile of B in z-direction in Figure 2.6.

In addition, Figure 2.6 shows the propagation of the concentration profile of species B in radial direction. The concentration profiles up to $t = 0.5\,\text{s}$ show that the concentration profile has not yet propagated to the gap-ring-boundary. Consequently, no ring current is detected up to this point. Only after $t = 1\,\text{s}$ the concentration profile breaks through the gap-ring-boundary layer (see Figure 2.6 (d)), which results in an increase of the ring current (see Figure 2.5). The time required for the transport of species B from the disc electrode to the ring electrode is called transfer time t_s. For the calculation of t_s different solutions are described in literature [129, 138]. One of this expressions is the following:

$$t_s = 3.58 \left(\frac{\nu}{D}\right)^{1/3} \left(\log\left(\frac{r_2}{r_1}\right)\right)^{2/3} \cdot \omega^{-1} \tag{2.10}$$

According to formula 2.10 the calculated time for the simulated system is 1.034 s, which is in good agreement with the breakthrough of the concentration front through the gap-ring boundary.

Furthermore, the time evolution of the concentration profiles in Figure 2.6 shows another interesting detail. When looking at the spread of the concentration profile in radial direction, it can be seen that it spreads slower near the electrode surface than at a certain distance from the electrode. For $z = 10\,\mu\text{m}$ this results in a shoulder in the concentration profile (particularly well recognizable in Figure 2.6 (c) and (d)), which propagates in a radial direction. These observations are due to the velocity field of the electrolyte. Near the electrode the velocity of the electrolyte is 0 and the transport is determined by diffusion and therefore slow. With increasing distance from the electrode the velocity of the electrolyte increases and therefore favours the transport of species B. Thus, a shoulder of the concentration profile in radial direction is observed.

Another important parameter for an RRDE experiment is the transfer ratio N. If the ring potential is chosen in such a way that the back reaction in relation to the reaction at the disk electrode is occurring mass transfer controlled, N is defined as:

$$N = \frac{I_{ring}}{I_{disk}} \tag{2.11}$$

Finding a mathematical expression to calculate N proved to be a challenging problem. The first equations were only approximations that yielded a deviation of 15% or more from the experimental values [137]. Only 6 years after the first attempts Albery and Feldmann succeeded to find a sufficiently accurate expression for N [139, 140]. It is also noticeable by its complexity:

$$N = 1 - F(\alpha/\beta) + \beta^{2/3}(1 - F(\alpha)) - (1 + \alpha + \beta)^{2/3}(1 - F[(\alpha/\beta)(1 + \alpha + \beta)]) \tag{2.12}$$

Where $\alpha = (r_2/r_1)^3 - 1$. β and the function F are defined as follows:

$$\beta = \frac{r_3^3}{r_1^3} - \frac{r_2^3}{r_1^3} \tag{2.13}$$

$$F(\theta) = \frac{\sqrt{3}}{4\pi} \ln\left(\frac{(1+\theta^{1/3})^3}{1+\theta}\right) + \frac{2}{2\pi} \arctan\left(\frac{2\theta^{1/3} - 1}{3^{1/2}}\right) + \frac{1}{4} \tag{2.14}$$

This expression for N has two important conclusions as a consequence:

- N is depended on the RRDE geometry (r_1, r_2 and r_3)
- N is independent of ω and D

With the help of numerical simulations it can be shown that these consequences result from the simplifications in the derivation of the equations 2.11-2.13 (see Appendix D). However, these effects are generally so small that the experimental error dominates. Therefore, the formulas listed above can be chosen for the evaluation of the experimental data. It is also possible to determine N experimentally, for example with a reversible redox system.

2.3 | Differential electrochemical mass spectrometry

For electrochemists, it has always been of interest to combine electrochemical experimental methods with a well-known method from chemical analysis, since cyclic voltammetry, for example, does not provide information about the nature of the species formed/consumed (functional groups, atomic composition, ...). In 1971 Bruckenstein and Gadde introduced an experimental setup combining mass spectrometry with electrochemistry [141]. The vacuum of the mass spectrometer is separated from the electrolyte by a hydrophobic porous PTFE membrane. A volatile species in the electrolyte, can now diffuse through the PTFE membrane into the evacuated system of the mass spectrometer where it can be ionized and detected. In Bruckenstein's experiments, gaseous products of an electrochemical reaction are first collected in a vacuum system and then detected by a mass spectrometer. The disadvantage of this method is the integration approach. Here the signal of the mass spectrometer is correlated with the flowing electrical charge. By improving the vacuum system, Wolter and Heitbaum introduced differential electrochemical mass spectrometry (DEMS) in 1984 [142]. This enables the immediate detection of volatile electrochemical reaction products. Due to the higher time resolution a combination of cyclic voltammetry and mass spectrometry is possible. A plot of the potential against the ion current recorded with the the mass spectrometer is called MSCV.

In literature as well as in the working group Batruschat different electrochemical cells have been developed in order to couple them with DEMS. These cells satisfy a broad range of requirements. For example:

- Application of single crystal electrodes [143–145]
- Generator collector approaches [146]
- Combination with the electrochemical quartz crystal microbalance [147]
- Combination of DEMS with IR spectroscopy [148, 149]
- Battery applications [150–152]

Since the DEMS measurements in this study were performed exclusively with the cell whose functional principle is described in Chapter 4, this chapter will not discuss the electrochemical cell used or other electrochemical cells for DEMS. This chapter therefore focuses on the DEMS methodology.

2.3.1 | The interface between electrolyte and vacuum

A major component of the DEMS experiments is the hydrophobic porous PTFE membrane, which is used as a phase boundary between the electrolyte and the vacuum of the mass spectrometer. A schematic drawing of the phase boundary between electrolyte and vacuum is shown in Figure 2.7.

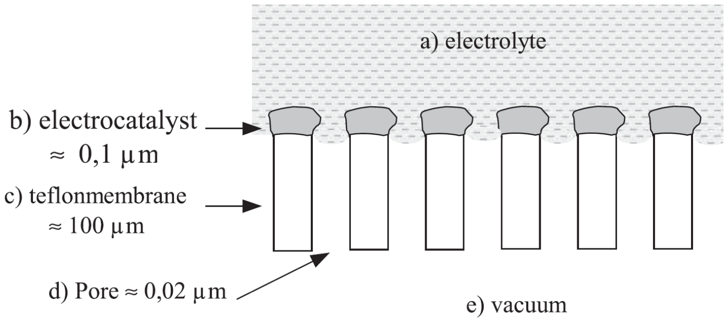

Figure 2.7: Schematic representation of a sputtered PTFE membrane. Shown are a) the electrolyte, b) the deposited electrocatalyst, c) the PTFE membrane and d) the pores in the membrane. The PTFE membranes used in this study are 50 µm thick. Taken from [153].

The PTFE membrane has the task to separate the electrolyte from the vacuum of the mass spectrometer. At the same time the membrane must be permeable for gaseous and volatile species. These species can diffuse through pores in the membrane into the vacuum. To avoid diffusion resistance of the volatile products, the pores must be free of electrolyte. A critical pore radius r can be calculated using the capillary equation:

$$r < -\frac{2\sigma \cdot \cos\gamma}{p_0} \tag{2.15}$$

Where σ is the surface tension of the electrolyte, γ the contact angle between the electrolyte and the PTFE membrane and p_0 is the atmospheric pressure. This results in a critical pore size of 0.8 µm for pure water [142]. Experience has shown that a much smaller pore diameter of 20 nm is practicable. Metals such as Au or Pt can be evaporated onto the PTFE membrane, allowing this newly created surface to be used as a working electrode (see Figure 2.7). Another benefit by using this approach is that the delay time between the electrochemical detection and the mass spectrometric signal is drastically reduced as volatile species are directly formed at the electrolyte-vacuum interface.

A limitation of this approach is the evaporation of the solvent at the electrolyte-vacuum interface into the vacuum of the mass spectrometer, as the mass spectrometer could only be operated at low pressure. Based on molecular flow of the evaporated solvent within the pores Wolter and Heitbaum estimated the flux of solvent molecules into the vacuum [142]:

$$q = 3.1 \cdot 10^4 \frac{r}{l} \frac{\mathrm{cm}}{\mathrm{s}} (p_1 - p_2) \tag{2.16}$$

In equation 2.16 l is the thickness of the membrane and $p_1 - p_2$ is the pressure difference in the pores. If we assume that the thickness of the membrane is 50 µm, the pore diameter 20 nm and use for the pressure difference the vapor pressure of water $p_1 - p_2 = 31.7\,\mathrm{mbar}$ [154], the resulting flux through a pore is:

$$q_{\mathrm{H_2O}} \approx 393\ \mathrm{mbar\,cm\,s^{-1}} \tag{2.17}$$

Of interest is now the maximal allowed membrane area A_{tot}, which can be exposed to the vacuum inlet to guarantee a pressure in the vacuum system of $p_{max} = 10^{-3}\,\mathrm{mbar}$. In practice turbo molecular pumps with a pumping speed of $S = 200\,\mathrm{L\,s^{-1}}$ are used. The porosity of the PTFE membrane α is usually 50%. With this information A_{tot} can be calculated from the following relationship:

$$q_{\mathrm{H_2O}} \cdot A_{tot} \cdot \alpha = p_{max} \cdot S \tag{2.18}$$

Thereby A_{tot} was estimated with approximately $1\,\mathrm{cm^2}$. Therefore the PTFE membrane areas of $0.283\,\mathrm{cm^2}$ used in the present study are applicable.

In summary, this discussion describes the difficulties that arise for the success of a DEMS experiment: The electrolyte should not flood the pores of the PTFE membrane. In addition, a practicable pressure has to be established in the vacuum system in order to perform the measurement. The consequence for this study was that DEMS measurements could be performed with dimethyl sulfoxide and tetraglyme based electrolytes. Other solvents of interest such as acetonitrile or tetrahydrofuran do not fulfill at least one of the above requirements.

2.3.2 | The DEMS vacuum system

The DEMS vacuum system used in this study is similar to that described by Wolter and Heitbaum [142]. A schematic representation of this system is shown in Figure 2.8. The vacuum is generated by a differential pumping stage consisting out of two turbo molecular pumps (TPU, turbo pump unit) with a pumping speed of $200\,\mathrm{L\,s^{-1}}$ and $50\,\mathrm{L\,s^{-1}}$. The TPU with $S = 200\,\mathrm{L\,s^{-1}}$ is located directly above the connection to the electrochemical cell. This ensures that a large proportion of the volatile species is pumped out here already. The resulting pressure at the ion source is between $10^{-6}\,\mathrm{mbar}$ (TEGDME) and $5 \cdot 10^{-5}\,\mathrm{mbar}$ (DMSO). As ion source a cross beam ion source consisting out of two rhenium filaments with an acceleration voltage of 100 V is used. A second TPU with $S = 50\,\mathrm{L\,s^{-1}}$ is located behind the ion source. This TPU is reducing the pressure in the mass analyzer, a quadrupol filter, to enlarge the mean free path length of the charged species generated in the ion source. A reduced pressure is also beneficial for the secondary electron multiplier (SEM) as higher pressure would lower the lifetime of the SEM.

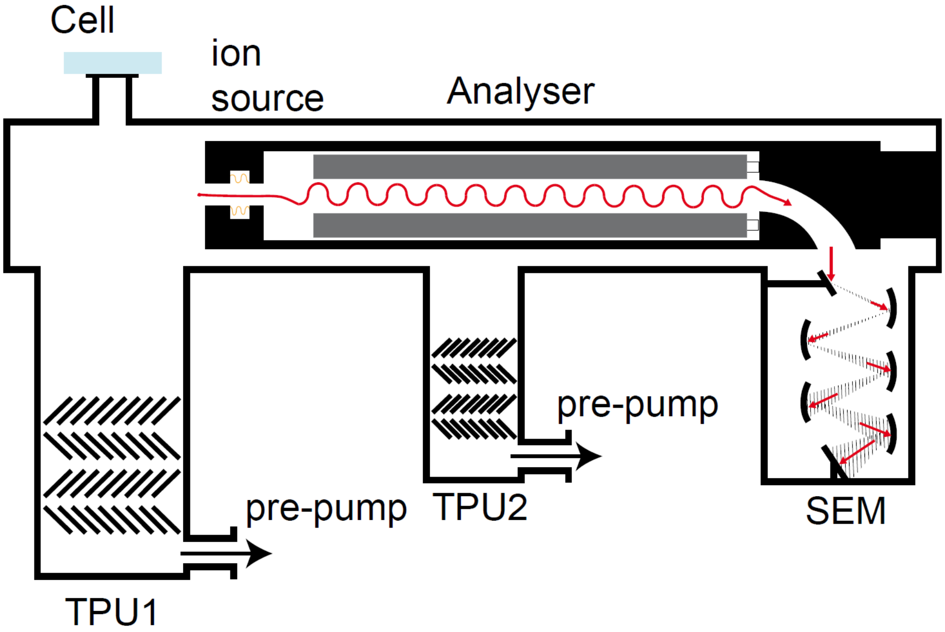

Figure 2.8: Schematic drawing of the DEMS vacuum system. Shown are the turbo molecular pumps (TPU), the connection of a electrochemical DEMS cell to the vacuum system and the ion source with the quadrupole mass spectrometer. Taken from [96].

2.3.3 | Evaluation of product forming rates in DEMS

The detected intensity I_i of species with the mass to charge ratio $i = m/z$ is proportional to the partial pressure of this species $p_{m/z}$ in the vacuum chamber. The following equation can be formulated:

$$I_i = ap_i = K^\circ J_i \tag{2.19}$$

Here a and K° are proportionality constants. K° contains all settings of the mass spectrometer as the electron emission current, the multiplier voltage, the pump speed and the ionization probability of the detected species. J_i is the molecular flux (in $\mathrm{mol\,s^{-1}}$). If species i is formed electrochemically, J_i results from the Faraday current I_F. The relationship between J_i and I_f can be described as follows:

$$J_i = N\frac{I_F}{zF} \tag{2.20}$$

z is the number of electrons transferred, F is the Faraday constant and N is the transfer ratio. N indicates the proportion of the species, which are detected in the mass spectrometer, to the proportion of the species, which are generated/consumed at the electrode. N can be less than 1, because it is conceivable that the species do not diffuse into the vacuum of the mass spectrometer but into the electrolyte and are therefore not detected. In this study porous electrodes as described in in section 2.3.1 are used. Therefore the diffusion path from the electrode to the pore is significantly shorter than the Nernstian diffusion layer thickness into the electrolyte in front of the electrode (estimated by taking reasonable diffusion coefficients between $10^{-5}\,\mathrm{cm^2\,s^{-1}}$ and $10^{-6}\,\mathrm{cm^2\,s^{-1}}$ into account) . Therefore $N = 1$ can be assumed. Equation 2.19 and 2.20 result in:

$$I_i = K^* \frac{I_F}{z} \qquad \text{with } K^* = \frac{NK^\circ}{F} \tag{2.21}$$

In this work the DEMS measurements were performed to quantify the oxygen reduction and oxygen evolution in the systems under investigation. The determination of the calibration constant K^* was therefore carried out with an electrochemical oxygen reduction with known stoichiometry. For this purpose the ORR in $\mathrm{TBAClO_4}$ in DMSO was used. It is generally known that the reduction of oxygen in this electrolyte leads to the formation of superoxide [92, 155]:

$$\mathrm{O_2 + e^- \longrightarrow O_2^{\cdot -}} \tag{2.22}$$

By correlating the faradaic current of reaction 2.22 as well as the decrease of the intensity of the oxygen signal I_{32}, K^* can be calculated according to 2.21.

2.4 | X-ray photoelectron spectroscopy

In this study X-ray Photoelectron Spectroscopy (XPS) is used for ex situ characterization of the electrode surfaces. This chapter will work out the experimental challenges by which this technology is mainly used ex situ. However, it should be pointed out to the reader that especially in recent studies an electrochemical in situ XPS method are described [156, 157]. This method is called Ambient Pressure XPS (AP-XPS) and the experimental challenges are even greater (complex differential pumping of the electron analyzer, synchrotron X-rays) than for ex situ XPS experiments.

The importance of this method becomes obvious when one considers the number of Nobel Prizes and well-known scientists related to discoveries that made XPS applicable. The pioneering work in the year 1887 by Heinrich Hertz [158] and Wilhelm Hallwachs [159] to the external photoelectric effect showed the emission of electrons from photocathodes (metals or semiconductors) by bombarding them with electromagnetic radiation. Furthermore Hallwachs could observe that it was not the intensity of the radiation but its frequency that determined whether or not an emission of electrons occurred. The first person to carry out such experiments in a high vacuum device was Phillip Lenard who thereby identified the emitted charges as electrons [160]. The theoretical explanation of the phenomenon was achieved by Albert Einstein in which he postulated the conservation of energy in the photoelectric effect [161]. For this work he received the Nobel Prize for physics in 1921. In 1924 Karl Manne Siegbahn received the Nobel Prize in Physics "for his discoveries and research in the field of X-ray spectroscopy" [162], which contained some basics for the development of the XPS. In the 1950s, his son Kai Siegbahn succeeded in obtaining high-resolution spectra of the energy levels of atoms by utilizing the photoelectric effect [163] - the birth of XPS. With this work he was honoured in 1981 with the Nobel Prize in physics.

2.4.1 | Theory of the photoelectron spectroscopy

By irradiating electromagnetic radiation with sufficient energy, an electron can be knocked out of the valence band or core level of a solid. The kinetic energy of this electron E_{kin} can be calculated by Einstein's photoelectric equation:

$$E_{kin} = h\nu - E_b + \phi \tag{2.23}$$

Herein $h\nu$ is the energy of the electromagnetic radiation. In this study X-rays from a non-monochromized Mg Anode are used (Mg K$\alpha_{1,2}$, $h\nu = 1253.6\,\text{eV}$). E_b is the binding energy of the electron in the core level and ϕ is the work function of the material. An illustration of this process is shown in Figure 2.9. The photoelectron current can be detected in a hemispherical electron analyser (also shown in Figure 2.9). For the detection of the photo electron the work function of the spectrometer must be overcome. If the sample and the spectrometer are in electrical contact, the Fermi levels are at the same energy level. Thus equation 2.23 can be modified by a device-dependent value ϕ_s.

$$E_{kin} = h\nu - E_b + \phi_s \tag{2.24}$$

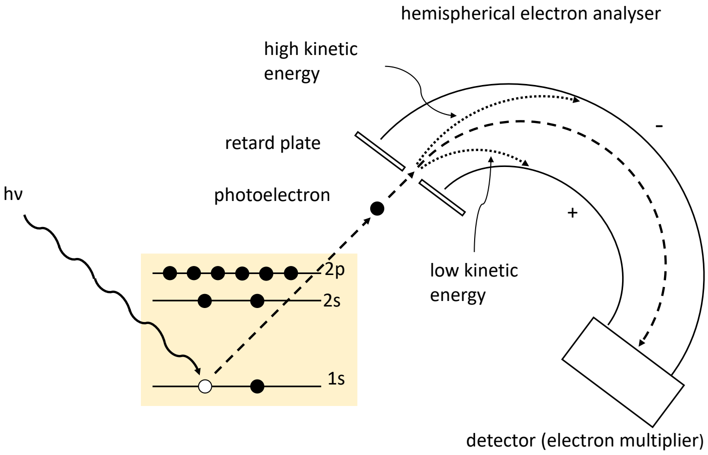

Figure 2.9: Schematic representation of the X-ray excitation of a 1s core level and the detection of the generated photoelectron.

A XP spectrum is the count of photo electrons as a function of E_b. The detection of photo electrons imposes an important requirement for a XPS experiment: XPS experiments are performed under ultra high vacuum (UHV, $p < 10^8$ mbar) since the traveling length of the photo electron from the sample to the detector is approximately 1 m and collisions between gas molecules and the photo electrons should be excluded. To estimate a sufficient low pressure in the vacuum chamber to conduct an XPS experiment the mean free path λ of a gas molecule according to the kinetic gas theory can be calculated, assuming ideal gas behaviour, with:

$$\lambda = \frac{RT}{\sqrt{2}\pi d^2 N_A p} \tag{2.25}$$

If now λ of an emitted electron in the substrate is considered, the situation changes completely. Due to the high density of solids the emitted photoelectron is inelastically scattered and loses its kinetic energy. The intensity of photoelectrons I as a function of distance into the solid d can be calculated by a first-order decay (compare Beer law):

$$I(d) = I_0 \exp\left(\frac{-d}{\lambda(E_{kin})}\right) \tag{2.26}$$

where I_0 is the initial photoelectron intensity and $\lambda(E_{kin})$ the inelastic mean free path which is dependent from the kinetic energy of the photoelectrons. $\lambda(E_{kin})$ is defined as the distance at which the photoelectrons intensity is decaying to 1/e. Seah and Dench suggested an empirical formula to calculate $\lambda(E_{kin})$ [164]:

$$\lambda_m = \frac{538}{E_{kin}^2} + 0.41\,(aE_{kin})^{1/2} \tag{2.27}$$

where λ_m is the inelastic mean free path of photoelectrons in monolayers of the substrate, E_{kin} is the energy of the photoelectron in eV and a is the monolayer distance in nm. a was defined as:

$$a = \left(\frac{MN_A}{\rho}\right)^{1/3} \tag{2.28}$$

where M is the molar mass of the element, N_A is the Avogadro number and ρ is the density of the solid. With the help of equation 2.27 λ_m can be calculated, which was exemplary done for a gold substrate (see Figure 2.10). These calculations shown in Figure 2.10 illustrate that the intensity of the photoelectron comes from a surface layer of a few monolayers. Therefore XPS is a surface sensitive spectroscopic method. This results in a further necessary condition for the use of UHV equipment. It is well known from common considerations in surface chemistry that the time it takes to form a monolayer of an adsorbate on a surface (assuming a sticking coefficient of 1) is only sufficiently long when using low pressure [165]. Therefore low pressures ($p < 10^{-8}$ mbar) have to be used to avoid that the surface is covered during the experiment by several monolayers of an adsorbate and makes otherwise a characterization of the substrate of interest not possible.[3]

XPS measurements are able to probe the chemical environment of the core level excitation (oxidation state of the atom). This sounds rather surprising since chemical bonds are formed with the valence electrons and XPS is mainly probing the core level orbitals. This connection can be understood by the fact that a chemical bond changes the effective charge of the atom. Therefore this changes the attraction between the atomic nucleus and the core level electrons and thus the binding energy of the core level electrons. This relationship could be explained in the simplest picture with the help of Coulomb's law.

To investigate the chemical environment of the substrate, it is advisable to record the XP spectrum with a high energy resolution. The energy resolution is influenced by the line width of the X-rays, the material under investigation and by the electron energy analyzer used. In this study a hemispherical electron analyzer (see Figure 2.9) is used. The working principle of the hemispherical analyzer can be simplified explained by three major components. First

---

[3] For a pressure of 10^{-6} mbar the time to adsorb one monolayer is in the range of several seconds and therefore this pressure is not applicable for XPS measurements. For lower pressures as 10^{-10} mbar this time is increasing to several hours.

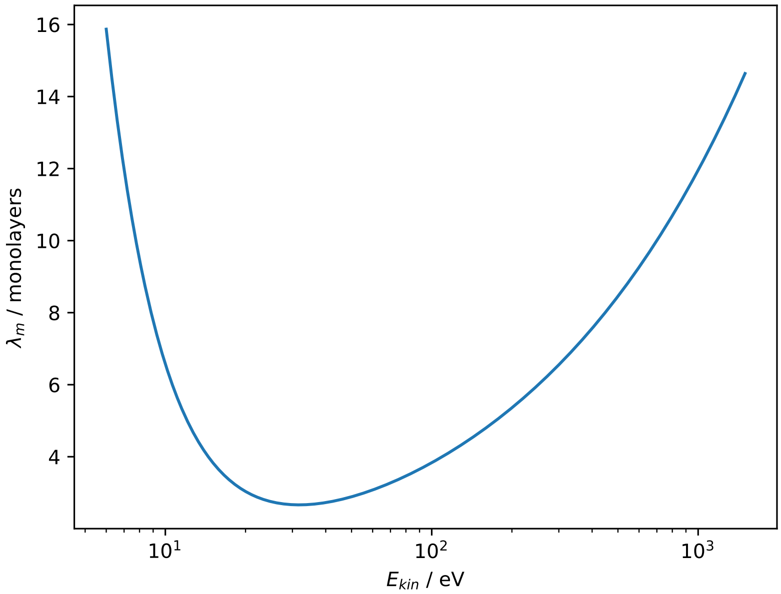

Figure 2.10: Inelastic mean free path of photoelectrons λ_m from an Au substrate as a function of the kinetic energy of the photoelectron E_{kin}.

there is the retard plate. There the kinetic energy of the electrons is in the first place reduced to the "pass energy" by applying a negative potential. The "pass energy" is the kinetic energy the electrons are chosen to have to pass the electrostatic field of two concentric electrically isolated spheres. Electrons which have a lower kinetic energy as the chosen pass energy are attracted by the positive charged inner sphere. Electrons with a higher kinetic energy than the pass energy are hitting the outer sphere. Therefore only electrons with a kinetic energy comparable to the chosen pass energy can pass through the hemispherical electron analyzer (see dashed line in Figure 2.9). These electrons are detected by an electron multiplier. By lowering the pass energy the overall resolution of the XP spectrum can be improved by decreasing the Full Width at Half Maximum (FWHM) of the core level excitation peaks. At the same time, the intensity of the peaks is reduced. In the experiment it is therefore necessary to find a balance between the energy resolution of the spectrum and the intensity of the peaks in the spectrum. Figure 2.11 is showing the 4f core level excitation of Au for different pass energies. There the FWHM as well as the intensity of Peaks I (normalized to the spectrum with a pass energy of 50 eV) is noted. These spectra were recorded with the experimental setup used in this study. It is shown that an energy resolution of 1 eV could be achieved. In order to improve the signal to noise ratio at lower pass energies several spectra can be recorded and averaged (not shown in Figure 2.11).

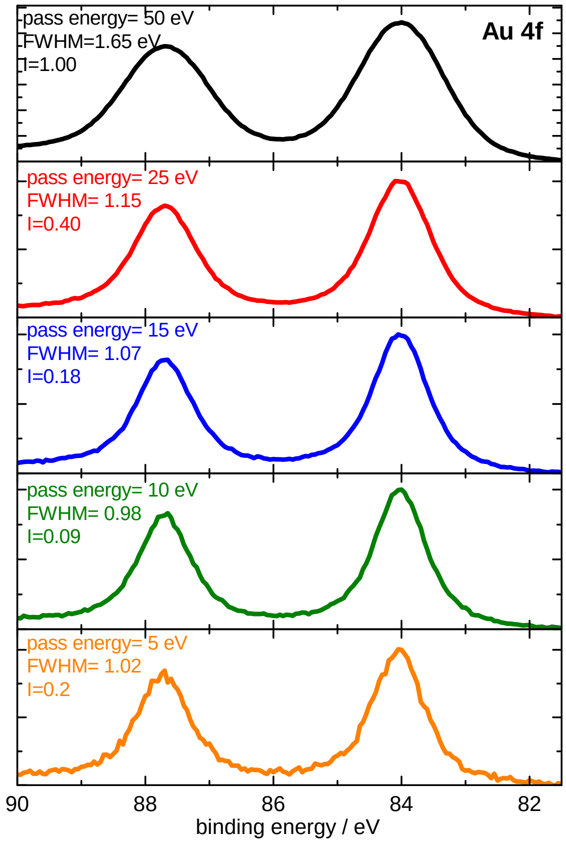

Figure 2.11: Impact on the Au 4f core level excitation region of an XP spectrum for different pass energies of the hemispherical energy analyzer.

Furthermore some important information about the XPS will be given as a keyword list:

- **Valance band spectra**: The valence band of the substrate can be investigated in a range of binding energies between 0 - 20 eV. The emission occurs from molecular orbitals and energy bands of solids. A differentiation between conductors and non-conductors is possible due to the absence of electron states at the Fermi level for non-metals (band gap). However, for a detailed analysis UV light is often used instead of X-rays, since higher resolutions of the valence band can be achieved.
- **Multiplett splitting**: The interaction of the spin of an electron with its orbital angular momentum results in a splitting of p, d and f orbitals into duplets with intensities with the following ratios for the emission of photoelectrons: 1:2 for p orbitals, 2:3 for d orbitals, 3:4 for f orbitals.

- **Auger electron**: Another type of emitted photoelectrons can be observed in an XP spectrum. This results from relaxation of the energy-rich ion after the photoprocess as shown in Figure 2.12. Thereby the kinetic energy of the emitted photoelectron is the energy difference between the initial ion and the doubly-charged final ion.

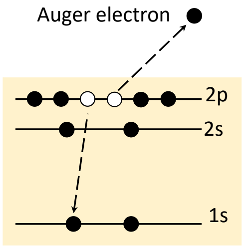

Figure 2.12: Relaxation of the energetic ion after the photoelectron (see Figure 2.9) by emitting an auger electron.

- **Background** In general, XP peaks show an increase in baseline to higher binding energies. Physically, this can be explained by the inelastic scattering of the photoelectrons in the substrate. For an evaluation of the spectra a subtraction of the baseline is therefore necessary. In literature the correction by a linear baseline, a Shirley-type baseline [166] and a Tougaard-type baseline[167, 168] are described. It has been shown that the Tougaard-type baseline produces much lower relative errors (10-15% deviation) compared to the linear and Shirley methods (35% and 25%) [169]. Therefore the Tougaard-type baseline was used to interpret the spectra in this study. There are special cases in which the Tougaard-type baseline is not applicable and therefore a Shirley-type baseline will be used (this will be mentioned during the data interpretation).

- **X-ray satellites**: If the emitted X-ray Bremsstrahlung of an X-ray tube is not monochomatized (as in this study), it has to be considered that the emission spectrum of the X-ray radiation consists of a variety of different excitations. Thus, the XP spectrum also contains other peaks resulting from excitation with less intense X-rays. These excitations are called X-ray satellite peaks and the possible shifts to the Mg K $\alpha_{1,2}$ line are shown in table 2.1.

Table 2.1: X-ray satellite energies and intensities for a Mg Anode.Values taken from [170].

	$\alpha_{1,2}$	α_3	α_4	α_5	α_6	β
displacement / eV	0	8.4	10.2	17.5	20.0	48.5
relative height	100	8.0	4.1	0.55	0.45	0.5

- **Quantification:** With the help of atomic sensitivity factors ASF [171] the share of a species W_x can be calculated:

$$W_x = \frac{I_x / ASF_x}{\sum_i I_i / ASF_i} \tag{2.29}$$

  Here I is the integrated peak area after integration. At this point it should be mentioned that this method is limited in accuracy. If for example layered structures are investigated this method is underestimating the amount in the top layer, as intensities of the underlying layers are also contributing to the overall signal. Therefore calibrations with defined layered structures, as for example a monolayer of iodide on an electrode, are used for these investigations.

2.4.2 | Combining XPS with electrochemical experiments

The UHV system used in this study has been in use in the Baltruschat working group for several years [172–176]. The focus of the work was to run the electrochemical experiments and the UHV measurements as close as possible. This means that a transfer of the electrodes through the laboratory air after the electrochemical experiment had to be avoided. Therefore, the electrochemical experiments were performed in a pre-chamber of the analysis chamber of the UHV system under Ar atmosphere (see chamber III in Figure 2.13 (a)). After the experiment the pre-chamber is evacuated and the electrode is transferred to the analysis chamber to perform XPS, LEED or Auger spectroscopy (see chamber IV in Figure 2.13 (b)). However, this experimental procedure has one disadvantage: The electrolytes which are used in electrochemical experiments (at that time only aqueous electrolytes) are introduced into the pre-chamber. This leads to the adsorption of water on the stainless steel walls of the pre-chamber. If the pre-chamber is evacuated again, the water desorbes from the steel walls and can thus enter the analysis chamber when the connection between the pre-chamber and the analysis chamber is open. As a result, the base pressure of the analysis chamber deteriorates during intensive use of the UHV system. Therefore, an exhaustive bakeout of the system was necessary from time to time to accelerate the desorption of adsorbed molecules from the steel walls and thus regenerate the UHV conditions.

A large part of the planned measurements in this study should be performed with organic solvents. In addition, we knew that some of these solvents, such as TEGDME, have a low vapor pressure. These solvents can particularly contaminate the UHV system and, due to low vapor pressures, make it difficult to regenerate the UHV conditions by baking out. Therefore the electrochemical experiments in this study were performed in a glove box filled with Ar gas. For the transfer between the glove box and the UHV system a transfer chamber was constructed in cooperation with the workshops of the Institute for Physical and Theoretical Chemistry (see

Figure 2.13 (a) and (b)). The transfer chamber is made out of an elastomer-sealed rotary/linear feedthrough. The volume of the transfer chamber is sealed with a high vacuum gate valve. The overall size of the transfer chamber has been kept compact so that it can be transferred via the glove box gate. When the gate valve is closed, a transfer to the UHV chamber under inert gas is possible to protect sensitive samples. The transfer chamber can be connected to the UHV chamber via an ISO KF flange. This creates an air-filled volume between the transfer chamber and the UHV system (see volume II in Figure 2.13 (a)). This volume is evacuated three times to 10^{-3} mbar using a rotary vane pump and flooded with Ar. Then the gate valve separating volumes I and II is opened. During this time the gate valve between chambers III and IV is closed. Both chambers have a base pressure of $5 \cdot 10^{-10}$ mbar at this time. Chamber I and II are evacuated and then the gate valve between chamber II and III can be opened. The pressure in chamber III rises to 10^{-5} mbar. The sample can then be attached to the manipulator of the UHV chamber. Afterwards the gate valve between chamber II and III can be closed again. Once the pressure in chamber III drops below 10^{-7} mbar the gate valve between chamber III and IV is opened. The sample can then be moved to the XPS position. Normally the pressure in the analysis chamber is 10^{-9} mbar until recording the first XP spectrum. Figure 2.13 (b) shows a photograph of the UHV chamber used in this study. The transfer chamber is highlighted in this photograph.

Regarding the coupling with the electrochemical experiments we wanted to minimize the necessary preparations of the electrode for the XPS measurement. Therefore, the electrochemical experiments are performed with the electrode already attached to the UHV electrode holder (see Figure 2.14 (a) and (c)). This saves the need to attach the electrode to the UHV electrode holder and thus avoid possible damage to the sample. The existing UHV electrode holder had to be modified so that it could fit through all the gates of the UHV system during the transfer procedure without touching the steel walls. The UHV electrode holder has a threaded hole for mounting on the feedthrough of the transfer chamber as well as four screws for the mounting on the UHV manipulator (see Figure 2.14 (a)). The four screws are also used to attach the UHV crystal holder to the electrochemcial experiment (see Figure 2.14 (c)). Figure 2.14 (b) shows a photography of the sample mounting to the UHV manipulator taken through the window of the pre-chamber. Single crystals and electrodes with a diameter of 1 cm can be attached to the UHV crystal holder using a connection made of a wire fabricated out of the respective electrode material (see Figure 2.14 (a)). It has been shown within this study that this construction also allows the preparation of single crystals in the butane flame. Furthermore, electrodes with a diameter of 0.5 cm can be attached to the UHV electrode holder using a rectangular tantalum plate (see Figure 2.14 (b) and (c)).

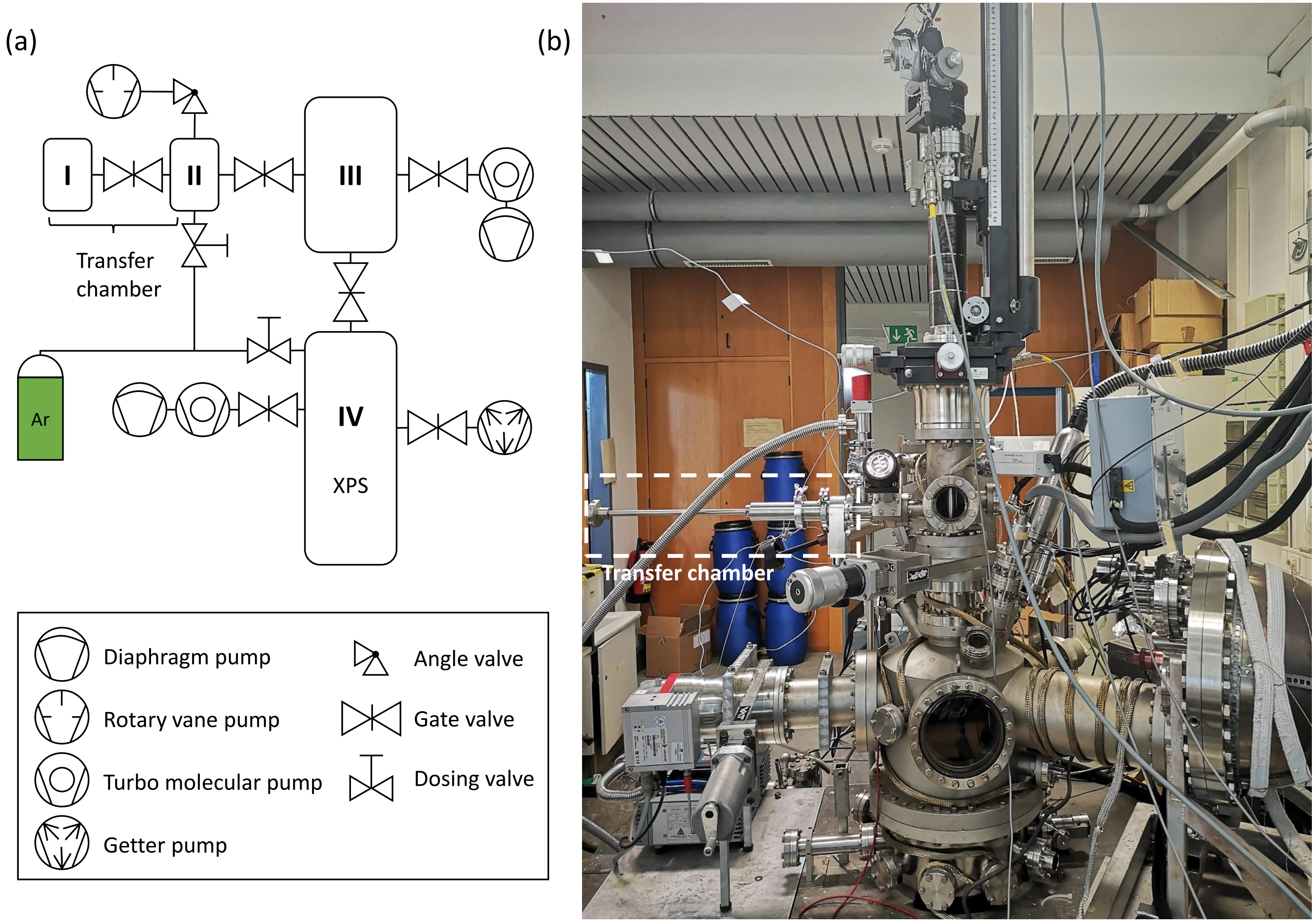

Figure 2.13: (a) Schematic representation of the UHV chamber used for the XPS experiments. Shown are the used vacuum pumps amt the used valves to separate the diffrent chambers. Chamber **I** is the transfer chamber for the transfer of an electrode into the UHV. Volume **II** is formed if the transfer chamber is connected to the UHV chamber. Chamber **III** is the first UHV chamber for the sample receipt. Chamber **IV** is the analysis chamber with the XPS devices. This illustration shows only a part of the equipment attached to the UHV system. (b) Photography of the UHV chamber. The transfer chamber is highlighted in the image.

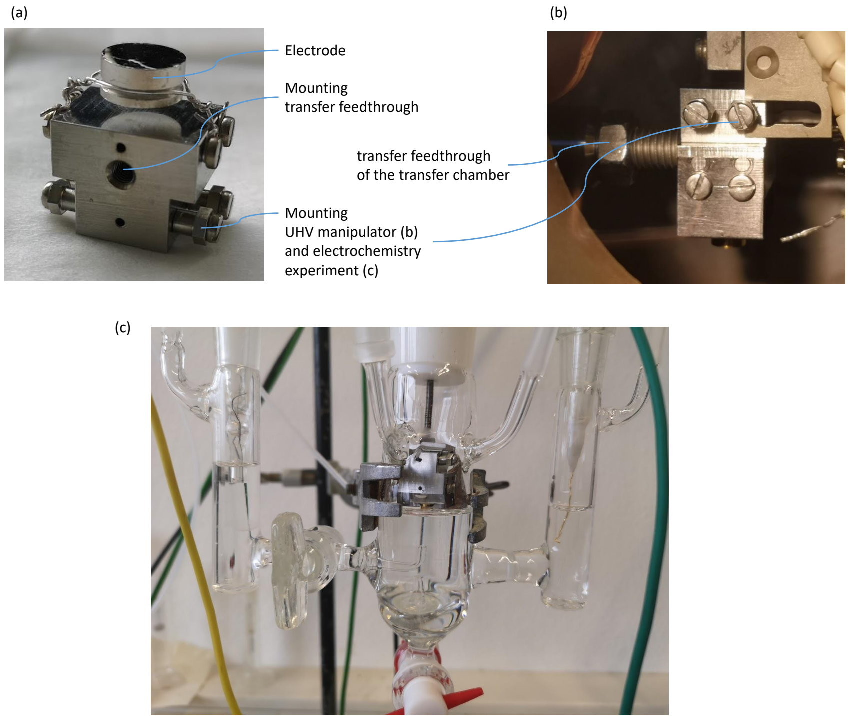

Figure 2.14: (a) Close up photograph of the UHV electrode holder with a Pt electrode. (b) Photograph of the transfer of the UHV electrode holder from the transfer chamber to the UHV manipulator (transfer between chamber II and III in Figure 2.13 (a)). (c) UHV electode holder mounted into an double H-cell electrochemical cell.

3

Finite difference simulations

Even for many simple electrochemical experiments, finding a mathematical analytical solution that, for example, represents the flowing current is not always trivial [129]. If homogeneous chemical kinetics as well as convection have to be taken into account, the derivation of some expressions is only possible under strong simplifications [133]. With the help of computer simulations it is possible to reproduce the experimental data more accurately. The simulations described in this chapter are mainly based on the work of S. W. Feldberg [129, 130, 177–179]. If this algorithm is considered from the point of accuracy and speed, there are superior alternatives [179]. However, they are also more complex to implement. With today's computing power of office computers and the use of state of the art programming languages, the algorithm from Feldberg can also deliver sufficiently accurate results in a shorter time. The Feldberg algorithm convinces by its simplicity whereby modifications, for example through new boundary conditions of an electrochemical experiment, are quickly implemented. As programming language Julia was used in this work (version 1.0 since August 2018) [180]. It has a simple syntax, such as Python or MATLAB. Nevertheless, it reaches execution speeds of C or Fortran and is therefore superior to the scientific languages MATLAB or Octave.

In general, this chapter gives an introduction to the numerical finite difference methodology. The derivation of the formulas is skipped at some passages. For a derivation of the equations the reader is referred to the literature [129, 130, 177–179]. Instead, the space grids, the working principle of the algorithm and the most important expressions for the implementation in a programming language are described. Simulated electrochemical experiments will also be compared with the experimental data.

3.1 | Chemical kinetics

For chemists, the finite difference method is best introduced using the example of a coupled chemical reaction. The time-dependent concentration profile of the species involved in the chemical reaction is described using coupled differential equations. These have to be integrated to find an analytical expression for the time-dependent concentration profile. For complicated reaction networks, finding a solution can be very time-consuming or the solution does not exist. Here numerical integration methods are used. By means of the following reaction network of two coupled first order chemical reactions the method of finite differences will be explained:

$$\mathrm{A} \xrightarrow{k_1} \mathrm{B} \tag{3.1}$$

$$\mathrm{B} \xrightarrow{k_2} \mathrm{C} \tag{3.2}$$

A, B and C stand for chemical species. k_1 and k_2 are the rate constants of the reactions. For species B the following rate law can be formulated:

$$\frac{d[\mathrm{B}]}{dt} = k_1[\mathrm{A}] - k_2[\mathrm{B}] \tag{3.3}$$

The values in the square brackets indicate the concentration of the involved species and t stands for the time. In the finite difference scheme, the total time t_E is now divided into K time steps under which one can see the time evolution of reactions 3.1-3.2:

$$\Delta t = \frac{t_E}{K} \tag{3.4}$$

In the finite difference scheme equation 3.3 is integrated using the discrete time steps:

$$[\mathrm{B}]_{i+1} = [\mathrm{B}]_i + k_1[\mathrm{A}]_i\Delta t - k_2[\mathrm{B}]_i\Delta t \tag{3.5}$$

To obtain the new concentration value ($[\mathrm{B}]_{i+1}$), the change in concentration is added to the old concentration value ($[\mathrm{B}]_i$). This procedure has to be repeated until $i = K$. For the first time step, $i = 1$, $[\mathrm{B}]_{i=1}$ the concentration change is added to the concentration at the beginning of the experiment (boundary condition). The common notation for this is $[\mathrm{B}]_0$. If $\Delta t \rightarrow 0$ is set in equation 3.5, the algorithm converges against the exact solution for the time profile of the concentration of species B. In order to minimize the error of the simulation, small time steps Δt should therefore be chosen.

Furthermore, the result of the finite difference algorithm for the discussed reaction network will be compared with the exact analytical solution. Assuming that $[B]_0 = [C]_0 = 0$ the exact solution for the rate equations based on the reactions 3.1 and 3.2 is:

$$[\mathrm{A}(t)] = [\mathrm{A}]_0 e^{-k_1 t} \tag{3.6}$$

$$[\mathrm{B}(t)] = \begin{cases} \frac{k_1[\mathrm{A}]_0}{k_2-k_1}\left(e^{-k_1 t} - e^{-k_2 t}\right) & \text{if } k_1 \neq k_2 \\ k_1[\mathrm{A}]_0 t e^{-k_1 t} & \text{if } k_1 = k_2 \end{cases} \tag{3.7}$$

$$[\mathrm{C}(t)] = [\mathrm{A}]_0 - [\mathrm{A}(t)] - [\mathrm{B}(t)] \tag{3.8}$$

Figure 3.1 shows the concentration development of A, B and C in respect to time calculated using equations 3.6-3.8 (solid lines). Furthermore, the concentration curves were calculated by numerical integration using the finite difference method ($\Delta t = 0.1\,\mathrm{s}$) (see circles in 3.1). In both calculations $k_1 = 0.1\,\mathrm{s}^{-1}$, $k_2 = 0.05\,\mathrm{s}^{-1}$ and $[\mathrm{A}] = 1$ mM were used. It turns out that the numerical procedure reflects the exact curve in an excellent way. If the deviation in mM from the exact solution is calculated (see lower figure in Figure 3.1), it is obvious that the numerical error of the finite element algorithm is smaller than the error that occurs when determining the concentrations experimentally with common analytical methods.

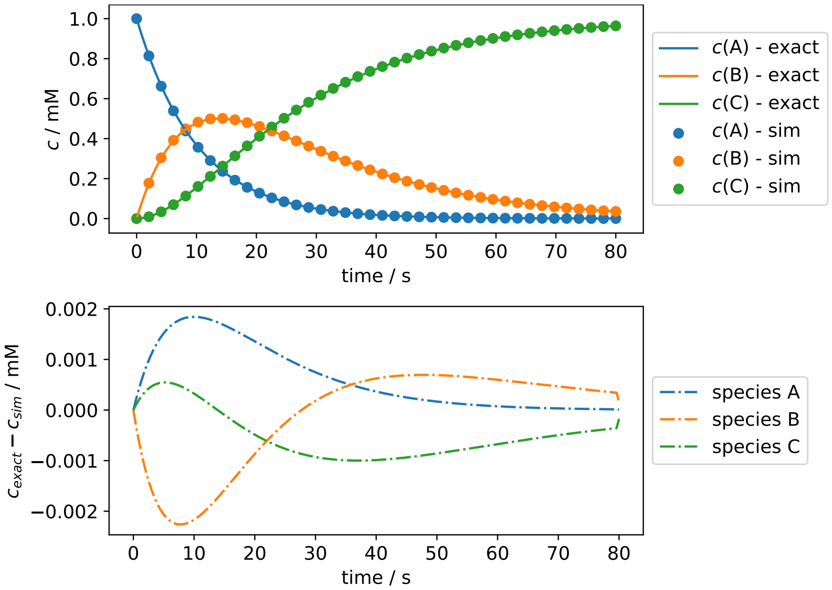

Figure 3.1: Concentration evolution for a coupled chemical reaction network as described in the reaction equations 3.1 and 3.2. The parameters used are: $k_1 = 0.1\,\mathrm{s}^{-1}$, $k_2 = 0.05\,\mathrm{s}^{-1}$ and $[\mathrm{A}] = 1\,\mathrm{mM}$. The concentration curves were calculated using the exact solution according to equation 3.6-3.8 (see lines in the upper figure) and calculated using a numerical integration according to the finite difference method (circles in the upper figure, $\Delta t = 0.1\,\mathrm{s}$). The lower figure shows the deviation $c_{exact} - c_{sim}$.

3.2 | Diffusion in one dimension - Simulating electrochemical experiments and DEMS experiments

At first impression it may seem a bit strange that the simulation of electrochemical experiments deals with diffusion in one dimension. However, this approximation is the most common one when considering diffusion problems to a planar electrode. This is due to the planarity of the electrode. It is further assumed that edges of the electrode are negligible compared to the surface of the electrode. As a result, no radial concentration profiles are formed and diffusion only occurs perpendicular to the electrode. The diffusion problem can therefore be reduced to one spatial dimension, which also makes numerical simulation simpler. If one considers the mass transport in a resting solution (and neglects natural convection), the mass transport is determined by diffusion. The laws of this transport can be described by the Fick's laws:

$$J(x,t) = -D\frac{\partial c(x,t)}{\partial x} \tag{3.9}$$

$$-\frac{\partial c(x,t)}{\partial t} = \frac{\partial J(x,t)}{\partial x} \tag{3.10}$$

This law of diffusion must now be translated into the finite diffrence scheme. For this purpose, the time is discretized, as already described in chapter 3.1, and the space in front of the electrode is discretized in N parts of length Δx:

$$\Delta x = \frac{x}{N} \tag{3.11}$$

A sketch of the resulting space grid is shown in Figure 3.2. The space grid can be understood as a series of boxes. Each box represents the concentration c of a species at a discrete distance in front of the electrode ($j\Delta x$) at a certain discrete time ($i\Delta t$) in the experiment.

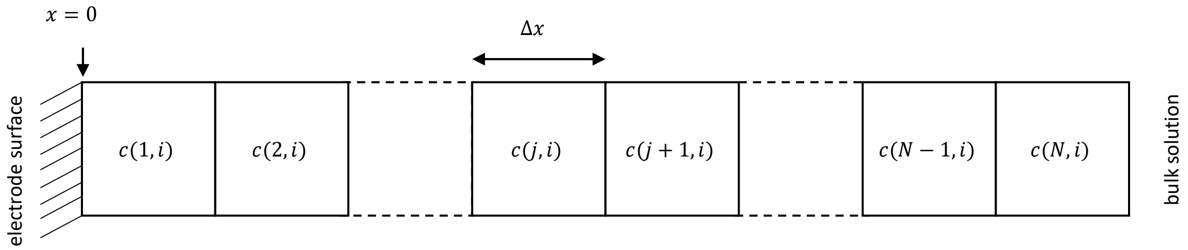

Figure 3.2: Illustration of the space grid used to simulate an electrochemical experiment.

From Fick's diffusion laws (see equations 3.9-3.10) the finite difference scheme for the one-dimensional diffusion problem can now be derived (for the derivation see [129, 130]). The results are summarized in the following equations:

$$c(j,i+1) = \begin{cases} c(E,i+1) & \text{if } j = 1 \\ c(j,i) + \frac{D\Delta t}{\Delta x^2}[c(j+1,i) - 2c(j,i) + c(j-1,i)] & \text{if } 1 < j < N \\ c(j,i) + \frac{D\Delta t}{\Delta x^2}[c_0 - 2c(j,i) + c(j-1,i)] & \text{if } j = N \end{cases} \tag{3.12}$$

The variable $c(j,i)$ denotes the concentration of a species in the volume increment j at time i. The new concentration in each box must be calculated for each time step. This procedure is repeated until $i = K$. Boundary conditions are formulated at the edges of the box array ($j = 1$ and $j = N$). For $j = 1$ the expression $c(E,i+1)$ stands for the electrode reaction that determines the concentration and is usually dependent on the electrode potential E. Expressions such as the Nernst equation or the Butler-Volmer equation are used to calculate $c(E,i+1)$. The total length of the box array is chosen so that the last box $j = N$ represents a concentration close to the bulk concentration c_0 and is therefore found in expression 3.12. Furthermore, a necessary stability condition for the algorithm must be formulated:

$$\frac{D\Delta t}{\Delta x^2} \leq 0.45 \tag{3.13}$$

If D is known and a Δx is chosen, a value for Δt can be calculated so that equation 3.13 is fulfilled. Furthermore, the Faraday current I_F can be calculated in the electrochemical simulation by applying the first Fick's law 3.9 to the first two boxes:

$$I_F(i) = nFAD\frac{c(1,i) - c(2,i)}{\Delta t} \tag{3.14}$$

Where n is the number of electrons transferred in the electrochemical reaction, F is the Faraday constant and A is the electrode surface.

With the help of these considerations it is possible to simulate experimental CVs by adding the sweep rate v to the electrode potential:

$$E(i) = E_{start} \pm v\Delta t i \tag{3.15}$$

A comparison of an experimental CV with a simulated one can be found in Figure 3.3. The experimental CV is that of the redox system 2,5-di-tert-butyl-1,4-benzoquinone (DBBQ), which was investigated for its use as a redox mediator for the ORR in Li-O_2 batteries in Figure 6. This molecule can be successively reduced to $DBBQ^-$ and $DBBQ^{2-}$ by lowering the electrode potential. The standard potentials of these two reactions are sufficiently separated to observe two peaks for reduction in the CV. If the sweep direction is changed, the reverse reaction are observed. It can be seen that finite difference simulation reproduces this process very well (see right figure in Figure 3.3). Deviations from the experimental CV are due to the fact that the cell used to record the experimental CV is the DEMS thin layer cell described in chapter 4. Within this cell, the current distribution resulting from the cell geometry would have to be considered which was neglected in the simulation.

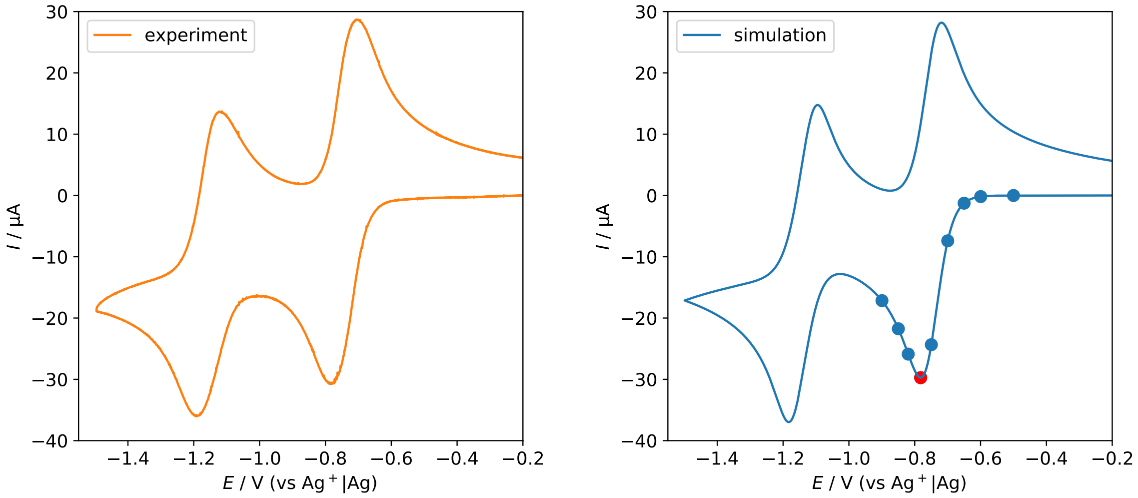

Figure 3.3: A comparison of an experimental CV (left Figure) of the redox system DBBQ to the a simulated one (right Figure). The experimental CV is taken from chapter 6. The supporting electrolyte is made out of 2 M $LiClO_4$ in DMSO with 7.5 mM DBBQ. The sweep rate was $v = 10\,\mathrm{mV\,s^{-1}}$. In the simulated CV some points are highlighted. This points correspond to the concentration profiles in Figure 3.4.

The simulation of electrochemical experiments is particularly helpful in understanding the shape of CVs. For this purpose the concentration profiles of the CVs involved in the electrochemical reaction are considered. For example, it can be explained that peaks are observed in the CV for the reduction/oxidation of dissolved species. This will be done exemplary for the first reduction peak in the DBBQ CV (see Figure 3.3). The concentration profiles of DBBQ as a function of the distance from the electrode surface at the highlighted times in the simulation were plotted in Figure 3.4. At the beginning of the experiment the concentration profile shows a horizontal line representing the bulk concentration of DBBQ (in this case 7.5 mM). If the electrode potential is reduced and approaches the standard potential of DBBQ reduction, DBBQ is reduced to $DBBQ^-$. This results in a consumption of the DBBQ near the electrode. With further reduction of the electrode potential the reaction rate of the reduction increases until the surface concentration becomes 0. At the same time, new DBBQ is transported from the electrolyte volume to the electrode, which results in a depletion of the DBBQ concentration in the x-direction. To calculate the current, the slope of this concentration profile near the electrode surface is of interest, since the current flowing in the CV is proportional to this slope. The concentration profiles show that the slope decreases, reaches a minimum (concentration profile colored red in Figure 3.4) and then increases again. This minimum slope is responsible for observing a peak in the CV.

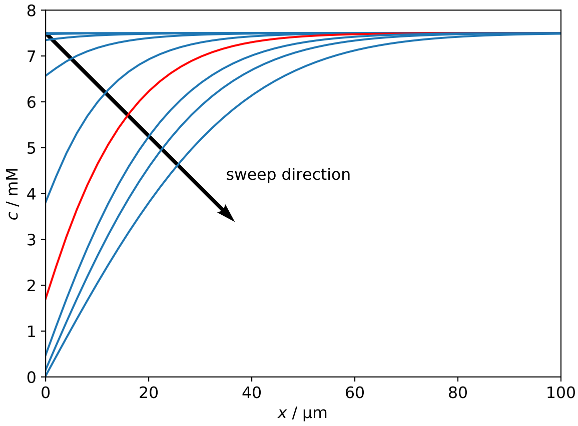

Figure 3.4: Concentration profiles of DBBQ in front of the electrode. The profiles are taken at the highlighted points in Figure 3.3.

For electrochemical experiments, special cells are often made for a particular experiment. In order to reproduce the experimental data with a finite difference simulation, the challenge is to reproduce the boundary conditions of the cell appropriately in the code. For the DEMS thin layer cell described in chapter 4 this will be illustrated. Figure 3.5 shows a modified space grid for the DEMS thin layer cell, which can also be treated as a one-dimensional diffusion problem due to symmetry reasons. A modification is necessary for the transport equations, since it is a thin layer cell with an electrolyte thickness of l and the electrolyte space is therefore limited in the x-direction. Therefore the transport of all species in the system (except O_2) is corrected over the following term:

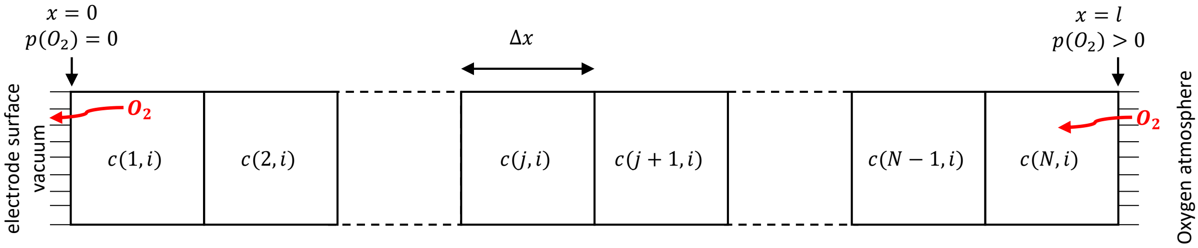

Figure 3.5: Illustration of the space grid used to simulate an electrochemical DEMS experiment. The cell architecture is in detaile described in chapter 4.

$$c(j,i+1) = c(j,i) + \frac{D\Delta t}{\Delta x^2}[c(j-1,i) - c(j,i)] \qquad \text{if } j = N \tag{3.16}$$

The task in this DEMS cell is to investigate the OER and ORR. Therefore the finite difference code must adequately reflect the oxygen transport through the cell. For this purpose the oxygen concentrations at the interfaces, the vacuum system ($x = 0$, $p(\mathrm{O_2}) = 0$) and the oxygen atmosphere ($x = l$, $p(\mathrm{O_2}) > 0$) are calculated. The concentrations are calculated according to Henry's law:

$$c_{\mathrm{O_2}}(j,i) = \begin{cases} 0 & \text{if } j = 1 \\ K_H p(\mathrm{O_2}) & \text{if } j = N \end{cases} \tag{3.17}$$

Where K_H is the Henry constant. The MSCV of oxygen can be calculated from the concentration gradient at $x = 0$. Using these considerations, the shape of the CVs and MSCVs recorded in the DEMS thin layer cell can be reproduced and supposed reaction mechanisms can be validated. Especially for the pressure jump experiment in chapter 6 this finite difference algorithm was used. A more detailed illustration can be found in chapter 6.6.

Furthermore, as an example, a DEMS measurement from chapter 6 shall be reproduced here using the finite difference code. The object of investigation is the ORR mediated by DBBQ. The mechanism can be simplified by the following reaction equations:

$$\text{At the electrode:} \quad \mathrm{DBBQ} + \mathrm{e}^- \longrightarrow \mathrm{DBBQ}^- \tag{3.18}$$

$$\mathrm{DBBQ}^- + \mathrm{e}^- \longrightarrow \mathrm{DBBQ}^{2-} \tag{3.19}$$

$$\text{In solution:} \quad \mathrm{DBBQ}^- + \mathrm{O_2} \longrightarrow \mathrm{DBBQ} + \mathrm{O_2}^{\cdot -} \tag{3.20}$$

$$\mathrm{DBBQ}^{2-} + 2\,\mathrm{O_2} \longrightarrow \mathrm{DBBQ} + 2\,\mathrm{O_2}^{\cdot -} \tag{3.21}$$

Here, a distinction must be made between reactions that are caused by an electron transfer at the electrode (reactions 3.18-3.19) and homogeneous kinetics within the electrolyte (reactions 3.20-3.21). In the finite difference algorithm the individual terms are calculated one after the other. A comparison between the experimental data and the simulated data can be found in Figure 3.6. It can be seen that the simulation reflects the experimental data well. Again, deviations can be explained by not taking the current distribution within the cell into account. In this case, it was of interest that the shoulder in the MSCV of $\mathrm{O_2}$ at -0.8 V could be reproduced. The simulations have shown that this can be explained by a slower reaction rate of $\frac{d[\mathrm{O_2}^{\cdot -}]}{dt}$ in reaction 3.20 versus 3.21. A detailed analysis of the reaction rates can be found in chapter 6.

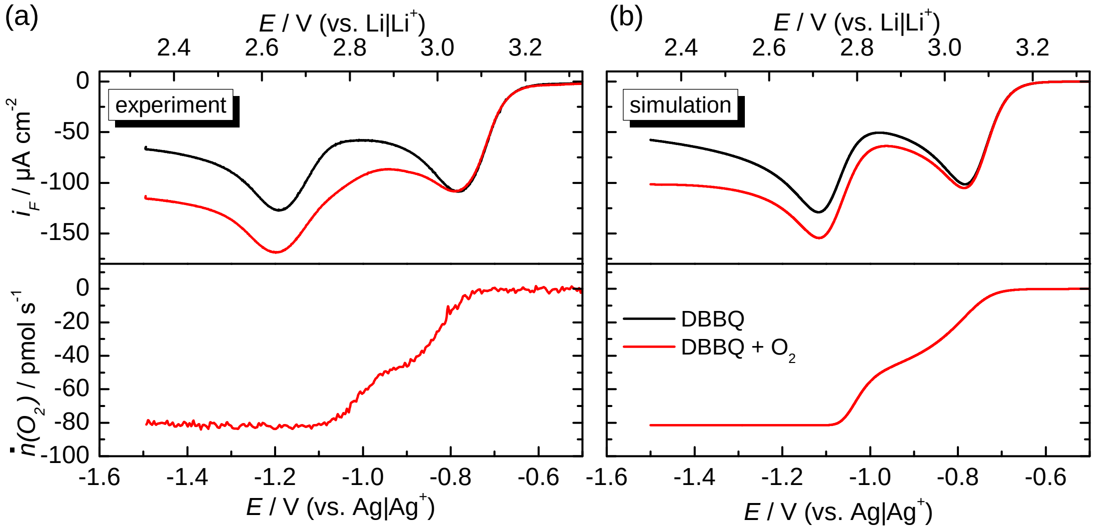

Figure 3.6: (a) Comparison of the experimental data of the DBBQ reduction in the oxygen-free electrolyte and in the electrolyte saturated with oxygen (red) to (b) finite difference simulations. The experimental data are the measurements in 2 M $LiClO_4$ in DMSO with 10 mM DBBQ from chapter 6. There the sweep rate was 10 mV s^{-1}. As diffusion coefficient of oxygen $1.32 \cdot 10^{-5}$ cm^2 s^{-1} was taken [128]. The other parameters were estimated so that they reflect the experimental pattern. A detailed analysis of the reaction rates can be found in chapter 6.

3.3 | Diffusion in two dimensions - Simulating RRDE experiments

To calculate the concentrations of species dissolved in the electrolyte in an RRDE experiment, both the diffusion of these species and the velocity of the electrolyte generated by the rotation of the RRDE must be calculated. In general, this is a coupled system of differential equations which must be solved in the three spatial dimensions of a Cartesian coordinate system (x, y, z). If the velocities of the electrolytes are denoted as V_x, V_y and V_z , the change in concentration c is given by the following expression:

$$\frac{\partial c}{\partial t} = D\left[\frac{\partial^2 c}{\partial x^2} + \frac{\partial^2 c}{\partial y^2} + \frac{\partial^2 c}{\partial z^2}\right] - \left[V_x \frac{\partial c}{\partial x} + V_y \frac{\partial c}{\partial y} + V_z \frac{\partial c}{\partial z}\right] \tag{3.22}$$

The first sum describes the transport due to diffusion according to Fick's law. A solution in the finite difference scheme was provided by Feldberg *et. al.* [177]. The algorithm shall be briefly summarized here. The first step is to define a spatial grid. In the RRDE experiment, the radial transport to the ring electrode of species generated at the disc electrode takes place. In addition, the electrode used for this purpose is symmetrical around the center of the disc electrode. Therefore a two-dimensional space grid can be used for the calculations. A sketch of the spatial grid is given in Figure 3.7. A discretization takes place in vertical and radial direction. The concentration is given by the box elements (j, k). j describes the box elements perpendic-

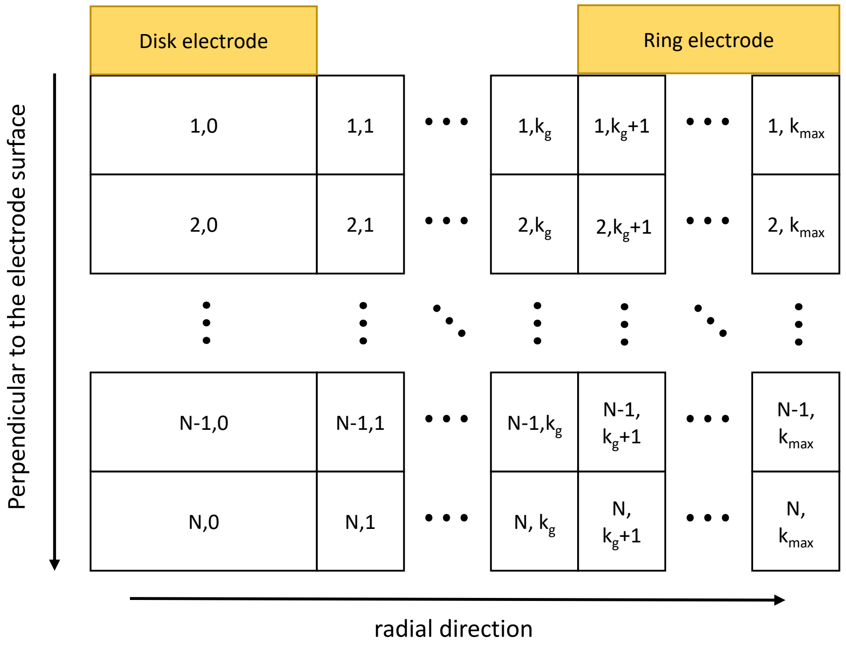

Figure 3.7: Representation of the two dimensional space grid for finite difference RRDE simulations.

ular to the electrode, analogous to chapter 3.2. k are the box elements in radial direction. The discretization is carried out with the use of the RRDE radii r_1, r_2 and r_3 with the following equations:

$$r_1 = \Delta r k_0 \tag{3.23}$$

$$r_2 = \Delta r (k_0 + k_g) \tag{3.24}$$

$$r_3 = \Delta r (k_0 + k_{max}) \quad \text{with } k_0, k_g, k_{max} \in \mathbb{N} \tag{3.25}$$

For the volume in front of the disk electrode only a one-dimensional array is necessary, because there it is assumed that $\frac{\partial c}{\partial r} = 0$ (see (j,k=0) in Figure 3.7). For the velocity field, the Karman and Crohan velocity field discussed in the chapter 2.2 is used [134, 135]. The velocity components perpendicular to the electrode v_j and radial $v_{j,k}$ can be calculated for each box using the following equations:

$$\bar{v}_j'' = -\bar{\beta} j^2 \Delta t / \Delta z \sum_{k=2}^{n} \frac{a_k}{a_2} j^{k-2} \bar{\gamma}^{k-2} \tag{3.26}$$

$$\bar{v}_j' = -\bar{\beta} (j-1)^2 \Delta t / \Delta z \sum_{k=2}^{n} \frac{a_k}{a_2} (j-1)^{k-2} \bar{\gamma}^{k-2} \tag{3.27}$$

$$\bar{v}_{j,k}'' = -\Delta t / \Delta r (\bar{v}_j'' - \bar{v}_j')(k_0 + k)/2 \tag{3.28}$$

$$\bar{v}_{j,k}' = -\Delta t / \Delta r (\bar{v}_j'' - \bar{v}_j')(k_0 + k - 1)/2. \tag{3.29}$$

The notation $'$ indicates the flow into the box and $''$ indicates the flow out of the box. This distinction is necessary because the volume of the boxes increases radially and thus also the boundary surface of the boxes. a_k are the Kraman-Crohan coefficients. The other simulation parameters are defined as follows:

$$\bar{\beta} = \beta \Delta z \Delta t = -0.5102326\, \omega^{3/2} \nu^{-1/2} \Delta z \Delta t \tag{3.30}$$

$$\bar{\gamma} = \gamma \Delta z = \left(\frac{\omega}{r}\right)^{1/2} \Delta z \tag{3.31}$$

$$\bar{D} = D \Delta t / \Delta z^2 \tag{3.32}$$

To calculate the change in concentration in the boxes, it is also necessary to calculate the concentrations at the box edges:

$$s''_j(j,k) = \frac{c(j+1,k) + c(j,k)}{2} \quad \text{for } j \geq 1 \tag{3.33}$$

$$s'_j(j,k) = \frac{c(j,k) + c(j-1,k)}{2} \quad \text{for } j \geq 2 \tag{3.34}$$

The calculation of the value $s'_1(1,k)$ is not necessary, because $v'_1 = 0$. Special conditions were derived for the boxes along the disc electrode-gap and gap-ring electrode boundaries:

$$s'_k(j,1) = c(j,0) \tag{3.35}$$

$$s''_k(j,k_g) = \frac{3c(j,k_g) - c(j,k_g-1)}{2} \tag{3.36}$$

$$s'_k(j,k_g+1) = s''_j(j,k_g) \tag{3.37}$$

$$s''_k(j,k_{max}) = \frac{3c(j,k_{max}) - c(j,k_{max}-1)}{2} \tag{3.38}$$

The remaining boxes are treated as follows:

$$s'_k(j,i) = \frac{c(j,k) + c(j-1,k)}{2} \tag{3.39}$$

$$s''_k(j,i) = \frac{c(j,k) + c(j+1,k)}{2} \tag{3.40}$$

These expressions can be used to calculate for each time step i the change in concentration in each box for which $j \geq 2$, with the following expression:

$$\begin{aligned} \Delta c(j,k) = {} & \bar{D}(c(j+1,k) - 2c(j,k) + c(j-1,k)) \\ & - \bar{v}''_j s''_j(j,k) + \bar{v}'_j s'_j(j,k) - \bar{v}''_{j,k} \frac{2s''_k(j,k)(k_0+k)}{2(k_0+k)-1} + \bar{v}'_{j,k} \frac{2s'_k(j,k)(k_0+k-1)}{2(k_0+k)-1} \end{aligned} \tag{3.41}$$

The following applies to the row of boxes directly before the electrode (j=1):

$$\begin{aligned}\Delta c(1,k) = \bar{D}(c(2,k) - c(1,k)) + \frac{\bar{v}''_1 - \bar{v}'_1}{2(k_0+k)-1}\left[s''_k(1,k)(k_0+k)^2 - s'_k(1,k)(k_0+k-1)^2\right] \\ - f(j)\Delta t/\Delta z \end{aligned} \tag{3.42}$$

where $f(j)$ is the flux at the electrode surface for the j-th segment. Here again electrode reactions based on a Nernst behaviour or a Butler-Volmer Kinetic can be implemented.

Some results generated with this algorithm are already shown in chapter 2.2. In addition, appendix D is comparing some simulated results of the RRDE simulation to the mathematical expressions derived to describe phenomena of the RRDE.

4

A new thin layer cell for battery related DEMS-experiments: the activity of redox mediators in the Li–O_2 cell

Pawel Peter Bawol*, Philip Heinrich Reinsberg *, Christoph Johannes Bondue*, Abd-El-Aziz Abd-El-Latif*, Heinz-Peter Königshoven* and Helmut Baltruschat*

*Institut für Physikalische und Theoretische Chemie, Universität Bonn, Römerstraße 164, D-53117 Bonn, Germany

Reprinted (adapted) from
P. P. Bawol, P. H. Reinsberg, C. J. Bondue, A. A. Abd-El-Latif and H. Baltruschat, *Phys. Chem. Chem. Phys.* **2018**, 20, 21447-21456, DOI: 10.1039/C8CP03592J

Own manuscript contributions:

- designing the thin layer DEMS cell
- performing the experiments
- data evaluation
- interpretation of the results
- writing the manuscript

4.1 | Abstract

The reversibility of current Li–O_2 batteries suffers from high charging overpotentials. To address this problem, the use of redox mediators has been proposed, which are supposed to improve the sluggish reaction kinetics of the oxygen evolution reaction via a solution mediated oxidation of lithium peroxide. In this study, we present a new thin layer cell for battery related differential electrochemical mass spectrometry (DEMS) experiments, which exhibits a high electrode surface area to electrolyte volume ratio which is closer to the situation in batteries other approaches/cells with their usually large electrolyte excess. The confined volume also allows a better distinction between the mediating activity of a redox system and a near continuous electrochemical reaction of this species. One further benefit of the new thin layer cell is that experiments can easily be performed under different O_2-partial pressures. This new set-up allows the highly sensitive detection of volatile species formed during the OER. Therefore, small changes in the number of electrons transferred per oxygen molecule are observable. These changes help to identify side reactions and possible decomposition of the reaction products. During our experiments, we investigated the impact of TTF, TMPD, Fc and TEMPO on the oxidation of Li_2O_2. Within our experiments, we are able to precisely determine the potential at which the catalytic activity of the redox mediation starts. A comparison between the potential at which we observe the activity of the redox mediator to the half wave potential of the redox system could be explained with an outer sphere electron transfer for the oxidation of Li_2O_2 by a redox mediator. This observation is confirmed by a theoretical treatment of the redox mediation mechanism. Moreover, insights into the number of transferred electrons per oxygen molecule during the activity of the different redox mediators reveal the presence of side reactions. This finding is also underlined by an unexpected shift of the CO_2 evolution onset for the redox mediator containing electrolytes. Our experiments also reveal that a Li–O_2 cell, which contains a redox mediator, undergoes less fluctuation in its reversibility compared to a cell without a redox mediator.

4.2 | Introduction

The development of new energy storage systems with high capacities and good cycle performance is one of the challenging tasks in electrochemistry. Due to its high theoretical specific energy density of $3458\,\mathrm{W\,h\,kg^{-1}}$ (assuming Li_2O_2 as the main discharge product and including the weight of oxygen) the lithium–oxygen (Li–O_2) battery is a promising candidate for a new energy storage system [67].

Using DEMS to quantify the oxygen reduction reaction (ORR) and the oxygen evolution reaction (OER) in metal–O_2 batteries allows the determination of the true reversibility of the system

in respect to consumed and evolved oxygen. Moreover, the presence of side reactions including the formation of volatile reaction products like CO_2 is discernible. An important quantity to judge the performance of the ORR and OER is the number of electrons transferred per oxygen molecule (electron number), which can be determined by relating the flux of oxygen into the mass spectrometer to the faradaic current measured at the electrode. The highest expected value of the electron number in a Li–O_2 cell during the ORR and OER is 2 e^-/O_2 for the formation and oxidation of Li_2O_2. Derivations of this value towards higher electron numbers identify the presence of parasitic side reactions. In the past, many studies with DEMS were done to examine metal–O_2 systems [26, 52, 70, 90, 97, 98, 155, 181–184].
One of the problems of the Li–O_2 battery is the fact that the discharge product Li_2O_2 is non conducting. In the absence of any water it is deposited as a thin film on the electrode surface (one or two monolayers in the case of smooth Au), thus blocking the electrode and diminishing the capacity of a battery. Water catalyzes the ORR [26, 185] at least in DMSO based electrolytes it impedes the direct second reduction step, thus shifting the mechanism to the solution pathway: LiO_2 is dissolved in the electrolyte and then disproportionate to Li_2O_2, forming the well-known toroid structures. The solvation pathway is favored by solvents with a high polarity and by additives impeding the direct transfer of the second electron.
One of the challenges that must be overcome to obtain an energy economic Li–O_2 battery thus is to make Li_2O_2 accessible to reoxidation and reduce the charging overpotential. Recently Liu *et al.* reported that on a gold electrode the oxidation of Li_2O_2 first occurs at an interface between the gold electrode and the Li_2O_2 deposits [186]. The remaining particles are losing mechanically contact with the electrode resulting in a higher overpotential for an oxidation of the Li_2O_2 particles. It is also reasonable to avoid high charging potentials in Li–O_2 batteries since at higher potentials the formation of singlet oxygen [115] and the decomposition of the electrolyte was observed [187]. Recently Mahne *et al.* showed, that small amounts of singlet oxygen are also formed from the onset of the charge of a Li–O_2 cell [116]. To address the issues related to battery charging, Chen *et al.* introduced in 2013 the concept of soluble redox mediators in Li–O_2 batteries [50]. A redox mediator is a redox system with an oxidation potential more positive than the equilibrium potential of Li_2O_2 (2.96 V vs. $Li \mid Li^+$, calculated from standard free enthalpy of formation [188]). The redox mediator is oxidized on the electrode surface to RM^+. RM^+ can now act as an electron–hole transfer agent, which diffuses to the Li_2O_2 surface. There RM^+ oxidizes Li_2O_2, forming Li^+, oxygen and RM (see Figure 4.1).

Since 2013 many redox mediators like TTF [50, 51, 183], TEMPO [52, 189, 190], LiBr [57], LiI [53, 191, 192] and some transition metal complexes [183, 193] were suggested as possible candidates for a Li–O_2 battery. These studies show that a homogeneous catalysis of the OER can reduce the charging voltage of a Li–O_2 battery effectively. Nevertheless, the search for a long-

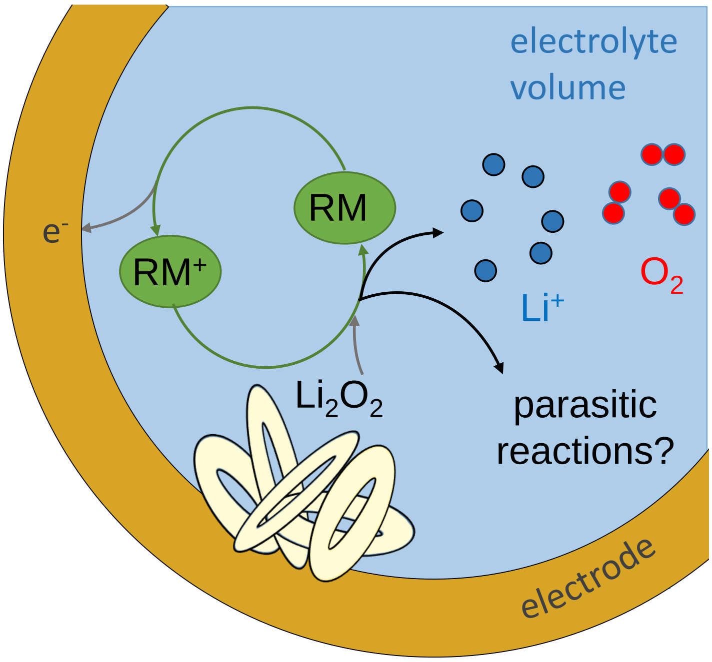

Figure 4.1: Drawing of the electron–hole transfer mechanism induced by the oxidation of a redox mediator (RM), between the electron surface and the solid Li_2O_2.

term stable redox mediator with an oxidation potential slightly above the standard potential of Li_2O_2 is an ongoing research topic. Due to the reactive nature of the oxygen species in a Li–O_2 battery, redox mediators have to resist side reactions such as H-abstraction and nucleophilic attacks of various oxygen compounds [105, 123, 194–197]. In a recent viewpoint McCloskey argued about the chemical stability of redox mediators and the need of a quantitative analysis to detect side products of decomposition reactions of the redox mediators [198].

In this article, we introduce a new thin layer DEMS-cell (with a small electrolyte volume to electrode surface ratio) which can be used to perform battery related experiments in a three electrode arrangement with smooth model electrodes. In this study, we will discuss the impact of tetrathiafulvalen (TTF), *N,N,N′,N′*-tetramethyl -p-phenyl-enediamine (TMPD), 2,2,6,6-tetramethylpiperidinyloxyl (TEMPO) and ferrocene (Fc) as RMs regarding the oxidation of Li_2O_2. In general, we will show that during the activity of RM the oxygen formation rate is increased. Moreover, the experiments show that small concentrations of RM^+(in the range of 10^{-3} to 10^{-6} M) in front of the electrode are sufficient to oxidize Li_2O_2. This necessary concentration of RM^+ is decreasing as the oxidation potential of the RM used is increasing. From the mass spectrometric cyclic voltammograms of mass 32 (plot of the ion current of mass 32 or, after calibration the O_2-flux into the MS versus the electrode potential in the CV) we can determine the potential at which the catalytic cycle in Figure 4.1 starts precisely. Since the ratio of electrolyte volume to electrode surface in the thin layer cell is low, the concentration of products formed during ORR and OER is high. This high concentration of reactive species like $O_2^{\cdot -}$ or singlet oxygen might be the reason why we are able to detect parasitic reactions in the oxidation of Li_2O_2 by a redox mediator. The purpose of this paper is to present an experiment in which the electron numbers of redox mediators could be determined in a battery related environment under a O_2-atmosphere in situ. Moreover, we derived a model for the oxidation of Li_2O_2 by a redox mediator by combining the Marcus theory as well as a Nernstian behaviour for the ratio between RM to RM^+ in front of the electrode surface. These reflections line up in the current discussion about the mechanism of Li_2O_2 oxidation by a redox mediator [60].

4.3 | Experimental

Chemicals

The supporting electrolyte consists of a 0.5 M $LiClO_4$ (batterygrade, Sigma Aldrich) in extra dry DMSO (99.7%, over molecular sieve, Acros Organics). As an electrolyte for the chemical calibration of our DEMS system, we used a 0.5 M $TBAClO_4$ (99.9%,Sigma Aldrich) in extra dry DMSO. All electrolytes were prepared and stored in an MBraun glovebox. The water content was determined by a coulometric Karl Fischer Titrator (C20 Metler Toledo) and never exceeded a value of 20 ppm. As redox mediators TTF (97%, Alfa Aesar), TMPD (99%, Sigma Aldrich), Fc (98%, Sigma Aldrich) and TEMPO (99%, Sigma Aldrich) were used. These redox mediators were added to the supporting electrolyte to obtain a concentration of 10 mM of the redox mediator in the supporting electrolyte. The atmosphere in the glove box consists of highly pure argon (99.999%, air liquid). The humidity inside the glovebox never exceeded 0.5 ppm. Highly pure oxygen (99.995%, air liquid) was used to saturate the electrolyte.

Reference electrode

A silver wire immersed in 0.1 M $AgNO_3$ (99%, Chempur) in DMSO was used as a reference electrode. In order to avoid contamination of silver in the electrolyte, the connection between the electrolyte and the reference electrode was closed with the help of a rough surface of a glass bead. A detailed description of the reference electrode can be found elsewhere [90]. The potential of the reference electrode is approximately 3.83 V versus the $Li^+ | Li$ couple or 0.43 V vs. NHE [132].

DEMS-experiments

DEMS-experiments were carried out with a self-built differentially pumped DEMS-system similar to the DEMS-setup which was previously described by O. Wolter and J. Heitbaum [142]. In our case, the first pumping stage has a pumping speed of 200 $\mathrm{L\,s^{-1}}$ (TMU 260, Pfeiffer Vacuum) and the second one 50 $\mathrm{L\,s^{-1}}$ (TPU 062, Pfeiffer Vacuum). The mass spectrometer is a QMA 430 by Balzers. A detailed technical drawing of our DEMS-system can be found in reference [153]. To calculate the flux of a species $\dot{n}_{m/z}$ with the mass to charge ratio m/z into the mass spectrometer the calibration constant $K^*_{m/z}$ is needed:

$$\frac{dn_{m/z}}{dt} = \dot{n}_{m/z} = \frac{I_{m/z}}{K^*_{m/z}F} \tag{4.1}$$

Here $I_{m/z}$ is the baseline corrected ionic current with m/z and F is the Faradaic constant. Due to the baseline correction, positive values of $\dot{n}_{m/z}$ can be interpreted as an evolution of a species with m/z. Negative $\dot{n}_{m/z}$ are related to an consumption of a species with m/z. For this study, the fluxes of mass 32 (O_2) and 44 (CO_2) are of interest. The calibration constant K^*_{32} was determined by a electrochemical oxygen reduction in a 0.5 M $TBAClO_4$ solution in DMSO. Previous experiments showed that in $TBAClO_4$ containing electrolyte O_2 is reduced only to superoxide [90, 92, 146]. K^*_{32} was determined each day an experiment was performed. K^*_{44} was determined from the relative ionization probabilities (IP) of O_2 and CO_2 as follows [199]:

$$K^*_{44} = K^*_{32}\frac{IP_{44}}{IP_{32}} = 1.4K^*_{32} \tag{4.2}$$

The number z of transferred electrons per oxygen molecule is of special interest in this study. To calculate z, the faradaic current in the CVs was first corrected for the additional faradaic current resulting from the mere oxidation of the redox mediator without oxidizing Li_2O_2. A detailed description of the data evaluation can be found in the supporting information (see chapter 4.6). With the help of the corrected faradaic current ΔI_F, z can be calculated:

$$z = \frac{\Delta I_F}{\dot{n}_{32}F} \tag{4.3}$$

Experimental design

The new thin layer cell is based on the design described by Hartung and Baltruschat [200]. A general overview of electrochemical cells (in a 3 electrode arrangement) used so far in DEMS experiments is given in reference [153]. Figure 4.2 shows a schematic drawings of (a) the top view of the cell body and (c) the cross section view of the assembled cell. The cell body and the T-pieces are made out of Kel-F. The working electrode (WE) as well as three counter electrodes

(CE 1, CE 2 and CE 3) are made out of gold. The counter electrode is positioned outside of the thin layer cell. The distance between the CEs and the WE is approximately 25 mm. The experimental setup described in this paper is not a completely assembled battery but a kind of a half-cell in a three-electrode arrangement. The WE in this study is therefore comparable to an oxygen cathode in metal–air batteries. The gold counter electrodes and a reference electrode (RE) are connected to the electrolyte with the T-pieces. CE 1 and CE 2 are connected via a 1 Ω-resistance to a self made potentiostat whereas CE 3 is connected via a 4 MΩ-resistance to the potentiostat. In this arrangement, an optimal current distribution from CE 1 and CE 2 towards the working electrode is achieved. To avoid oscillations in the faradaic current as well as high iR-drops, CE 3 is separated from CE 1 and CE 2 over a 4 MΩ resistance. For the electrolyte inlet, a 3 mL syringe is used. During the measurements, no convection of the electrolyte through the cell takes place.

A porous PTFE membrane is pressed in between the upper part of the cell body (see Figure 4.2 (c)) and a cone shaped cell holder. The PTFE membrane has a porosity of 50% and an average pore diameter of 20 nm. Mechanical support of the PTFE membrane is realized through a porous steel frit. Figure 4.2 (b) shows a schematic drawing of the connection tubes used for the oxygen saturation of the working electrode compartment as well as for the transfer of volatile species into the mass spectrometer. The volume of the connection tubes above the thin layer cell can be evacuated using a rotary vane pump (DUO 2.5, Pfeiffer Vacuum). Small amounts of oxygen can be added to the volume using a metering valve (V4 in Figure 4.2 (b)). The pressure change is recorded by a pressure sensor (TPG 202, Pfeiffer Vacuum). For all experiments in this study, an oxygen pressure of 900 mbar was applied to the connection tubes over the cell body. The electrolyte volume in the working electrode compartment is saturated with oxygen through the porous PTFE membrane. The electrolyte volume in front of the working electrode is defined by four PTFE O-rings with an inner diameter of 6 mm and an outer diameter of 14 mm. The overall thickness of the PTFE spacers is 200 µm. Thus, the resulting volume in the working electrode compartment is 5.6 µL. A gold sputtered porous PTFE membrane is used as the working electrode. The thickness of the deposited gold is 50 nm. The contact area between the working electrode and the electrolyte is 0.283 cm^2. The porosity and the pore diameter are 50% and 20 nm respectively. Volatile species in front of the electrode can evaporate into the vacuum of the mass spectrometry tubes. Therefore the change of volatile species produced or consumed during an electrochemical experiments can be detected through the ionic current of the mass spectrometer. The working electrode is electrically contacted via a 0.05 mm thick gold wire to the lower cell holder. Hence, the connection to the working electrode can be made over the steel holders.

The cell itself is placed in a glovebox to avoid high water amounts in the electrolyte. All experiments shown in this publication are done in the glovebox

In order to be able to also carry out experiments outside a glovebox, a Kalrez O-ring is used to seal the lower part of the cell from the laboratory atmosphere. A capillary (see Figure 4.2 (a)) is used to flush the PTFE-spacers with argon. A detailed description showing the relation between the flux of oxygen into the mass spectrometer and the applied oxygen partial pressure to saturate the electrolyte can be found in the supporting information (chapter 4.6).

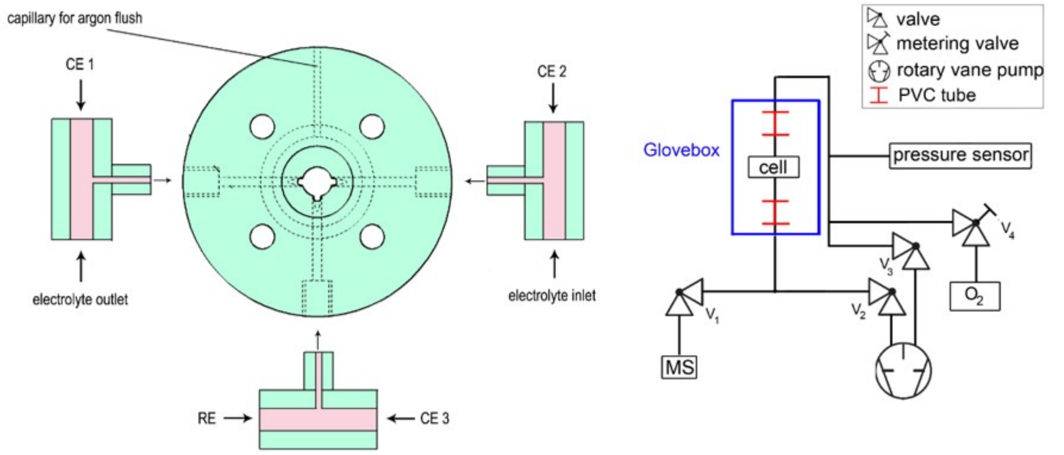

(a) Top view of the thin layer cell:

(b) Schematic drawing of the connection tubes

(c) Cross section view of the assembled thin layer cell:

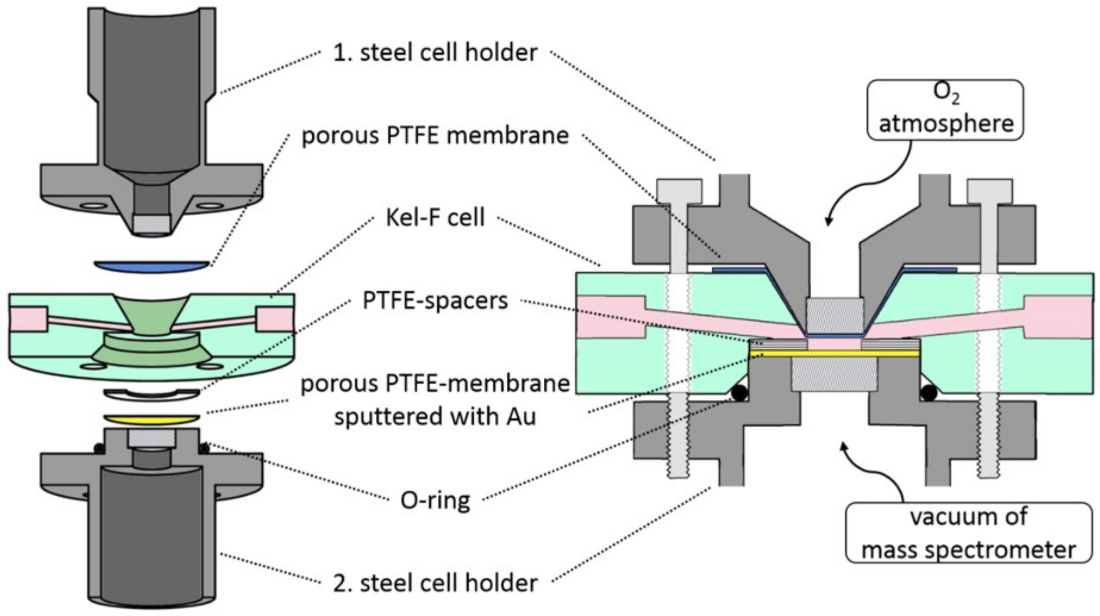

Figure 4.2: (a) Top view on the cell body built out of Kel-F (green) with the connections for the counter electrodes (CE 1, CE 2 and CE 3) and the reference electrode (RE). (b) Schematic drawing of the connection tubes used to saturate the electrolyte with oxygen and to transfer volatile species into the vacuum of the mass spectrometer chamber. (c) Cross section view of the assembled cell.

4.4 | Results and discussion

4.4.1 | Oxygen evolution using a redox mediator

To emphasize the catalytic effect of the used redox mediators in this study, DEMS-experiments for the supporting electrolyte (0.5 M $LiClO_4$ in DMSO) were performed before adding the redox mediator to the supporting electrolyte. Although side reactions of DMSO with reactive oxygen species produced in the ORR were reported [187, 194, 201], it shows a good stability for a short time exposure during a cyclic voltammetry run and was therefore chosen as a solvent for this study. The experiments with a 0.5 M $LiClO_4$ in DMSO are plotted in a blue color for the remainder of this study (see Figure 4.3).

Combining cyclic voltammetry and mass spectrometry, the ORR in a 0.5 M $LiClO_4$ in DMSO can be clearly observed beginning at -0.95 V in cathodic direction. The number of electrons transferred per oxygen molecule was calculated according to equation 4.3 and is close to $2\,e^-/O_2$ over the whole potential window of ORR (see Figure 4.13). This was previously observed on a rough gold electrode [90]. On smooth gold electrodes, there is a transition from the one electron process (formation of $O_2^{\cdot -}$) to the two electron process (formation of O_2^{2-} [26, 110, 111]). The absence of the one electron process on sputtered gold electrodes is due to the roughness. In fact, it has been observed that the formation of Li_2O_2 is mainly limited by the nucleation rates at low overpotentials [35, 202]. A similar effect concerning the ORR was previously observed for platinum electrodes with different surfaces roughness [26]. The shape of the ORR-region differs slightly in the different measurements shown in Figure 4.3 and in the supporting information. The reason for this is the porous Teflon membrane sputtered with gold, which is used as a working electrode. Since we used for every experiment with a new redox mediator a new gold electrode, the roughness of the electrodes might slightly vary. Thus, the amounts of deposited Li_2O_2 is also different resulting in slightly different shapes in the ORR region (see slighter differences in the blue curves in Figure 4.3 (a) and (b)). Further experimental data concerning the effect of surface roughness of Au-electrodes on the shape of the ORR region in a CV is shown in the supporting information. The onset of the OER is shifted about 300 mV towards more positive potentials compared to the onset of the ORR, which is close to the thermodynamically expected potential of Li_2O_2 (-0.87 V). It is remarkable that the OER at gold occurs over a wide potential window during a cyclic voltammetry experiment. This was observed by many groups before, whereas it is worth mentioning that the CVs differ in the different publications dealing with the OER in Li-containing DMSO based electrolytes on gold electrocatalyst in the shape of the OER-region [110, 186, 194, 203]. Bondue *et al.* performed cyclic voltammetry with an Au(111)- electrode [26]. In their work, the authors showed that the OER-region is clearly

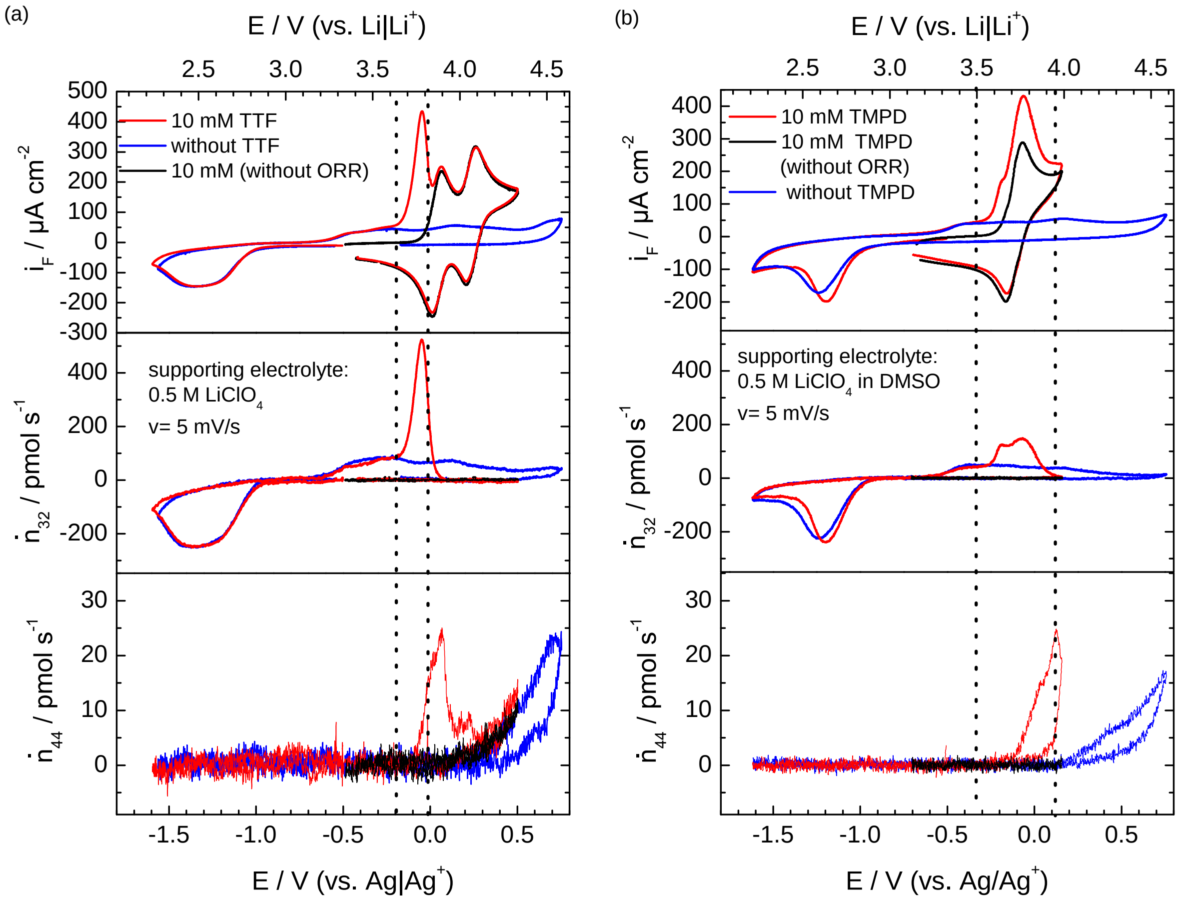

Figure 4.3: (a) CVs and MSCVs on mass 32 and 44 with a sweep rate of 5 mV s^{-1} in 0.5 M $LiClO_4$ solution in DMSO with 10 mM TTF (black and red trace) and without TTF (blue trace). (b) CVs and MSCVs on mass 32 and 44 with a sweep rate of 5 mV s^{-1} in 0.5 M $LiClO_4$ solution in DMSO with 10 mM TMPD (blackand red trace) and without TMPD (blue trace). During all measurements the oxygen pressure used to saturate the electrolyte was 900 mbar.

changing in every cycle of the cyclic voltammetry experiment. Due to the low activity of gold in the OER it is particularly suitable to observe changes in the OER forced by a redox mediator. Figure 4.3 shows the cyclic voltammetry and the MSCVs for mass 32 and 44 with 10 mM TTF added to the supporting electrolyte. The ORR-region is not affected by the presence of TTF. Neither is the onset of the OER is affected. At -200 mV a steep rise of I_F and $\dot{n}_{32}$ can be observed, which is absent in the electrolyte only containing Li^+. I_F and $\dot{n}_{32}$ exhibit a maximum at -45 mV. At higher potentials, the shape of the CV is similar to that one avoiding a preceding ORR indicating that there is no additional contribution from the oxidation of Li_2O_2 at more positive potentials (red trace and black trace in Figure 4.3). This can be clearly seen by the sharp decrease of $\dot{n}_{32}$ at the above mentioned potential. The high catalytic activity of TTF towards the OER can be directly seen from the comparison of the MSCVs for mass 32. In the presence of TTF there is a steep increase of $\dot{n}_{32}$ and a narrow peak is exhibited. The onset of the increase of IF and $\dot{n}_{32}$ at -200 mV during the anodic sweep can be understood as follows: during the anodic sweep, oxidation of Li_2O_2 starts at -0.5 V resulting in the partial reactivation of the electrode (Li_2O_2 itself is insulating). When the potentials approaches the standard potential of the TTF^+/TTF couple, the electrochemical oxidation of TTF^+ starts in front of the working electrode. Considering the CV in Figure 4.3 (a), in which the potential region of ORR is avoided (black trace) one would guess that at -200 mbar no TTF^+ is generated yet, because there was no rise of the faradaic current detected at this potential. The rise of I_F and $\dot{n}_{32}$ in the red traced measurement in Figure 4.3 at -200 mV shows that the catalytic cycle shown in Figure 4.1 starts. This demonstrates that extremely small concentration of TTF^+ (at a potential of -200 mV, the concentration of TTF^+ is according to the Nernst equation in the range of 10^{-5} M) are sufficient to observe a significant catalytic oxidation of Li_2O_2.

From a thermodynamic point of view, TTF^+ should also be able to oxidize LiO_2 and $O_2^{\cdot -}$. However, during the ORR we mainly observed the formation of Li_2O_2 (see Figure 4.13 in the supporting information). Therefore we are generalizing the discussion towards the oxidation of Li_2O_2. As the potential of the working electrode rises, the concentration of TTF^+ increases in front of the working electrode. Consequently, more catalytic cycles can occur resulting in an increase of the faradaic current combined with an oxygen evolution. IF and $\dot{n}_{32}$ are exhibit a peak just before the entire Li_2O_2 on the working electrode is consumed.

As we proposed above, the lower potential of the OER activity of TTF (compared to the onset of TTF oxidation) is due to the small concentration of TTF^+ given by the Nernst equation. This means that increasing the TTF concentration in electrolyte would shift the needed TTF^+ concentration to start the oxidation of Li_2O_2 to more negative electrode potentials. As shown in Figure 4.4 we could indeed observe this effect while increasing the concentration of TTF in the electrolyte: the peak p_a is shifting in the CV as well as in the MSCV for mass 32 to negative electrode potentials, while increasing the concentration of TTF form 10 mM (traced red in Figure 4.4) to 40 mM (traced green in Figure 4.4).

In the case of the TMPD containing electrolyte (see Figure 4.3(b)) the onset of its activity as redox mediator is observed at more negative potential compared to the standard potential of the redox couple TMPD/$TMPD^+$ as well (as a rough measure for the standard potential we consider the half wave potential of the redox couple). During the activity of TMPD as a redox mediator, we observe two peaks in the MSCV of mass 32 at -186 mV and -69 mV. In the faradaic current no additional peak appears but a shoulder appears at -190 mV and the faradaic current is also increased in comparison to the current in the cyclic voltammetry in which the potential of the ORR is avoided. The presence of two peaks in the MSCV of mass 32 leads us to the conclusion that the oxidation of Li_2O_2 by $TMPD^+$ has to take place in two different processes.

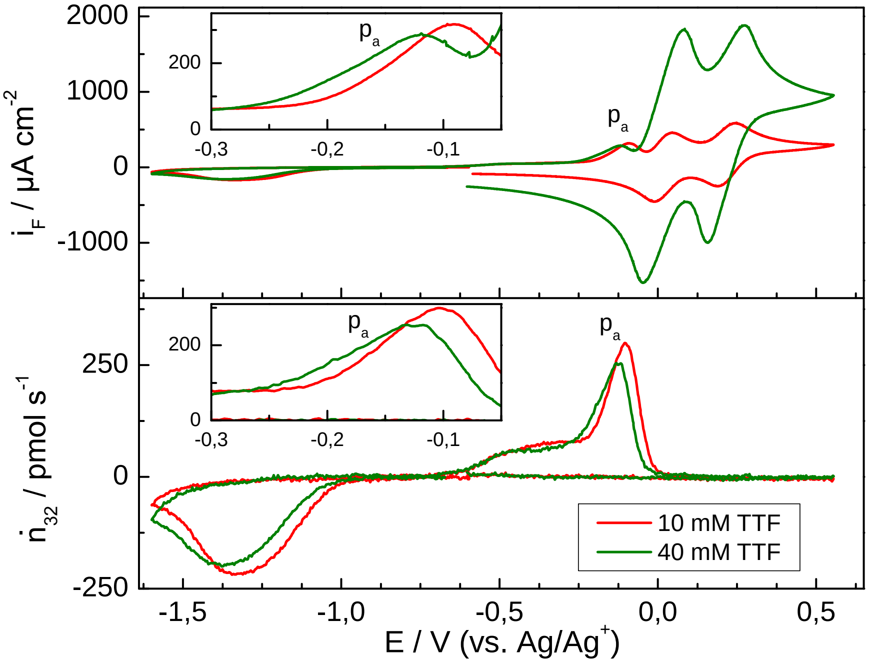

Figure 4.4: CVs and MSCV on mass 32 with a sweep rate of 10 mV s^{-1} in 0.5 M $LiClO_4$ solution in DMSO with various TTF concentrations: 10 mM (red trace) and 40 mM (green trace). During all measurements the oxygen pressure used to saturate the electrolyte was 900 mbar. Each of the experimental datasets shows a close up to peak p_a.

The comparison of TTF and TMPD as redox mediators also reveals, that in the case of TTF the oxidation of Li_2O_2 by TTF$^+$ is faster than by TMPD$^+$ as can be seen on the higher oxygen flux in the OER and broadness of the OER region.

During the experiment $\dot{n}_{44}$ was also recorded. This flux is assigned to the formation of CO_2. As previously reported for DMSO based electrolytes, reaching higher electrode potentials lead to an evolution of CO_2 (see blue traced measurements in Figure 4.3 (a) and (b)) [90, 201]. In this study, the CO_2-evolution starts at 150 mV in the supporting electrolytes. The source of this CO_2-evolution was already attributed to the oxidation of solid Li_2CO_3 and other decomposition products formed during the ORR [84, 90, 204]. In presence of the redox mediator, the onset of the CO_2-evolution shifts towards negative potentials. In the case of TTF containing electrolyte, the onset is located at -90 mV and in the case of TMPD at -140 mV. From a thermodynamical point of view, it is not reasonable that the oxidation of Li_2CO_3 or other CO_2 releasing species, which are normally observed in the supporting electrolyte, shifts towards more negative electrode potential. Therefore, we suggest that in the presence of the redox mediator a new CO_2 releasing species is formed in a side reaction between the redox mediator and a reactive oxygen species. This new species could then be oxidized at lower electrode potentials.

Before all experiments we convinced ourselves that the in this study used mediators are stable to an oxygen exposure. Only in the cases of a ferrocene containing electrolyte, we observed instabilities of the Fc^+-ion towards oxygen, which is already known from literature [205]. The stability Test of TTF is shown in the supporting information.

4.4.2 | Evaluation of the electron numbers for the OER

To judge on the stability of the redox mediators, we used the number of electrons transferred per oxygen molecule as an indicator for side reactions in the OER. Determining the electron number from the ratio of the charging current of a battery to the amount of oxygen formed in a Li–O_2 battery will not give any information about the stability of the used redox mediator since the diffusion of RM^+ towards the Li anode occurs as a side reaction. This contribution cannot be corrected for afterwards and therefore the number of electrons transferred per oxygen molecule is always higher then $2\,e^-/O_2$ when the Li–O_2 battery is charged with a redox mediator containing system as can be seen in literature [183, 192]. Chen *et al.* determined the electron numbers for the oxygen evolution for TTF, TMPD and Fc [50]. In their experiments, they electrochemically produced RM^+. Afterwards, the authors mixed this amount of RM^+ with a solution containing an excess of Li_2O_2 (compared to RM^+, under Ar-atmosphere). The amount of formed oxygen was determined with a mass spectrometer. In their experiment Chen *et al.* observed that TTF is a stable redox mediator ($2.01\,e^-/O_2$) whereas Fc and TMPD are not stable ($2.24\,e^-/O_2$ and $4.55\,e^-/O_2$).

According to equation 4.3 the number of electrons transferred per oxygen molecule during the OER was calculated using the known calibration constant. A plot of the electron number versus the working electrode potential for the TTF and TMPD containing electrolytes is shown in Figure 4.5. The doted lines in Figure 4.3 and 4.5 show the same potential window to insure a better overview between the electron numbers and the experimental data.

As can be seen in Figure 4.5 (a) the electron number for the TTF containing system is in between $1.82\,e^-/O_2$ and $2.06\,e^-/O_2$ in a potential range between -0.4 V and -0.2 V. This value fits well with the oxidation of Li_2O_2. Since we are also observing the same electron numbers in this potential range without adding a redox mediator to the system we can assign the observed OER to the direct electron transfer to the electrode. When the potential of the working electrode is increased to -0.2 V an increase of the electron number towards $2.3\,e^-/O_2$ is observed. In this potential window (between -0.2 V and -0.05 V) the catalytic activity of TTF towards the oxidation of Li_2O_2 was noticed. Because the observed value is greater than the theoretical value of $2.00\,e^-/O_2$, calculated for the proposed catalytic cycle in Figure 4.1, additional side reactions have to be taken into account leading to products, which are susceptible to oxidation.

The analysis of the number of transferred electrons per oxygen molecule in the TMPD contain-

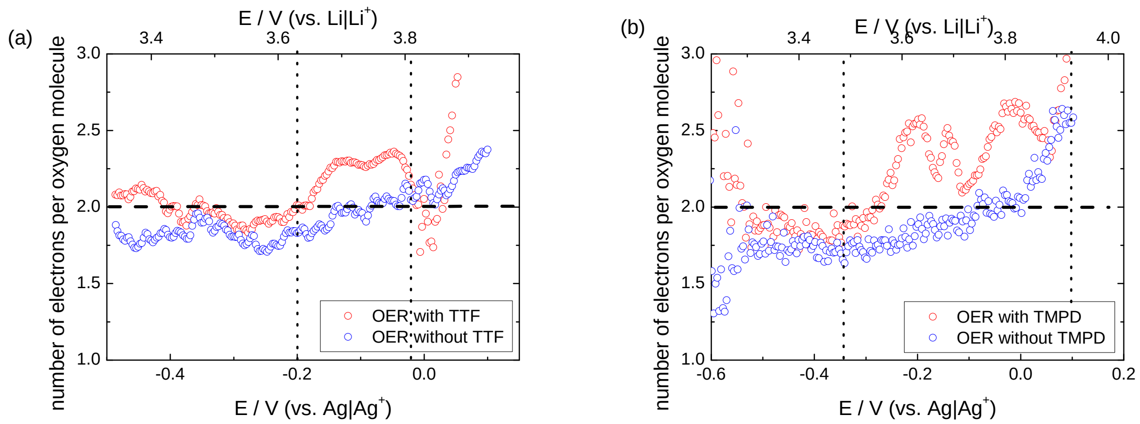

Figure 4.5: Calculated electron numbers concerning the evolved oxygen for (a) the TTF containing electrolyte and (b) the TMPD containing electrolyte. The electron numbers are plotted versus the working electrode potential. The doted lines in both plots are located at the same potentials as in the CVs and MSCVs for TTF (Figure 4.3 (a)) and TMPD (Figure 4.3 (b)).

ing system yields similar results as in the TTF containing system. During the oxidation of Li_2O_2 by $TMPD^+$ (between -0.3 V and 0.1 V in anodic direction), the electron number is also increased in comparison to the measurement in the supporting electrolyte without TMPD as can be seen in Figure 4.5(b). For TMPD, this increase of the electron number seems to be more severe than for to TTF implying a lower stability of TMPD. For further discussion of possible side reactions, the catalytic cycle shown in Figure 4.1 should be modified into a more microscopic mechanism (see reaction scheme 4.4).

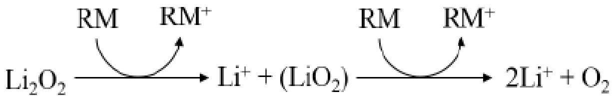

$$Li_2O_2 \xrightarrow{RM \rightarrow RM^+} Li^+ + (LiO_2) \xrightarrow{RM \rightarrow RM^+} 2Li^+ + O_2 \qquad (4.4)$$

As can be seen in the CVs and the MSCVs for mass 32 for the two electron redox couple (TTF) the oxidation of Li_2O_2 has finished before RM_2^+ is generated. Therefore the oxidation of Li_2O_2 has to take place in two steps. In the first step RM^+ generated at free parts of the sample is diffusing towards the Li_2O_2 surface releasing LiO_2 or Li^+ and $O_2^{\cdot -}$ and 2 Li^+. In the next step, another RM^+ molecule has to approach the previously generated superoxide to oxidize it to finally release oxygen. It is possible that a side reaction between this intermediately formed superoxide and RM or RM^+ in the presence of Li^+ occurs. One more source for a side reaction in which TTF could be involved is a reaction between TTF and singlet oxygen. As previously shown, singlet oxygen is formed during the OER as well as during the ORR in Li–O_2 systems [115][116]. Electron rich olefins such as vinyl ethers [206], vinyl sulfides [207] and enamines [208] can undergo a [2+2]-cycloaddition with singlet oxygen. Therefore, this could also be favored reaction between TTF and singlet oxygen. To understand the underlying mechanism

of the TTF decomposition a more detailed product analysis using other analytical methods is needed. Nevertheless, our measurements demonstrate that side reaction of the mediator occur in the Li–O_2 cell.
As already described in Section 4.4.1 another indication for side reactions including the redox mediator is the shift of the onset of CO_2 evolution towards more negative electrode potentials. The reversibility of the redox mediators concerning the amount of oxygen evolved during in the OER to the amount of oxygen consumed during the ORR was calculated (see Table 4.1). The experimental data of the systems containing TMPD and TTF are shown in Figure 4.3, whereas the experimental data of Fc is show in Figure 4.12 and TEMPO in Figure 4.11.

Table 4.1: Calculated reversibilities of the electrolytes containing 10 mM of the redox mediator rev_{RM}.

Redox mediator	rev_{RM}
TMPD	0.55
TTF	0.63
Fc	0.60
TEMPO	0.81

Our results show that TEMPO shows the highest reversibility of all four tested mediators. This is in agreement with the result the Janek group has shown [52]: TEMPO containing systems show an overall better cycle performance than TTF containing systems.
Moreover we wanted to compare the reversibilities shown in Table 4.1 with the reversibilities in the measurements performed in the supporting electrolyte to see if the redox mediator leads to any improvement. In our experiments, we observe that the reversibility for the redox mediator containing system undergoes only little fluctuation. As an example, Table 4.2 shows the reversibilities for the TMPD containing system in four different experiments (i.e. four experiments performed on four different days with freshly prepared electrolytes and new assembled experimental set ups). As can be seen in Table 4.2 rev_{TMPD} varies by a value of ±0.02. On the other hand, the reversibility of the experiment performed in the supporting electrolyte varies by a value of ±0.06, i.e. 3 times as much. Our conclusion to these results is that the reversibility of the system is very sensitive to the morphology of the electrode surface and thus creating bigger fluctuation in the reversibilities of the measurements performed in the supporting electrolyte. Whereas the solution mediated oxidation of Li_2O_2 by a redox mediator creates more stable reversibilities within the Li–O_2 cell. Another reason for the fluctuations of revsupport could also be caused by the wide potential region of the OER and the related small $\dot{n}_{32}$-flux. The baseline correction during the data evaluation is sensitive to this small flux. Since $\text{rev}_{\text{support}}$ was determined out of the integral of $\dot{n}_{32}$ we can assume a higher experimental error on $\text{rev}_{\text{support}}$ then for rev_{RM}.

Table 4.2: Calculated reversibilities for 4 different measurement series carried out in a 0.5 M $LiClO_4$ solution in DMSO ($rev_{support}$) as well as in the presence of 10 mM TMPD within the supporting electrolyte (rev_{TMPD}).

Measurement no.	$rev_{support}$	rev_{TMPD}
1	0.47	0.55
2	0.59	0.51
3	0.57	0.52
4	0.53	0.54

4.4.3 | Kinetics of Li_2O_2 oxidation by a redox mediator

In this study we examined the catalytic activity of four different organic redox mediators with different chemical structures. Out of the cyclic voltammetry for the different redox mediators' experiments in which the potential of the ORR is avoided, we determined the half wave potential $E_{1/2}$ for the first electron transfer in anodic direction. In addition, we estimated the potential at which the initiation of the catalytic activity of the redox mediator E_{onset} starts. E_{onset} was estimated out of the MSCV of mass 32 by a comparison of the MSCV of mass 32 in the pure supporting electrolyte (all traced blue in this publication) to the MSCV of mass 32 when 10 mM of the redox mediator was added (all traced red in this publication). E_{onset} is the potential at which the oxygen flux into the mass spectrometer in the RM-containing experiment is increased over 5 pmol s^{-1} above that observed in the measurement in the supporting electrolyte. In Figure 4.6 a plot of E_{onset} as a function of $E_{1/2}$ is shown. A linear fit through the data points gives a linear function with a slope of 0.67±0.9. To our knowledge, no theoretical treatment for the oxidation of Li_2O_2 by a redox mediator was done yet. Bruce and coworkers recently gave some evidences, that the reaction between Li_2O_2 and RM^+ could not be explained by an outer sphere mechanism [60]. Nevertheless, this paper lacks theoretically based arguments. To tackle this problem, we assumed, that the electron transfer between Li_2O_2 and redox mediator could be an outer sphere reaction by combining the Marcus theory as well as a Nernstian behavior for the ratio between RM to RM^+ in front of the electrode surface. A detailed description of our considerations can be found in chapter 4.6. All this consideration ends up in the following expression:

$$E_{onset} = \frac{1}{2}E^0_{RM/RM^+} + const2 + \ln\left(\frac{d[O_2^{\cdot -}]}{dt}\right)_{E_{onset}} \frac{RT}{F} \tag{4.5}$$

We assumed that the amount of $O_2^{\cdot -}$ going into side reactions is negligible with respect to the amount of $O_2^{\cdot -}$ oxidized to O_2. Therefore the term $\ln\left(\frac{d[O_2^{\cdot -}]}{dt}\right)_{E_{onset}}$ is constant since E_{onset} was determined at a constant value for the O_2 flux into the mass spectrometer. As an approximation for the standard potential of the RM/RM^+ redox system E^0_{RM/RM^+} we used the half wave potential $E_{1/2}$. Formula 4.5 predicts a slope of 0.5 in a plot of E_{onset} vs. $E_{1/2}$. For a better overview all constant values were includes into *const*2. Considering all the simplifications that lead us to formula 4.5 the experimental determined slope of 0.67±0.9 is in good agreement with the predicted one. Deviation from the theoretical value could also be caused by different reorganization energies for the solvent shell of the different mediators. The reorganization energy is included into *const*2. Overall, we can conclude that the electron transfer between Li_2O_2 and RM^+ is in agreement with our theoretical considerations.

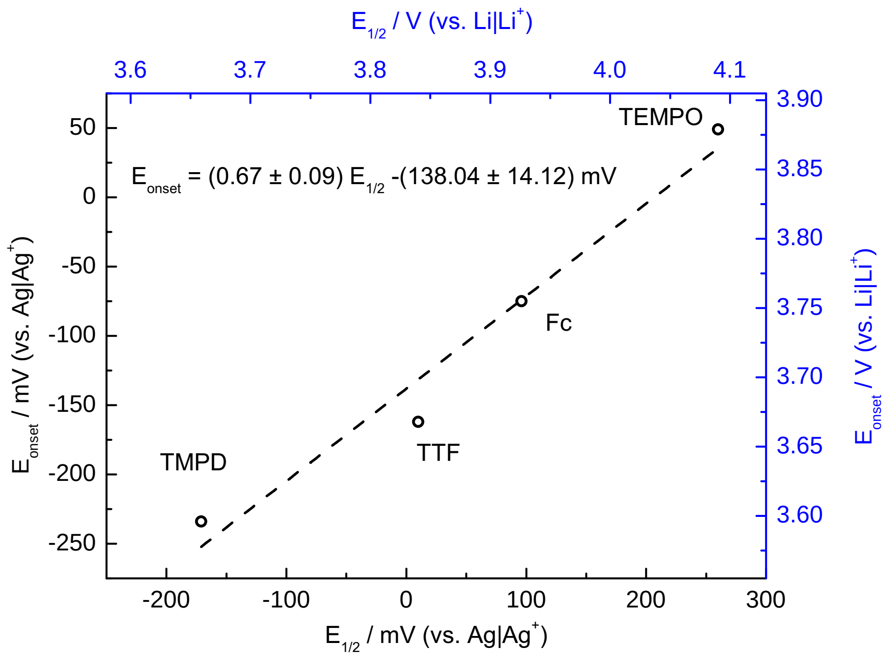

Figure 4.6: Plot of E_{onset} as a function of $E_{1/2}$ for the different studied mediators. The dotted line indicates a linear fit through the plotted points with the linear function $E_{onset} = (0.67\pm\ 0.09)E_{1/2}$ (138.04±14.12) mV.

4.5 | Conclusion

We have presented a new thin layer cell for battery related DEMS experiments. This new cell is ideally suited to investigate the activity of redox mediators during the OER. We believe this experimental setup will be of interest for future researchers to identify new redox mediators for Li–O_2 batteries. The activity of the used redox mediators is detected in situ and the experiment provides the potential at which the mediator becomes active. The new setup is sensitive enough to detect small changes in the number of transferred electrons per oxygen molecule during the activity of the RM and could therefore help to design stable redox mediators. A

further advantage of the new thin layer cell is less contamination from the electrolyte due to the low volume of the cell. Moreover, the experiment is comparable to batteries since products of side reactions would also accumulate within the cell volume.
We investigated the activity of TTF, TMPD, Fc and TEMPO towards the OER. The catalytic activity of the redox mediators towards the OER could be clearly observed in the MSCVs of mass 32. For TTF we showed that increasing the TTF concentration in electrolyte shifts the oxidation of Li_2O_2 by TTF^+ to lower electrode potentials. During the OER for the redox mediator containing electrolytes, we observed an additional CO_2 evolution. From a comparison of the measurements in the supporting electrolyte, we presented clear evidences that the redox mediator is the carbon source of the CO_2 evolution. In addition, the analysis of the number of transferred electrons per oxygen molecule during the OER also reveals the presence of side reactions. We attributed the source of these side reactions to the high concentration of reactive oxygen species formed during the OER. The TEMPO containing system showed the best reversibility in our study. Moreover, our experiment shows that the reversibility of the Li–O_2 cell is more stable in presence of a redox mediator. Combining the Marcus theory and the Nernst equation to the electron transfer between Li_2O_2 and RM^+ shows that our experimental data fit well into that model. Therefore, the nature of the electron transfer between Li_2O_2 and RM^+ could be in agreement with an outer sphere reaction. The aim of this work was to introduce a new DEMS experiment, which is able to check redox mediators for metal–O_2 batteries towards their stability against reactive oxygen species.

Conflicts of interest

There are no conflicts to declare.

Acknowledgements

The authors gratefully acknowledge the Federal Ministry of Education and Research (BMBF) for funding this work. This work is part of the LiBaLu-project in the framework of the "Vom Material zur Innovation"-initiative (03XP0029A). P. R. wishes to thank the German National Merit Foundation for financial support. The authors would like to thank Dr S. Ernst for his helpful discussion.

4.6 | Supporting information

Relation between oxygen partial pressure and ionic current of mass 32

In the presented thin layer cell the saturation of oxygen within the electrolyte is determined through the applied partial pressure of oxygen. According to *Hernry's Law* the equilibrium concentration of dissolved oxygen within the chosen electrolyte in the thin layer cell is proportional to the pressure. Therefore, the flux of oxygen into the mass spectrometer also has to be proportional to the oxygen pressure. To give a more detailed illustration, the concentration profile of the oxygen species within the thin layer cell is shown in Figure 4.7.

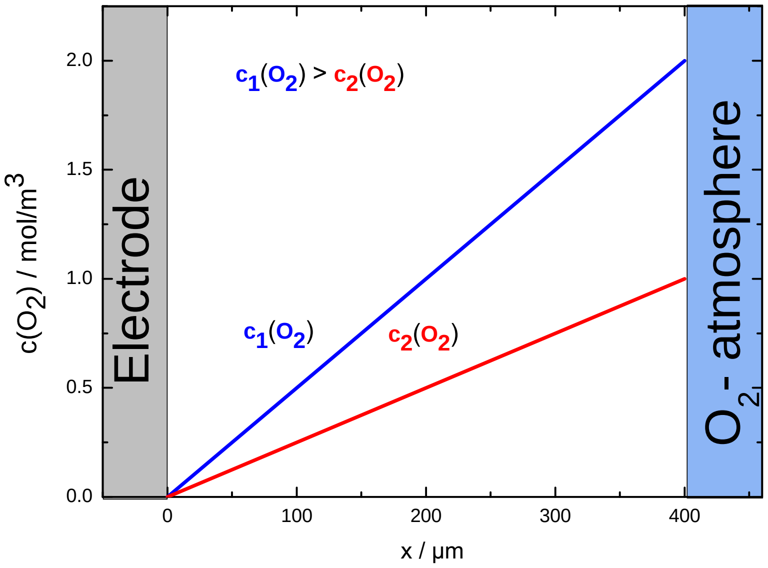

Figure 4.7: Schematic representation of the oxygen concentration profile along the thickness of the working electrode compartment.

After an equilibrium phase, the concentration profile show a linear trend. At the boundary to the oxygen atmosphere the concentration of oxygen within the electrolyte is given by *Hernry's Law* (we assume that there is an equilibrium at the gas/electrolyte interface).

$$c_{O_2} = k_H \cdot p_{O_2} \tag{4.6}$$

Because we are using a gold sputtered porous PTFE membrane as working electrode in all experiments, the dissolved oxygen is evaporating into the vacuum of the mass spectrometer.

Therefore, the concentration of oxygen at the electrode-vacuum boundary is zero. The flux of oxygen into the mass spectrometer can be simply calculated by *Fick's first law*.

$$J_{O_2} = -D_{O_2} \cdot \frac{\partial c_{O_2}}{\partial x} \tag{4.7}$$

For a linear concentation profile, the term $\frac{\partial c}{\partial x}$ simplifies to $\frac{\Delta c}{\Delta x}$. Taking into account that Δx is the thickness of the working electrode compartment as shown in Figure 4.7 the term $\frac{\Delta c}{\Delta x}$ can be further simplified to $\frac{c_{O_2}}{\Delta x}$. Combining all these simplifications into equation 4.6 and equation 4.7 will finally lead to equation 4.8:

$$J_{O_2} = -D_{O_2} \cdot \frac{k_H \cdot p_{O_2}}{\Delta x} \tag{4.8}$$

Equation 4.8 implies a proportionality between the flux of oxygen into the vacuum of the mass spectrometer and the applied partial pressure of oxygen to saturate the electrolyte with oxygen. To test the applicability of the above equations experimentally, we varied the partial pressure of oxygen to saturate the DMSO filled thin layer cell with oxygen. Simultaneously the ionic current of mass 32 I_{32} was recorded (see Figure 4.8 (a)). This ionic current is proportional to the flux of oxygen into the mass spectrometer. Indeed, we found the proportionality between I_{32} (J_{O_2}) and p_{O_2} as can be seen in Figure 4.8 (b).

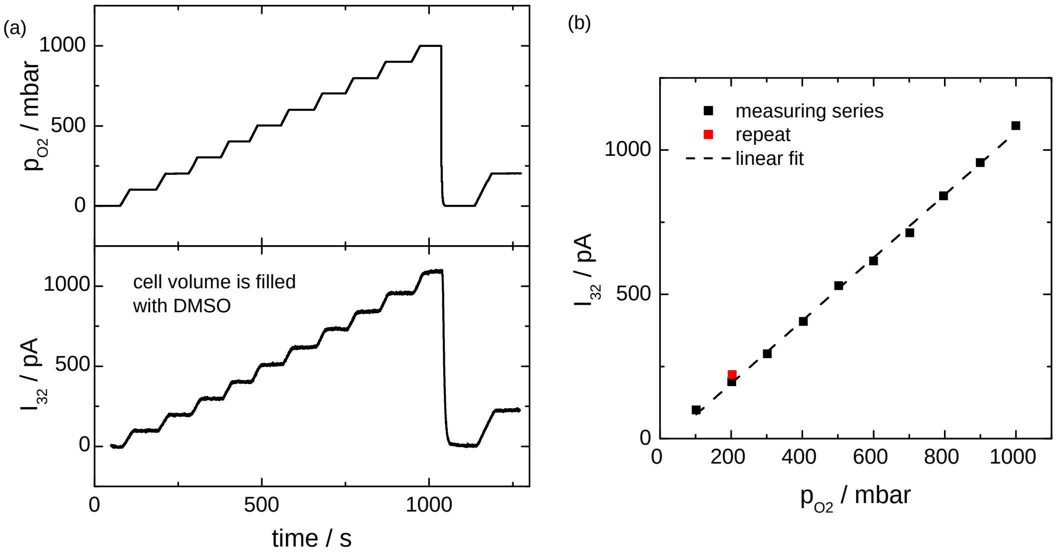

Figure 4.8: (a): Applied oxygen partial pressure to saturate DMSO within the thin layer cell with oxygen (upper figure). Simultaneously recorded ionic current of mass 32 (lower figure). This figure shows the time development of both measurements. (b) Plot of the ionic current as function of the partial pressure. The ploted values were taken in the plateaus of Figure 4.8 (a). In this case the thickness of the working electrode compartment was 300 µm.

Stability of TTF in deoxygenated solution

The measurement shown in Figure 4.9 shows that there is no effect on the cyclic voltammetry response of TTF in a deoxygenated solution to an oxygenated solution. In the measurement in the deoxygenated solution, the potential window was also opened to -1.6 V vs Ag | Ag$^+$. Even at lower electrode potentials, TTF is not undergoing any redox processes. In addition, the absence of a CO_2 flux indicates that TTF is not undergoing a decomposition reaction, which is releasing CO_2.

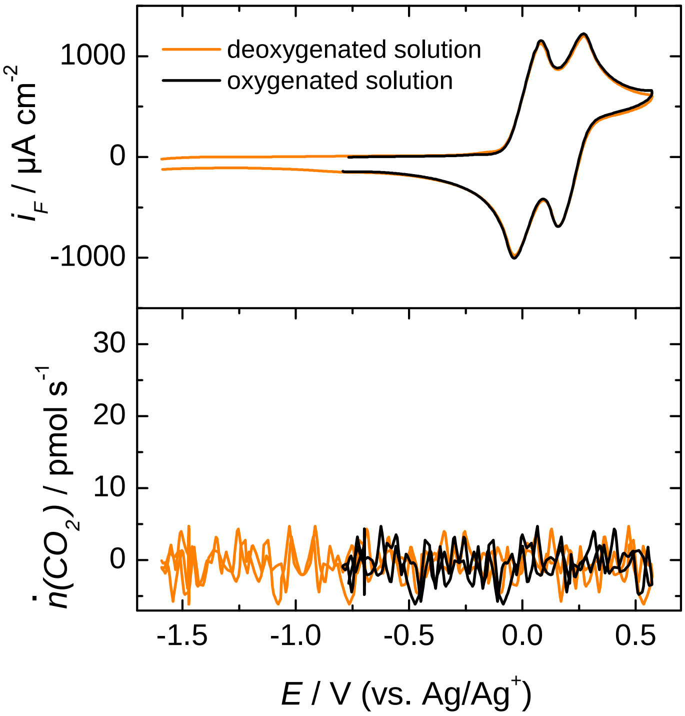

Figure 4.9: CV of 10 mM TTF in a 0.5 M $LiClO_4$ in DMSO in a deoxygenated solution (orange traced) and an oxygenated solution (black traced). The lower graph shows the simultaneously recorded CO_2 flux. The measurements were performed with a sweep rate of 50 mV s^{-1}.

Determination of the number of electrons during the OER for RM containing electrolytes

During the OER, the measured faradaic current consists of three different processes:

1) Direct oxidation of Li_2O_2 on the electrocatalyst surface.

2) Oxidation of Li_2O_2 through RM$^+$ followed by an oxidation of RM to RM$^+$ on the electrocatalyst surface.

3) Oxidation of RM to RM$^+$ on the electrocatalyst surface, followed by a diffusion process of RM$^+$ into the electrolyte without oxidizing any Li_2O_2.

To determine the numbers of transferred electrons per oxygen molecule for the OER processes (first and second process), the overall faradaic current has to be corrected for the contribution of the third process. Here we will briefly describe the correction procedure choosing the TTF containing experiments shown in Figure 4.3 (a) of our publication as an example. First of all, a part of the anodic sweep in the TTF containing supporting electrolytes is taken for the analysis. The measurements shown in Figure 4.10 (a) differ in their lower potential limit, which was chosen in the experiment. In the black traced measurement, the lower limit was set at -0.5 V. Therefore, no ORR takes place. In the red traced measurement, the lower limit was -1.6 V. Since in the red traced measurement the potential was low enough to perform the ORR, one is able to observe all three processes, which were mentioned above, during the anodic sweep. On the other hand, the black traced measurement only contains the third process, as mentioned above. To isolate the OER processes, one can subtract the black traced measurement from the red traced measurement. The resulting current ΔI_F is shown in Figure 4.10 (b). ΔI_F is further correlated with the ionic current of mass 32 to get the number of transferred electrons per oxygen molecule.

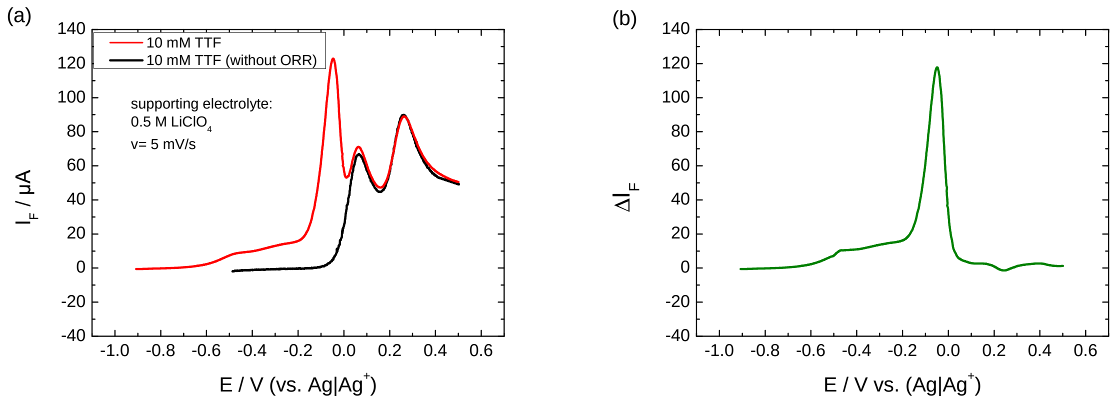

Figure 4.10: (a): Extract of the anodic sweep for the TTF containing 0.5 M $LiClO_4$ in DMSO. For the red curve the potential was previously cycled into the ORR-region. In the black traced measurement the ORR potential region was avoided. (b): Current profile obtained out of the difference of the currents shown in (a).

Using TEMPO as redox mediator

2,2,6,6-Tetramethylpiperidinyloxyl (TEMPO) was used as a redox mediator. The cyclic voltammetry and the MSCVs of mass 32 and 44 are shown in Figure 4.11. It is remarkable that for the DMSO based electrolyte, we observe an irreversible TEMPO-redox system. The previous article including TEMPO as redox mediator in Li-O_2 cells were performed in Tetraglyme based electrolytes [52, 189]. Nevertheless, this experiment was used to determine the potential at which the activity of the redox mediator starts as well as the half wave potential of the TEMPO oxidation peak.

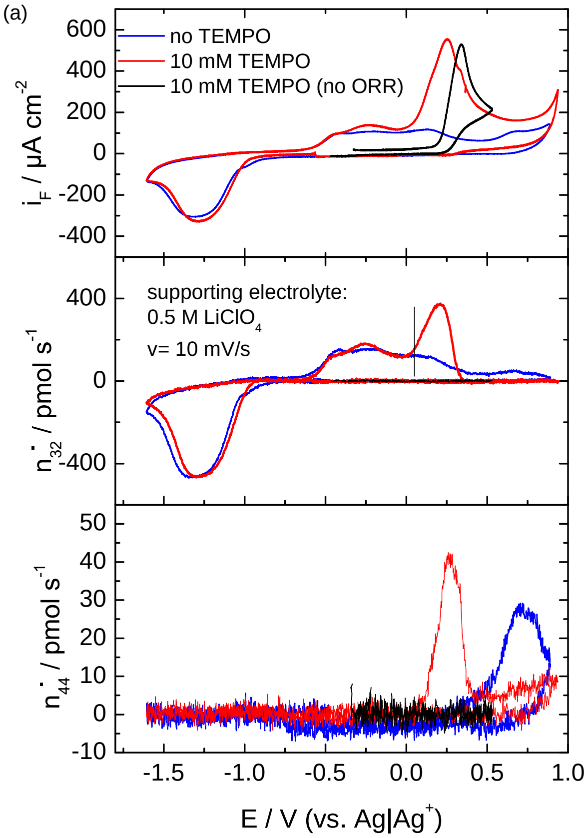

Figure 4.11: CVs and MSCVs on mass 32 and 44 with a sweep rate of 5 mV/s in 0.5 M $LiClO_4$ solution in DMSO with 10 mM TEMPO (black and red trace) and without TEMPO (blue trace).

Using ferrocene as redox mediator

Ferrocenium (Fc) was also used as a redox mediator. The cyclic voltammetry and the MSCVs of mass 32 and 44 are shown in Figure 4.12 (a). It is well known, that the Fc$^+$ is very sensitive to small amounts of oxygen [205]. Therefore, the black traced measurement was performed without oxygen (system to saturate the electrolyte with gas was evacuated). For the red traced measurement, the ORR was performed under an oxygen partial pressure of 900 mbar. During the anodic sweep, at a potential of -0.5 V, the potential was kept. The tubes with the oxygen atmosphere were evacuated under potential control. Afterwards, the anodic sweep was continued. The calculated number of transferred electrons per oxygen molecule are shown in Figure 4.12 (b).

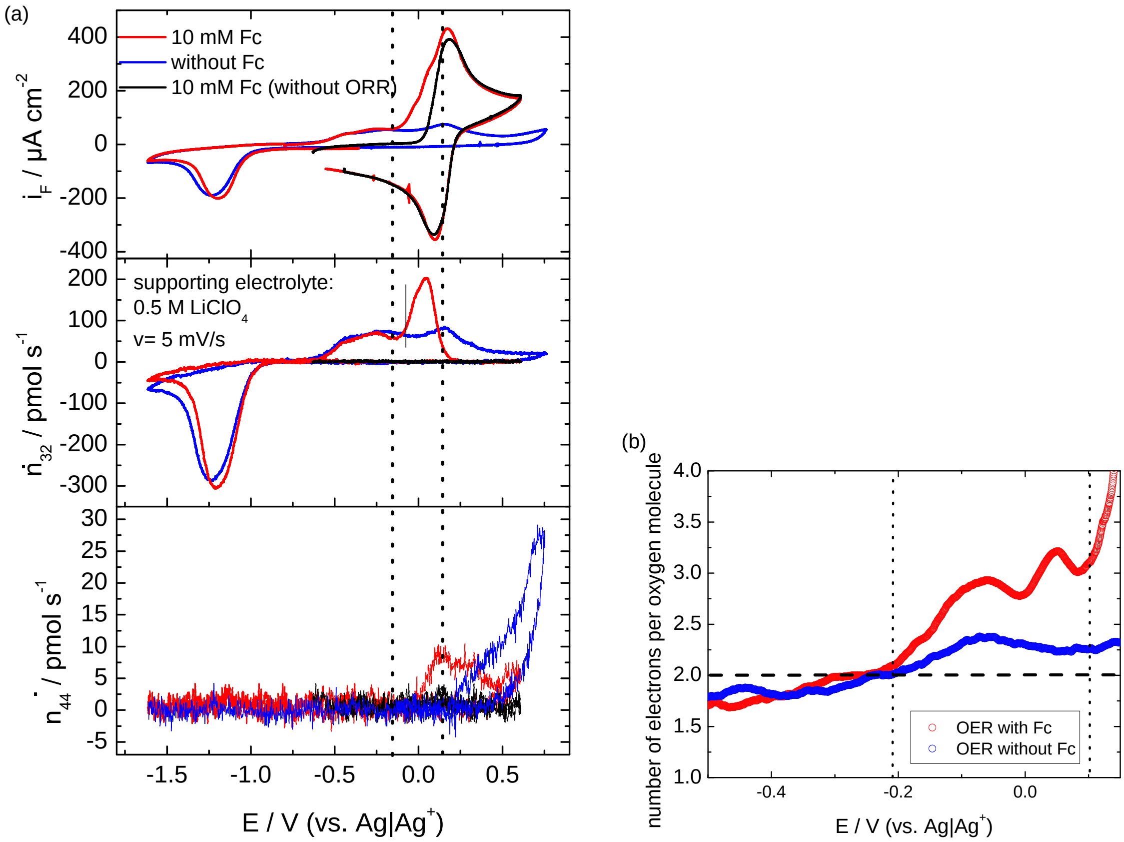

Figure 4.12: CVs and MSCVs on mass 32 and 44 with a sweep rate of 5 mV s^{-1} in 0.5 M LiClO$_4$ solution in DMSO with 10 mM Fc (black and red trace) and without Fc (blue trace). (b) Calculated number of transferred electrons per oxygen molecule *z*.

Number of transferred electrons during the ORR

The typical number of electrons, which we observe during the ORR in DMSO based electrolytes is shown in Figure 4.13. Our work group previously reported about this observation [90].

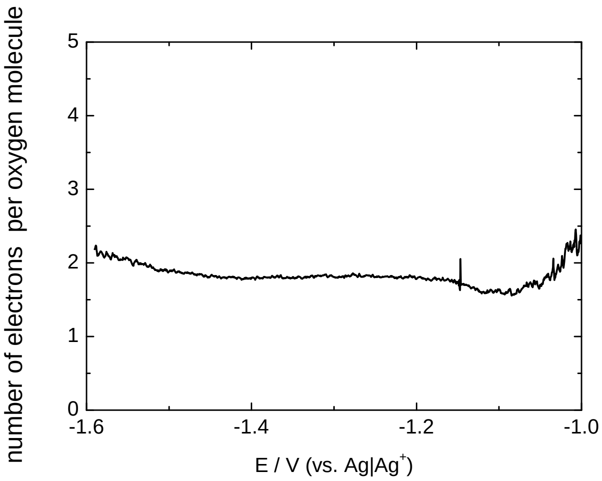

Figure 4.13: Number of electrons transferred per oxygen molecule during the ORR for a 0.5 M $LiClO_4$ in DMSO.

A thermodynamic and kinetic analysis of the Li_2O_2 oxidation through a redox mediator

In our analysis, the following chemical and electrochemical reactions were considered:

$$\mathrm{RM} \underset{k_{-1}}{\overset{k_1}{\rightleftharpoons}} \mathrm{RM}^+ + \mathrm{e}^- \tag{4.9}$$

$$\mathrm{RM}^+ + \mathrm{Li_2O_2} \xrightarrow{k_2} \mathrm{RM}^+ + \mathrm{O_2}^{\cdot -} + 2\,\mathrm{Li}^+ \tag{4.10}$$

$$\mathrm{O_2}^{\cdot -} \underset{k_{-3}}{\overset{k_3}{\rightleftharpoons}} \mathrm{O_2} + \mathrm{e}^- \tag{4.11}$$

$$\mathrm{RM}^+ + \mathrm{O_2}^{\cdot -} \xrightarrow{k_4} \mathrm{RM} + \mathrm{O_2} \tag{4.12}$$

In this reaction scheme it is reasonable to assume that the reaction 4.10 is the rate determining step. According to reaction 4.10, the $O_2^{\cdot -}$ production rate can be formulated as followed:

$$\frac{d[\mathrm{O_2^{\cdot -}}]}{dt} = k_2[\mathrm{Li_2O_2}][\mathrm{RM}^+] \tag{4.13}$$

Expressing the concentration of RM^+ through *Nernst law* leads to:

$$\frac{d[O_2^{\cdot-}]}{dt} = k_2[Li_2O_2][RM] \cdot e^{-\left(E-E^0_{RM/RM^+}\right)F/RT} \tag{4.14}$$

In equation 4.14 stands for the electrode potential and E^0_{RM/RM^+} for the standard potential of RM. Including the initial concentration of RM, $[RM_0]$:

$$[RM_0] = [RM] + [RM^+] \tag{4.15}$$

This leads to the following expression:

$$\frac{d[O_2^{\cdot-}]}{dt} = k_2[Li_2O_2][RM_0] \cdot \left(1 + e^{-\left(E-E^0_{RM/RM^+}\right)F/RT}\right)^{-1} \tag{4.16}$$

In the next step we assumed that the rate constant k_2 is given by *Marcus'* expression:

$$k_2 = k_{2,0} \cdot e^{-\frac{(\lambda+\Delta G_0)^2}{4\lambda RT}} \tag{4.17}$$

Where λ is the reorganization energy and ΔG_0 the free enthalpy of the electron transfer. With the help of reaction 4.10 ΔG_0 can be expressed as follows:

$$\Delta G_0 = -F\left(E^0_{RM^+/RM} - E^0_{Li_2O_2/O_2^{\cdot-}}\right) = -FE_R \tag{4.18}$$

Combing equation 4.17 and 4.18 results in:

$$k_2 = k_{2,0} \cdot e^{-\frac{\lambda}{4RT} + FE_R\left(\frac{1}{2RT} - \frac{FE_R}{4\lambda RT}\right)} \tag{4.19}$$

For DMSO one can assume a reorganisation energy of 80 kcal/mol [209]. E_R is for the investigated redox mediators between 0.7 V and 1.1 V. Taking these numbers into account, one can neglect $\frac{FE_R}{4\lambda RT}$ over $\frac{1}{2RT}$. Overall expression 4.19 simplifies to the following expression:

$$k_2 \approx k_{2,0} \cdot e^{-\frac{\lambda}{4RT} + \frac{FE_R}{2RT}} \tag{4.20}$$

If the reaction should be an inner sphere reaction, the factor in the second term of the exponent would have to be replaced by a factor α similar to that in the *Butler-Volmer* equation.
Combing equation 4.16 and 4.20 leads to:

$$\frac{d[O_2^{\cdot-}]}{dt} = k_{2,0} \cdot e^{-\frac{\lambda}{4RT} + \frac{FE_R}{2RT}}[Li_2O_2][RM_0] \cdot \left(1 + e^{-\left(E-E^0_{RM/RM^+}\right)F/RT}\right)^{-1} \tag{4.21}$$

Taking the logarithm and summing up all constant values as *const* gives the following expression:

$$\ln\left(\frac{d[O_2^{\cdot-}]}{dt}\right) = const + \frac{FE_R}{2RT} - \frac{-\left(E - E^0_{RM/RM^+}\right)F}{RT} \tag{4.22}$$

Our experiments showed, that the difference $E - E_0$ is in the range between 60 mV and 200 mV. Therefore, the 1 in the right hand side logarithm term of equation 4.22 can be excluded giving the following equation:

$$\ln\left(\frac{d[\mathrm{O}_2^{\cdot-}]}{dt}\right) = const + \frac{FE_R}{2RT} - \frac{-\left(E - E^0_{\mathrm{RM/RM^+}}\right)F}{RT} \tag{4.23}$$

$$\frac{RT}{F}\ln\left(\frac{d[\mathrm{O}_2^{\cdot-}]}{dt}\right) = const2 + \frac{1}{2}E^0_{\mathrm{RM/RM^+}} + E - E^0_{\mathrm{RM/RM^+}} \tag{4.24}$$

In equation 4.24 the expression for E_R , defined in equations 4.18 and 4.19, was used. The resulting term $-\frac{E^0_{\mathrm{Li_2O_2/O_2^{\cdot-}}}}{2}$ was included into *const* giving *const*2 .

To explain the trend shown in Figure 4.6, equation 4.24 was rearranged as followed:

$$E = \frac{1}{2}E^0_{\mathrm{RM/RM^+}} + const2 + \ln\left(\frac{d[\mathrm{O}_2^{\cdot-}]}{dt}\right)_E + \frac{RT}{F} \tag{4.25}$$

The term $\ln\left(\frac{d[\mathrm{O}_2^{\cdot-}]}{dt}\right)_E$ is constant, due to our determination of E: E is the potential at which the oxygen flux into the mass spectrometer in the RM-containing experiment is increased over $5\,\mathrm{pmol\,s^{-1}}$ above that observed in the measurement in the supporting electrolyte. If one assumes that the chemical side reactions of $\mathrm{O}_2^{\cdot-}$ are negligible, $\mathrm{O}_2^{\cdot-}$ will be oxidized by a following electrochemical reaction resulting into the oxygen flux into the mass spectrometer. Thus, E in formula 4.25 is the same as the used E_{onset} within the discussion of the underlying paper of this supporting information.

All in all, our combination of the Marcus' expression as well as a Nernstian behavior for the examined oxidation of the $\mathrm{Li_2O_2}$ by a redox mediator shows that one would expect in a plot of E_{onset} as a function of the redox potential of the redox mediator a slope of 0.5.

The effect of the surface roughness on the ORR at Au-electrodes

To examine the roughness effect of Au-surfaces on the ORR DEMS studies in a dual thin layer cell were performed (for details towards the experiment see [153]). A polycrystalline Au electrode with a roughness factor (RF) of 1 was used as a working electrode. After the measurements in a 0.5 M $\mathrm{LiClO_4}$ $\mathrm{O_2}$-saturated DMSO electrolyte the surface of the electrode was roughened to a RF of 3 and the measurement in a 0.5 M $\mathrm{LiClO_4}$ $\mathrm{O_2}$-saturated DMSO electrolyte was repeated. The RF values were determined by a method described by Trasatti and Petrii [210]. The experimental data is shown in Figure 4.14.

The experimental data shows, that the shape of the ORR is influenced by the different roughness factors. The transferred charge in the ORR is higher for the rougher surface. This is

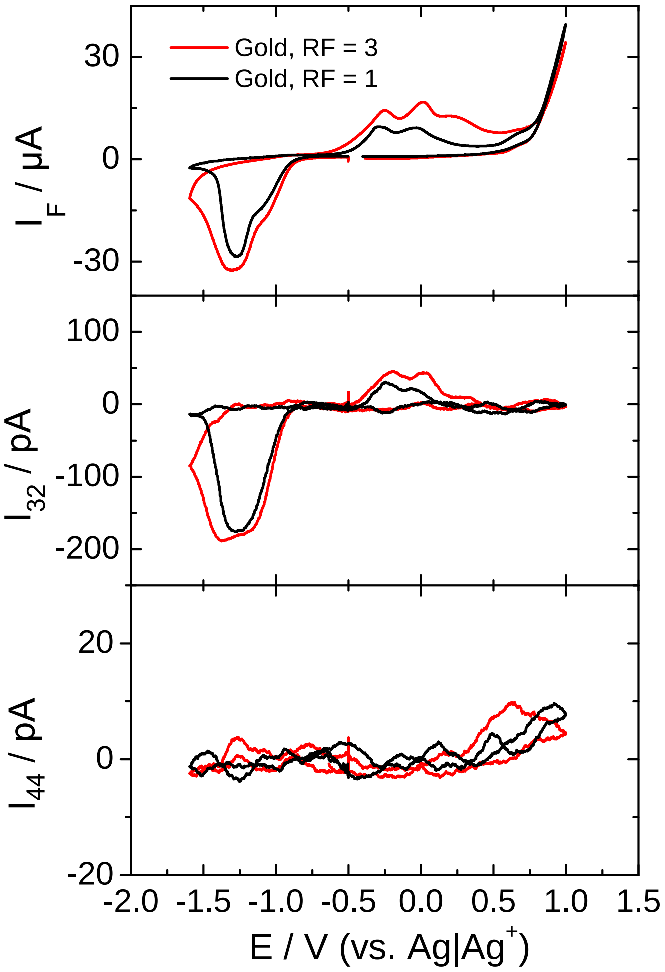

Figure 4.14: DEMS study of Au-electrodes with two different roughness factors (RF). In red: RF= 3 and in blue RF=1. The figure shows the cyclic voltammetry data (top), the ionic current of mass 32 (middle) and the ionic current of mass 44 (bottom).

because the rougher surface is able to uptake more Li_2O_2 before the poisoning of the electrode starts, because of its higher surface area. This result show that the slightly different shapes of the ORR region within the underlying main manuscript could be explained through different roughness factors of the sputtered Au-electrodes.

5

Fast and Simultaneous Determination of Gas Diffusivities and Solubilities in Liquids Employing a Thin-Layer Cell Coupled to a Mass Spectrometer, Part I: Setup and Methodology

Pawel Peter Bawol[*], Philip Heinrich Reinsberg[*] and Helmut Baltruschat[*]

[*] Institut für Physikalische und Theoretische Chemie, Universität Bonn, Römerstraße 164, D-53117 Bonn, Germany

Reprinted (adapted) with permission from
P. P. Bawol, P. H. Reinsberg and H. Baltruschat, *Anal. Chem.* **2018**, 90, 14145-14149,
DOI: 10.1021/acs.analchem.8b04319 ©2018 American Chemical Society

The presented paper has a second part in which a number of electrolytes were investigated for their diffusion and solubility properties of oxygen (DOI: 10.1021/acs.analchem.8b04320).

The whole project was carried out in close cooperation with Dr. Philip Heinrich Reinsberg. Furthermore a a German patent application has been filed (DE 10 2017 128 269.6).

Own manuscript contributions:

- design of the experiment
- development of computer programs for the data evaluation
- data evaluation
- support P. H. Reinsberg in writing the manuscript

5.1 | Abstract

Transport properties and solubilities of volatile species in liquid solutions are of high interest in different chemical, biological, and physical systems. In this work, a new approach for determining the diffusivity and solubility of gases in liquids simultaneously is presented. The method presented relies on the diffusion of a volatile species through a thin, liquid layer and the subsequent detection of the species using a mass spectrometer. Evaluation of the time development of the resulting transient yields the diffusion coefficient, while the concentration of the species in the liquid layer can be calculated from the steady-state value of the flux into the mass spectrometer. Apart from the geometry of the thin-layer and the calibration constant of the mass spectrometer no additional or external data are required. Experimental results of the temperature-dependent solubility and diffusivity of oxygen in dimethyl sulfoxide are presented in our companion paper Part II and serve as a proof of concept.

5.2 | Introduction

Proper knowledge of the solubility and diffusion coefficients of volatile species in liquids was rarely as important as it is today with the growing interest in nonaqueous metal-air batteries [97, 100, 123, 211, 212]. Because of the variety of electrolytes employed for research and also because of rapid developments related to the electrolyte's composition, as exemplarily illustrated by different articles regarding Li-air batteries [36, 46, 67, 82, 89, 213–215], there is a need for a method to determine the relevant parameters sufficiently accurate, fast, and ideally with small amounts of electrolyte. The latter might be of interest if the electrolyte itself is very expensive, which is the case for most of the ionic liquids used in metal-air research [216–218].

Methods currently used for the determination of the oxygen solubility in the context of metal-air batteries usually rely on a combination of volumetric and gravimetric measurements[219–221], spectroscopic techniques, either directly detecting oxygen [222] or detecting probes for oxygen [223], mass spectrometric methods [222, 224, 225] pressure measurements [226–228], and electrochemical techniques, which allow for the simultaneous determination of the solubility and diffusion coefficient [91, 229–231]. It is noteworthy that the mass spectrometric determination of the oxygen solubility by Khodayari *et al.* also allows for the determination of the diffusivity, which is achieved by changing the electrolyte flow rate [224]. Most of these methods need a rather large electrolyte volume owing to the limited sensitivity of the measurement devices or the conditions under which the solubility can be determined (e.g., flow-through cells). Regarding simultaneous determination of the Henry constant K_H and the diffusion coefficient D, electrochemical techniques, such as chronoamperometry [230, 231], are promising. Nevertheless, electrochemical techniques can only be applied if there is a reaction, which can be electrochemically followed within the potential window of the solvent, and some basic knowledge of the reaction mechanism is available (i.e., the number of electrons transferred per molecule). The latter often is not guaranteed in organic electrolytes due to the usual complex reaction mechanisms and unwanted side reactions. Although determination of D in experiments under well-defined convective conditions does not explicitly rely on knowledge of a reaction mechanism, the precision of these experiments is usually unsatisfactory [95, 138].

In this article we present a new method for simultaneously determining gas solubilities and diffusion coefficients using a thin-layer cell with a low electrolyte volume (down to 20 µL) coupled to a differentially pumped mass spectrometer (MS). The diffusion coefficient can be determined by fitting a signal, which is simulated according to Fick's laws, to the timeresolved MS signal observed after a sudden change in gas pressure, while the absolute concentration of volatile species in the electrolyte can be obtained from the steady-state value of the MS signal applying Fick's first law of diffusion.

5.3 | Experimental

Thin-Layer Cell

A sketch of the cross-section of the thin-layer cell used for determination of the solubility and diffusivity data is shown in Figure 5.1.

Thin-layer cells in combination with DEMS have been previously used in electrochemical applications [58, 200, 232]. The upper cell holder, which is connected to an oxygen-containing chamber, and the lower cell holder, which is connected to the vacuum chamber of a mass spectrometer, are made of stainless steel, while the cell body itself is made from brass. Each cell holder contains a porous steel frit, which mechanically stabilizes the porous poly-(tetrafluoroethylene) (PTFE) membranes M1 and M2 and allows the gas transport from the gas reservoir into the liquid layer and from the liquid layer into the vacuum of the mass spectrometer. The porous PTFE membranes (Goretex, porosity of 50%, pore diameter 20 nm) separate the liquid phase in the cell body from the vacuum below and the gas phase above the solution. Water-perfused tubes made from copper are attached to the holders to enable temperature control of the whole measurement setup via a thermostat, with the temperature directly measured in a cavity within the cell body using a previously calibrated type K thermocouple. The cell body itself is constructed in a way that there is a small cavity of known height h (h = 700 µm) and radius r (r= 3 mm) between the upper membrane M1 and the lower membrane M2. The height of this cavity defines the thickness of the thin-layer. The two small capillaries (diameter 1 mm) are used as in- and outlet for the electrolyte.

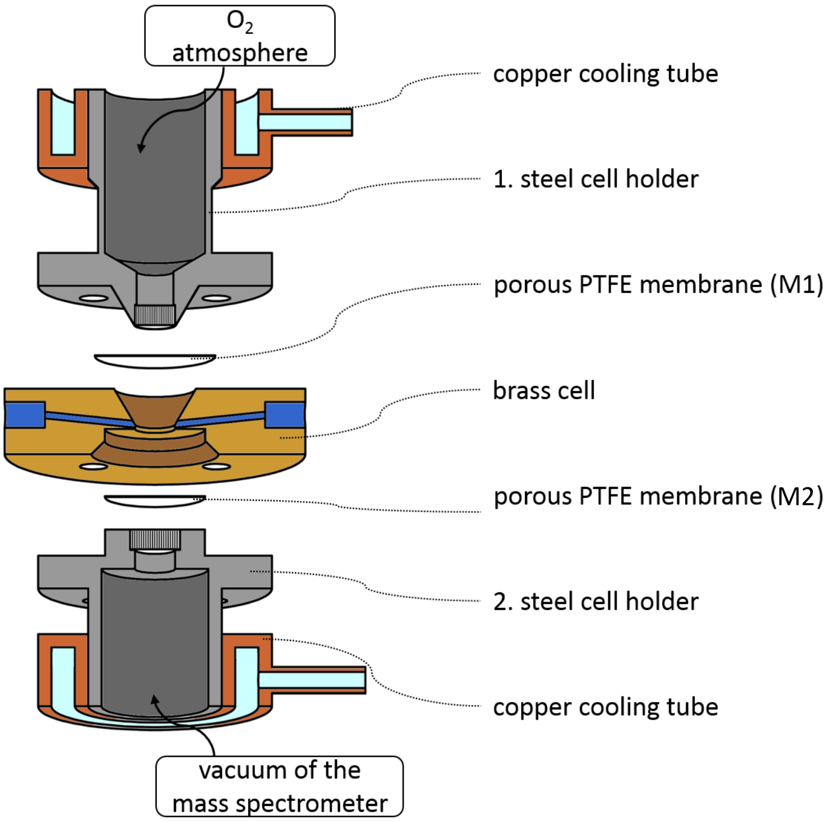

Figure 5.1: Cross-section of the measurement cell. The upper cell holder is connected to an oxygen reservoir, while the lower cell holder connects the cell body to the vacuum of a mass spectrometer. Two porous PTFE membranes separate the liquid from the vacuum and the gas phase. Both membranes are mechanically stabilized by porous steel frits flush-mounted into the cell holders. Copper tubes attached to the steel holders ensure proper temperature control of the whole setup.

Setup and Experimental Procedure

The complete setup consisting of the thin-layer cell, a differentially pumped mass spectrometer (see MS in Figure 5.2, QMA 430, Pfeiffer Vacuum), and the gas cylinder including the connecting valves as well as the pressure sensor (see P in Figure 5.2, TPG 202, Pfeiffer Vacuum) is shown in Figure 5.2.

The experiment proceeds as follows: First, the solution is introduced into the cell via the capillaries. Immediately after that, the volume below and above the cell is evacuated by opening V_2 as well as V_5 and V_3. By this approach, the thin-layer of solution can be degassed (usually for 5 min), and additional contaminations from the ambient air are avoided. After that V_2 is closed and V_1 is opened to establish a connection between the high vacuum of the mass spectrometer and the cell.

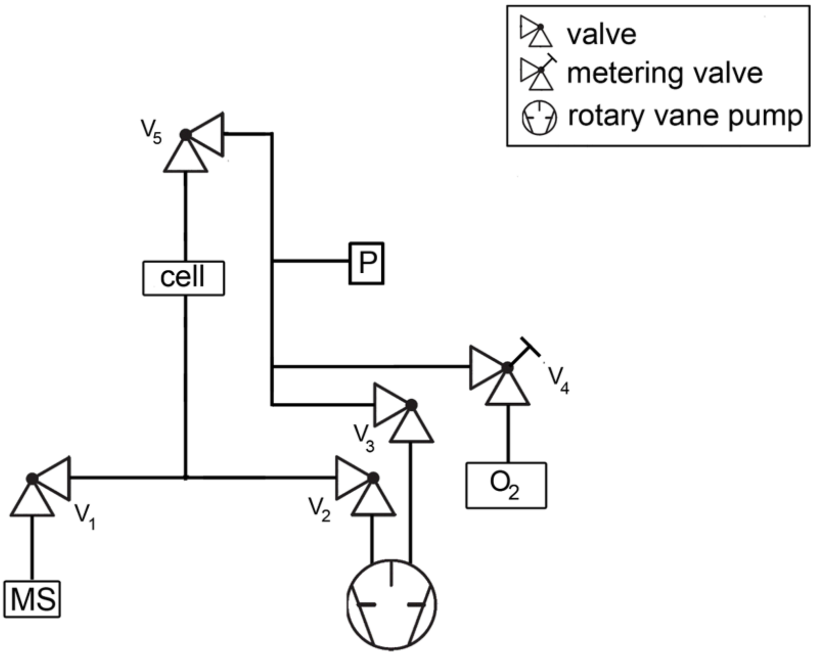

Figure 5.2: Measurement setup. After the solution is introduced to the measurement cell, it can be evacuated from below via valve V_2 and from above via V_5 and V_3. The connection to the mass spectrometer (MS) is established via V_1, while V_4 and V_5 connect the cell to a gas cylinder. With V_4 open and with V_3 and V_5 closed, the vacuum tubes are filled with gas. After V_4 is closed, the abrupt opening of V_5 leads to a slight decrease in pressure (as monitored by the pressure sensor P), and the gas can saturate the solution in the cell. The time-resolved detection of gaseous species in the MS is directly proportional to flow of gaseous species through the solution.

In the next step valves V_5 and V_3 are closed, and the throttle valve V_4 is opened, flushing the evacuated tubes between V_4 and V_5 with oxygen from the gas cylinder. After valve V_4 is closed, oxygen is then removed again via V_3, and the procedure is repeated at least three times to reduce possible contaminations arising from residual amounts of gas in the tube. After that, a certain oxygen pressure (usually 900 mbar) is adjusted via the help of pressure sensor P while V_5 is closed. To start the measurement, V_5 is abruptly opened, and the flux of volatile species through the liquid layer into the mass spectrometer is measured with a time resolution of 20 ms. Because of the volume of the stainless steel holder connecting the cell and the valve V_5, an almost instantaneous drop in pressure can be observed when V_5 is opened, which gives us the starting point (t_0) of the measurement.After $\sim$150 s the steady-state value of the ionic current is achieved, indicating the end of the measurement. As a first proof of concept, a transient of the oxygen signal in pure water is shown in Figure 5.3.

With a theoretical thickness of 700 µm and the calibration constant of the mass spectrometer as determined via the electrochemical oxygen reduction reaction in a 0.5 M tetrabutylammo-

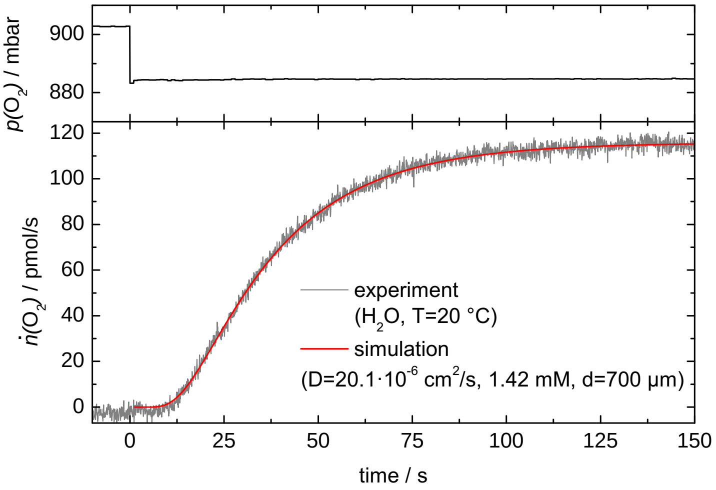

Figure 5.3: A typical example of a measurement obtained in ultrapure water (18.2 MΩ cm) at 20 °C. Top figure: The oxygen pressure within the tubes over membrane M1. The starting point of the measurement can be set through the sudden oxygen pressure drop. Bottom figure: The measured flux transient of mass 32 together with a simulated transient.

nium perchlorate (TBAClO$_4$) containing dimethyl sulfoxide (DMSO) [90] ($K^* = 25 \cdot 10^{-6}$), the diffusivity and solubility can be evaluated. The electrochemical cell we are using for the determination of K^* is described in ref [58]. For a more detailed description of the calibration procedure, see chapter 5.4.3 in the Methods Section.
The resulting diffusivity of $20.1 \cdot 10^{-6}\,\mathrm{cm^2\,s^{-1}}$ and solubility of oxygen 1.42 mM at a temperature of 20 °C are in close agreement with values reported in the literature (c = 1.39 mM [233, 234], $D(O_2) = 19.6 \cdot 10^{-6}\ \mathrm{cm^2\,s^{-1}}$ [235], $D(O_2) = 20.1 \cdot 10^{-6}\,\mathrm{cm^2\,s^{-1}}$ [236]).

5.4 | Results and discussion

5.4.1 | Evaluation of the Solubility and Diffusivity

For determination of the diffusivity of the gaseous species, analysis of the time-dependent development of the concentration gradients (Figure 5.4 (a)) or the transients of the ionic currents (Figure 5.4 (b)) is necessary.

Mathematical treatment of this planar diffusion problem was performed by Aiba based on the work of Carslaw and Jaeger [237, 238]. The most important boundary conditions are as follows: The concentration at the boundary between gas and liquid ($x = 0$, Figure 5.4 (a)) equals the equilibrium or saturation concentration; the concentration at the boundary between liquid and vacuum ($x = h$, Figure 5.4 (a)) is 0 (and thus, the partial pressure of the gas in the vacuum

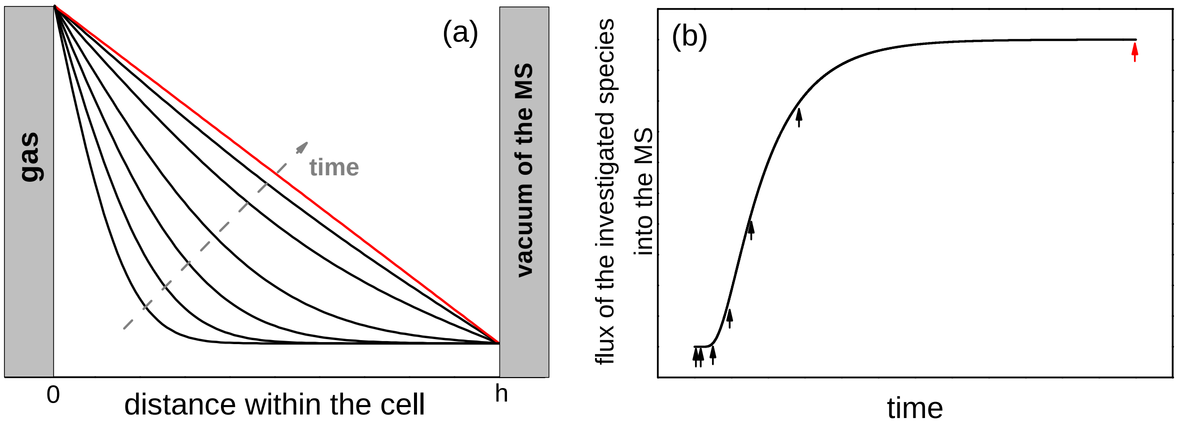

Figure 5.4: Concentration gradients within the thin-layer and the resulting current transient. (a) Concentration gradients for different times t. The concentration at $x = 0$ always equals the equilibrium concentration c_0, while the one at $x = h$ remains 0. The concentration profiles have been derived via finite difference simulation. (b) Resulting current transient of the flux of the investigated species into the vacuum of the MS. The arrows indicate the points in the transients resulting out of the concentration profiles in (a).

is sufficiently close to 0 on a linear scale, even though the exact partial pressure of the gas must be nonzero to be able to measure a signal in the MS). This implies that both absorption and desorption are arbitrarily fast compared to diffusion of the gas in the liquid and that the partial pressure of the gas at the vacuum side is close to zero. Furthermore, the pressure at $x = 0$ is assumed to be constant, which is true due to the large amount of gas contained in the tubing ($\sim 5 \cdot 10^{-2}$ mol) as compared to the low flow rates (in the range of $1 \cdot 10{-}10$ mol/s). It is noteworthy that the diffusion problem differs significantly from the semi-infinite diffusion problem invoked in the derivation of the well-known *Cottrell* equation, where the initial concentration at the electrode's surface equals the bulk concentration, and thus, a current signal is observed immediately after a change in potential (which is the analogy to the change in pressure).

Applying the different boundary conditions and treating the problem in terms of a one-dimensional (1D) planar diffusion problem a series expansion is obtained describing the transient of the flux (equation 5.1) [239]:

$$\eta(t) = 1 + 2\sum_{n=1}^{\infty}(-1)^n \exp\left(-(\pi n)^2 \frac{t}{6t_c}\right) \tag{5.1}$$

with $\eta(t)$ as the normalized flux, n as a natural number, t as time measured in the experiment, and t_c is defined as

$$6t_c = \frac{h^2}{D} \tag{5.2}$$

In equation 5.2, h is the thickness of the layer, and D represents the diffusion coefficient. To

obtain the diffusion coefficient D, current transients with different values for D were simulated ($n = 25$) and fitted to the experimental current transients via the least-square method.
The thus calculated diffusion coefficient can be used to evaluate the solubility or rather *Henry's* constant by applying *Fick's* first law of diffusion (see equation 5.3), which correlates the flux of volatile species (J) to the diffusion coefficient D, the opening for the gas at the site of the MS with a cross section area of A and the concentration gradient at $x = h$:

$$J = -D \cdot A \left(\frac{\partial c}{\partial x} \right)_{x=h} \tag{5.3}$$

Although the theoretical steady-state maximum of the flux is never achieved, the current after 110 s equals already 99% of the maximum flux and can be interpreted as a steady-state value, for which the concentration gradient is approximately linear between $x = 0$ and $x = h$ (see red pictured gradient in Figure 5.4 (a)). Therefore, equation 5.3 can be simplified, directly yielding a relation between gas solubility c and the steady-state ionic current (I_{max}):

$$c = \frac{h \cdot I_{max}}{D \cdot A \cdot K^0} \tag{5.4}$$

The constant K^0 is a calibration constant of the mass spectrometer containing the ionization probability of the investigated species and can be determined in different ways.
From the concentration c and the partial pressure p the *Henry* constant K_H can be calculated according to

$$K_H = \frac{c}{p} \tag{5.5}$$

5.4.2 | Calibration of the System for Determination of the Diffusivity

Although it is not required theoretically, for practical purposes proper determination of the thickness of the layer h is useful to increase accuracy of the diffusion coefficients. Therefore, the following procedure was used for calibration: Ultrapure water (18.2 MΩ cm) was introduced in the cell, and a pressure step experiment as described above was performed. From the time-dependent current transients and the diffusion coefficient of oxygen in water at 20 °C ($D = 20.1 \cdot 10^{-6}\,\mathrm{cm^2\,s^{-1}}$) [236] the thickness of the cell can be evaluated. The thus-obtained thickness h equals $h = 693 \pm 13$ µm, where the uncertainty reflects the t-distributed standard error of mean of a series of seven independent experiments. This value is in excellent agreement with the ∼700 µm thickness obtained by a simple length measurement.

5.4.3 | Calibration of the System for Determination of the Solubility

According to equation 5.4 for the determination of the solubility c the knowledge of the calibration constant of the mass spectrometry system K^0 as well as the cross-sectional area A is needed. While A and h can be manufactured with relatively high precision, K^0 has to be determined in an external experiment. The calibration constant K^0 can either be evaluated from the correlation of the ionic current and the known flux of the specific gas under investigation through a throttle valve in terms of a calibration leak experiment [153], by using a solvent in which the equilibrium concentration as well as diffusivity of the gas is known or by performing an electrochemical reaction of known stoichiometry [26]. The latter approach only yields the calibration constant K^*, which, due to the high transfer efficiency of nearly 100% between cell and vacuum, only has to be multiplied with Faraday's constant to yield K^0 [153]. On the contrary, the calibration leak experiment directly gives K^0, but it does not yield information about A and h. In this study, K^0 has initially been determined by using the electrochemical oxygen reduction in 0.5 M $TBAClO_4$ in DMSO with an experimental setup described in reference [58]. It is known that, in this electrolyte system, the electrochemical reduction of oxygen quantitatively yields superoxide [90]:

$$O_2 + e^- \longrightarrow O_2^{\cdot -} \tag{5.6}$$

Correlating the faradaic current for reaction 5.6 to the ionic current measured by the mass spectrometer, a value of $2.38\,\mathrm{C\,mol^{-1}}$ for K^0 was obtained.

To account for changes in the calibration constant due to aging of the filament, the oxygen solubility in pure DMSO at 19 °C was determined before every measurement and was used as an internal reference. This allowed us to recognize changes in K^0 and correct our determination of the solubilities. Furthermore, these measurements in pure DMSO showed that the shape of the transients did not change even after 130 days (see Figure 5.5). This is an indication of the reproducibility and the quality of the performed experiments.

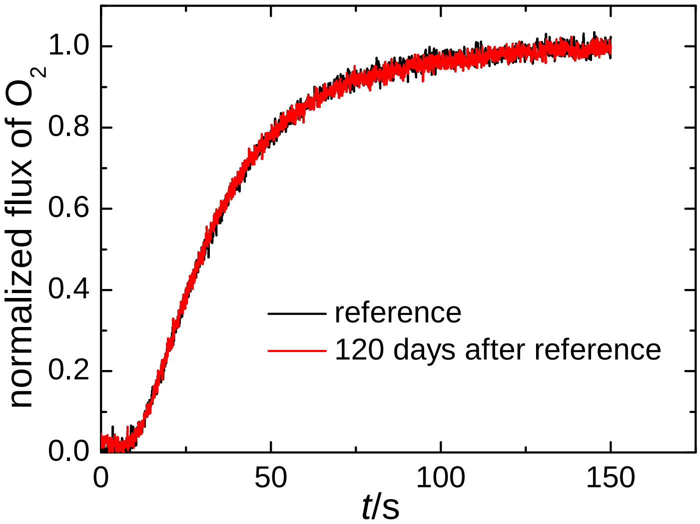

Figure 5.5: Typical transients obtained in pure DMSO at 19 °C. The curve in red was obtained 130 d after the black curve. Most of the experiments were performed within this time frame.

5.5 | Conclusion

A new thin-layer cell for determination of temperature-dependent diffusivities and solubilities of volatile species in liquid phase coupled to a mass spectrometer is presented. A major advantage of this cell as compared to, for example, electrochemical measurements is that the diffusivity and solubility can be measured simultaneously without any external knowledge, such as the stoichiometry of a reaction. Moreover, the duration of a single run is below 5 min enabling the cell for high throughputs. The measurement includes the following steps: Initially, the thin-layer is evacuated from both sides to remove any residual, volatile species. The diffusivity is subsequently determined by applying an abrupt change in the pressure of the (gaseous) analyte and evaluating the transient signal in the mass spectrometer. Finally, from the steady-state value of the transient and the calibration constant of the mass spectrometer the solubility can be calculated.

Acknowledgments

The authors gratefully acknowledge financial support by the German Federal Ministry of Education in the framework of the LiBaLu-project (Grant No. 03XP0029A), which is part of the "Vom Material zur Innovation" initiative. P.H.R. wishes to thank the National German Merit Foundation for a PhD scholarship.

6

Unraveling the mechanism of the solution mediated ORR in metal-O_2 batteries: The importance of ion association

Pawel Peter Bawol*, Jan Hendrik Thimm * and Helmut Baltruschat*

*Institut für Physikalische und Theoretische Chemie, Universität Bonn, Römerstraße 164, D-53117 Bonn, Germany

Reprinted (adapted) from
P. P. Bawol, J. H. Thimm and H. Baltruschat, *ChemElectroChem* **2019**, 6, 6038 – 6049,
DOI: 10.1002/celc.201901590 ©2019 The Authors. Published by Wiley-VCH Verlag

Own manuscript contributions:

- performing the experiments
- development of computer programs for the data evaluation
- data evaluation
- interpretation of the results
- writing the manuscript

6.1 | Abstract

One of the bottlenecks in Li-O_2 batteries is the film like growth of Li_2O_2 on the electrode surface during discharge leading to early cell death. To tackle this problem 2,5-Di-tert-1,4-benzoquinone (DBBQ) was introduced as a soluble redox mediator. This redox mediator is avoiding the Li_2O_2 layer-by-layer growth on the electrode surface and thus leading to higher discharge capacities of the Li-O_2 cell. In this study, we investigate the ion pairing between the cation of the conducting salt and the DBBQ monoanion and the resulting impact on the ORR activity of the DBBQ monoanion. We investigate TBA^+, K^+ and Li^+ as cations and TEGDME and DMSO as solvents. We found out that there is a direct correlation between the ORR activity of $DBBQ^-$ and the ion pairing of $DBBQ^-$ with the cation of the supporting electrolyte: Only if DBBQ is strongly associated with the cations of the electrolyte it will reduce oxygen in the electrolyte. Increasing the Li^+ concentration in the electrolyte shifts the ORR potential to more positive electrode potentials. In addition, we are describing a new experimental approach to investigate the kinetics of the homogeneous ORR via time resolved mass spectrometry. With this approach we found out, that the reaction $\mathrm{Li}\cdots\mathrm{DBBQ}_{(sol)} + \mathrm{O}_{2(sol)} \underset{k_{-1}}{\overset{k_1}{\rightleftharpoons}} \mathrm{Li}\cdots\mathrm{DBBQ}\cdots\mathrm{O}_{2(sol)}$ is 80 times faster in a TEGDME based electrolyte than in a DMSO based electrolyte. We determined k_1 with $5.1 \cdot 10^2\,\mathrm{s}^{-1}\,\mathrm{M}^{-1}$ and k_{-1} with $3.7 \cdot 10^2\,\mathrm{s}^{-1}\,\mathrm{M}^{-1}$ in TEGDME whereas the constants in DMSO are $k_1 = 4.5\,\mathrm{s}^{-1}\,\mathrm{M}^{-1}$ and $k_{-1} = 5.5\,\mathrm{s}^{-1}\,\mathrm{M}^{-1}$.

6.2 | Introduction

Metal-O_2 batteries are considered as a promising alternative to the Li-Ion technology due their high theoretical specific energy. Unfortunately, this technology is facing many challenges: During charge and discharge, reactive oxygen species like singlet oxygen and superoxide are formed, which are leading to side reactions with carbon electrodes and the electrolyte [95, 115, 117, 119, 240, 241]. Moreover, the main discharge products in Li-O_2, Na-O_2, K-O_2 and Mg-O_2 batteries are Li_2O_2, NaO_2, KO_2 and MgO_2, which are electronically insulating [58, 98, 111, 242–247]. For the electrochemical deposition of Li_2O_2, Bondue *et al.* performed studies on model electrodes and found out that if the thickness of the deposited Li_2O_2 layer is in the range of 2-3 monolayers the electrode is already passivated [26]. In batteries, this phenomenon is leading to a big discrepancy between the experimental and the theoretical capacity of the operating system. Therefore, a lot of publications in the metal-O_2 field are dealing with the research on improving the crystal growth of the insulating discharge products (toroidal growth of Li_2O_2)[34–36, 245]. One promising idea is the use of soluble redox mediators for the ORR. In the Li-O_2 field ethyl viologen [41, 42], phthalocyanine [43] and benzoquinones [45–47] were suggested. One of the benzoquinones, 2,5-Di-tert-1,4-benzoquinone (DBBQ) showed an increase of the discharge capacity in glyme electrolytes based Li-O_2 cells by a factor of 80-100 [46]. In 2016 by Gao *et al.* suggested a mechanism for the mediated ORR by the electrochemically formed DBBQ monoanion [46]:

$$\mathrm{DBBQ}_{(\mathrm{sol})} + \mathrm{e}^- \longrightarrow \mathrm{DBBQ}^-_{(\mathrm{sol})} \tag{6.1}$$

$$\mathrm{Li}_{(\mathrm{sol})}{}^+ + \mathrm{DBBQ}^-_{(\mathrm{sol})} \longrightarrow \mathrm{Li}\cdots\mathrm{DBBQ}_{(\mathrm{sol})} \tag{6.2}$$

$$\mathrm{Li}\cdots\mathrm{DBBQ}_{(\mathrm{sol})} + \mathrm{O}_{2(\mathrm{sol})} \underset{k_{-1}}{\overset{k_1}{\rightleftharpoons}} \mathrm{Li}\cdots\mathrm{DBBQ}\cdots\mathrm{O}_{2(\mathrm{sol})} \tag{6.3}$$

DBBQ is reduced at the electrode surface to the DBBQ monoanion (reaction 6.1). As benzoquinones anions are known to undergo ion-pairing [248–250], this reaction is also expected for DBBQ monoanion. Gao *et al.* gave thermodynamic evidences that the ORR mediated by DBBQ has to proceed via a $\mathrm{Li}\cdots\mathrm{DBBQ}\cdots\mathrm{O}_{2(\mathrm{sol})}$ complex as intermediate. Thus, the ORR mediated by DBBQ is not an outer sphere electron transfer. Two possible reaction pathways were formulated by Gao *et al.*, which lead to Li_2O_2 as the ORR product:

$$2\mathrm{Li}\cdots\mathrm{DBBQ}\cdots\mathrm{O}_{2(\mathrm{sol})} \xrightarrow{k_2} \mathrm{Li}_2\mathrm{O}_{2\,(\mathrm{s})} + \mathrm{O}_{2(\mathrm{sol})} + 2\mathrm{DBBQ}_{(\mathrm{sol})} \tag{6.4}$$

$$\mathrm{Li}\cdots\mathrm{DBBQ}\cdots\mathrm{O}_{2(\mathrm{sol})} + \mathrm{Li}\cdots\mathrm{DBBQ}_{(\mathrm{sol})} \xrightarrow{k_3} \mathrm{Li}_2\mathrm{O}_{2\,(\mathrm{s})} + 2\,\mathrm{DBBQ}_{(\mathrm{sol})} \tag{6.5}$$

Recently, Liu *et al.* [47] modified the mechanism of Gao *et al.* and proposed the following reactions as a possible pathway for the mediated ORR by DBBQ:

$$\mathrm{Li}\cdots\mathrm{DBBQ}\cdots\mathrm{O}_{2(\mathrm{sol})} \longrightarrow \mathrm{LiO}_{2\,(\mathrm{sol})} + \mathrm{DBBQ}_{(\mathrm{sol})} \tag{6.6}$$

$$2\mathrm{LiO}_{2\,(\mathrm{sol})} \longrightarrow \mathrm{Li}_2\mathrm{O}_{2\,(\mathrm{s})} + \mathrm{O}_{2(\mathrm{sol})} \tag{6.7}$$

Liu *et al.* showed indirectly, by analyzing the amount of side reactions in DME and TEGDME based electrolytes, that another intermediate of the ORR mediated by DBBQ is LiO_2.
With the mechanism formulated in reactions 6.1-6.7, the higher capacities of the DBBQ containing Li-O_2 cells could be explained by a solution growth of Li_2O_2 as shown in reactions 6.4, 6.5 and 6.7.
This paper also deals with DBBQ as a mediator for the ORR. The focus of this study is on the impact of the ion pairing of the DBBQ monoanion with the cations of the electrolyte (see reaction 6.2) on the overall ORR.
Therefore, we will shortly explain the thermodynamic effect on the reduction potential of a reduced molecule caused by ion pairing. As an example, we assume that a species A is undergoing a fast electron transfer at the electrode forming A^-:

$$\mathrm{A}_{(\mathrm{sol})} + \mathrm{e}^- \longrightarrow \mathrm{A}^-_{(\mathrm{sol})} \tag{6.8}$$

In solution A^- can now form ion pairs with cations M^+ of the supporting electrolyte:

$$A^-_{(sol)} + pM^+_{(sol)} \longrightarrow AM^{(1-p)+}_{(sol)} \tag{6.9}$$

Herein p is the number of pairing cations. If reaction 6.8 is in equilibrium, for the ratio between A^- and A as a function of the electrode potential E is given by the Nernst equation. For a fast reaction 6.9 the concentration of the educts and products is given by chemical equilibrium with an equilibrium constant K. Combing these two assumptions will give the following expression for the half wave potential $E_{1/2}$ of reactions 6.8 and 6.9 [251]:

$$E_{1/2} = E^0_{A \to A^-} + \frac{RT}{F} \ln \left(1 + Kc(M^+)^p\right) \tag{6.10}$$

In equation 6.10 $E^0_{A \to A^-}$ is the standard potential of reaction 6.8, R is the ideal gas constant, T the temperature and F the Faraday constant. Equation 6.10 simplifies if $1 << Kc(M^+)^p$ to [248]:

$$E_{1/2} = E^0_{A \to A^-} + \frac{RT}{F} \ln (K) + \frac{RT}{F} p \ln(c(M^+)) \tag{6.11}$$

$$E_{1/2} = const + \frac{RT}{F} p \ln(c(M^+)) \tag{6.12}$$

In equation 6.12 all constants were summarized into $const$. Equation 6.12 shows, that if A^- is undergoing ion pairing the half wave potential of the reductive process is shifting to positive electrode potentials. The expected slope at room temperature in a plot of $E_{1/2}$ as a function of $\log(c(M^+))$ is $p \cdot 60$ mV/dec. Especially quinones are prone to undergo ion pairing in non aqueous solvents [248–250].

Our investigations described in this paper show, that the DBBQ monoanion is only active for the ORR if there is a strong interaction between $DBBQ^-$ and the cation of the electrolyte. To investigate the ORR kinetics in DBBQ containing electrolytes we are using the differential electrochemical mass spectrometry (DEMS) and the rotating ring disc electrode (RRDE). The formation of crystalline ORR reaction products (in the presence of DBBQ) is analyzed with the RRDE in Li^+ and K^+ containing TEGDME. There we found out that more insoluble reaction products are formed in Li^+ containing solution. In addition, we are measuring the oxygen consumption rates of the DBBQ monoanion containing solutions via mass spectrometry with a novel experimental approach. In this approach the diffusion of oxygen through a thin electrolyte layer is measured via the time resolved ionic current of m/z =32. A homogeneous reaction that is consuming O_2 perturbs the diffusion of oxygen through the thin electrolyte layer. Out of finite element simulation, this perturbation can be isolated, giving kinetic insights into the ORR mediated by the DBBQ monoanion in the absence of other electrode reactions.

Moreover, we will show that increasing the Li^+ concentration in the supporting electrolyte will not only shift the equilibrium potential of the DBBQ reduction but also the onset of the ORR to more positive potentials.

The paper is organized in two parts:

- In part I the homogeneous ORR kinetics in DBBQ- containing solution is examined using the new experimental approach of pressure jump experiments via mass spectrometry.
- In part II the ORR kinetics is examined with DEMS and RRDE. First, we are presenting the results in Li^+ containing TEGDME based electrolytes. Secondly, the results in Li^+ containing DMSO based electrolytes are discussed.

6.3 | Experimental

Chemicals

All electrolytes were prepared in an MBraun or GS glovebox. Lithium perchlorate ($LiClO_4$, battery grade, Sigma-Aldrich), silver nitrate ($AgNO_3$,$\geq$99%, ChemPure), Tetrabutylammonium perchlorate ($TBAClO_4$, $\geq$99%, Sigma-Aldrich), 2,5-Di-tert-1,4-benzoquinone (DBBQ, 99%, Sigma-Aldrich) and extra dry dimethyl sulfoxide (DMSO, 99.7%, over molecular sieve, Acros Organics) were used as received. Potassium perchlorate ($KClO_4$, $\geq$99.99%, Sigma-Aldrich), was dried under reduced pressure and increased temperature in a Büchi oven before using them as supporting salts. Tetraglyme (TEGDME, 99%, Acros Organics) was refluxed over sodium and distilled under reduced pressure. Afterwards TEGDME was stored over molecular sieve. Highly pure argon (Air Liquid 99.999%) and highly pure oxygen (Air Liquid 99.995%) were used to saturate the electrolytes.

Reference electrode

The reference electrode consists of a silver wire immersed in a solution of 0.1 M $AgNO_3$ in DMSO. In the measurement cells the reference electrolyte is separated via a glass bead or a glass stopcock from the supporting electrolyte to avoid contaminations of the supporting electrolyte with Ag^+. A detailed description of our reference electrode used for the DEMS measurements can be found elsewhere [90].The potential of the $Ag^+ | Ag$ reference in acetonitrile was calibrated against Li metal in DMSO and TEGDME in [252]. On this basis and with the listed values [132] of $Ag^+ | Ag$ values we calculated our reference potential with -3.198 V vs $Li^+ | Li$ in

TEGDME and -3.742 V in DMSO. A sketch towards the calculation of the reference potential is given in the supporting information.

RRDE-Experiments

Rotating ring disc electrode (RRDE) experiments were carried out with a Pt-Pt thin gap electrode with a fixed geometry (AFE7R8PTPT, Pine Research Instrumentation). The disc radius is $r_1 = 2.285\,\mathrm{mm}$, the inner ring radius is $r_2 = 2.465\,\mathrm{mm}$ and the outer ring radius is $r_3 = 2.69\,\mathrm{mm}$. With the kinematic viscosity ν, the diffusion coefficient of a transferred species from the disc electrode to the ring electrode D, and the rotation frequency f of the RRDE electrode, one can calculate the transfer time of the species under investigation with the modified formula of Bruckenstein *et al.* [138] by Prater *et al.*[253]:

$$t = 3.58\left(\frac{\nu}{D}\right)^{1/3}(2\pi f)^{-1}\left[\log\left(\frac{r_2}{r_1}\right)\right]^{2/3} \tag{6.13}$$

For the RRDE electrode used in this study, using $D = 1.66 \cdot 10^{-6}\,\mathrm{cm^2\,s^{-1}}$(diffusion coefficient of the DBBQ monoanion in a TEGDME based electrolyte, determined by us in RRDE potential jump experiments) and the kinematic viscosity of TEGDME $\nu = 0.03294$ [254] this leads to $t = 396\,\mathrm{ms}$ for $f = 4\,\mathrm{ms}$ and $t = 32\,\mathrm{ms}$ for $f = 49\,\mathrm{ms}$. A fundamental property of the RRDE is that the theoretical collection efficiency N_0 is only dependent on the RRDE radii. On the other hand, one can determine the apparent collection efficiency N:

$$N = \left|\frac{I_{ring}}{I_{disc}}\right| \tag{6.14}$$

In equation 6.14 I_{ring} and I_{disc} are the faradaic current at the ring electrode and at the disc electrode, respectively. Deviation of N from the theoretical collection efficiency N_0 of the RRDE geometry, which is 0.218 for the used Pt-Pt-thin gap electrode, can be caused by a homogeneous reaction occurring in the gap-ring-region, if the homogeneous reaction is creating a species, which is not undergoing an electrochemical reaction at the applied ring potential.
The RRDE experiments were carried out in an argon filled GS glove box. As electrochemical cell we were using a self-built glass cell.

DEMS experiments

Our DEMS setup consist of an self-built differentially pumped vacuum system with two pumping stages of $200\,\mathrm{L\,s^{-1}}$ (TMU 260, Pfeiffer Vacuum) and $50\,\mathrm{L\,s^{-1}}$ (TPU 062, Pfeiffer Vacuum) as described by O. Wolter and J. Heitbaum previously [142]. As mass spectrometer, we are using a QMA 430 by Balzers.

The ionic current of O_2 ($m/z = 32$) and CO_2 ($m/z = 44$) detected in the mass spectrometer are calculated into a mass flux $\dot{n}_{m/z}$:

$$\frac{dn_{m/z}}{dt} = \dot{n}_{m/z} = \frac{I_{m/z}}{K^*_{m/z}F} \tag{6.15}$$

In equation 6.15 $I_{m/z}$ is the baseline corrected ionic current detected in the mass spectrometer, $K^*_{m/z}$ calibration constant of a species with m/z and F is the faraday constant. The baseline correction leads to negative $\dot{n}_{m/z}$ which are due to a consumption of a species with m/z whereas positive values correspond to an evolution of a species with m/z.
The cell used in this study is a thin layer cell that was recently introduced in [58]. The cell body is manufactured out of Kel-F. As working electrode, we are using a porous PTFE membrane sputtered with gold ($A = 0.283\,\mathrm{cm}^2$). The pore diameter is 20 nm. Since the membrane is used as interface between vacuum of the mass spectrometer and the electrolyte, volatile species in the electrolyte or those formed at the electrode can evaporate into the vacuum and be detected in the mass spectrometer. The overall electrolyte volume in front of the working electrode is 5.6 µL. The electrolyte volume is saturated with oxygen via a oxygen reservoir through another porous PTFE membrane opposite of the WE. Three gold electrodes are used as counter electrodes. The electrolyte contact of these counter electrodes is realized through capillaries. As reference electrode we used the $Ag^+ \mid Ag$ reference described above. More details about the cell are described in [58].

6.4 | Results an discussion

6.4.1 | Part I: Homogeneous ORR kinetics of DBBQ- in various solvents

Our aim was to investigate the homogeneous kinetics of ORR mediated by $DBBQ^-$ for electrolytes that are containing different supporting salts and solvents, decoupled from the electrochemical experiment. This was achieved by measuring the consumption of oxygen in the presence of the DBBQ monoanion while it is diffusing through a thin electrolyte layer. A schematic representation of the experimental setup, which we call "Pressure jump experiment", is shown in Figure 6.1.

The procedure of the pressure jump experiments and a proof of the principle was recently published [128, 255]. In short, the pressure jump experiments are performed as follows: The volume of the O_2 tank as well as the volume above the first Teflon membrane (left membrane in Figure 6.1) is evacuated; afterwards the valve connecting the oxygen tank and the thin layer cell is closed. The oxygen tank is then filled with an oxygen partial pressure below the atmospheric

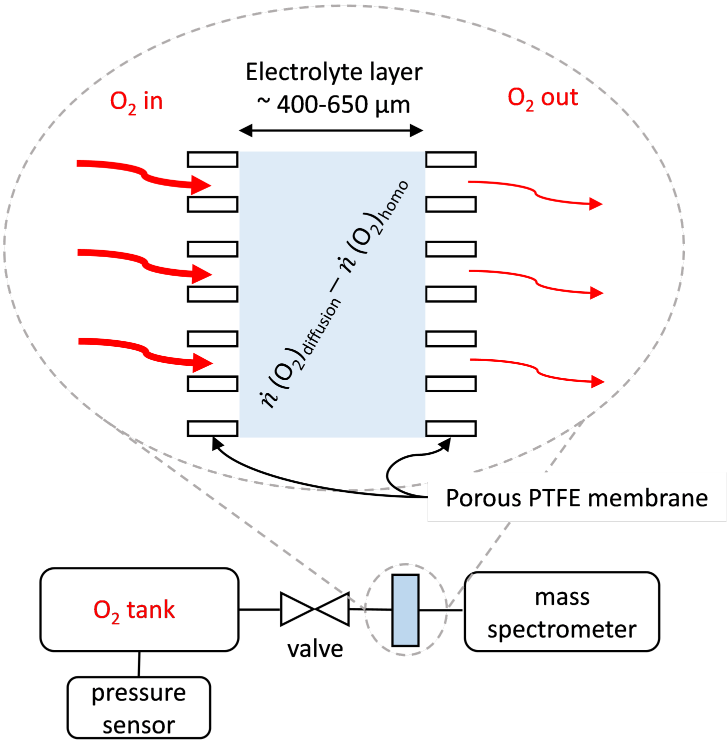

Figure 6.1: Schematic representation of the experiment used to determine the oxygen consumption of the ORR by DBBQ- in various electrolytes. An electrolyte layer is filled with a DBBQ containing solution. The oxygen pressure is abruptly changed on the left porous PTFE membrane (see red arrow labeled with “O_2 in”). At the other end of the cell the O_2 flux through the electrolyte layer is measured via mass spectrometry. In general, the signal contains information about the diffusion flux of oxygen $\dot{n}\,(O_2)_{diffusion}$ as well as the consumption of O_2 by DBBQ$^-$ $\dot{n}\,(O_2)_{homo}$.

pressure. Opening the valve to the cell again generates a pressure drop in the oxygen tank, which is recorded via a pressure sensor. The pressure drop represents the zero time stamp of the experiment. After opening the valve, oxygen is diffusing through the electrolyte layer into the vacuum of the mass spectrometer. The time dependent diffusion of oxygen through the thin layer is measured as oxygen flux $\dot{n}(O_2)$ with the mass spectrometer. In the absence of a chemical reaction consuming O_2, the transient is only defined by the diffusion of oxygen through the thin electrolyte layer $\dot{n}(O_2)_{\text{diffusion}}$. In the presence of DBBQ$^-$, O_2 can also be consumed in the mediation cycle as described in equations 6.3-6.7 , which effectively reduces the flux of O_2 into the vacuum of the mass spectrometer. Therefore the overall detected oxygen flux into the mass spectrometer $\dot{n}(O_2)_{\text{total}}$ is:

$$\dot{n}(O_2)_{\text{total}} = \dot{n}(O_2)_{\text{diffusion}} - \dot{n}(O_2)_{\text{homo}} \tag{6.16}$$

To extract the kinetic information from the transient finite difference element simulations as well as several experiments are necessary.

Figure 6.2 shows the needed experiments as well as the information flow between the different experiments, to extract the rate constants of the ORR mediated by $DBBQ^-$.

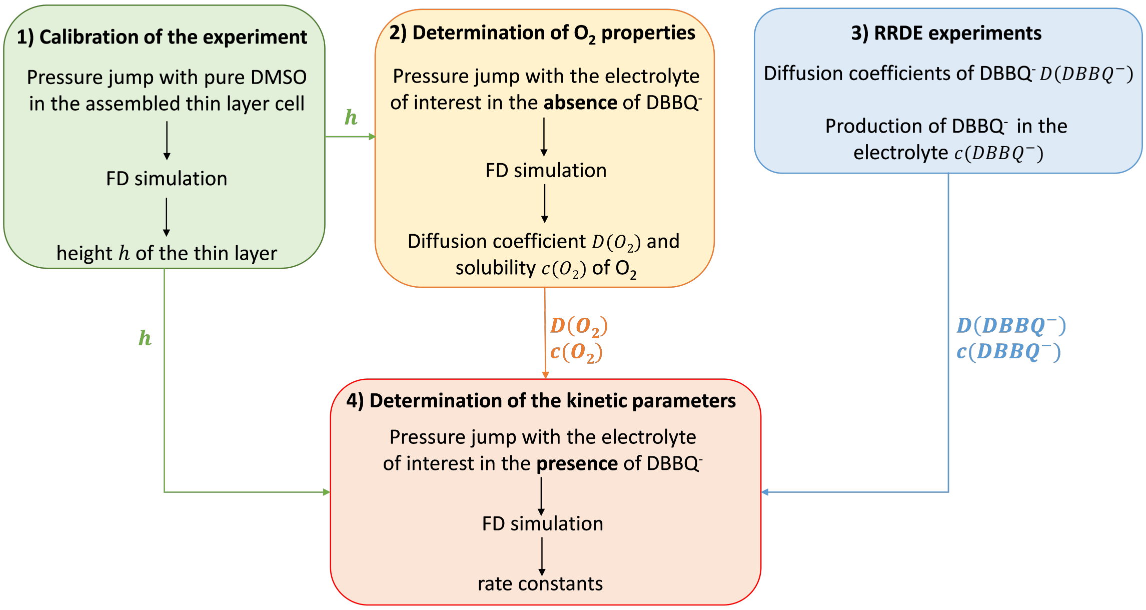

Figure 6.2: Schematic workflow of the experiments, which are performed to determine the kinetics of the ORR mediated by $DBBQ^-$.

First, it is necessary to calibrate the experimental setup. This is achieved by performing a pressure jump in pure DMSO solvent (see green box in Figure 6.2). There the diffusion coefficient and the solubility of O_2 are known ($D(O_2) = 24.3 \cdot 10^{-6}\,\mathrm{cm^2\,s^{-1}}$, $c(O_2) = 2.04\,\mathrm{mM}$)[128, 255]. Therefore the solvent layer thickness h can be calculated, which is needed for all following pressure jumps experiments. Secondly, $D(O_2)$ and $c(O_2)$ in the electrolyte that will be used to investigate the ORR mediated by $DBBQ^-$ will be determined (see yellow box in Figure 6.2). To determine $D(O_2)$ and $c(O_2)$ in these electrolytes, pressure jumps in the absence of $DBBQ^-$ are performed. Finite difference simulations of the experimental data gives the values of $D(O_2)$ and $c(O_2)$. In RRDE experiments $D(DBBQ^-)$ and $c(DBBQ^-)$ are determined (see blue box in Figure 6.2). $D(DBBQ^-)$ is determined by producing $DBBQ^-$ in a potential jump experiment at the disc electrode. The transfer of $DBBQ^-$ to the ring electrode is studied by extracting the transfer time t, which it takes $DBBQ^-$ to be detected at the ring electrode at different rotation frequencies. According to equation 6.3, $D(DBBQ-)$ can be determined in a plot of $f^{-0.5} \rightarrow t$. The RRDE setup is also used to produce $DBBQ^-$ containing solutions. There the disc potential is held for approximately 12 h such that DBBQ is reduced to $DBBQ^-$. After the 12 h, the $c(DBBQ^-)$ can be determined out of the diffusion limited current for the

$DBBQ^-$ oxidation in a cyclic voltammetry measurement according to the Levich-equation. Finally, the parameters determined in the three experiments are used in a last experiment to determine the kinetic parameters of the ORR mediated by the DBBQ-monoanion (see red box in Figure 6.2). There a pressure jump in a $DBBQ^-$ containing electrolyte is performed. Interpreting the oxygen flux transient with a finite element simulation, in which reactions 6.3-6.5 are implemented, is unraveling the chemical kinetics of the ORR mediated by $DBBQ^-$. The diffusion coefficient of $\mathrm{Li} \cdots \mathrm{DBBQ} \cdots \mathrm{O}_{2(\mathrm{sol})}$ is experimentally not determinable and therefore we set $D(\mathrm{Li} \cdots \mathrm{DBBQ} \cdots \mathrm{O}_{2(\mathrm{sol})}) = D(\mathrm{DBBQ}^-)$.

For the one-dimensional diffusion problem of O_2 in the thin electrolyte layer, analytical solutions exist, which can be used to benchmark our finite element code [239]. The finite element simulation is in excellent agreement with the analytical solution (see Figure 6.12 in the supporting information), which is verification of the used code. Even though the analytical solution of the diffusion problem is available, the use of finite difference simulation is necessary, due to introducing chemical kinetics and different diffusion coefficients into the analysis of the experimental data. To give the reader a tool to get a deeper understanding of this experiment, we formulated a chapter in the supporting information, which is explaining with a model reaction the shape of the transients. In addition the evolution of concentration profiles of the different species is shown.

Figure 6.3 shows the pressure jump experiment in 0.5 M $TBAClO_4$ in DMSO. The black traced oxygen flux into the mass spectrometer was recorded in the absence of $DBBQ^-$ in the electrolyte and in the orange traced measurement 8 mM $DBBQ^-$ was previously produced in the electrolyte volume. The comparison of this measurement shows, that both oxygen flux transients are congruent. This means that $DBBQ^-$ is not disturbing the transport properties of O_2 by chemical reaction. Thus, $DBBQ^-$ is not mediating the ORR in 0.5 M $TBAClO_4$ in DMSO.

Introducing Li^+ into the electrolyte is changing the outcome of the experiments. In Figure 6.4 the pressure jump experiments in (a) 0.5 M $LiClO_4$ in DMSO and (b) 0.5 M $LiClO_4$ in TEGDME are displayed.

First of all the oxygen flux into the mass spectrometer in the absence of $DBBQ^-$ were analyzed (grey traced measurements in Figure 6.4). The finite difference simulation is in this case providing the solubility and diffusivity of oxygen in the electrolyte system. The simulated oxygen flux transients are reproducing the experimental data excellently (see black traced oxygen flux transients in Figure 6.4). The current of the experiments in two different electrolytes is reaching the same diffusion limited current due to different applied oxygen pressures in the ex-

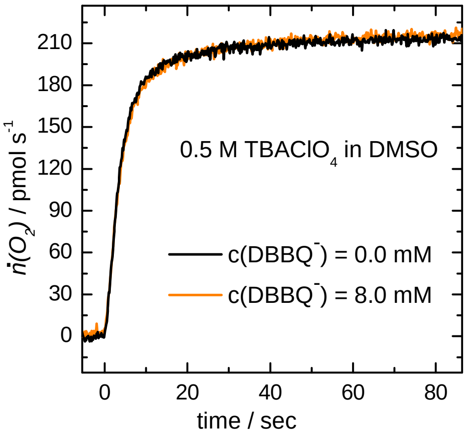

Figure 6.3: Pressure jump in a 0.5 M TBAClO$_4$ in DMSO electrolyte. The black curve was recorded in absence of DBBQ$^-$. In the orange transient, a 8 mM DBBQ$^-$ containing solution was used. The thin electrolyte layer had a thickness of 400 µm and during the pressure jump, a pressure of 700 mbar of oxygen was applied on the cell.

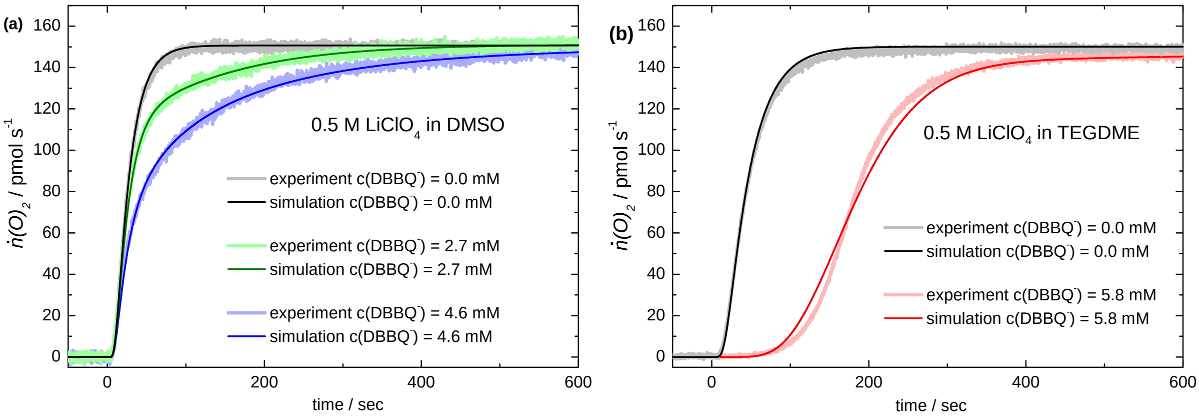

Figure 6.4: Experimental and simulated oxygen flux transients after a pressure jump in (a) 0.5 M LiClO$_4$ in DMSO with 2.7 mM (green) and 4.6 mM (blue) DBBQ$^-$ in the electrolyte. In (b) 0.5 M LiClO$_4$ in TEGDME was used as an electrolyte. The red transients the electrolyte contained 5.6 mM of DBBQ$^-$. The grey displayed measurements are showing the transients in the absence of DBBQ$^-$. In the DMSO based measurements, the electrolyte layer thickness was determined with 581 µm and in the TEGDME measurement with 646 µm. The applied oxygen pressure in the DMSO based measurements was 875 mbar and in the TEGDME based measurements 682 mbar.

perimental procedure ($p(O_2, \text{DMSO}) = 877$ mbar $p(O_2, \text{TEGDME}) = 681$ mbar). The received values are summarized in Table 6.1, and in good agreement with previously reported values [128, 228, 255]. Table 6.1 also shows the diffusion coefficient for DBBQ$^-$, which was determined in potential jump experiments with a RRDE experiment (for details see the supporting information).

The shape of the oxygen flux transients is changing when $DBBQ^-$ is added to the electrolyte (see green, blue and red traces measurements in Figure 6.4). There the oxygen flux reaching the mass spectrometer is delayed in the DBBQ monoanion containing electrolyte as compared to the DBBQ monoanion free solution, implying a consumption of O_2 via a reaction with the DBBQ monoanion. This observation is more pronounced in the TEGDME base electrolyte. Here the detection of an oxygen flux starts 60 s after the beginning of the experiment. For our further interpretation of the experimental data, we implemented equations 6.3-6.5 into the finite difference simulation. The associated rate constants are k_1, k_{-1}, k_2 and k_3. With these reactions, we were able to reproduce the experimental data. The received rate constants are summarized in Table 6.2. In the fitting routine, it was sufficient to exclude k_3 out of the analysis. The received rate constants show that there is a significant change in the rate constants of reaction 6.3 when the solvent of the electrolyte is changed from DMSO to TEGDME. In a TEGDME based electrolyte we observe approximately 80 times faster formation of the $Li \cdots DBBQ \cdots O_{2(sol)}$ -complex compared to the DMSO based electrolyte. To show the reader the sensitivity of our experimental approach towards changes in the rate constants of the suggested mechanism, we are showing the change of the transients when different rate constants are assumed (see Figure 6.15 in the supporting information).

Table 6.1: Resulting values for the diffusion coefficient of oxygen and solubility of oxygen out of fitting the experimental pressure jump experiments in the absence of $DBBQ^-$ in Figure 6.4. The diffusion coefficient of $DBBQ^-$ is determined in potential jump experiments in a RRDE experiments (see supporting information).

electrolyte	$c(O_2)$ / mM	$D(O_2)$ / $cm^2\,s^{-1}$	$D(DBBQ^-)$ / $cm^2\,s^{-1}$
0.5 M $LiClO_4$ in DMSO	1.850	$18.95 \cdot 10^{-6}$	$1.12 \cdot 10^{-6}$
0.5 M $LiClO_4$ in TEGDME	3.616	$13.78 \cdot 10^{-6}$	$0.32 \cdot 10^{-6}$

Table 6.2: Resulting values for the rate constants of reactions 6.3 and 6.4. These values result out of the simulations of the pressure jump transients in Figure 6.4. Reaction 6.5 was also taking into the simulation. The evaluations shows that this reaction was not needed to fit the experimental data.

solvent	$c(DBBQ^-)$ / mM	k_1 / $s^{-1}\,M^{-1}$	k_{-1} / $s^{-1}\,M^{-1}$	k_2 / $s^{-1}\,M^{-1}$
DMSO	4.6	6	6	11
DMSO	2.7	3	5	3
TEGDME	5.8	512	371	3

6.4.2 | Part II: Electrochemical studies of the ORR mediated by DBBQ-

6.4.2.1 | Electrochemical studies in TEGDME based electrolytes

We investigated the mediated ORR by DBBQ in a TEGDME based electrolyte by combining cyclic voltammetry and mass spectrometry (see Figure 6.5).

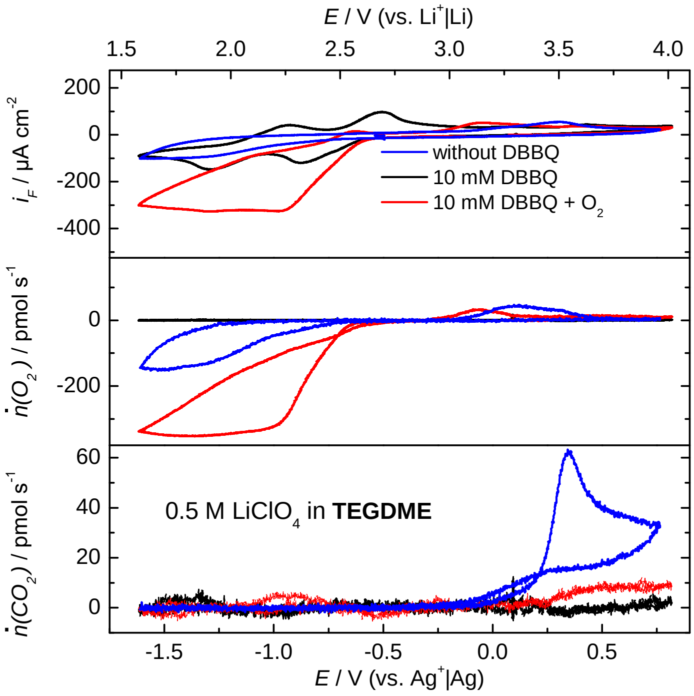

Figure 6.5: CVs, O_2 flux and CO_2 flux in a 0.5 M $LiClO_4$ solution in TEGDME. The blue traced measurement was performed in the presence of O_2, but in the absence of DBBQ. The black curves are representing measurements when DBBQ is added to the electrolyte, but O_2 is not present. The experiment in the presence of O_2 and DBBQ is shown in red. Gold was used as working electrode in all measurements and the sweep rate was 10 mV/s. The oxygen pressure on the gas side was 700 mbar.

The cyclic voltammetry of DBBQ in the absence of O_2 shows, that in TEGDME the reduction of DBBQ occurs at higher potentials (- 0.6 V vs. Ag^+ | Ag) than the reduction of O_2 in the supporting electrolyte without DBBQ (- 0.75 V vs. Ag^+ | Ag). Indeed the decrease of the oxygen flux in a DBBQ containing TEGDME based electrolyte is observed at potentials at which the onset of the DBBQ reduction in a deoxygenated solution starts (compare red traced measurement to the black traced measurement in Figure 6.5). This gives a clear evidence that the mediation of the ORR by DBBQ in a TEGDME based electrolyte occurs via the DBBQ monoanion and could be described with reactions 6.1-6.7. The increase of the reduction current in the red traced measurement compared to the black traced measurement in Figure 6.5 results from the reoxidation of $DBBQ^-$ to DBBQ due to O_2 as shown in reactions 6.4-6.6, followed by the back diffusion and reduction of DBBQ at the working electrode. In the presence of DBBQ in the electrolyte, the overall oxygen reduction charge transferred is higher than in the supporting electrolyte without DBBQ. This was previously explained by the solution growth of Li_2O_2, which therefore is suppressing the poisoning of the electrode surface. Moreover, we observe a CO_2 evolution in our DEMS experiments, which is more pronounced in the DBBQ free solution. The significant decrease of the CO_2 flux into the mass spectrometer at higher electrode potential in a DBBQ containing TEGDME electrolyte compared to a DBBQ free electrolyte can be explained by less deposition of CO_2 releasing species on the electrode surface during the ORR. Already known species that would be oxidized to CO_2 and that is described in literature on the Li-O_2 system are Li_2CO_3 and other electrolyte decomposition products[90, 204].

In the presence of DBBQ in the electrolyte the oxygen flux into the mass spectrometer in the OER potential region is decreased compared to the measurements in DBBQ free electrolytes. This can be explained by the formation of large Li_2O_2 particles with bad electrical contact to the electrode or the formation of these particles at the walls of the cell as expected for the ORR mediation mechanism by DBBQ. Thus, Li_2O_2 has bad or no electric contact to the electrode surface and is therefore not completely oxidizable. This underlines the need of introducing a redox mediator for the OER into the electrolyte [34, 58, 84, 204].

The homogeneous formation of Li_2O_2 was also investigated using the RRDE by analyzing the rotational dependency of the collection efficiency [138, 253, 256]. In more recent work in the field of metal-air batteries with a RRDE even the evolution of superoxide during charge was reported [109, 252, 257]. In these experiments, we used $KClO_4$ and $LiClO_4$ supporting salts in a TEGDME based electrolyte. The experimental data in oxygen containing electrolyte is shown in Figure 6.6. The lower potential limit in each experiment was set such that only the DBBQ monoanion was produced in the reductive wave. It is worthwhile to mention that a layer of Li_2O_2 is normally blocking the disc electrode, if the experiments shown in Figure 6.6 are performed without DBBQ in the electrolyte. This shows again that in the presence of DBBQ in the electrolyte the insulating products of the ORR are not formed on the electrode surface but in the electrolyte volume. Another explanation could be that large particles on the electrode surface are blocking a negligible surface area.

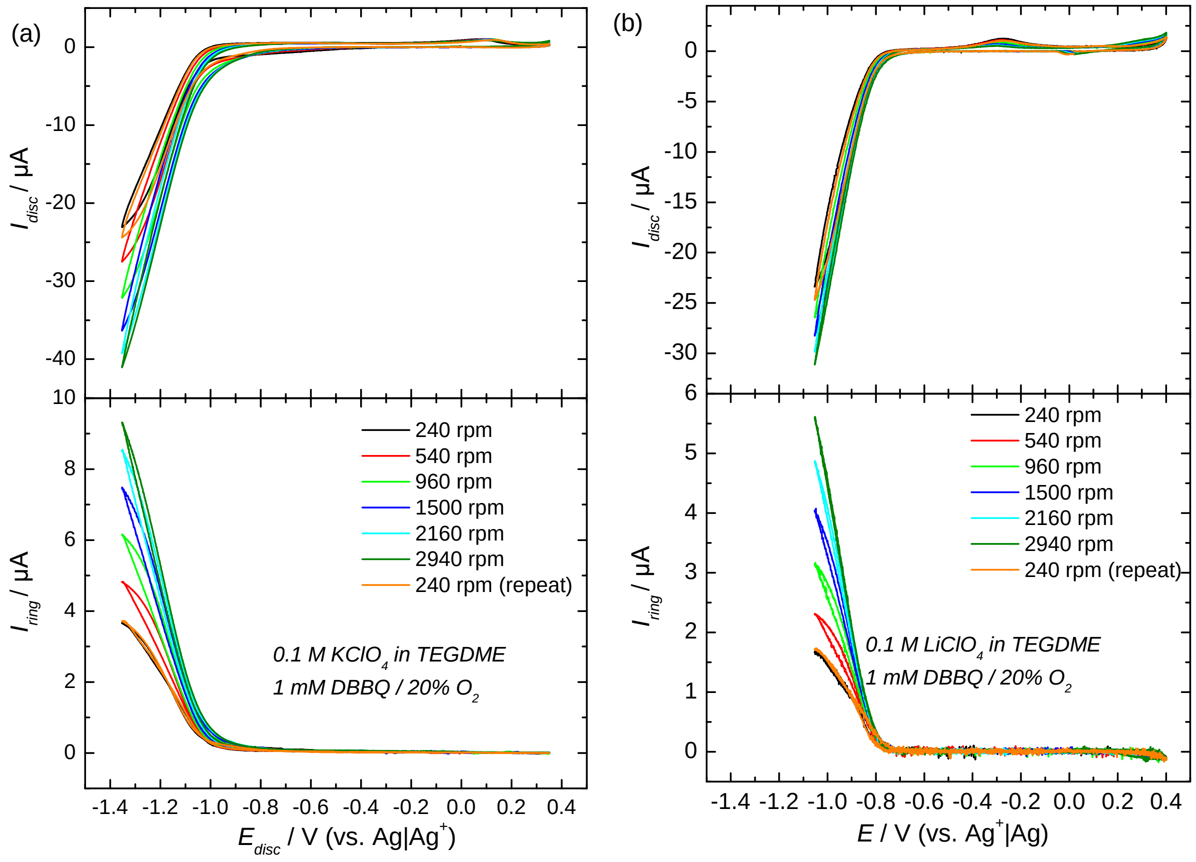

Figure 6.6: CV study at a Pt-Pt-thin gap RRDE assembly for various rotation rates. The electrolyte was saturated with a 20 % O_2 mixture in Ar. The ring potential was held at a constant potential of 0.0 V vs. Ag$^+$| Ag. The sweep rate of the disc potential was 10 mVs^{-1}. The supporting electrolyte always consist of 1 mM DBBQ in TEGDME with (a) 0.1 M $KClO_4$ and (b) 0.1 M $LiClO_4$.

To analyze the homogeneous reaction kinetics, the rotational dependency of the collection efficiency N is evaluated. The ratio between the experimental collection efficiency N to the theoretical collection efficiency N_0 as a function of the rotation frequency is shown in Figure 6.7 (a). N_0 was determined by reducing DBBQ at the disc electrode and oxidizing DBBQ$^-$ at the ring electrode in the Ar-saturated electrolyte (see Figure 6.22 and Figure 6.23 in the supporting information). There the collection efficiency shows no rotational dependency and was determined to be 0.239, which is in good agreement with the one calculated from the radii of the electrodes (0.218).

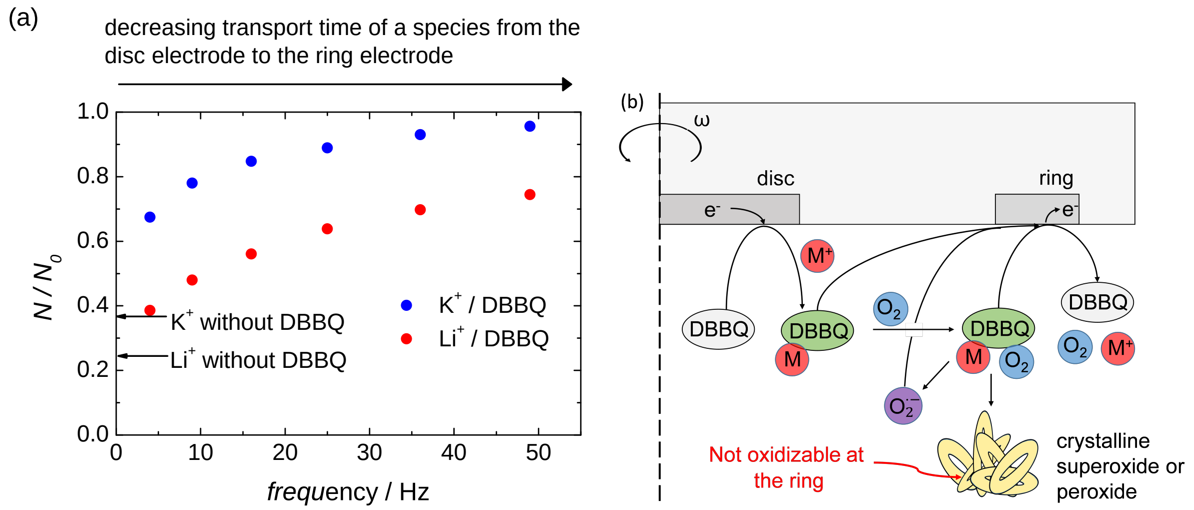

Figure 6.7: (a) Plot of the ratio between the experimental collection efficiency N of the data shown in Figure 6.6 and the theoretical collection efficiency N_0 as a function of the rotation frequency. The experimental collection efficiency is the mean value of the collection efficiencies determined in the potential range in which a reductive current was observed at the disc electrode in the experiment shown in Figure 6.6. The values of N/N_0 in DBBQ free electrolytes did not show a rotational dependence and are shown as arrows with the respective caption. (b) Sketch of the possible reactions that could occur in the electrolyte volume in front of the RRDE electrode.

The value N/N_0 for the experiments shown in Figure 6.6 shows a dependence on the rotation frequency of the RRDE electrode: N/N_0 is strictly monotonically rising with increasing rotation frequency. The values of N/N_0 are always lower in the Li^+ containing solution than in the K^+ containing solution. For the K^+ containing solution the experimental collection efficiency nearly reaches the theoretical collection efficiency for the highest rotation frequency of 49 Hz ($N/N_0 = 0.96$). We also performed studies in 0.1 M $LiClO_4$ [47] and 0.1 M $KClO_4$ (see Figure 6.24 in the supporting information) in TEGDME without DBBQ. There we did not observe a rotational dependency of N/N_0. Those values are also lower than the values with DBBQ in the electrolyte (see arrows in Figure 6.7 (a)) which is due to the parallel formation of Li_2O_2 with is deposited on the disc electrode and thus not oxidized at the ring electrode. This shows that the ORR is following a non-homogenous reaction mechanism in DBBQ free electrolytes: A large part of the reaction products is deposited at the electrode surface as also evidenced by the reduced ORR activity of the electrode in the subsequent anodic sweep.
To interpret these results we summed up the reactions formulated in 6.1-6.7 in a simplified reaction scheme together with to a sketch of the RRDE geometry (see sketch in Figure 6.7 (b)). In the supporting information we are discussing why we concluded that the ORR in the RRDE experiments is mainly due to the mediation by DBBQ and that the direct reduction of oxygen at the electrode surface can be neglected. In principle, this sketch shows that we assume that

all species, which are soluble, are also oxidizable at the ring electrode. These species are soluble superoxide and reduced DBBQ-anions associated to the cations of the electrolyte as well as to oxygen. The only species that are not oxidizable at the ring should be crystalline (non-dissolved) potassium superoxide and potassium and lithium peroxides (the toroidal structures shown in the sketch are used as a symbol for the crystalline nature). The rotation frequency dependence of N/N_0 is due to the increase of the transfer time of a species from the disc electrode to the ring electrode for decreasing the rotation frequency (see equation 6.13. Therefore, for smaller rotation rates more non-oxidizable species can be formed by reactions 6.1-6.7 which leads to a decrease of N/N_0. The overall lower values of N/N_0 in a Li^+ containing solution compared to a K^+ containing solution show that the homogeneous ORR is faster in a Li^+ containing system than in a K^+ containing solution. At the same time we observe a shift of the half wave potentials of the DBBQ reduction in measurements in the Li^+ containing system of 200 mV compared to the K^+ containing system (see Figure 6.22 in the supporting information). This suggests a stronger ion association between Li^+ and $DBBQ^-$ than between K^+ and $DBBQ^-$.

6.4.2.2 | Electrochemical studies in DMSO based electrolytes

We also performed DEMS studies on the mediation of the ORR by DBBQ in DMSO based electrolyte (see Figure 6.8). Comparing the measurements in DMSO based electrolyte to the already discussed DEMS data in TEGDME gives evidences that the ORR mediated by DBBQ is slower in the DMSO based electrolyte than in the TEGDME based electrolyte, as already observed in the pressure jump experiments. This can be seen in the low rate of oxygen consumption between the onset of the first electron transfer to DBBQ (- 0.7 V vs. $Ag^+|$ Ag) and the onset of ORR in the supporting electrolyte without DBBQ (-0.9 V vs. $Ag^+|$ Ag). The ORR activity trend of the measurements in the DMSO based solvent and in the TEGDME based solvent also follows a similar trend as the previous K^+ and Li^+ comparison: As the Li^+-$DBBQ^-$ association is stronger in the TEGDME based electrolyte the ORR activity is also faster in the TEGDME based electrolyte compared to the DMSO based electrolyte. The stronger ion association can be seen by a 140 mV positive shift of the first reduction wave of DBBQ in TEGDME compared to the measurement in DMSO (see Figure 6.20 in the supporting information). Also a comparison in the CVs of DBBQ in the absence of oxygen (see black traced measurement Figure 6.8) and in the presence of oxygen in the electrolyte (see red traced measurement in Figure 6.8) gives an indication for the minor activity of DBBQ on the ORR in DMSO based electrolyte: The reduction current in the oxygenated solution is only slightly increased compared to the deoxygenated solution, which might be explained by the parallel, direct reduction of O_2 on the electrode surface. Thus back diffusion and reduction of generated DBBQ out of reactions 6.4-6.6 is less pronounced than in a TEGDME based electrolyte. However, the comparison to the measurement in supporting electrolyte without DBBQ shows, that the electrode surface is not poisoned by deposited Li_2O_2 in the presence of DBBQ. This is an indication that the ORR is undergoing a solution mediated growth of Li_2O_2. Since the monoanion of DBBQ showed a minor activity towards the ORR, the solution growth of Li_2O_2 seems to be mainly mediated by the dianion of DBBQ at lower electrode potentials as -1.2 V vs $Ag^+|$ Ag (onset of the $DBBQ^{2-}$ formation). At this point, we want to highlight, that it is reasonable to assume that the underlying mechanism of the mediated ORR by $DBBQ^{2-}$ is different to that of $DBBQ^-$: The $DBBQ^{2-}$ formation takes place at potentials significantly lower as compared to the potential of the unmediated ORR. Therefore, $DBBQ^{2-}$ can reduce O_2 in the electrolyte volume by an outer sphere electron transfer. An analogous mediator-oxygen-complex like in equation 6.3 is thus not coherent.

The measurements in a DMSO based electrolyte do not show a significant decrease of the CO_2 flux when DBBQ is added to the electrolyte. This shows that Li_2CO_3 or other decomposition product which are releasing CO_2 are still deposited on the electrode surface in DMSO based electrolytes.

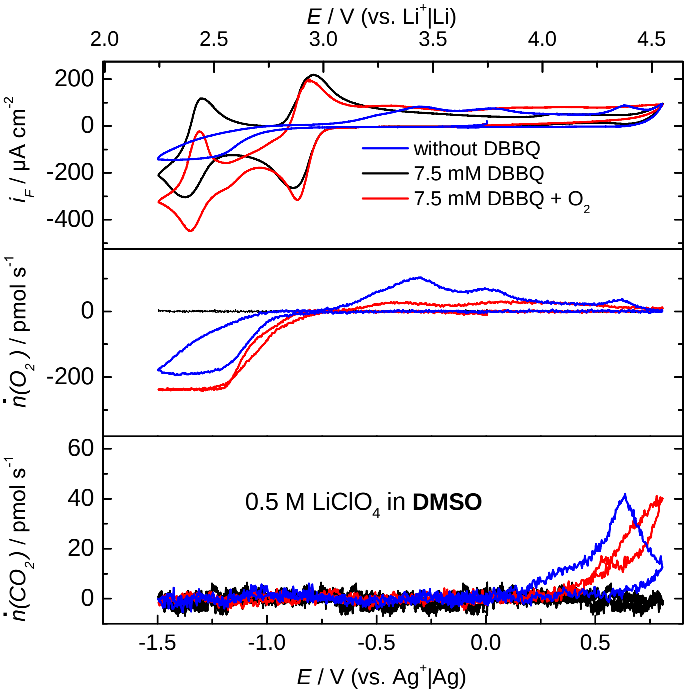

Figure 6.8: CVs, O_2 flux and CO_2 flux in a 0.5 M $LiClO_4$ solution in DMSO. The blue traced measurement was performed in the presence of O_2, but in the absence of DBBQ. The black curves are representing measurements when DBBQ is added to the electrolyte, but O_2 is not present. The experiment in the presence of O_2 and DBBQ is shown in red. Gold was used as working electrode in all measurements and the sweep rate was 10 mV/s. The oxygen containing solutions were saturated with an oxygen partial pressure of 700 mbar.

6.4.2.3 | Li$^+$ concentration dependency of the ORR mediated by DBBQ in DMSO based electrolyte

The previous results are showing that the mediated ORR is strongly influenced by the cation-DBBQ$^-$ association. Therefore, we investigated the effect of an increasing cation -DBBQ$^-$ association on the ORR in a Li$^+$ containing DMSO based electrolyte. The Li$^+$-DBBQ$^-$ - association is increased by increasing the Li$^+$ concentrations in the DMSO based electrolyte and investigated with cyclic voltammetry. The black traced CVs in Figure 6.9 (a) are normalized to the first reduction wave and show the faradaic current of the DBBQ reduction and oxidation in a deoxygenated solution. In these measurements, the concentration of LiClO$_4$ in DMSO was increased from 0.5 M to 2.5 M (see labeling in Figure 6.9 (a)). The current waves of the first and second reduction step of DBBQ are shifting to more positive electrode potentials as the Li$^+$ concentration in the supporting electrolyte is increased, indicating a stronger Li$^+$-DBBQ$^-$ association

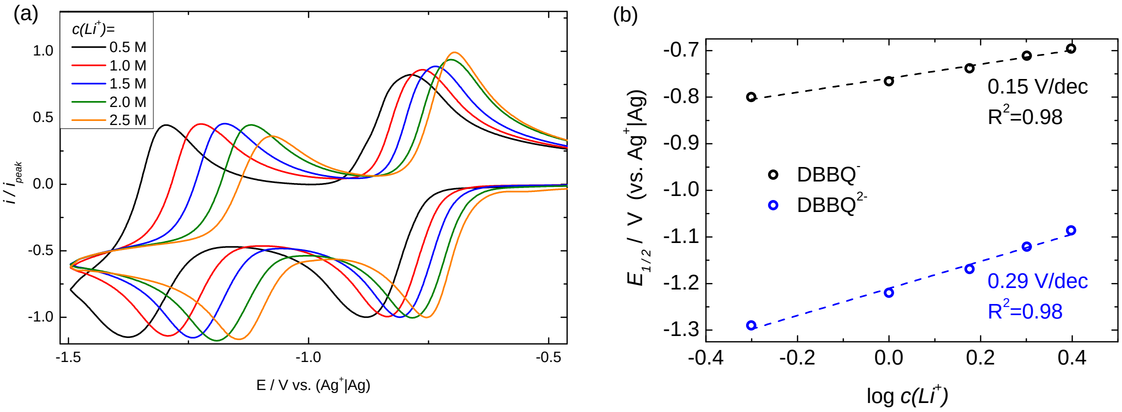

Figure 6.9: (a) CVs for measurements in a deoxygenated DMSO based electrolytes with different LiClO$_4$ concentrations and $v = 10\,\mathrm{mV\,s^{-1}}$. The concentration of LiClO$_4$ is increasing from the top shown measurement to the bottom shown measurement (see labeling in the Figure (a)). The CVs were recorded in the thin layer DEMS cell on a sputtered Au electrode on PTFE. All CVs are normalized to the first reduction peak. (b) Plot of the half wave potentials $E_{1/2}$ of the first DBBQ reduction step (black circles) and the second DBBQ reduction step (blue circles) vs. $\log c\left(\mathrm{Li}^+\right)$. The linear fit through the data points (see dashed lines) as well as the slopes and the adjusted R-square R^2 is included. The data of this plot was extracted from the black traced CVs in Figure 6.9 (a).

The potential shift of the DBBQ monoanion and dianion reduction steps is shown in Figure 6.9 (b) (overall the peak currents of the redox system are decreasing with increasing supporting salt concentration see Figure 6.18 in the Supporting Information). Therein the half wave potential of the first (black circles) and the second (blue circles) reduction step of DBBQ is plotted vs. $\log c\left(Li^+\right)$. As predicted in formula 6.12 $E_{1/2}$ is showing an excellent linear trend with respect to $\log c\left(Li^+\right)$ for both reduction. The slope of the linear fits in Figure 6.9 (b) shows that the potential shift of the second reduction step with 0.29 V/dec is more pronounced than the first reduction step with 0.15 V/dec. From of the slope for the first reduction step it can be estimated that DBBQ$^-$ is associated with 2 to 3 Li^+-cations (see equation 6.12).

To investigate the ORR mediated by DBBQ, the measurements shown in Figure 6.9 (a) were repeated in oxygen saturated solution (see red traced measurements in Figure 6.10). To give the reader a comparison to the deoxygenated solution the measurements shown in Figure 6.9 (a) were also included in Figure 6.10 (see black traced measurement). Moreover, the ORR reduction was also investigated for variously concentrated $LiClO_4$ in DMSO based electrolytes without DBBQ (see blue traced measurements in Figure 6.10). Figure 6.10 (a) is showing the CVs and Figure 6.10 (b) the oxygen fluxes, which were normalized to the diffusion limited oxygen flux through the electrolyte layer. The non-normalized oxygen flux is also shown in Figure 6.17 in the supporting information.

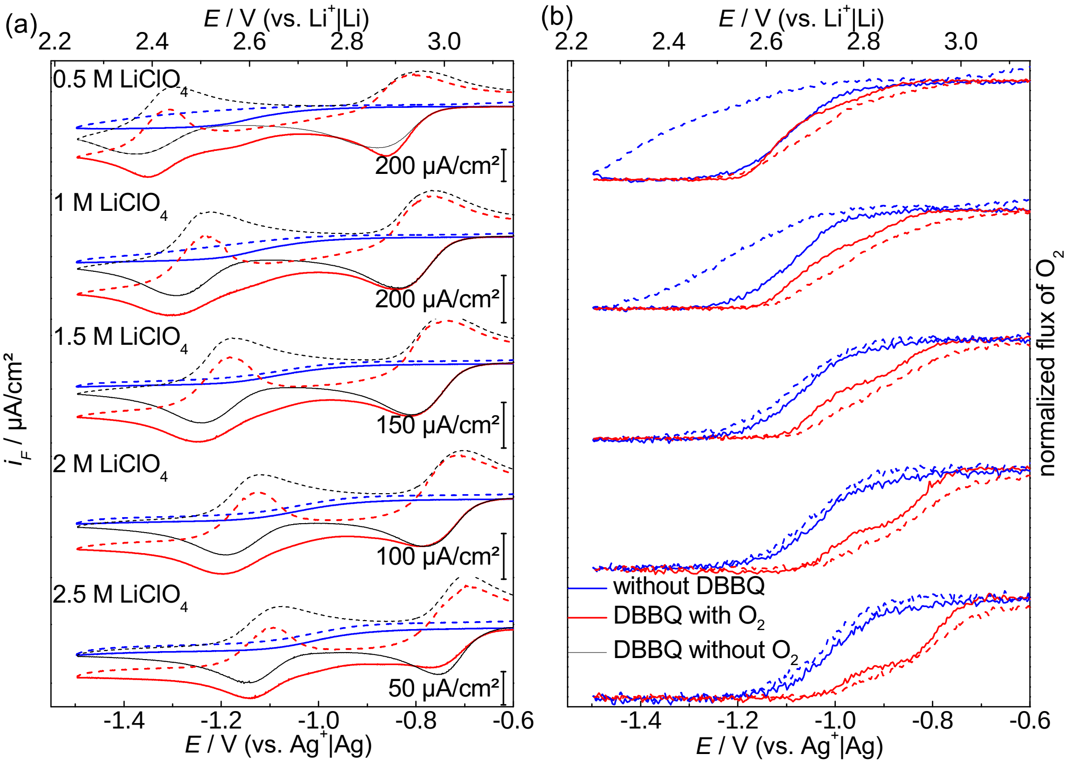

Figure 6.10: CVs (a) and oxygen flux (b) for measurements in a DMSO based electrolytes with different $LiClO_4$ concentrations and $v = 10\,\mathrm{mV\,s^{-1}}$. The concentration of $LiClO_4$ is increasing from the top shown measurement to the bottom shown measurement (see labeling in the figure (a)). The DBBQ concentration in all measurements was 7.5 mM. The oxygen flux into the mass spectrometer was normalized to the diffusion limited oxygen flux through the thin electrolyte layer of the DEMS cell. The solid lines are showing the cathodic sweeps and the dashed lines the anodic sweeps.

First, we will discuss the influence of the differently concentrated $LiClO_4$ electrolytes without DBBQ on the ORR. The waves in cathodic sweep direction of the ORR are undergoing a positive potential shift when the concentration of $LiClO_4$ is increased (see close up of Figure 6.10 in Figure 6.11).

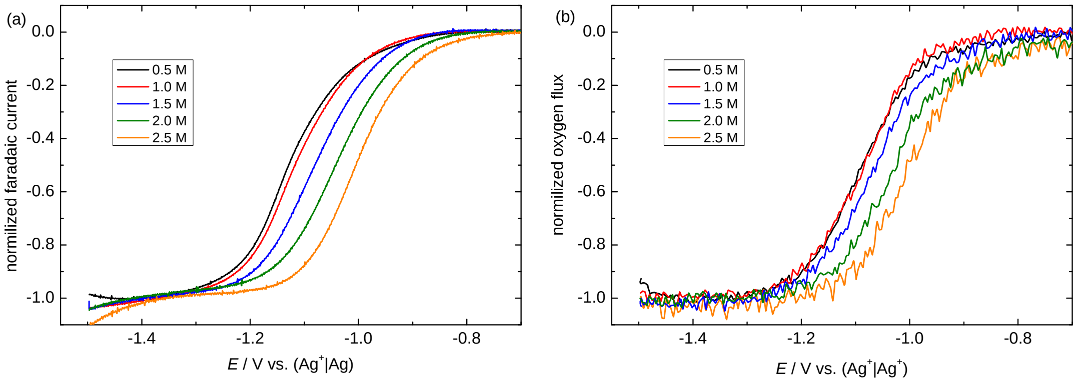

Figure 6.11: Close up to the cathodic sweep of the faradaic current (a) and the oxygen flux (b) in the ORR region of the DBBQ free solution with various $LiClO_4$ concentrations (see caption) shown in Figure 6.10. The currents were normalized to the diffusion limited currents.

Previously Tatara *et al.* investigated the effect of concentrated LiTFSI solution in DMSO on the ORR [258]. With RRDE and Raman studies, the authors found that the amount of LiO_2, as an ORR intermediate, is decreasing in higher concentrated solution. The authors related this observation to the lack of free DMSO in the electrolyte at higher concentration and thus to the lack of a solvent that is able to dissolve LiO_2. We would in addition suggest a second effect that could play a role. The ORR can be described with the following reaction equation:

$$2\,Li^+ + 2\,O_2 + 2\,e^- \longrightarrow 2\,LiO_2 \longrightarrow Li_2O_2 + O_2 \tag{6.17}$$

One identifies LiO_2 as an intermediate in this reaction cascade. The electron transfer to form LiO_2 is occurring at the electrode interface and therefore potential dependent. It was previously shown that the disproportionation of LiO_2 is a first order reaction with respect to the Li^+ concentration [124]. Therefore, a higher Li^+ concentration would increase the LiO_2 disproportionation rate and therefore decrease the concentration of LiO_2 in front of the electrode. The decrease of the LiO_2 concentration would lead to a positive Nernstian shift of the potential of the ORR [129]. Therefore this argumentation would also explain the observations of Tatara *et al.* [258]. There is a third explanation for this potential shift. We previously reported that on Au electrodes we observe a direct reduction of oxygen to peroxide without involving any soluble intermediates [111]. For this reaction one would also expect a Nernstian shift of the reaction with increasing Li^+ concentration.

The influence of the reduced DBBQ species on the ORR in various concentrated electrolytes is best illustrated by comparing the oxygen flux in DBBQ free (see blue traced measurement in Figure 6.10 (b)) and DBBQ containing solution (see red traced measurement in Figure 6.10 (b)). In these measurements, the oxygen flux was normalized to the diffusion limited oxygen flux through the electrolyte layer.

For 0.5 M $LiClO_4$ in DMSO, the oxygen flux in the DBBQ containing electrolyte and the DBBQ free electrolyte are overlapping in the cathodic sweep with respect to the electrode potential (see top measurement in Figure 6.10 (b)). This shows that, the direct oxygen reduction on the Au-surface and the mediated by DBBQ are occurring in the same potential range. As the Li^+ concentration in the electrolyte was increased, the onset of the oxygen consumption in presence of DBBQ is shifting to higher electrode potentials. The same trend was also described in the beginning of this chapter for the potential shift of the DBBQ reduction in oxygen free solution. The comparison to the measurements in DBBQ free electrolyte shows that there is not an as pronounced shift in the ORR as in the DBBQ containing solution. Thus the ORR shift can be explained with the shifted DBBQ reduction. Therefore, for higher Li^+ concentrations the ORR is mainly mediated by DBBQ. This observation also shows, that the ORR is mediated by a $(Li^+)_p$-$DBBQ^-$ ion pairs (p stands for the stoichiometry of Li^+ within the ion pair). This effect is of great interest for the development of a Li-O_2 battery because it shows that one could increase the discharge voltage of a Li-O_2 battery. In addition, this would lower the hysteresis of the discharge and charge plateau in Li-O_2 batteries which is always observed in this battery systems.

The oxygen flux of the measurements in the DBBQ containing electrolytes in Figure 6.10 (b) shows some more interesting details in cathodic direction: For higher Li^+ concentrations the oxygen flux is passing through a shoulder and ends in a diffusion limited current. We believe that the shoulder indicates the ORR mediated by the DBBQ monoanion while the diffusion limited oxygen flux (at Li^+ concentrations higher than 0.5 M) is mediated by the DBBQ dianion and the direct ORR on the electrode surface. The mediation of the ORR by the DBBQ monoanion is passing through a shoulder because the reaction of the ORR is slower than the diffusion of oxygen through the thin layer is occurring.

6.5 | Conclusion

The mediation of the ORR by DBBQ was investigated in TEGDME and in DMSO based electrolytes. Our focus was to examine the impact of the cation on the redox mediation. As experimental techniques, DEMS combined with cyclic voltammetry as well as time resolved oxygen transients through a thin electrolyte layer and RRDE experiments were used. The analysis of time resolved oxygen transients in MS experiments is a new technique to investigate homogeneous reactions that are involving the consumption of a gaseous species. The main results of our study are:

1. We clearly showed that the DBBQ monoanion is responsible for the mediation of the ORR. Herein the formation of a DBBQ$^-$-cation ion pair is necessary to observe an ORR mediated by the DBBQ monoanion, as we could conclude from the absence of the mediated ORR in a TBA$^+$ containing solution.
2. We could show that the rate of first reaction of the postulated mediated ORR $\mathrm{Li} \cdots \mathrm{DBBQ}_{(sol)} + \mathrm{O}_{2(sol)} \rightleftharpoons \mathrm{Li} \cdots \mathrm{DBBQ} \cdots \mathrm{O}_{2(sol)}$ is increasing of factor 80 if the solvent is changed from DMSO to TEGDME. We believe that this reactivity difference is due to the overall higher cation-DBBQ$^-$ association, which can be explained by two physical properties of the solvent that affect ion association:
    a) The permittivity ϵ of DMSO (ϵ (DMSO)=46.7 [259]) differs greatly from the permittivity of TEGDME (ϵ (TEGDME)=7.78 [260]). The critical length of an ion pair can be estimated by calculating the Bjerrums length l_b [261]. Regarding DMSO and TEGDME the Bjerriums lengths are 11.8 Å and 74.8 Å respectively. For separations of cations smaller than l_b the coulomb interactions becomes more significant than the thermal energy. Therefore, the formation of ion pairs is more favorable in TEGDME based electrolytes.
    b) The donor number (DN) of TEGDME (DN (TEGDME)= 12 $\pm$ 4 [102]) is also lower than the DN of DMSO (DN(DMSO)=29.8 [262]. It is known that Li$^+$ (which is a Lewis acid) is stronger interacting with high DN solvents [263]. Computational results of Kwabi *et al.* showed, that the solvation free energy of Li$^+$ is linearly increasing with DN of the solvent [264]. Thus in higher DN solvents the cation solvent association is competing with the DBBQ$^-$ - cation association in equation 6.2.

    Experimental evidences that the ion association of Li$^+$ and DBBQ$^-$ is stronger in TEGDME than in DMSO is again given by the 140 mV positive shift of the first reduction wave of DBBQ in TEGDME compared to the measurement in DMSO.
3. The formation of insoluble reaction products of the ORR mediated by DBBQ was investigated by analyzing the collection efficiency in RRDE experiments. We showed that the formation of insoluble products is faster in Li$^+$ containing TEGDME than in K$^+$ containing TEGDME, which is again in agreement with the strength of ion pairing between the cation of the electrolyte and DBBQ$^-$.

4. Increasing the Li^+ concentration in the supporting electrolyte leads to a positive shift of the ORR mediated by the $DBBQ^-$ and $DBBQ^{2-}$. This was explained by the positive potential shift of the DBBQ reduction due to the ion pairing of the DBBQ-anions Li^+ and the thus resulting positive potential shift of the DBBQ reduction. The theoretical expected shift ($E_{1/2} = const + \frac{RT}{F} p \ln\left(c\left(M^+\right)\right)$) was observed in these experiments. This results in a formation of the redox mediator at more positive electrode potentials.

Acknowledgment

The authors gratefully acknowledge the Federal Ministry of Education and Research (BMBF) for funding this work. This work is part of the LiBaLu-project in the framework of the “Vom Material zur Innovation” -initiative (03XP0029A).

6.6 | Supporting information

Finite difference simulations of DEMS experiments

Simulation of oxygen flux transients through a thin electrolyte layer coupled with a homogeneous reaction consuming oxygen

We implemented a finite difference code in the Julia programming language [180]. To validate our code we used the row expansion published by Wichterlová *et al.* [239]. This series expansion is a solution for the one dimensional diffusion problem in our cell geometry. We already used it to evaluate diffusion coefficients and solubilities of oxygen in different electrolytes in this cell [128, 255]. A modified form of this series expansion, which is also taking the diffusing limited current of the transient into account is given by equation 6.18.

$$\eta(t) = \frac{Ac(\mathrm{O_2})D(\mathrm{O_2})}{h}\left[1 + 2\sum_{n=1}^{\infty}(-1)^n \exp\left(-(\pi n)^2 \frac{t}{6t_c}\right)\right] \tag{6.18}$$

Herein $c\left(\mathrm{O_2}\right)$ is the solubility of oxygen for a given partial pressure of oxygen, $D\left(\mathrm{O_2}\right)$ is the diffusion coefficient of oxygen, A is the cross section area of the thin electrolyte layer and h is the thickness of the electrolyte layer. In Figure 6.12 a comparison of a transient calculated according to equation 6.18 and simulated with the finite difference algorithm is shown. Both transients are in excellent in agreement with each other, which is also illustrated by a maximum deviation of 0.025 % . This shows, that the finite difference code is appropriate working.

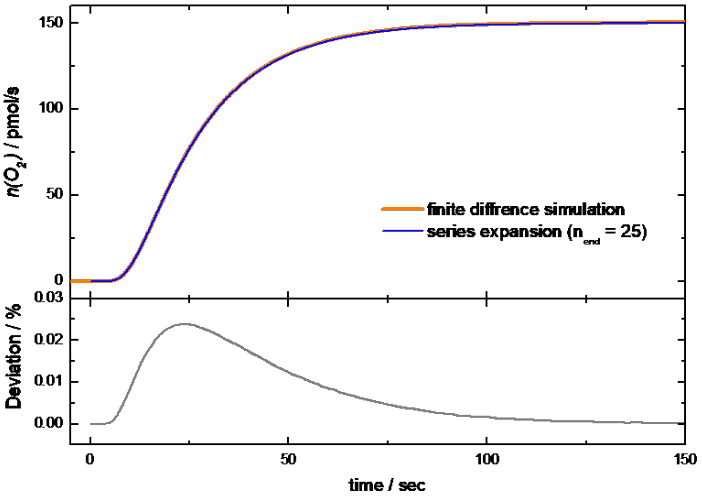

Figure 6.12: Comparison of a transient simulated according to equation 6.18, where the series expansion was aborted for $n_{end} = 25$ (blue) and the transient resulting out of a finite difference simulation (orange). For both transients same parameters were used: h=580 µm, $D\,(O_2)$ = 1.91 · 10^{-9} m^2/s, $c\,(O_2)$ = 1.84 mM and $p\,(O_2)$ = 876.8 mbar. In addition, the deviation of both transients in % is shown ($\frac{n_{\text{series expansion}} - n_{\text{finite diffrence simmulation}}}{n_{\text{series expansion}}}$).

Introducing chemical kinetics into the pressure jump experiments

To give an introduction into the experiment and to discuss the shape of the transients, especially what information we get about the homogeneous reaction, we start with a simpler chemical reaction then expected for the ORR mediation by DBBQ:

$$A_{(\text{sol})} + O_{2\,(\text{sol})} \xrightarrow{k} B_{(\text{sol})} \tag{6.19}$$

Oxygen is consumed in a second order reaction by species A forming B with a reaction rate constant k . For the concentration c and the diffusion coefficient D of oxygen and species A the following assumptions were made:

$$c(O_2) = c(A) = 1\,\text{mM} \tag{6.20}$$

$$D(O_2) = D(A) = 1 \cdot 10^{-9}\,\text{m}^2\,\text{s}^{-1} \tag{6.21}$$

With these parameters we performed finite difference simulations of the pressure jump experiments. We exemplary defined the thin electrolyte layer to be 200 µm thick. In the finite difference scheme the electrolyte layer is separated into 40 elements (“boxes”), which are giving the concentration of all involved species to a given time step.

In the beginning of the finite difference simulation the concentration of species A is in all boxes is 1 mM. The concentration of oxygen is 0 mM. Only in the first box (x =0 µm) the oxygen concentration is 1 mM (t=0, begin of the pressure jump experiment). Oxygen is diffusion through the electrolyte layer as well as consumed by reaction 6.19. The resulting transient is calculated by applying Fick's first law to the last two boxes (x =195 µm and x =200 µm). Figure 6.13 and Figure 6.14 are showing the resulting transients and the concentration profiles of species A and oxygen as well as the resulting transient. The corresponding time of the concentration profiles is displayed as blue circle in the transient. For a better comparison, the transient of the system without taking reaction 6.19 into account is also shown (see black dashed line in Figure 6.13 C and Figure 6.14 C). The reaction rate constant k of reaction 6.19 is in Figure 6.14 500 times faster than in Figure 6.13 ($2 \cdot 10^{-3}$ $M^{-1}s^{-1}$ in Figure 6.13 and k =1 $M^{-1}s^{-1}$ Figure 6.14). The comparison of these two simulations shows, that in the case of the smaller rate constants species A is not completely consumed over the time scale of the experiment. This is resulting in a lower diffusion limited current of the transient compared to the transient without taking the homogeneous reaction into account (see Figure 6.13 C). For the faster reaction rate constant, species A is consumed on the time scale of the experiment. The comparison of the concentrations profiles of oxygen and species A is showing, that the chemical reaction is that fast that the consumption of oxygen by reaction 6.19 is happening first. After all of species A in a volume element is consumed the oxygen molecules can diffuse further into the thin layer. This is resulting in a shift of the transient on the time scale compared to a transient without a homogeneous reaction (see Figure 6.14 C). On a qualitative basis, we also observed the trend of a slower chemical reaction in 0.5 M $LiClO_4$ in DMSO in the presence of $DBBQ^-$ and the trend of a fast chemical reaction in 0.5 M in TEGDME in the presence of $DBBQ^-$ (see Figure 6.4 in the paper).

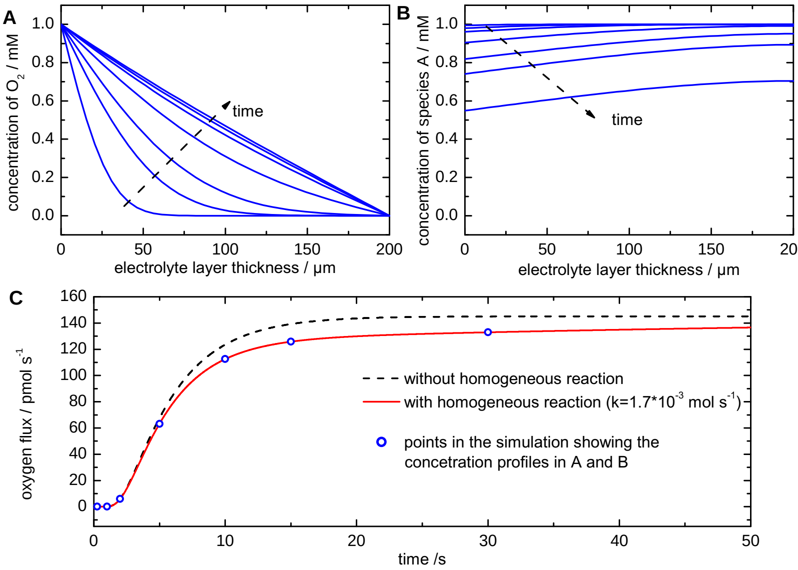

Figure 6.13: Simulated transients for the diffusion of oxygen through a 200 μ m thick layer (dashed line in (C)) and for including reaction (2) with $k = 2 \cdot 10^{-3}$ M^{-1}s^{-1} into the simulation (red line in (C)). The concentration profiles of species A (A) and O$_2$ (B) are also included. The time values of the shown concentration profiles are indicated by blue circles in (C).

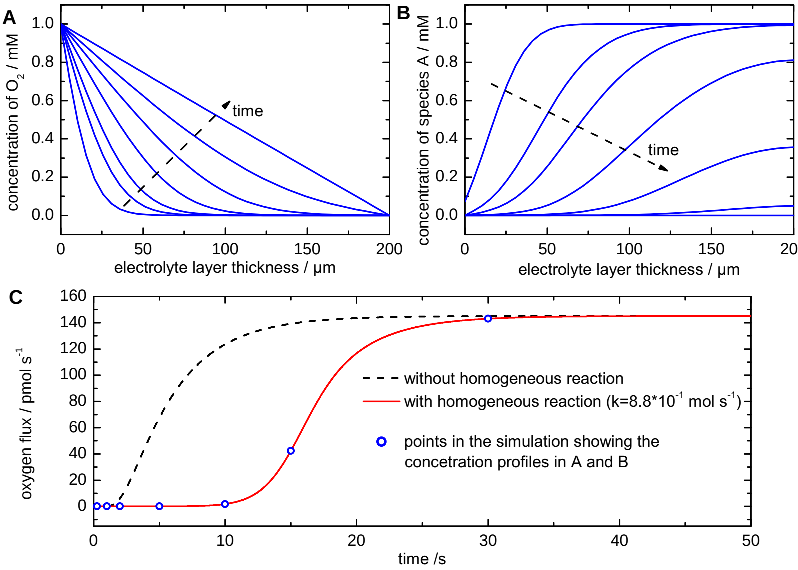

Figure 6.14: Simulated transients for the diffusion of oxygen through a 200 μ m thick layer (dashed line in (C)) and for including reaction (2) with $k = 1$ M^{-1}s^{-1} into the simulation (red line in (C)). The concentration profiles of species A (A) and O$_2$ (B) are also included. The time values of the shown concentration profiles are indicated by blue circles in (C).

Estimating the significance of the received rate constants

To estimate the significance of the received rate constants of the fitting of the pressure jump experiments (see Table 6.2 in the main article) we compared the change of the simulated transients to the experimental transient when changing the rate constants. In detail, we used the rate constants received in the DMSO based measurement with the rate constants received in the TEGDME based measurement and vice versa. Herein the diffusivity of oxygen, the solubility of oxygen and the applied pressure of oxygen is that used one in the TEGDME and DMSO experiment. Thus only the rate constants were changed. Figure 6.15 (a) is showing the experimental oxygen flux transient in 0.5 M LiClO$_4$ in DMSO with 4.6 mM DBBQ$^-$ in the electrolyte. This figure also contains a simulated transient in which the rate constants of the TEGDME based measurement were used (k_1 = 512 s^{-1} M^{-1}, k_{-1} = 371 s^{-1} M^{-1}und k_2 = 3 s^{-1} M^{-1}, see Table 6.2 in the paper). The simulation shows a big discrepancy from the experimental data. We also observe a huge discrepancy if the experimental oxygen flux transient in 0.5 M LiClO$_4$ in TEGDME with 5.8 mM DBBQ$^-$ is compared to a simulated transient in which the rate constants of the DMSO based measurement were used (k_1 = 3 s^{-1} M^{-1}, k_{-1} = 5 s^{-1} M^{-1}und k_2 = 3 s^{-1} M^{-1}), as displayed in Figure 6.15 (b). This shows that the transients are changing dramatically in the range of rate constants, which we received in our fitting procedure. The interpretation to these misfits is that we are indeed observing a deviation in the chemical rate constants of the ORR mediated by DBBQ$^-$ by changing the solvent from DMSO to TEGDME.

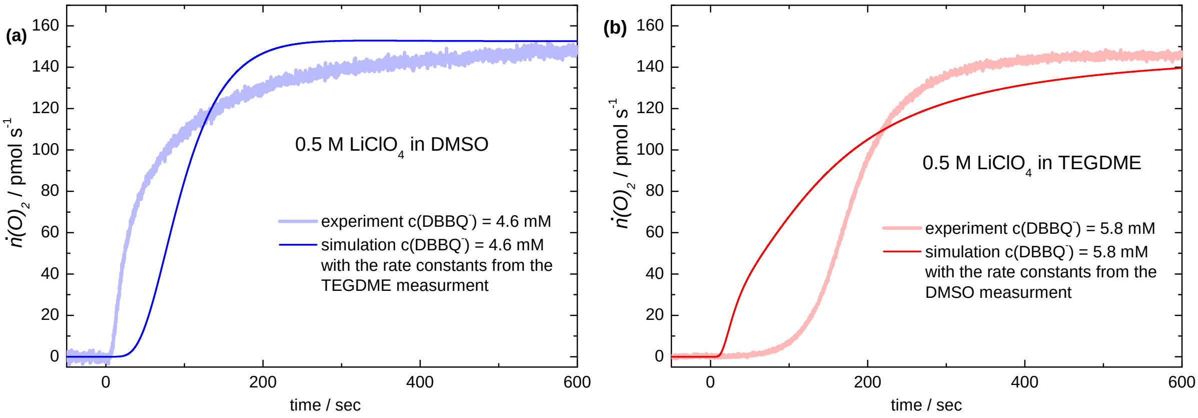

Figure 6.15: Comparison experimental oxygen flux transient in 0.5 M LiClO$_4$ in DMSO to a simulated transient with the rate constants received from the fitting of the TEGDME based measurement (k_1 = 512 s^{-1}M^{-1}, k_{-1} = 371 s^{-1}M^{-1}und k_2 = 3 s^{-1}M^{-1}). (b) Comparison experimental oxygen flux transient in 0.5 M LiClO$_4$ in TEGDME to a simulated transient with the rate constants received from the fitting of the DMSO based measurement (k_1 = 3 s^{-1}M^{-1}, k_{-1} = 5 s^{-1}M^{-1} and k_2 = 3 s^{-1} M^{-1}).

Determining the diffusion coefficient of DBBQ$^-$ in RRDE Experiments

In the finite difference simulations, the diffusion coefficient of DBBQ$^-$ $D\left(DBBQ^-\right)$ is needed. This is also used to have an approximation for $D\left(Li\cdots DBBQ\cdots O_{2(sol)}\right)$. $D\left(DBBQ^-\right)$ was experimentally determined in potential jump experiments at a rotating ring disc electrode (RRDE). In these experiments the potential of the disc electrode is abruptly jumped into a potential window were DBBQ is reduced. The ring potential is held at a potential were the reverse reaction is occurring. For the further evaluation, the resulting ring current transients are of interest. Exemplary two ring current transients for two different rotation rates, recorded in the DMSO based electrolyte are shown in Figure 6.16 (a). Out of the transients the transfer time t_s is extracted, which is the time at which 2% of the diffusion limited current of the transient is achieved (illustrated by arrows in Figure 6.16 (a)). According to equation 6.16 the diffusion coefficient of the transported species can be calculated.

$$t_s = 3.58\left(\frac{\nu}{D}\right)^{\frac{1}{3}}\left(2\pi f\right)^{-1}\left[\log\left(\frac{r_2}{r_1}\right)\right]^{2/3} \tag{6.22}$$

An appropriate way to evaluate the transfer times is to use a plot of $t_s\left(f\right)$ and use the slope of the resulting regression line to calculate D . Figure 6.16 (b) is showing this plot and the expected linear trend with the regression lines for the TEGDME and DMSO based electrolytes. This is resulting in a diffusion coefficient for DBBQ$^-$ in 0.5 M $LiClO_4$ in TEGDME of $0.32\cdot10^{-6}$ cm^2/s and for 0.5 M $LiClO_4$ in DMSO of $1.12\cdot10^{-6}$ cm^2/s.

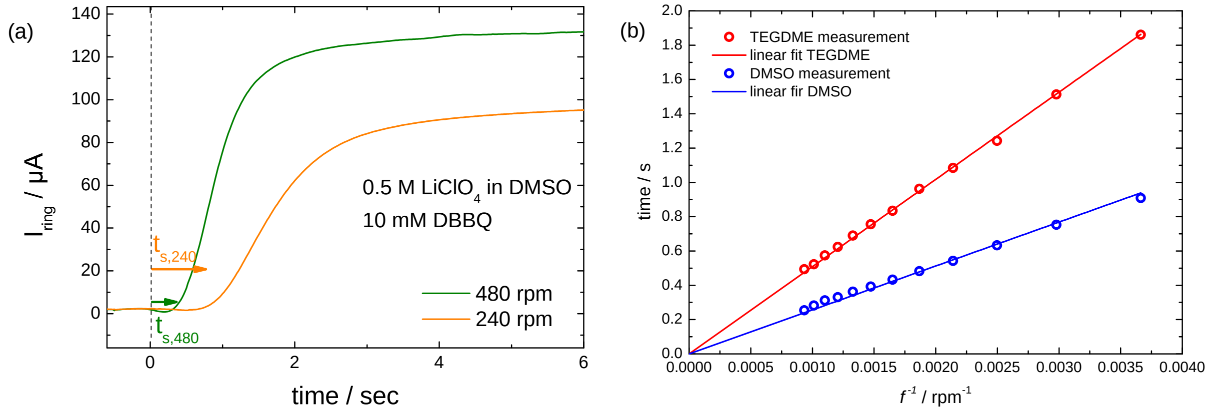

Figure 6.16: (a) Ring current transients for the oxidation of DBBQ$^-$ at the ring electrode after an abrupt potential jump at the disc electrode for two different rotation rates. The potential jump at the disc electrode is performed into a potential window in which DBBQ$^-$ is generated. (b) Plot of the transfer time of DBBQ$^-$ as a function of f^{-1} in the TEGDME and DMSO based electrolyte. The linear regression lines are shown, which are used to calculate the diffusion coefficient of DBBQ$^-$.

The effect of Li^+ concentration on the mediated ORR by DBBQ

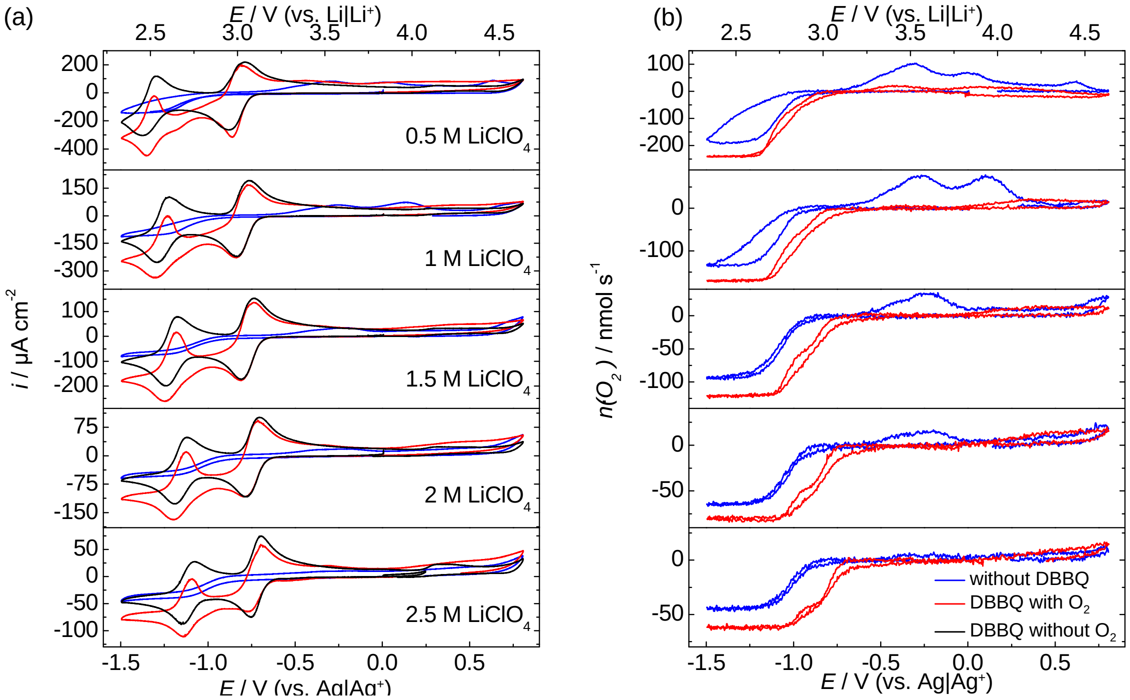

Figure 6.17: CVs (a) and oxygen flux (b) for measurements in a DMSO based electrolytes with different $LiClO_4$ concentrations and $v = 10\ mVs^{-1}$. The concentration of $LiClO_4$ is increasing from the top shown measurement to the bottom shown measurement (see labeling in the Figure (a)).

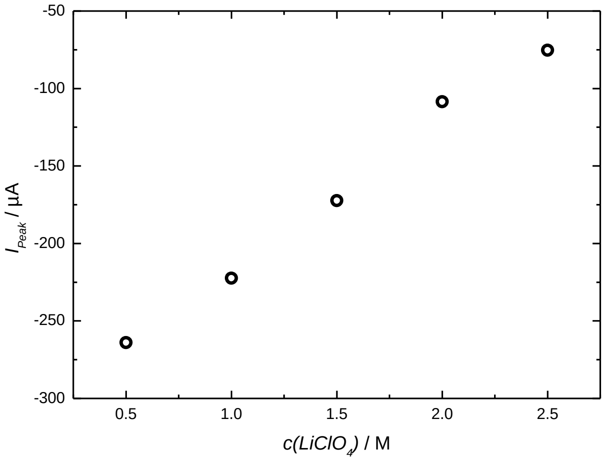

Figure 6.18: Decrease of the first reduction peak of DBBQ in respect to the concentration. The values are taken from Figure 6.17.

Comparison of the cyclic voltammetry of DBBQ in TBA^+ and Li^+ containing electrolyte

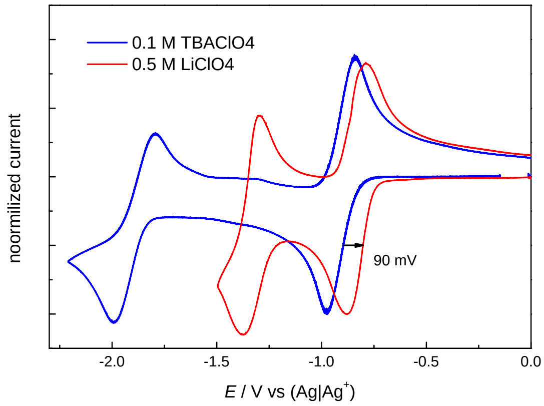

Figure 6.19: CVs, which were normalized to the first reduction, peak of the DBBQ reduction in 0.1 M $TBAClO_4$ in DMSO (blue traced measurement) and 0.5 M $LiClO_4$ in DMSO (red traced measurement). In both cases, an Au electrode was used as working electrode. The CVs were recorded with a sweep rate of 10 mV/s. The electrolytes were deoxygenated.

Comparison of the cyclic voltammetry of DBBQ in TEGDME and DMSO based electrolyte

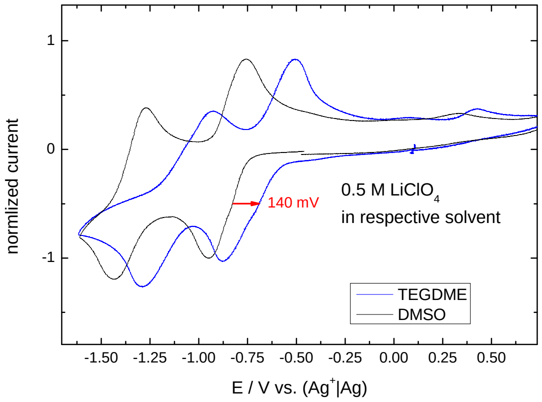

Figure 6.20: CVs, which were normalized to the first reduction, peak of the DBBQ reduction in 0.5 M $LiClO_4$ in TEGDME (blue traced measurement) and 0.5 M $LiClO_4$ in DMSO (black traced measurement). The measurements were taken from Figure 6.5 and Figure 6.8 in the paper. In both cases, an Au electrode was used as working electrode. The CVs were recorded with a sweep rate of 10 mV/s. The electrolyte were deoxygenated.

Oxygen electron numbers in the ORR for various $LiClO_4$ concentrations in DMSO

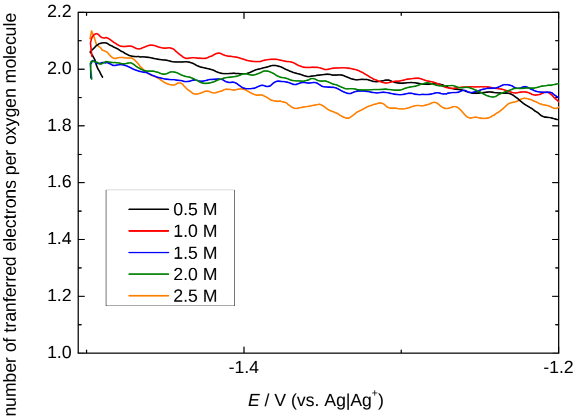

Figure 6.21: Number of transferred electrons per oxygen molecule in the potential window of the ORR from the measurements shown in Figure 6.11 in the paper. The electron number is calculated for various concentration of $LiClO_4$ in DMSO (see caption).

RRDE experiments in deoxygenated DBBQ containing electrolyte

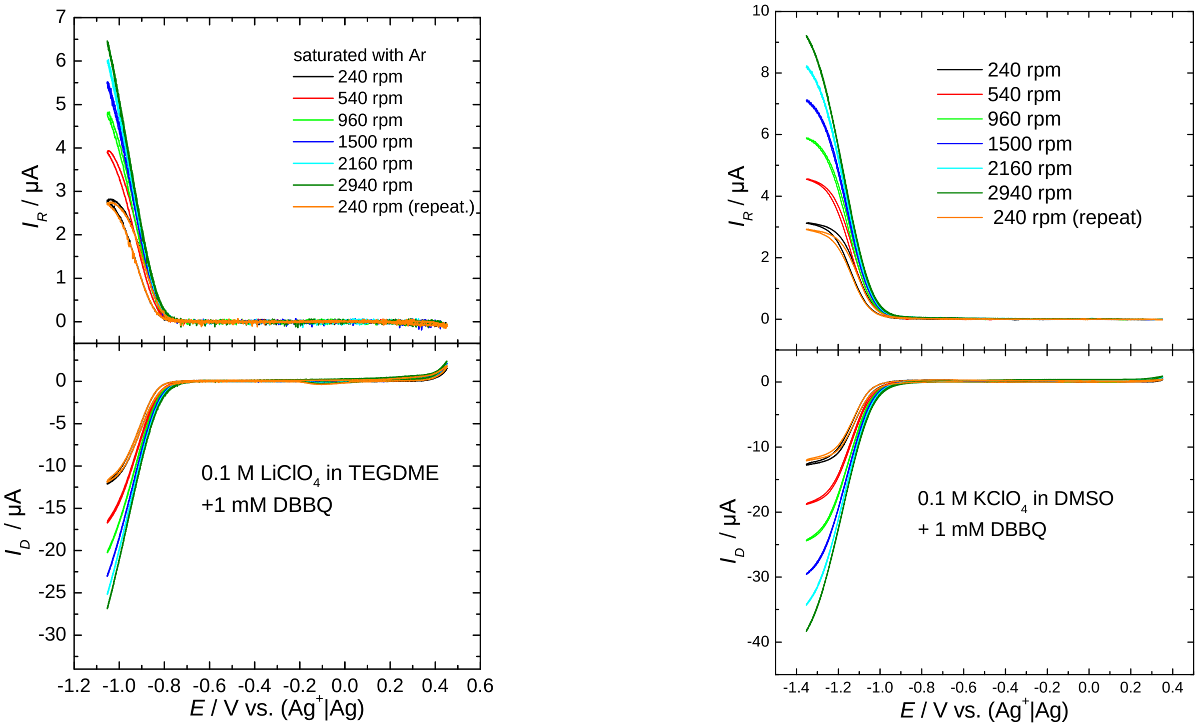

Figure 6.22: RRDE study of the DBBQ reduction in deoxygenated 0.1 M $LiClO_4$ in TEGDME (left figure) and 0.1 M $KClO_4$ in TEGDME (right figure). A Pt-Pt thin gap electrode was used as working electrode. The sweep rate was 10 mV/s. Notice that the diffusion limited current is not reached due to the high potential limit.

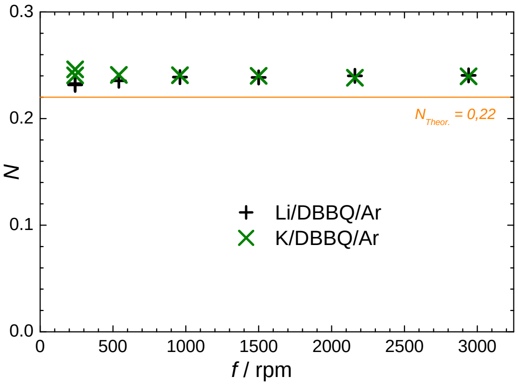

Figure 6.23: Collection efficiency for the measurements shown in Figure 6.22 that show no rotational dependency.

RRDE experiments towards the ORR in 0.1 M $KClO_4$ in TEGDME on a Pt electrode

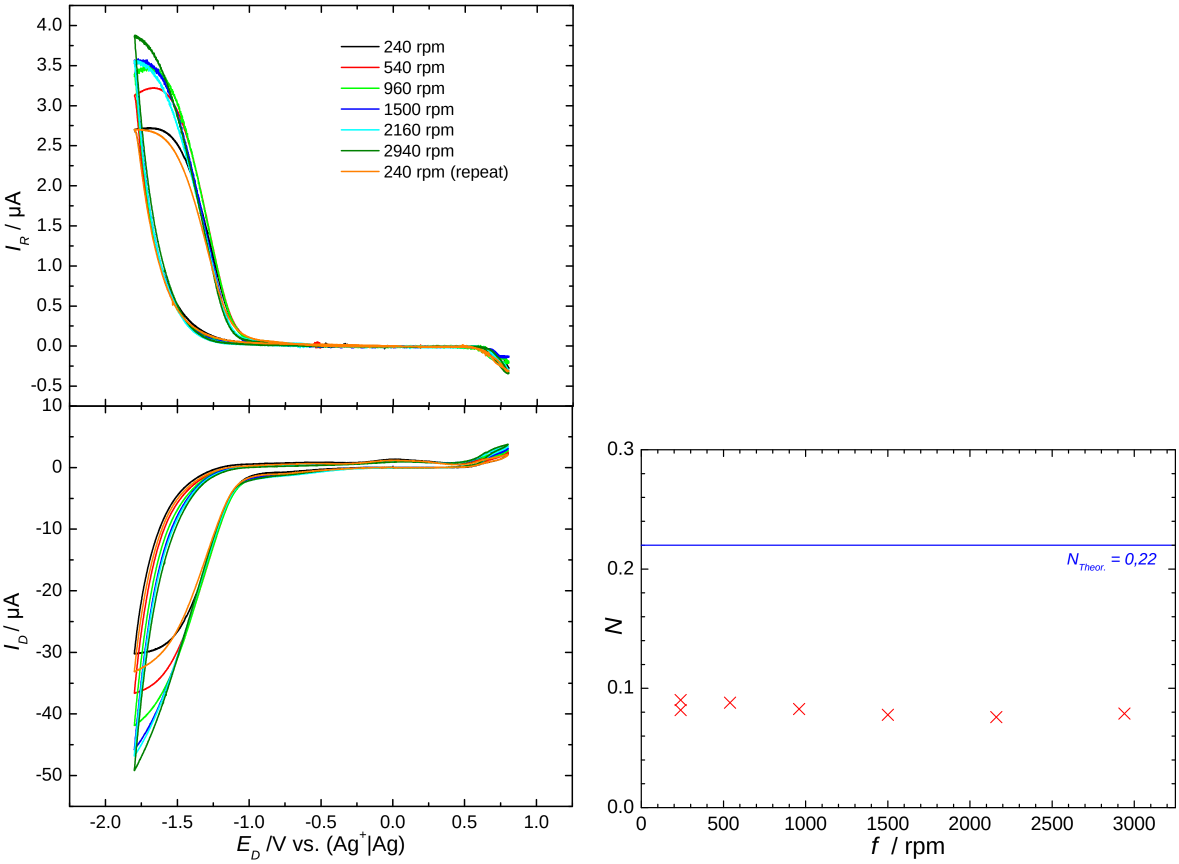

Figure 6.24: RRDE study of the ORR in 0.1 M $KClO_4$ in TEGDME (right figure). A Pt-Pt thin gap electrode was used as working electrode. The sweep rate was 10 mV/s. The right figure shows the collection efficiency as function of the rotation rate from the data of the left figure.

Comments towards the interpretation of the RRDE experiments given in the main manuscript

Within the main manuscript RRDE experiments with the redox mediator DBBQ in presence of oxygen are presented. The aim of these experiments is to show that the mediated ORR is slower in the K^+ containing TEGDME than in the Li^+ containing TEGDME. This is done by analyzing the rotational dependency of the ratio of the apparent collection efficiency N to the theoretical collection efficiency N_0. We performed the analysis on a qualitative basis (no fitting procedure of the experimental data is performed). Still these experiments strengthen the argumentation within the main manuscript, especially in relation to the pressure jump experiments. Due to the complexity of the underlying system, we want do discuss some major points that brought us to the conclusion that by introducing DBBQ into the solution the underlying ORR mechanism is determined by the mediator and not by the direct reduction of oxygen at the electrode.

a) The potential region of the RRDE experiments

A comparison between the RRDE CVs with DBBQ and without DBBQ in the respective solvent is showing that the onset of the DBBQ reduction is positively shifted with respect to the ORR on the platinum electrodes (see Figure 6.25). Especially in the Li^+ containing system the sweep in the presence of DBBQ is performed in a potential region in which we do not observe an ORR current on the Pt electrode. This is less pronounced in the K^+ containing system.

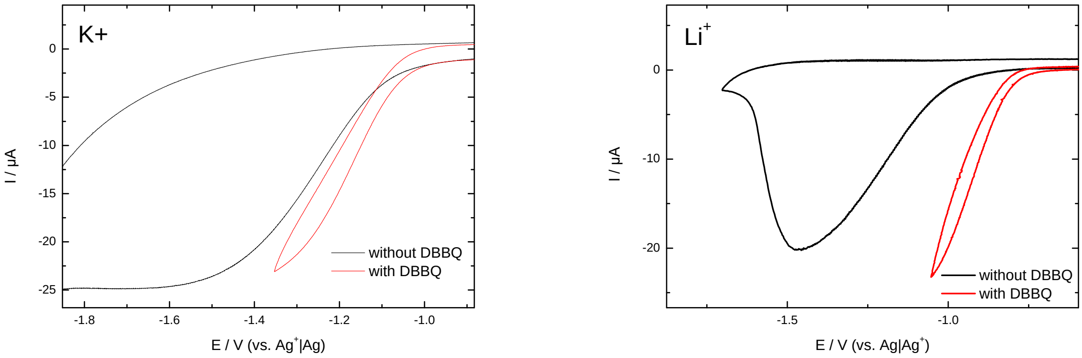

Figure 6.25: Comparison of the RRDE experiments with (red) and without (black) DBBQ in 0.1 M $KClO_4$ in TEGDME (left) and in 0.1 M $LiClO_4$ in TEGDME (right). In both cases, the electrolyte was saturated with 20% O_2 in Ar. The sweep rate was 10 mVs^{-1} and the rotation rate 240 rpm.

b) Concentration profiles

Taking concentration profiles into account it can be shown that, if at the disc electrode a species is generated that is consuming oxygen, it is not likely that oxygen is directly reduced at the disc electrode. This can be done by down breaking the complex reaction mechanism of the mediated ORR into the following reactions:

$$\mathrm{A} + \mathrm{e}^{-} \longrightarrow \mathrm{B}, \text{ at the disc electrode} \tag{6.23}$$

$$\mathrm{B} + \mathrm{O} \longrightarrow \mathrm{A} + \mathrm{X}, \text{ in solution} \tag{6.24}$$

Here A and B are the redox couple DBBQ/DBBQ^{-}, O stands for oxygen and X are the reaction products of the ORR. With the help of finite difference simulations [177] a linear sweep was calculated (see Figure 6.26). Equal diffusion coefficients for all species were assumed.

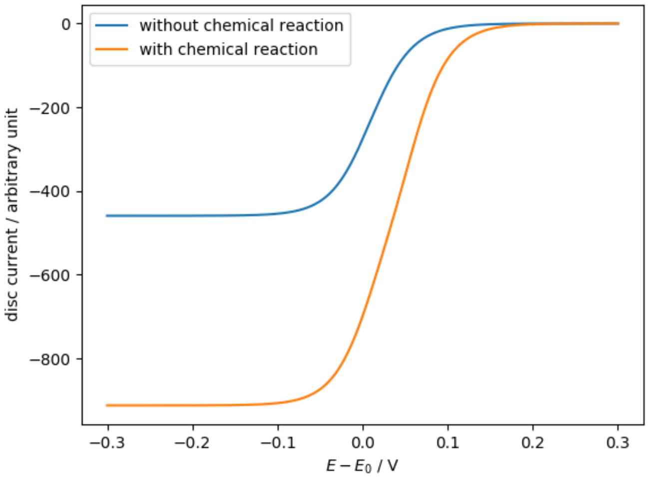

Figure 6.26: Simulated CVs for reaction 6.23 (blue) and for reactions 6.23-6.24 (orange).

The concentration profiles at the end of the sweep are shown in Figure 6.27. In the presence of a homogeneous chemical reaction, the concentration profiles of A and B are steeper than without homogeneous reaction. Moreover, the concentration of O is consumed before reaching the electrode surface. The reaction between O and B is occurring in the volume in front of the disc electrode and not at the disc electrode. In analogy to the DBBQ experiment, this means that oxygen will be consumed before it is reaching the electrode surface and thus the direct reduction of oxygen is not likely to happen.

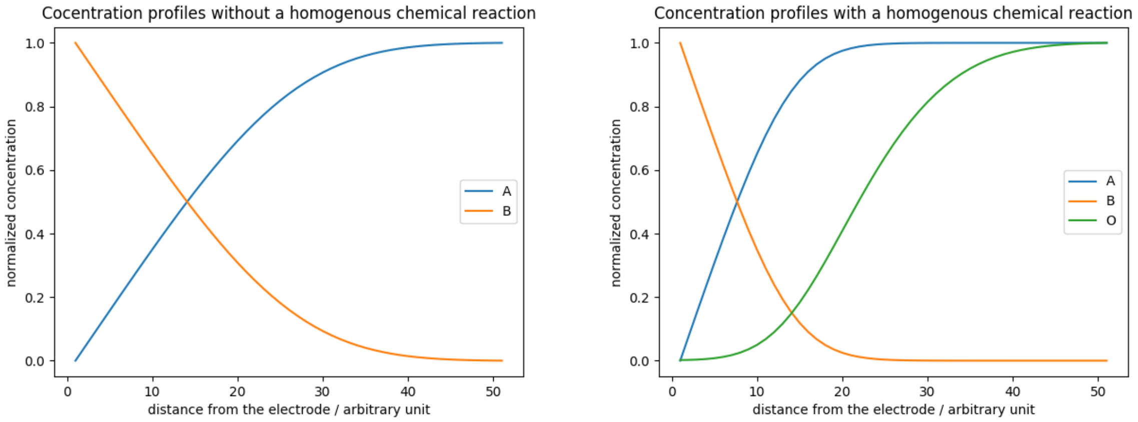

Figure 6.27: Concentration profiles at the end of the sweep (diffusion limited region) for the simulated CVs in Figure 6.26.

c) The apparent collection efficiency

In Figure 6.7 (a) in the main manuscript the change of the apparent collection efficiency (normalized to the theoretical collection efficiency) is shown for the Li^+ and K^+ containing system with and without DBBQ. By adding DBBQ to the electrolyte, one can make two observations:

I) A rotational dependency is observed.

II) The N/N_0 values are in both DBBQ containing electrolytes bigger than without DBBQ.

Both observation give an indication, that there is a complete change in the mechanism by adding DBBQ to the electrolyte.

d) Deposition of solid products

In the field of metal-air batteries, it is well known that the deposition of solid peroxides on the surface during the ORR is leading to an oxidative charge during the positive sweep. Due to the absence of a significant amount of such a charge in the measurements in Figure 6.6 in the paper we conclude that the direct reduction of oxygen at the electrode surface can be neglected. This is due to the large convection in this case.

All in all this discussion is giving strong evidences that only the mediated ORR is investigated in the presence of DBBQ and that the direct reduction of oxygen at the electrode surface can be neglected.

The reference potentials in the different solvents

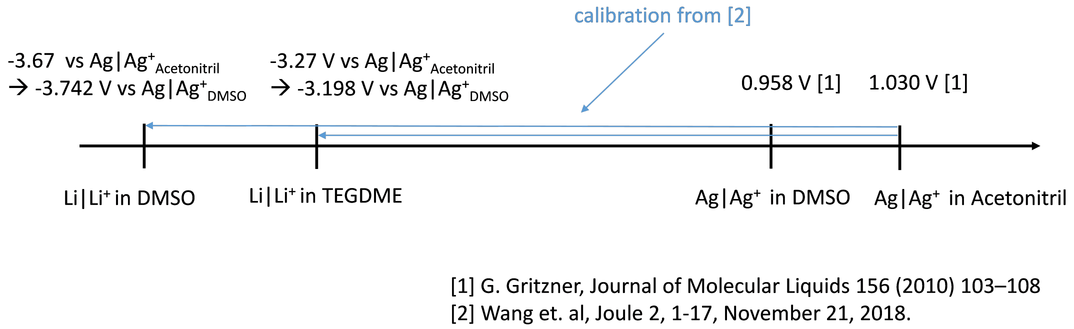

Figure 6.28: Sketch to illustrate the calculation of the reference potentials of Li| Li^+ and Ag| Ag^+ in the different solvents.

7

The ORR in Ca^{2+} containing DMSO: Reaction mechanism, electrode surface characterization and redox mediation

Pawel Peter Bawol*, Philip Heinrich Reinsberg*, Andreas Koellisch-Mirbach*, Christoph Johannes Bondue* and Helmut Baltruschat*

*Institut für Physikalische und Theoretische Chemie, Universität Bonn, Römerstraße 164, D-53117 Bonn, Germany

Uploaded as preprint:
P. P. Bawol, P. H. Reinsberg, A. Koellisch-Mirbach, C. J. Bondue and Helmut Baltruschat, ChemRxiv. Preprint, **2020**, DOI: 10.26434/chemrxiv.12480974.v1

Own manuscript contributions:

- performing parts of the experiments
- data evaluation
- interpretation of the results
- writing the manuscript

7.1 | Abstract

In this study we strengthen our fundamental understanding of the underlying reactions of a possible Ca-O_2 battery using a DMSO based electrolyte. Employing the rotating ring disc electrode, we find a transition from a mixed process of $O_2^{\cdot -}$ and O_2^{2-} formation to an exclusive $O_2^{\cdot -}$ formation at gold electrodes. We will show that in this system Ca-superoxide and Ca-peroxide are formed as soluble species. However, there is a strongly adsorbed layer of ORR products on the electrode surface which is blocking the electrode. Surprisingly the blockade is a partial blockade because the formation of superoxide can be maintained. During an anodic sweep the ORR product layer is stripped from the electrode surface. With X-ray photoelectron spectroscopy the deposited ORR products are shown to be $Ca(O_2)_2$, CaO_2 and CaO as well as side reaction products such as CO_3^{2-} and other oxygen containing carbon species. We will give evidences that the strongly attached layer on the electrocatalyst that is partially blocking the electrode could be adsorbed CaO. The disproportionation reaction of $O_2^{\cdot -}$ in presence of Ca^{2+} was demonstrated via mass spectrometry. Finally the ORR mediated by 2,5-Di-*tert*-1,4-benzoquinone (DBBQ) is investigated by differential electrochemical mass spectrometry (DEMS) and XPS. Similar products as without DBBQ are deposited on the electrode surface. The analysis of the DEMS experiments shows that $DBBQ^{-}$ is reducing O_2 to $O_2^{\cdot -}$ and O_2^{2-} whereas in the presence of $DBBQ^{2-}$ O_2^{2-} is formed. The mechanism of the ORR with and without DBBQ will be discussed.

7.2 | Introduction

To overcome future energy storage problems, several different technologies will be needed, among which batteries will potentially be a key player for mobile applications and transportation. Considering the scarcity of several elements used in today's lithium ion batteries (e.g. cobalt [265]) and, even more importantly, socio-economic impacts of, for example, cobalt mining [266], alternative battery technologies have to be developed to unleash the full potential of electrochemical energy storages. One possibility is to use other chemistries such as metal-air and metal-sulphur, which do not necessarily require the use of cobalt catalysts. Another problem for lithium technology is the lack of the resource lithium and the water consuming mining [12]. Therefore calcium, being the fifth most abundant metal on earth, combines a high abundance with a competitive volumetric capacity of 2072 mAh/cm^3 [267, 268] and thus, is a promising candidate as anode material in future battery applications. Early studies, however, showed the difficulties of Ca plating/stripping [269]. Fortunately, more recent studies revealed electrochemical systems in which the Ca plating/stripping becomes accessible [267, 268, 270, 271].

Combining Ca plating/stripping as anode reaction with an oxygen cathode promises impressive theoretical specific energy densities. This kind of batteries, where a metal anode is combined with an oxygen cathode, was extensively investigated and several combinations of alkali metals and oxygen have been proposed [272–274]. It is interesting that even on good catalysts for the oxygen reduction reaction (ORR) in aqueous media e.g. platinum, where oxygen is reduced to water and thus, the dioxygen bond is broken the situation is completely changing if a non-aqueous electrolyte is used. There the reaction typically stops at the superoxide or peroxide stage. Figure 7.1 is showing the theoretical OCV potentials of the formation of lithium, sodium, potassium and magnesium superoxides and peroxides in comparison to calcium superoxide and calcium peroxide. The resulting theoretical specific energy in Wh/kg is also displayed in Figure 7.1 (see numbers in brackets)

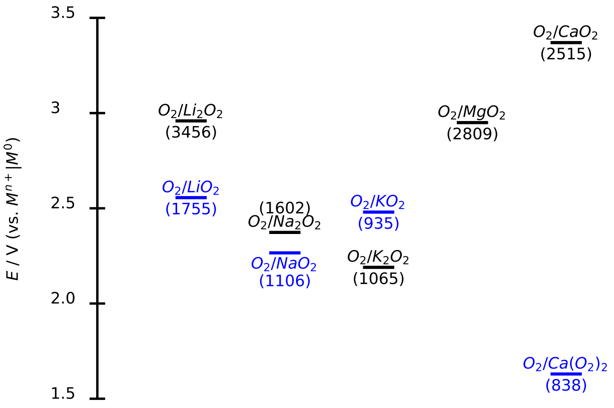

Figure 7.1: Thermodynamics of superoxides and peroxides in comparison to calcium superoxide and calcium peroxide (all in solid state). The standard potentials are given with respect to the corresponding metal of the superoxide/peroxide. Based on these potentials the theoretical specific energy (in Wh/kg) with respect to the mass of the product is displayed in brackets. To our knowledge no thermodynamic data is available for the $O_2/Mg(O_2)_2$ system. Note that the $O_2/Ca(O_2)_2$ system as it was previously miscalculated [97]. The correct value is displayed here.

Figure 7.1 shows, that especially the O_2/CaO_2 system is delivering the second highest theoretical specific energy density for the displayed systems. The $O_2/Ca(O_2)_2$ is showing the lowest theoretical specific energy with 838 Wh/kg. But even this value is higher than the value for the Li Ion technology ($C/LiCoO_2$) with a theoretical specific energy density of 387 Wh/kg [275]. Preceding studies on the oxygen reduction reaction (ORR) and oxygen evolution reaction (OER) in the Ca^{2+} system in DMSO were already done by us [275, 276]. There we observed a significant effect of the electrocatalyst on the ORR mechanism. On Au electrodes the formation of peroxide was observed via differential electrochemical mass spectrometry. In contrast to that, superoxide is the main product on Rh, Pt, Ru and glassy carbon. Further investigations of the system on Pt and glassy carbon electrodes were done using differential electrochemical mass spectrometry (DEMS) in a generator collector arrangement and rotating ring disc electrodes (RRDE). There we found that roughly 90% of the ORR product is soluble $O_2^{\cdot -}$. Taking also the amount of insoluble products into account, we observed a remarkable reversibility for a metal air system of 95% . In addition CV studies unraveled that $O_2^{\cdot -}$ is forming a contact ion pair with Ca^{2+}, which was also found in several other metal-O_2 systems [36, 277].

7.3 | Experimental

Chemicals

Calcium perchlorate tetrahydrate (99 % , Sigma Aldrich) was dried under reduced pressure and T=356 K in a Büchi-oven for 48h. Extra dry DMSO (99.7% , over molecular sieve, Acros Organics) and potassium superoxide (Acros Organics) were used as received. As supporting salt for the reference electrolyte $AgNO_3$ (>99.5% , ChemPure) was used. All electrolyte preparations were made in Ar (Air Liquid, 99.999 %) filled glovebox by GS.

Electrochemical treatment of the noble metal electrodes

Prior to the measurements in the organic solvents the noble metal electrodes (Au and Pt) were checked for cleanness. This was done by cycling the electrode in 0.5 M H_2SO_4 until the typical hydrogen adsorption/desorption region (for Pt) and the oxide formation (for Pt and Au) was observed in the cyclic voltammetry. Afterwards the crystals were washed with MilliQ water (18.2 MΩ) and dried under reduced pressure until further electrochemical measurements were performed.

RRDE Experiments

The RRDE-measurements were performed in a closed H-cell. The H-cell was purged with an Ar-O_2 mixture throughout the experiment to saturate with oxygen and avoid contamination of the electrolyte with water from the ambient air. A silver wire in a solution of 0.1 M $AgNO_3$ in DMSO was used as reference electrode. To avoid contamination of the working electrolyte with $AgNO_3$ the contact between reference electrode and working compartment was established via the wet surface of a closed glass stopcock. The water content of the electrolyte determined via Karl-Fischer titration was typically 40 ppm. A gold-disk platinum-ring electrode with a geometric surface area of 0.196 cm^2 (disk area) and a collection efficiency of 0.25 was used throughout the investigation.

DEMS Experiments

DEMS experiments were performed with a home built differentially pumped mass spectrometer as described by Wolter and Heitbaum [142, 153]. The spectrometer is connected via a flexible vacuum steel rod to a MBraun glove box filled with a 20:80 O_2:Ar atmosphere. The water content in this glovebox never exceeds a value of 0.3 ppm. As electrochemical cell a thin layer DEMS cell, which was optimized for the use in metal-O_2 systems was used. In this cell, we are using a porous Teflon membrane with sputter - deposited Au as working electrode, which is interfacing the vacuum of the mass spectrometer. The wall opposite to the working electrode of the thin layer cell is formed by a porous PTFE membrane interfacing an oxygen atmosphere, thus allowing continuous oxygen flow to the working electrode. Three counter electrodes (Au wires) and a reference electrode are connected via capillaries to the working electrode compartment. As reference electrode a silver wire immersed into a 0.1 M $AgNO_3$ in DMSO is used. The DEMS cell is operated without convection so that reaction products which are soluble in the electrolyte can accumulate in the working electrode compartment (V=5.6 µL). For a more detailed description of the experimental setup, see [58].

XPS analysis

To investigate the chemical state of sample surfaces X-Ray Photoelectron Spectroscopy (XPS) was used. In general the samples are Pt or Au electrodes (d=10mm) which were modified in an electrochemical experiment. The sample electrodes are mounted on a crystal holder manufactured out of steel. After the electrochemical experiment, the samples are washed with dry DMSO (99.7% , over molecular sieve, *Acros Organics*) and mounted into a homemade sample transfer system. This transfer system allows the transfer of a sample between the glovebox and the UHV chamber without contact to air. The XP Spectrometer is part of a homemade UHV chamber with a base pressure of $5 \cdot 10^{-10}$ mbar [172–174]. The used X-Ray source is a non-monochromatized Mg K_α (1253.6 eV) source. As electron energy analyzer a hemispherical electron analyzer (Omnicron NanoTechnology EA 125) is used. Survey spectra were recorded with a pass energy of 50 eV and an energy resolution of 0.5 eV. High-resolution spectra were recorded with a pass energy of 15 eV and an energy resolution of 0.1 eV. To increase the signal to noise ratio, the high-resolution spectra are an average of 9 spectra. By doing this the resolution of our device was determined with 1.07 eV (measured with the FWHM of the Au $4f_{7/2}$ peak). The binding energy was calibrated using the Au $4f_{7/2}$ peak at 83.95 eV or the Pt $4f_{7/2}$ peak at

71.09 eV [278], which were present in all recorded spectra. The XPS measurements were accompanied by Ar^+-etching (Physical Electronics Model 04-191, 3 kV, $I_{emission}$=25 mA, I_{sample}=1 µA) The electrochemical experiments were performed in a Glovebox filled with a 80:20 Ar: O_2 mixture. The humidity in the glovebox never exceeded a value of 0.3 ppm. Our experiments showed that the deposited films of electrically non-conducting species is thin and in good contact with the conducting Au or Pt crystal. Therefore, no charge compensation with an electron flood gun was needed.

7.4 | Results and Discussion

7.4.1 | RRDE and DEMS investigations of the ORR in Ca^{2+} containing DMSO

The ORR at a gold electrode in 0.1 M $Ca(ClO_4)_2$ is shown in Figure 7.2. After a rise in current at a potential of −0.8 V, a plateau is observed for a rotation rate of 4 Hz, which is close to the diffusion-limited current for a two-electron reduction of oxygen and thus agrees well with the previous observations made in the DEMS flow-through cell [276].

However, after a charge flow of 8200 $\mu C\,cm^{-2}$, the current starts to become less negative at a potential of −1.29 V and reaches a second plateau, which agrees well with the diffusion-limited current of the one-electron process and is also reflected in the share of superoxide (Figure 7.2 c). This is in principle reminiscent of the ORR in Li^+-containing DMSO, where a transition to superoxide formation was observed after the electrode was partially blocked by Li_2O_2 [111, 155]. However, a major difference between these measurements is the large charge which can be passed before this transition occurs: Even if the charge detected at the ring electrode is subtracted (2500 $\mu C\,cm^{-2}$), the remaining charge is still 5700 $\mu C\,cm^{-2}$ and thus in the order of several monolayers. Since it is well known that insoluble peroxides and superoxides are insulating and thus poisoning the electrode surface, this result implies that in fact most of the reduction charge is passed into soluble species. Considering that the charge detected at the ring only accounts for a small portion of the produced species, this can only be understood by assuming that the soluble species are not readily oxidizable at the ring [279]. Here we want to point out that the previously reported CVs in the DEMS cells showed a plateau for the $2\,e^-/O_2$ process in the ORR [97]. This difference to the measurement shown here is due to the higher convection in the RRDE experiment and thus a higher flowing charge which is sufficient to poison the electrode and trigger the transition from the $2\,e^-/O_2$ process to the $1\,e^-/O_2$ process.

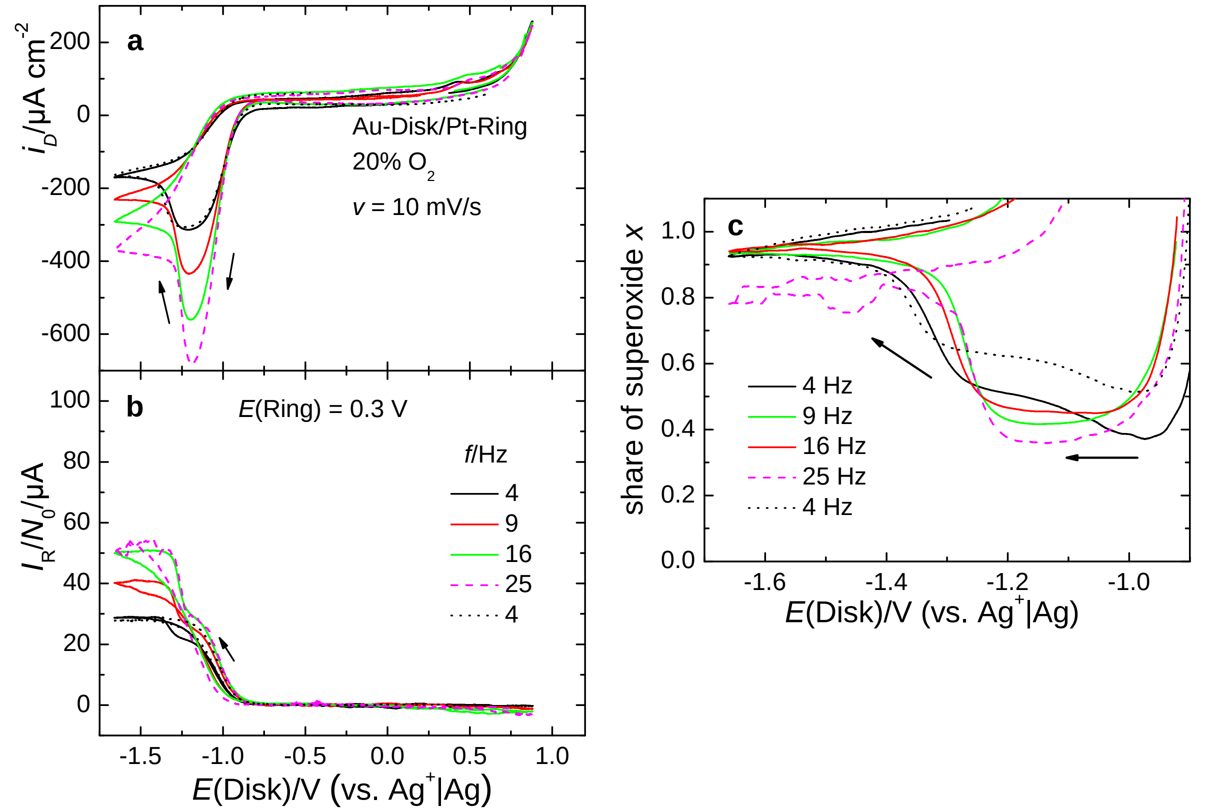

Figure 7.2: ORR in presence of Ca^{2+} at a gold-RRDE. (a) Currents at the gold-disk. (b) Corresponding currents at a platinum-ring. (c) Share of superoxide. Electrolyte: 0.1 M Ca(ClO$_4$)$_2$ in DMSO. A(Disk)= 0.196 cm^2, N_0=0.25.

Using the DEMS thin layer cell in stagnant electrolyte, it can also be shown that the peroxide formed during the ORR is soluble in the DMSO-based electrolyte by examining the electron number of the OER was examined (see Figure 7.3, the oxidation of a peroxide corresponds to a two-electron process). To probe for soluble, reduced oxygen species, the experiment was carried out as follows: First, the potential was swept to -1.5 V, where it was kept for 500 s and roughly 170 nmol of O$_2$ were reduced. Then, the electrolyte was exchanged and the potential was stepped to -0.5 V, before it was cycled to 0.75 V. The amount of O$_2$ evolved during the anodic sweep is only 1.5 nmol. In contrast to this, the amount of O$_2$ reduced in an experiment without a potential stop and without electrolyte exchange is 42 nmol and the amount evolved is 12 nmol (the difference between ORR and OER charge is probably caused by the transport of the soluble species into the capillaries of the cell). The large discrepancy between OER and ORR charge in the case of electrolyte exchange implies that the peroxide-species (as indicated by the two-electron process during reduction as well as oxidation) are at least partially soluble.

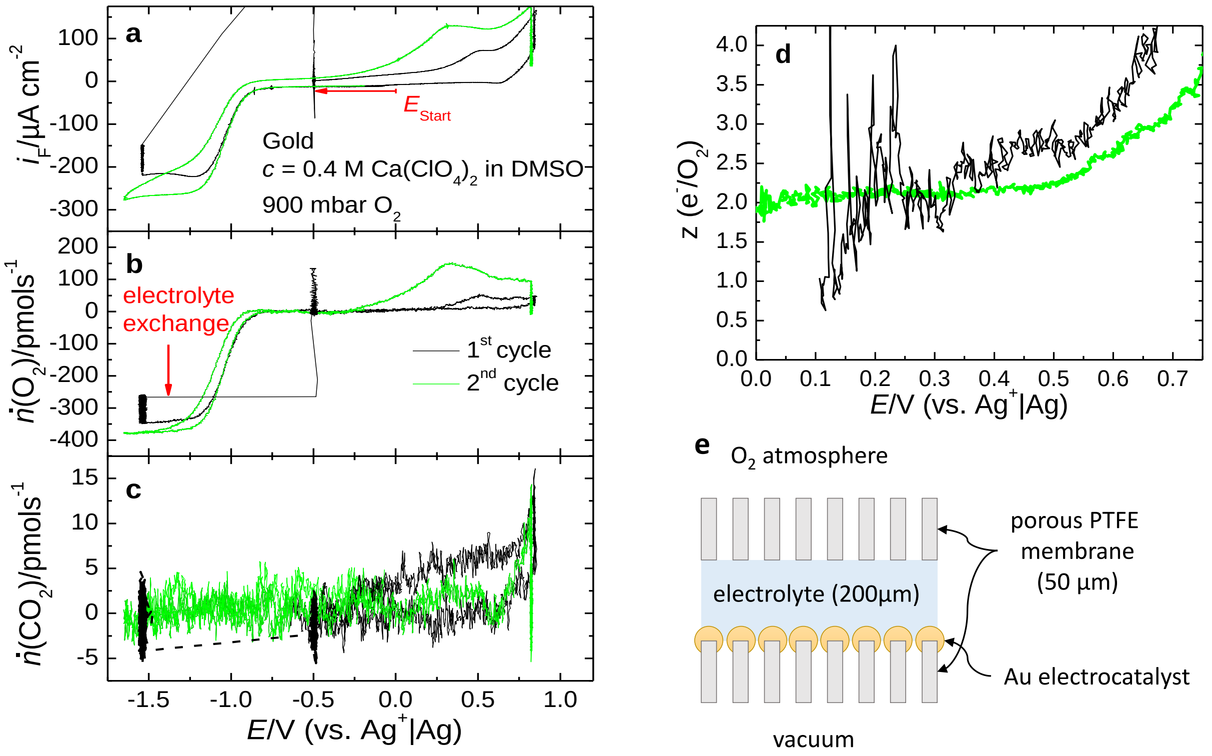

Figure 7.3: Thin-layer DEMS-measurement of ORR on porous Au/PTFE in presence of Ca^{2+}. (a) Currents at the gold working electrode. (b) Corresponding flux of oxygen. (c) Corresponding flux of CO_2. (d) Number of electrons transferred per evolved molecule of O_2. Black: After holding the potential for 500 s at -1.5 V, the electrolyte was exchange under potential control and then stepped to -0.5 V before continuing cycling. Green: DEMS measurement without potential step and without electrolyte exchange. Electrolyte: 0.4 M $Ca(ClO_4)_2$ in DMSO, 900 mbar O_2. The diffusion limited currents for oxygen consumption in the absence of convection is due to the special thin layer construction of the cell. (e) Cross section of the components that form the electrolyte volume of the thin layer cell. For more details about the DEMS electrochemical cell, see [58].

Since we have shown that the ORR products are soluble, it has to be shown if it is possible to reactivate the electrode by dissolving the ORR products. The reactivation of the electrode was investigated with the RRDE. The convection induced by the RRDE should favour the dissolution of the ORR products. The electrode was first blocked by a potential stop in the ORR. Then a CV was recorded in the potential range of the ORR (see Figure 7.4 (a)). Even with a blocked electrode we observe a faradaic current for the ORR. An explanation for this might be the electro migration of ions through the blocking insulating layer if higher field strengths are applied as we previously reported for the ORR in Mg^{2+} containing DMSO [247]. The potential window is successively opened positively by 100 mV. Reaching a potential of 0.3 V for the upper limit, the reactivation of the electrode can be recognized by an increase in the reduction current of the ORR (see arrows in Figure 7.4). At the same time, an oxidation peak is obtained at 0.3 V, which can be attributed to the oxidation of products deposited on the electrode (see magnification of the OER region in Figure 7.4). A further opening of the potential regenerates the electrode completely and shows the necessity of applying higher potentials for the reactivation of the electrode. This measurement shows that the electrode is not regenerated although the ORR products are soluble. simple by dissolution of the ORR products, but that a blocking surface layer (possibly an adsorbate) remains on the surface which can only be stripped at potentials around 0.3 V. In the first cycle reaching this potentials, this stripping is rather incomplete, as can be seen in the subsequent sweep into the ORR region. The more the blocking is lifted, the larger grows the corresponding oxidation peak and also shifts to lower potentials. This is indicative of a nucleation and growth behaviour: Oxidation of this layer is slow and only occurs at defects on the boundary between the layer and the free surface sites. As the disc electrode is reactivated the amount of detected superoxide at the ring electrode is increasing (see Figure 7.4 (a)). For the completely reactivated electrode (see black traced measurement in Figure 7.4 (a)), again a transition from the peroxide formation to the superoxide formation is observed, as can be seen in the share of superoxide in see Figure 7.4 (b). For a partially blocked electrode (see orange traced measurement in Figure 7.4 (a)) the formation of superoxide is shifting 200 mV in positive direction (see orange trace share of superoxide in Figure 7.4 (b)). This is showing, that the peroxide formation preferentially is occurring at active sites on the electrode, which are already blocked in the orange trace measurement and thus the superoxide formation is starting earlier during the sweep.

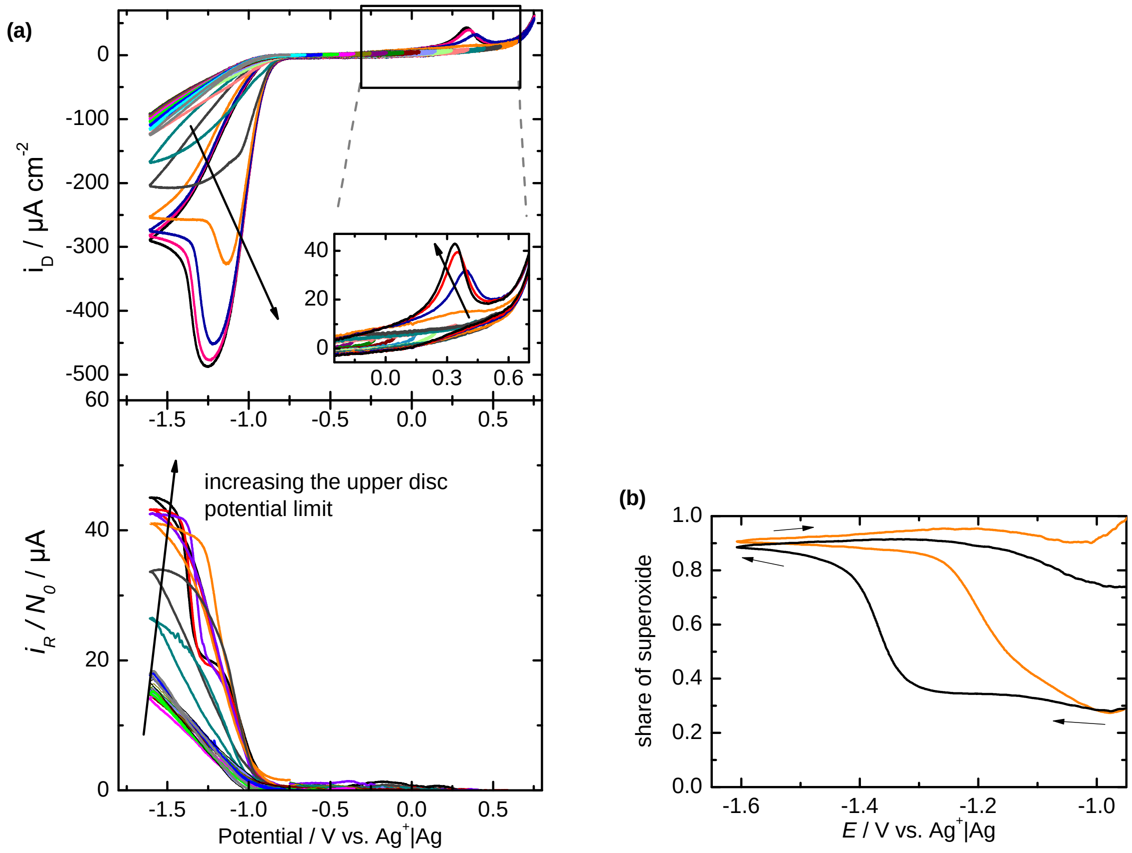

Figure 7.4: (a) RRDE study with a partially blocked Au electrode with $v = 20\,\mathrm{mV\,s^{-1}}$. The upper potential limit is increased by 100 mV per cycle. The dashed arrows indicate the reactivation of the electrode due to a potential opening. In all measurements 0.1 M Ca(ClO$_4$)$_2$ in DMSO with 20% O$_2$ was used. The rotation frequency is 9 Hz. The roughness factor of the disk electrode was 3. (b) Calculated share of superoxide for the black and orange traced measurement in (a) in the potential range of the ORR.

7.4.2 | Disproportionation of superoxide in the presence of Ca^{2+}

Another known reaction in non-aqueous metal air batteries is the disproportionation of the superoxide. The common procedure to test if superoxide is undergoing a disproportionation in the presence of a cation of interest is to use a solution of the stable superoxide compound KO$_2$ (in this study: KO$_2$ in DMSO) and add a solution containing the cation of interest (in this study: Ca(ClO$_4$)$_2$ in DMSO [118, 124, 280]. The products of the disproportionation of O$_2^{\cdot -}$ are O$_2^{2-}$ and O$_2$. Hence, this reaction can be followed by measuring the ionic current of mass 32 as shown in Figure 7.5.

After adding 3 mL of 1 M Ca(ClO$_4$)$_2$ in DMSO to 0.1 g KO$_2$ in 25 mL DMSO we observe an increase of the ionic current of mass 32. Further on the ionic current of mass 32 is going through

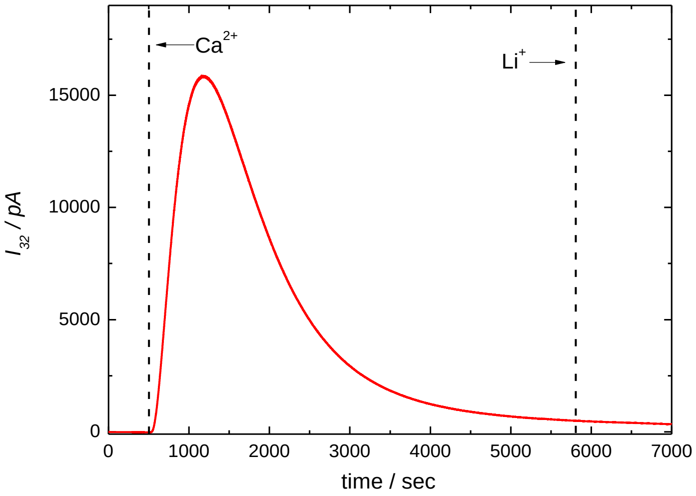

Figure 7.5: Ionic current of mass 32 (red) as a function of time. The gas phase over a stirred solution containing 0.1 g KO_2 in 25 mL DMSO was analyzed by MS after adding 3 mL of 1 M $Ca(ClO_4)_2$ and 1 M $LiClO_4$ in DMSO. The time at which the Ca^{2+} and Li^{+} containing DMSO were added, are indicated as dashed line in the graphs. For details on the experimental setup see Figure 7.11 in the supporting information.

a maximum and fading within 2h. This shows that $O_2^{\cdot -}$ is undergoing disproportionation in the presence of Ca^{2+}. Adding again 3 mL of 1 M $LiClO_4$ in DMSO to the solution is not increasing the ionic current of mass 32 further, which shows that the disproportionation of $O_2^{\cdot -}$ was finished. Otherwise, addition of Li^{+} should lead to another increase in the signal on mass 32 as the remaining superoxide will disproportionate under the formation of O_2 and insoluble Li_2O_2.

Astonishingly, parallel to oxygen formation, ion current transients corresponding to volatile species like H_2O (m/z:18), H_2CO (m/z:30), CO (m/z:28), CO_2 (m/z:44) and SO_2 (m/z:64) were observed (see Figure 7.12 in the supporting information). To our knowledge this was not reported so far in this kind of experiments or in DEMS experiments in metal-air systems during the ORR. A reason why we are observing these signals might be the sensitivity of our experiment, which was optimized by using the differentially pumped vacuum system as well as a relatively high pressure in the vacuum system that was adjusted by the leak valve. The formulation of a mechanism how these compounds are formed during disproportionation is currently not possible. The most plausible source would be a side reaction with singlet oxygen, which was observed as a by-product of disproportionation reaction in presence of various cations in significant amounts [116, 118]. Due to the high reactivity of singlet oxygen, it is plausible that DMSO is decomposed in a follow-up reaction under generation of the above species. Another side product of the disproportionation that was already reported is CO_3^{2-} [118, 119]. We prove the presence of carbonates after the disproportionation we proved by acidifying the solution with H_2SO_4 and observing a CO_2 formation from the chemical reaction as it was also done by Mahne *et. al.* [116] (see Figure 7.13 in the supporting information).

7.4.3 | XPS studies of the electrode surfaces

The Pt and Au electrode after the ORR are characterized by XPS at various stages of Ar$^+$-etching to get insights into the depth-profile of elemental distribution of the deposited film. The electrochemical experiments prior to the XPS measurements are described in the supporting information.

First of all the survey spectra of the Pt electrode after the ORR and after the OER are displayed in Figure 7.6.

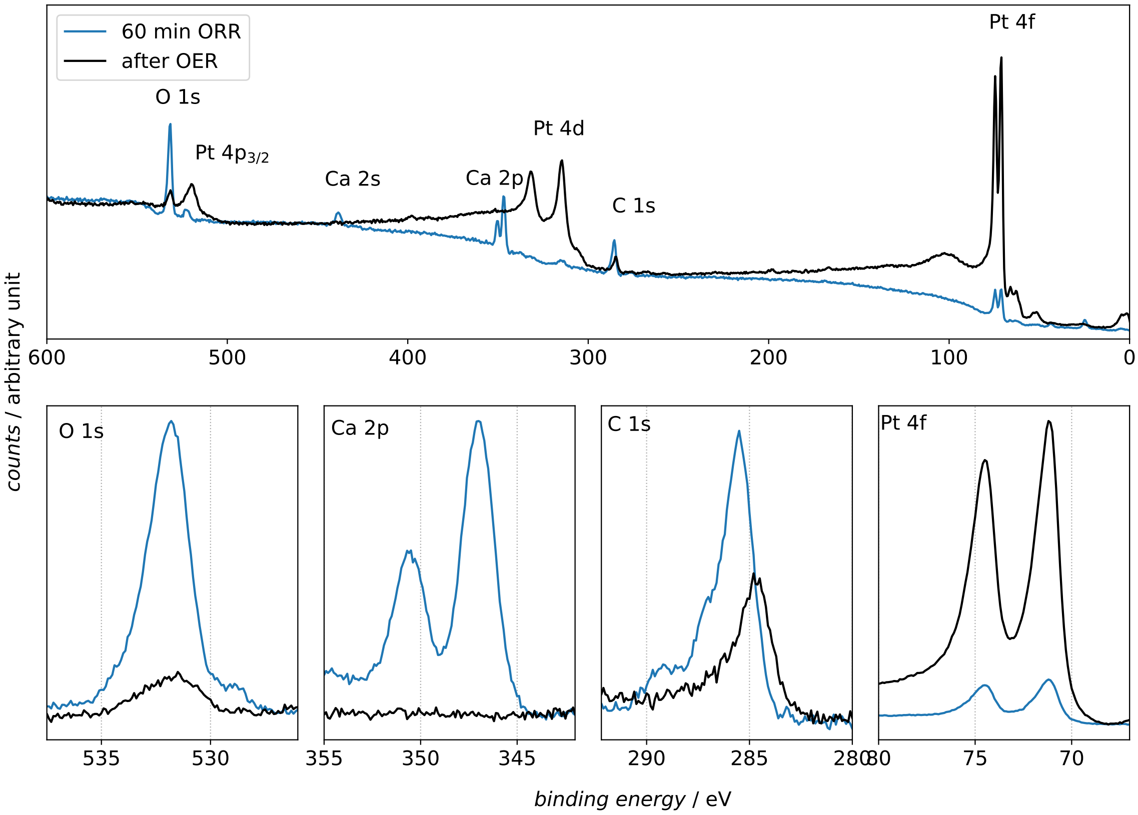

Figure 7.6: Top figure: Survey spectra of a Pt electrode after performing the ORR at -1.5 V vs Ag$^+$| Ag for 60 min (blue line) and after sweeping the potential into the OER (black line). Bottom figures: High-resolution XP spectra of the O 1s-, Ca 2p-, C 1s- and Pt 4f-region. The associated electrochemical experiment is shown in the supporting information.

After holding the electrode potential in the ORR region, the spectrum for the Pt electrode surface mainly shows peaks at binding energies that contribute to the core levels of carbon, calcium and oxygen. The Pt peaks are also visible in the measurement after the ORR and especially the 4f peaks of Pt show an interesting feature: The increase of the intensity towards higher binding energies after the 4f peaks is an indication of inelastic scattering of the Pt 4f electrons. This shows that Pt is buried under a layer of precipitated products of the ORR [281]. Also in the region in which the Pt 4d peaks are expected to appear (between 315 and 332 eV binding energy) the baseline is increasing. This is again showing that the X-rays excite the Pt 4d core levels and that the emitted photoelectrons are inelastically scattered as they are passing through the deposited thin layer. We made the same observation using an Au electrode see Figure 7.15 in the supporting information. Due to the surface sensitivity of the XPS experiment and the fact that the 4f peaks of the electrode material is observed is giving evidence that a thin film is deposited on the electrode surface. After a sweep into the OER region, the Pt peaks are largely increased, indicating that the surface now is only covered by a very thin film. This will be discussed below.

High-resolution XP spectra of the O 1s, the Ca 2p the C 1s as well as the 4f peaks of the electrode material (Au and Pt) were recorded and are shown for different Ar^+ etching times in Figure 7.7. In addition a literature survey on binding energies of CaO, $Ca(OH)_2$, $CaCO_3$ and CaO_2 was done. The results are plotted in the first row of Figure 7.7. The solid dots in Figure 7.7 are indicating the average of the binding energies available in literature, while the error bar denotes the standard deviation. The values used and references are summed up in the supporting information. Figure 7.7 also shows common binding energies of different carbon species.

Comparing the XP spectra in Figure 7.7 for the Pt and the Au electrode after the transfer and after 5 min Ar^+ treatment shows that the O 1s and Ca 2p peaks are observed at similar binding energies on the different electrode materials. This is an indication that the same species are deposited on both electrode materials. Only in the C 1s region in the spectra collected on the Pt electrode a shoulder is visible at a binding energy of 287.3 eV, indicating that more C-O-C and C-OH species are present on the surface. The comparable chemical state regarding the calcium oxygen compounds of the film deposited during ORR becomes clearer in Figure 7.8, where the O 1s and Ca 2p XP spectra after 5 min Ar^+ etching for the Au and the Pt electrode are plotted. The O 1s regions of the peak at a binding energy of 532.3 eV are overlapping. This shows that the same amount of oxygen is present in both experiments. The rather large FWHM of 2.34 eV of the peak at 523.3 eV indicates that this peak probably contains excitations from the O 1s core level out of different chemical environments and thus, different chemical compounds. In both spectra, the additional small peak at a binding energy of 529.5 eV shows the presence of another oxygen species with a higher electron density on both electrode materials. The peaks in the Ca 2p region are also appearing at the same binding energies again indicating that the

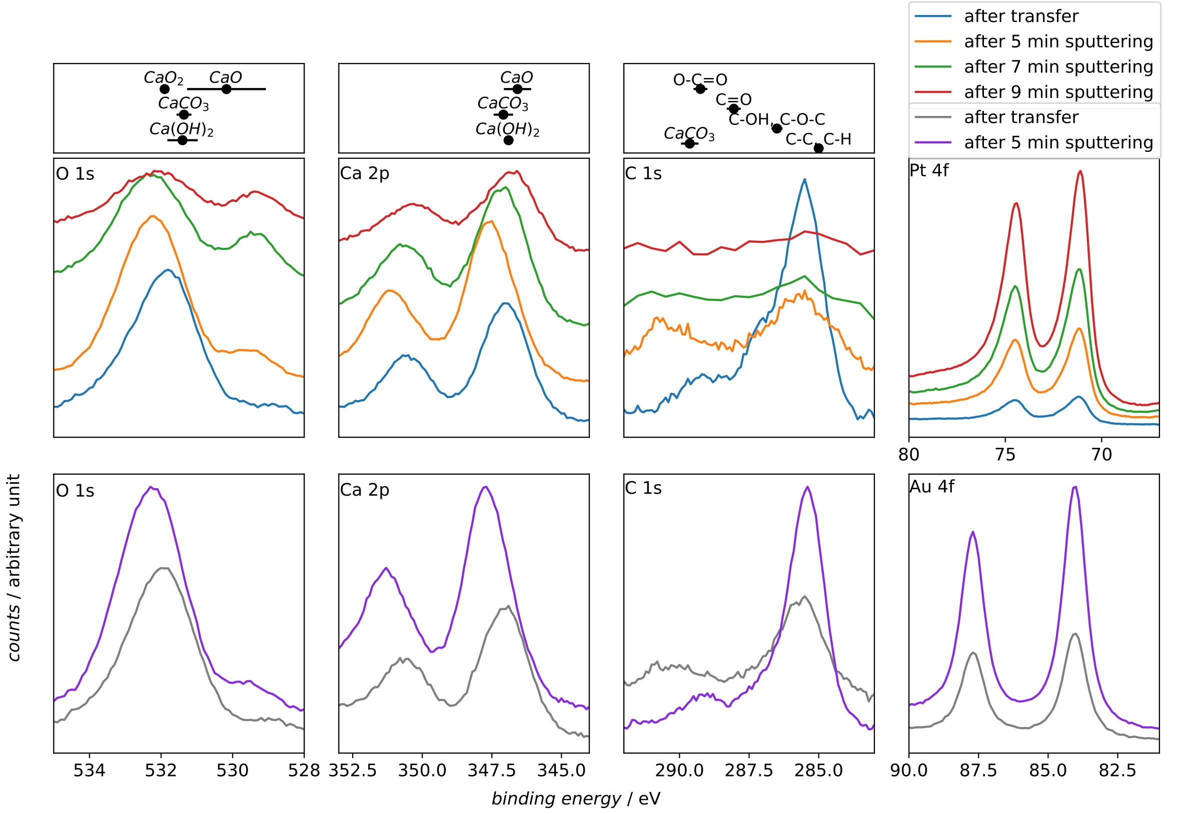

Figure 7.7: High resolution XP Spectra of various binding energy regions. The corresponding core shell orbitals are indicated in the plots. The XP spectra are recorded after 60 min of ORR in 0.2 M $Ca(ClO_4)_2$ in DMSO on a Pt electrode (middle row) and an Au electrode (bottom row). The different spectra are recoded after different Ar^+ etching times as indicated in the legend. Typical binding energy values for different chemical compounds are displayed in the first row. The displayed values are the average values (points) with the standard deviation from the average (error bar). An overview of the different values from the different references is shown in the supporting information.

same calcium oxygen species are deposited on the Au and Pt electrode. The higher intensity of the Ca 2p region towards higher binding energies is due to the superposition of the Au 4d peak and the Ca 2p peak (see survey spectra in Figure 7.14).

Since we have shown that the chemical composition of the ORR products on the gold and platinum electrode are the same, the further detailed analysis of the XP data will deal with the Pt electrode. The elemental composition of the film on the Pt electrode was calculated using atomic sensitivity factors [282] and assuming a uniform distribution of the elements in the investigated volume of photoelectron formation. The calculated values are summed up in Table **??**. Table **??** shows that carbonaceous species are located on the surface of the deposited film. After a total etching time of 7 min the C 1s signal vanishes (C 1s atomic ratio is less than

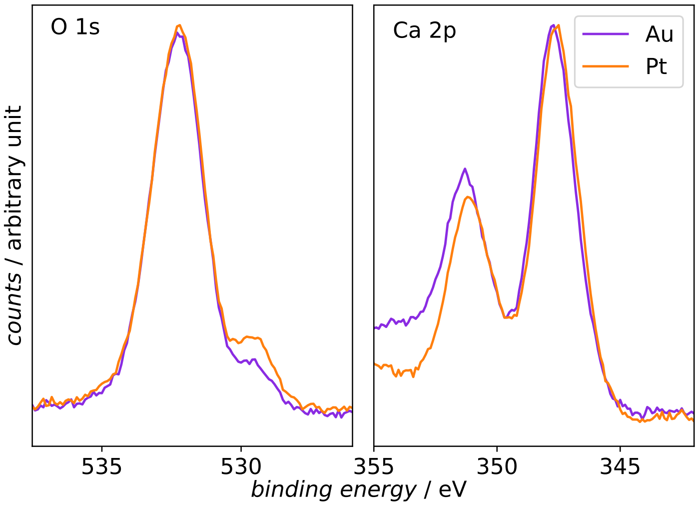

Figure 7.8: Comparison of the XP Spectra in the O 1s region and Ca 2p region of the experiments on the Au and Pt electrode. The spectra are both recorded after 5 min Ar^+ etching. For the Ca 2p region the counts were normalized to the Ca $2p_{3/2}$ peak. The O 1s region is displayed with no further normalization procedure.

5% of the total film, estimated from the survey spectra in Figure 7.16), thus inside the film the amount of carbonaceous species can be neglected. The film gets thinner through the Ar^+-etching, as indicated by the increase of the Au 4f and Pt 4f peaks. Close to the electrode surface, the film consists only out of calcium and oxygen.

Table 7.1: Surface composition (atomic ratio) calculated from the signal area of the high resultion spectra of the experiments with the Pt electrode shown in Figure 7.7. This was done by assuming a uniform elemental distribution of the volume where photoelectrons are emitted from.

$t(Ar^+)$ / min	C / %	Ca / %	O / %
0	40.2	15.3	44.4
5	20.3	23.9	55.8
7	0.0[a]	29.8	70.2
9	0.0[a]	33.3	66.7

[a] Due to the lower sensitivity of the experimental setup while recoding high resolution spectra it was not possible to detect carbon and therefore this value was set to zero. The survey spectra show that by doing this the absolute error is less than 5%

Moreover, the Ca 2p, O 1s and C 1s XP spectra are showing a shift in the binding energy for the different Ar^+-etching times. This implies a change in the oxidation state of the deposited film. A detailed discussion of the O 1s and C 1s region is made by considering the deconvolution of the recorded spectra. To our knowledge, there are no reports about binding energies of the Ca 2p core level of CaO_2 and $Ca(O_2)_2$ in literature. However, binding energies for the

O 1s levels for the peroxide are available. These two compounds are expected to be the main ORR products [97, 276], but the minor formation of CaO is also possible. In addition, the shift in binding energies of the Ca 2p core level is not as big as the shift of binding energies of the O 1s and C 1s core level, which from a chemical point of view is reasonable since in all calcium-oxygen-compounds Ca has the formal oxidation state +II. Therefore, a further discussion of the binding energy shift of the Ca 2p core level is not made here, but we will use the overall intensity of this excitation for quantification below. The C 1s region was also investigated in detail (see Figure 7.18 in the supporting information). There we observed contributions of C-O, O-C=O and ${CO_3}^{2-}$ species. These species are located on the surface of the deposited film and are disappearing after Ar^+ treatment. From previous studies on meatal-air batteries the formation of decomposition products like ${CO_3}^{2-}$ is well known and thus, it is not surprising to also find these species in the present system [283–286]. As source of the carbonate we would refer to the disproportionation of superoxide and the associated side reactions (presumably through the formation of singlet oxygen), as we also discussed in the context of Figure 7.5.

In the survey spectrum we observe a peak at 161.5 eV binding energy on the platinum electrode even after 9 min of Ar^+ treatment indicative of another decomposition product, which we attribute to S^{2-} (see Figure 7.17 in the supporting information). Previous results of Sharon and Aurbach et. al. on the Li-O_2 system in DMSO containing electrolyte showed the presence of higher oxidation states of sulphur on the electrode surface as $SO_3{}^{2-}$ and $SO_4{}^{2-}$ [194] which was attributed to a side reaction between DMSO and the reactive oxygen species generated during the ORR. In our case, the S 2p core level peak is observed after 9 min of Ar^+ treatment and therefore on the Pt electrode. Therefore the signal should in our case arise from a reaction of the electrocatalyst Pt with DMSO. It is well known that on Pt electrodes adsorption of layers of DMSO [287, 288] as well as further reduction of DMSO is occurring [289]. Overall, the decomposition mechanism of DMSO by reactive oxygen species generate during the ORR is still unclear. One of the best suggestion is the decomposition of the electrolyte by the highly reactive, electronically exited state of oxygen, i.e. singlet oxygen. Singlet oxygen was found to be a product during the ORR in organic solvents due to the disproportionation of superoxide compounds [118].

The O 1s region is deconvoluted for the experiments after 7 min and 9 min Ar^+ treatment (see Figure 7.9). We chose those two experiments for the analysis, due to the lack of oxygen containing carbon compounds as we showed before. Therefore the deposited layer consists exclusively of calcium-oxygen compounds.

The O 1s region in Figure 7.9 reveals a new peak at 529.4 eV binding energy after 7 min Ar^+ treatment, which was deconvoluted into the light green peak, which is assigned to CaO [290] (see also literature overview in Figure 7.7). Oxides were previously also found on electrodes of Lithium-Air systems [49, 291]. The origin of the oxide formation in these systems is still

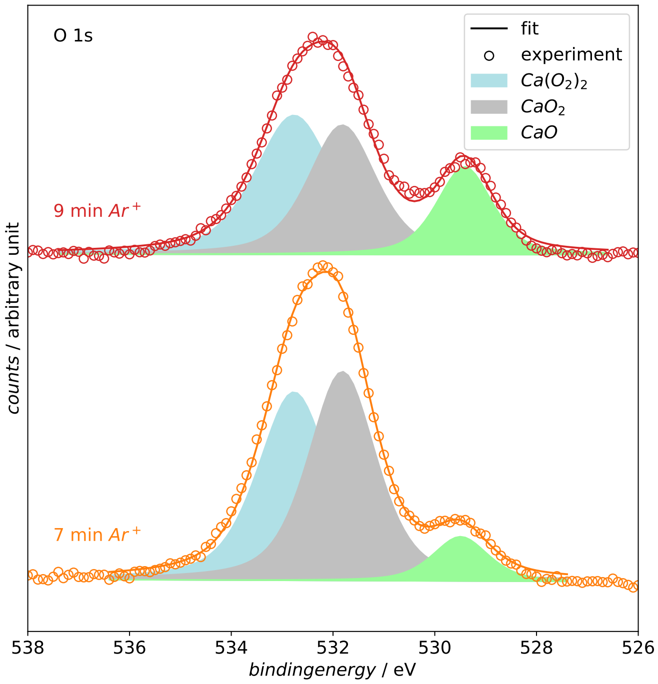

Figure 7.9: Deconvolution of the O 1s region of the spectra collected from the Pt electrode after 7 min Ar^+ treatment (yellow) and 9 min Ar^+ treatment (also shown in Figure 7.7). The experimental data is shown as circles and the resulting fit is plotted as line. The different deconvoluted species ($Ca(O_2)_2$, CaO_2 and CaO) are plotted as filled curves under the experimental data. The atomic atomic % of the different deconvoluted peaks is shown in Table **??**.

unclear. We assume that, the oxide is formed only as adsorbate in the monolayer range, as our previous DEMS measurements do not show evidence for a significant occurrence of the 4 e^--process [97, 276]. The formation of CaO might also occur as artefact from the XPS analysis procedure. In the supporting information we summed up our arguments why we exclude the formation of CaO as an artefact from the XPS analysis procedure.

Regarding the peak towards higher binding energies in the O 1s region, the high FWHM of 2.34 eV in Figure 7.7 of the peak after 5 min Ar^+ treatment is suggesting that several species are contributing to this peak. Therefore we deconvoluted the peak into a CaO_2 contribution (grey peak in Figure 7.9) and a $Ca(O_2)_2$ contribution (blue peak in Figure 7.9). The assignment towards CaO_2 and $Ca(O_2)_2$ is made by taking the binding energy into account as well as calculating the stoichiometry of the calcium-oxygen compound from the XPS data. Based on our analysis of the different binding energies of calcium-oxygen compounds there are two possible species that can contribute to the intensity in the binding energy region of the grey peaks in Figure 7.9: $Ca(OH)_2$ and CaO_2. In our literature search concerning the binding energy of CaO_2 we only found one value for the binding energy at 531.9 eV [292]. Since the number of transferred electrons per oxygen molecule is slightly higher than 1 e^-/O_2 on a Pt electrode during the ORR [97], it is plausible to assume that also minor amounts of peroxide are formed. Moreover, the precipitation of CaO_2, which is generated from the chemical disproportionation of $Ca(O_2)_2$ (as was shown above in the context of Figure 7.5), is also a possible origin of CaO_2 on the surface. The results concerning the formation of hydroxides during the ORR in DMSO in literature are equivocal. The stability of DMSO in a Li-O_2 cell was studied extensively. There are reports, that LiOH can be formed from LiO_2 and Li_2O_2 in presence of DMSO [187, 194, 293]. On the other hand, there are reports that DMSO is a stable electrolyte in a Li-Air cell [286, 294]. The formation of LiOH in these systems is observed on a timescale of 100-500 h. If the reactivity of CaO_2 and $Ca(O_2)_2$ is comparable to the Li-containing compounds, we would conclude, that the $Ca(OH)_2$ is not formed in our experiment (timescale 1h). Therefore, an assignment of the grey peak in Figure 7.9 as CaO_2 is conclusive. Concerning the blue peaks in Figure 7.9: To our knowledge, there are no binding energies of the O 1s core level of $Ca(O_2)_2$ reported in literature. From a chemical point of view the O 1s binding energy of $Ca(O_2)_2$ should be shifted positive compared to CaO_2, which is the case in the assignment of Figure 7.9.

The presence of $Ca(O_2)_2$ on the surface becomes obvious if the stoichiometry of the calcium-oxygen compound is calculated from the intensity of the Ca 2p and O 1s core level excitations. The calculated O / Ca ratios as well as the amount of different oxygen species resulting from the deconvolution is shown in Table **??**, for details of the calculation see the supporting information.

Table 7.2: Peak areas of the O 1s region in atomic % of the deconvoluted spectra in Figure 7.9. The calculated O / Ca is also shown. For the calcultaion of O / Ca only the areas of the peroxide and superoxide region were used. The area of the Ca 2p peaks was corrected over the expected amount of Ca calculated form the deconvoluted CaO O 1s peak.

$t(Ar^+)$ / min	CaO / %	peroxide / %	superoxide / %	O / Ca
7	8.2	46.9	44.9	2.97
9	19.9	35.9	44.2	3.12

Table **??** shows that the O / Ca ratio for 7 min and 9 min Ar^+ treatment is approximately 3. For the compounds of interests, $Ca(O_2)_2$ and CaO_2, the expected ratio of O / Ca are 4 and 2 respectively. Therefore, ratio of 3 is indicating the presence of $Ca(O_2)_2$ on the surface and moreover a nearly equal distribution of peroxide and superoxide. This calculated O / Ca ratio was also used in the deconvolution routine to define the ratio of deconvoluted peak areas after 7 and 9 min Ar^+ etching (see Figure 7.9). It can be see that by doing this, the deconvolution is well representing the experimental data.

The XP spectrum of the transferred Pt electrode after seeping the potential into the OER region is shown in Figure 7.6. The survey spectra shows that the surface now mainly consists of platinum. The Ca 2p core level peaks are not visible in the survey and in the high-resolution XP spectra. This is showing that all deposited calcium species can be stripped from the Pt surface by applying a high electrode potential, i.e. 0.7 V vs $Ag^+|$ Ag. The remaining contaminants on the surface now are mainly aliphatic carbon at a binding energy of 284.8 eV and oxygen containing carbon species at C 1s binding energies >285.5 eV accompanied by a O 1s signal at 531.4 eV (see C 1s and O 1s region in Figure 7.6). Aliphatic carbon is a well-known contaminant in XPS experiments. The origin of the oxygen containing carbon species is probably the exposure of the electrode to the glove box atmosphere, which contains organic solvent vapors and to contaminates adsorbed from the organic electrolyte. Therefore, we would conclude that the electrocatalyst Pt was fully regenerated by sweeping the electrode potential into the OER.

7.4.4 | Interpretation of the mechanism of the ORR in Ca^{2+} containing DMSO

It is rather surprising that according to the XPS results the same Ca–O species is present on Au as well as on Pt since our previous investigations showed fundamental differences with respect to the reduction mechanism on these two electrocatalysts. At gold initially a 2^--electron process is occuring, while at platinum 1-electron process is observed over the whole potential (and time) range. Moreover, the current transients in Figure 7.14 also imply that a different number of electrons are transferred and that the reduction mechanism, especially in the beginning of the ORR, is fundamentally different between both electrodes [97]. While there seems to be a blocking effect which alters the reaction mechanism to a 1-electron process also on Au, the RRDE experiments show that the blocking of the electrode stops after the transition to the 1-electron process and a diffusion-limited current is exhibited (see Figure 7.2). The transition of the mechanism of the ORR in DMSO based electrolytes from the 2 e^--process to the 1 e^--process was already observed in Li^+ containing solution [110, 111, 202]. There this observation was explained with a geometric effect of the deposited peroxide layer: The deposited peroxide covers adsorption sites on the electrocatalyst, which are needed to reduce oxygen to peroxide. However, in contrast to the observations in Li^+-containing electrolytes, the electrodes in the presence of Ca^{2+} are not fully blocked (the one electron process is maintained) which indicates a significant difference between the deposition mechanism of Li_2O_2 and CaO_2. Based on the knowledge of the Li^+ containing system, we will explain our finding that the apparent contradiction between the different reaction mechanisms and the observation of the same chemical species on the Au and Pt surfaces.

Au surfaces also showed an exclusive reduction path to reduce oxygen to peroxide in the Li^+ containing DMSO [111]. We suspect that there is a similarity concerning a direct reduction of oxygen to peroxide on Au electrocatalysts in Ca^{2+} containing DMSO, as it was previously observed in Li^{+} containing DMSO. We would like to postulate this statement here, since of course extensive kinetic measurements are necessary to confirm this statement.

On the Au electrode we observe a transition from the two electron process to the one electron process after a certain time. We believe that this is because adsorption sites, which are needed to perform the 2 e^{-}-process, are covered with CaO as adsorbate or strongly adsorbed peroxide or superoxide species. CaO is likely to form at lower electrode potentials and if formed as a small percentage of the overall ORR products it could accumulate on the electrode in the monolayer range. This is also supported by the fact that the electrocatalyst could only be reactivated by applying higher potentials and not by allowing slow dissolution of a superoxide or peroxide layer. The electrochemical oxidation of CaO is plausible, as the standard potential of the oxidation (3.35 V vs. $Ca^{2+} | Ca$ [295]) is reached in the experiment. Nevertheless the electrode remains active to maintain the one electron process after partial blocking. Therefore on both electrodes the main product of ORR is calcium superoxide. Still we also find appreciable amounts of calcium peroxide in our XPS measurements. Due to the disproportionation reaction of $Ca(O_2)_2$ it is likely that CaO_2 particles are forming on the Pt electrode. The one-to-one ratio of peroxide to superoxide as determined in the XPS measurements is probably due to different dissolution rates of the two substances. After an equilibrium time a final state is reached on both electrodes. Underneath the superoxide and peroxide layer a layer of CaO is located. On top of the superoxide and peroxide layer a layer of solvent decomposition products is located. This layer could also hinder the dissolution process of the superoxides and peroxides. Especially for the superoxide this would also hinder the further disproportionation to peroxide. In addition the stability of solid calcium superoxide was already reported [296, 297]. This would explain why we observed superoxide in the XPS experiments.

7.4.4.1 | The ORR mediation by DBBQ in Ca^{2+} containing DMSO

Within the Li -O_2 community, redox mediators for ORR have become common as they prevent the sudden death phenomenon due o blocking/passivation of the electrode surface by a solvent-mediated ORR mechanism [43, 46, 58, 298]. Despite of the solubility of calcium superoxide and calcium peroxide, it can be anticipated that the use of redox mediators is advantageous for the ORR in Ca^{2+} electrolytes for the following reasons:

1) If a redox mediator is used, the ORR potential can be shifted positively [46, 58, 298].

2) It has been observed that the use of redox mediators reduces the amount of undesired side reactions [47].

Therefore the ORR in Ca^{2+} containing DMSO mediated by DBBQ was also investigated using DEMS and XPS. The DEMS measurements are presented in Figure 7.10.

In a deoxygenated solution, the CV of DBBQ shows two reversible peak pairs a (see black traced measurement in Figure 7.10 (a)). We would like to point out that it is due to the special thin layer construction of the DEMS cell that in the CV diffusion limited currents are observed for the oxygen reduction in the absence of convection (for more details see in the [58]). In the presence of oxygen the decrease of the oxygen flux into the vacuum of the mass spectrometer at the onset potential of the DBBQ reduction shows that the DBBQ monoanion mediates the ORR in a 0.5 M $Ca(ClO_4)_2$ in DMSO. The CV of DBBQ in the presence of oxygen is shifted towards lower currents. This shift can be explained in analogy to the postulated mediation mechanism in Li^+ containing electrolytes [46]. Here the mechanism is formulated for Ca^{2+} containing electrolytes (here for the DBBQ-monoanion):

$$\mathrm{DBBQ} + e^- \longrightarrow \mathrm{DBBQ}^- \tag{7.1}$$

$$\mathrm{Ca}^{2+} + \mathrm{DBBQ}^- \longrightarrow [\mathrm{Ca}\cdots\mathrm{DBBQ}]^+ \tag{7.2}$$

$$[\mathrm{Ca}\cdots\mathrm{DBBQ}]^+ + \mathrm{O}_2 \longrightarrow [\mathrm{Ca}\cdots\mathrm{DBBQ}\cdots\mathrm{O}_2]^+ \tag{7.3}$$

DBBQ is reduced at the electrode (reaction 7.1). The reduced DBBQ species is forming an ion pair with Ca^{2+} (reaction (2)). This ion pair formation is well known for benzoquinones [248, 249] and was also investigated by us in the context of the ORR in Li^+ containing electrolyte [298]. It is expected that the DBBQ ion pair is forming a mediator-oxygen complex (reaction (3)). This is followed by the formation of peroxides or superoxides by the following reaction equations:

$$2\,[\mathrm{Ca}\cdots\mathrm{DBBQ}\cdots\mathrm{O}_2]^+ \longrightarrow \mathrm{CaO}_2 + \mathrm{O}_2 + 2\,\mathrm{DBBQ} + \mathrm{Ca}^{2+} \tag{7.4}$$

$$[\mathrm{Ca}\cdots\mathrm{DBBQ}\cdots\mathrm{O}_2]^+ + [\mathrm{Ca}\cdots\mathrm{DBBQ}]^+ \longrightarrow \mathrm{CaO}_2 + \mathrm{DBBQ} + \mathrm{Ca}^{2+} \tag{7.5}$$

$$[\mathrm{Ca}\cdots\mathrm{DBBQ}\cdots\mathrm{O}_2]^+ \longrightarrow {\mathrm{CaO}_2}^+ + \mathrm{DBBQ} \tag{7.6}$$

In reactions 7.4-7.6 the mediator, DBBQ, is regenerated. The regenerated DBBQ can diffuse to the electrode and be reduced again, which is explaining the decrease in the current in the presence of O_2. Taking the consumption of oxygen and the electrons flowing into the reduction of DBBQ into account, one can calculate the expected ratio between transferred electrons per oxygen molecule on the basis of the postulated reactions. This results in 2 e^-/O_2 for reactions (4) and (5) and 1 e^-/O_2 for reaction 7.6. For reaction 7.6 a following disproportionation reaction of the superoxide is plausible as we also showed in the beginning of this paper (see Figure 7.5). Based on the experimentally observed oxygen consumption in the diffusion limited region an oxygen flux of 200 pmol s^{-1}, the expected increase of the faradaic current was calculated for 1 e^-/O_2 and 2 e^-/O_2 and is shown as arrows in Figure 7.10 (b). The comparison to the experimental reduction waves of DBBQ in presence and absence of oxygen is showing that decrease of the reduction current in presence of oxygen is undergoing a change in the mediated ORR mechanism. In the first reduction peak of DBBQ we observe a mixed process between the 1 e^-/O_2 and 2 e^-/O_2 process. In the second reduction peak and in the diffusion limited region mainly the 2 e^-/O_2 process is observed. Overall, the mediated ORR is shifted 360 mV towards more positive electrode potentials (compare blue and red displayed measurements in Figure 7.10 (a)).

At higher electrode potentials the comparison of the CVs and the mass spectrometric data is showing that the positive current is due to the oxidation of oxygen releasing species e.g. $Ca(O_2)_2$ and CaO_2. The oxidation of CO_2 releasing species is also observed in the DBBQ containing measurement at electrode potentials higher than 0.5 V vs. $Ag^+|$ Ag.

In the DBBQ containing electrolyte the surface of a Au electrode was analyzed by XPS in the same manner as in the DBBQ free solution: The potential was held for 60 min at -1.5 V vs. $Ag^+|$ Ag, afterwards the electrode was washed with DMSO and transferred to the XP spectrometer. The corresponding XP spectra are shown in Figure 7.19 in the supporting information. The XP spectra analysis shows that after the transfer an over layer that mainly consists of ORR decomposition products (C-O, O-C=O and CO_3^{2-}, was deposited on the Au surface. This over layer is rather thin, since it can be removed after 120 s of Ar^+ etching. Most of the Au surface is recovered after the first Ar^+ etching stage, which is different from the experiments without the mediator. This is indicating that the deposited layer in the DBBQ containing electrolyte is thinner than in the DBBQ free solutions. After the first Ar^+ treatment of the surface, we still observe Ca_xO_y species with an overall high intensity of the Au 4f XP peaks. This is suggesting that the main part of the surface is free Au and that particles are deposited on the surface. The formation of large particles in the mediated ORR is well known [46, 299]. A comparison to the XP spectra in DBBQ free solution shown above reveals that these particles have the same chemical composition, i.e. CaO_2, $Ca(O_2)_2$ and CaO.

We also investigated the DBBQ - mediated ORR in Mg^{2+} containing solution (see DEMS measurements in Figure 7.20 in the supporting information. There we also observe a beneficial ORR potential shift of 280 mV. Unfortunately DBBQ is not a reversible redox system in the presence of Mg^{2+} and therefore not suited as mediator for the ORR.

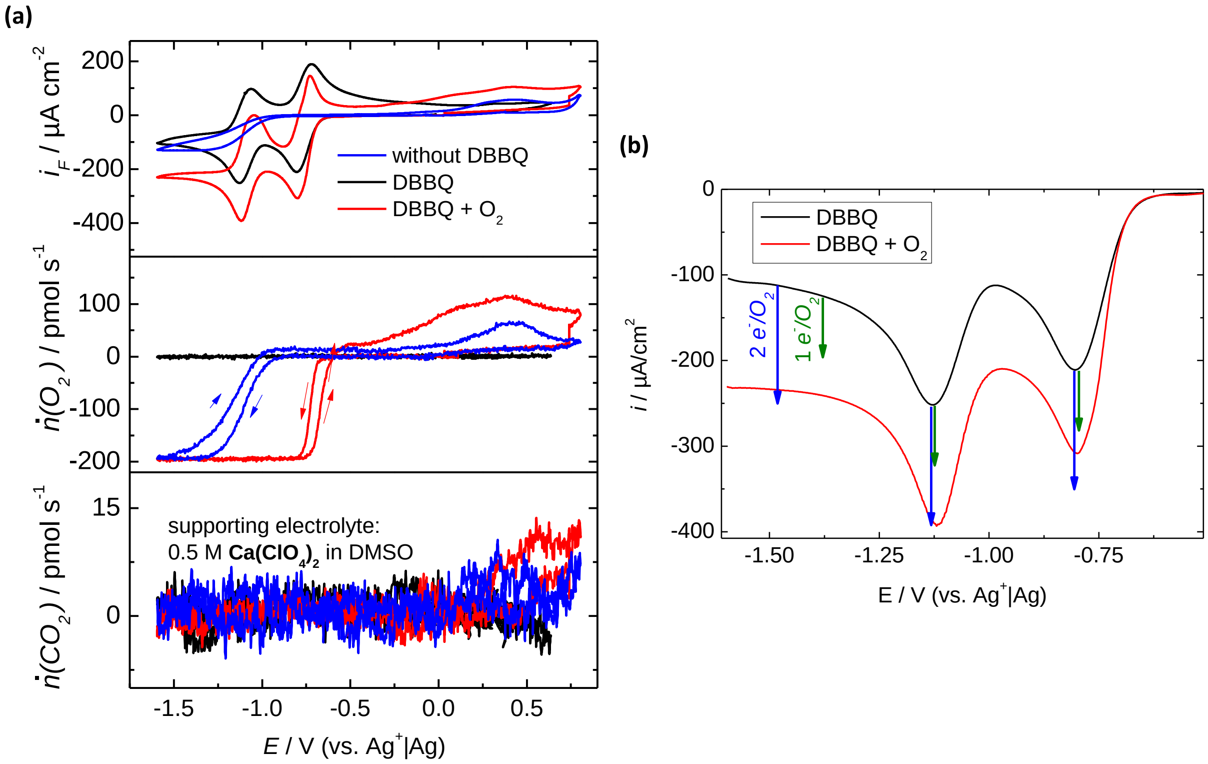

Figure 7.10: (a): CVs, O_2 flux and CO_2 flux in a 0.5 M $Ca(ClO_4)_2$ solution in DMSO. The blue traced measurements were recorded in the absence of DBBQ. In the black traced measurements (deoxygenated solution) and in the red traced measurements (solution saturated with 700 mbar O_2) 7.5 mM DBBQ was added to the supporting electrolyte. The applied sweep rate was 10 mVs^{-1}. We used a porous Teflon membrane sputtered with Au as working electrode. (b) Magnification of the cathodic sweep of the CVs in a DBBQ containing solution shown in (a). The arrows are indicating the increase in the reduction current based on 1 e^-/O_2 (green) and 2 e^-/O_2 (blue) reduction. This calculation was made with the observed diffusion limited oxygen consumption of 200 pmol s^{-1}.

7.5 | Conclusion

In this study we report about several findings concerning the ORR in Ca^{2+} containing DMSO:

- The share of superoxide as determined by RRDE shows that the mechanisms of the ORR on Au is changing from a mixed process of O_2^{2-} and $O_2^{\cdot -}$ formation to an exclusive $O_2^{\cdot -}$ formation.
- The unusually high charges for a metal air system in a non-aqueous solvent observed during the ORR in the RRDE experiments and in the potential step experiment are suggesting that the main products of the ORR are soluble in DMSO and therefore not poisoning the electrode surface. The solubility of CaO_2 together with the possibility to reoxidize it was proven using a thin layer DEMS cell. Poisoning is only occurring very slowly due to a

layer of ORR products is strongly attached to the electrocatalyst (CaO or strongly bound superoxide/peroxide species) and which is only removed at higher electrode potentials (0.3 V vs. $Ag^+ | Ag$) thus regenerating the electrocatalyst which shows that.

- The disproportionation reaction of $O_2^{\cdot-}$ in the presence of Ca^{2+} was demonstrated via mass spectrometry. This is accompanied by the evolution of several side products. We assume that these side products are generated by a reaction with $^1O_2$, which was reported to be a product besides $^3O_2$ during the disproportionation reaction in the presence of Li^+ [118]. The formation of side products during the disproportionation is, on one hand, a problem for metal-air technologies in general. On the other hand, the formation of CaO_2 from the disproportionation would boost the theoretical gravimetric energy density form 838 Wh/kg (superoxide as discharge product) to 2515 Wh/kg.
- With XPS the surface chemistry of a thin film, which was deposited on Pt and Au electrodes, was investigated. The following conclusion were made:
  - The top layer of the film contains decomposition products such as CO_3^{2-} and other oxygen containing carbonaceous species.
  - During Ar^+ etching $Ca(O_2)_2$, CaO_2 and CaO were found on the surface.
  - On Au and Pt electrodes the same species are deposited.
  - Sweeping the potential into the OER and performing an ex situ XPS measurement shows, that the surface of a Pt electrode is fully regenerated.
- The functionality of DBBQ as redox mediator for the ORR in Ca^{2+} containing DMSO was investigated. The ORR in the presence of DBBQ benefits from a 360 mV positive potential shift compared to the bare electrolyte. An analysis of the number of transferred electrons per oxygen molecule shows a transition from a mixed process of of O_2^{2-} and $O_2^{\cdot-}$ formation (during the generation of $DBBQ^-$) to an O_2^{2-} formation (during the generation of $DBBQ^{2-}$). Ex situ XPS measurements of the electrode surface after the ORR in the DBBQ containing electrolyte, show that a thinner film (compared to the bare electrolyte) was deposited. The same species were found on the electrode surface as in absence of DBBQ.

ACKNOWLEDGMENT

The authors gratefully acknowledge the Federal Ministry of Education and Research (BMBF) for funding this work. This work is part of the MeLuBat-project (03XP0110D) and the LuCaMag-project (03EK3051A) in the framework of the “Vom Material zur Innovation”-initiative. P. H. R. wishes to thank the German National Merit Foundation for financial support.

7.6 | Supporting information

Mass spectrometric measurement of the superoxide disproportionation

Sketch of the experimental setup

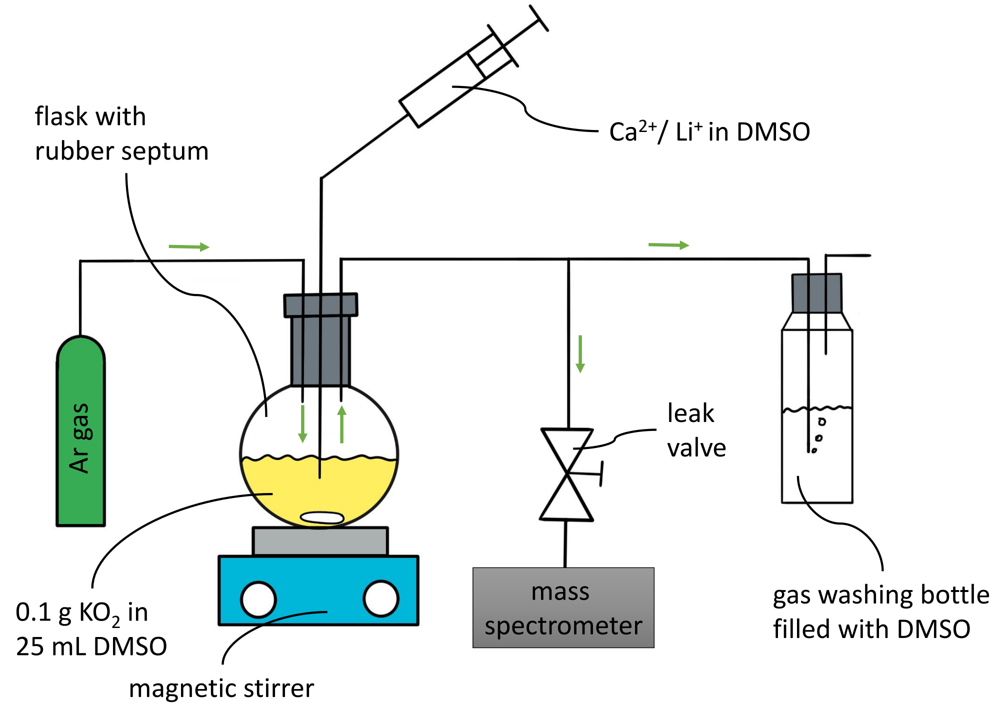

Figure 7.11: Schematic sketch of the experimental set up, which was used to detect the gaseous products via mass spectrometry during the disproportionation of superoxide in DMSO.

Full mass scans during the disproportionation reaction

In order to find out whether other gases are also produced during the disproportionation, mass scans of m/z=1-100 were taken in chronological order. Figure 7.12 shows the mass scans in a 2D plot. For a better presentation of the measurement results, the signals caused by the Ar carrier gas (m/z=20,40) were removed from the data series. To guarantee a better visibility of the signals, an intensity normalization was carried out: All signals were normalized to the most intense signal for m/z=44. Then the signal of m/z=32 was internally normalized to its maximum again.

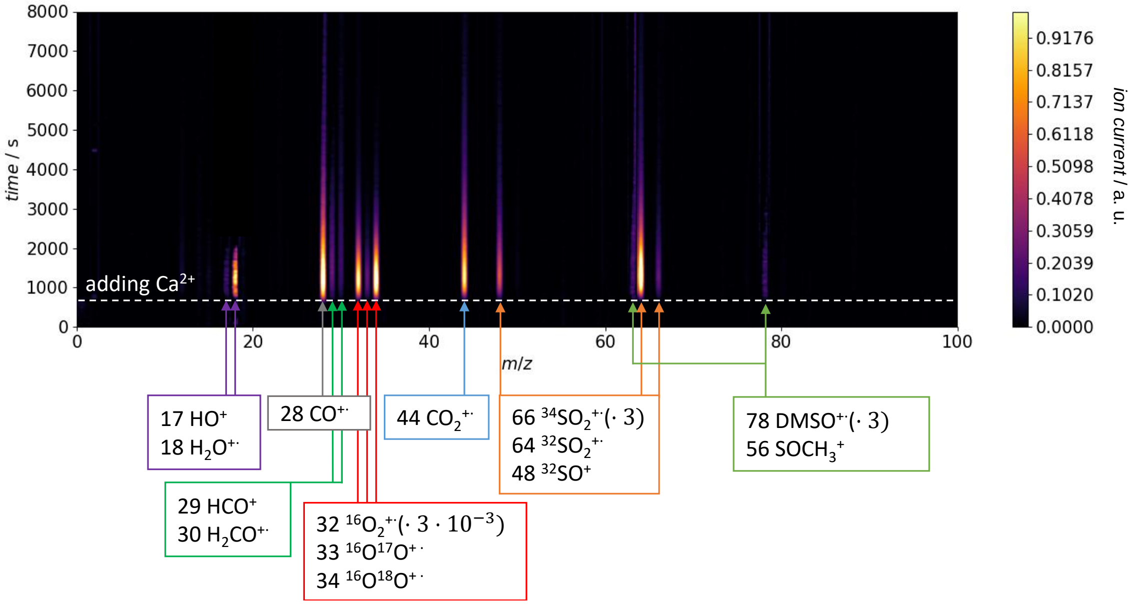

Figure 7.12: Mass scans from m/z=1 to 100 versus time. The dashed white line corresponds to the time at which 3 mL of 1 M $Ca(ClO_4)_2$ solution in DMSO were added to 0.1 g KO_2 in 25 mL DMSO. Ar was used as carrier gas and the experimental setup is sketched in Figure 7.11. The intensity is given in arbitrary units and the procedure of intensity calculation is described in the text.

As can be seen in the Figure 7.12, a number of other signals are observed in addition to the oxygen signal (m/z=32). A possible assignment to the different chemical species can also be found in Figure 7.12. The formulation of a mechanism how these compounds are formed during disproportionation is currently not possible. The most plausible source would be a side reaction with singlet oxygen, which was observed as a by-product of disproportionation in significant amounts [118] and is a highly reactive species.

An origin of the signal of mass 28 could also be an introduced contamination of N_2 by adding the electrolyte. We would argue that we should then observe a comparable signal for mass 28 after adding the Li^+ containing solution, which is not the case (see Figure 7.9 in the main manuscript).

The increase of the signal on mass 18 is probably related to the higher water content of the DMSO solution containing $Ca(ClO_4)_2$ as compared to the DMSO solution containing KO_2. Due to the bubble formation during disproportionation, the rate of water evaporation into the mass spectrometer is also increasing

Carbonate formation during the disproportionation reaction

It was already reported, that another side product during the disproportionation are carbonates [118, 119]. It is most likely that that generated singlet oxygen during the disproportionation reaction is undergoing side reactions with the solvent to produce carbonates. Figure 7.13 shows that an acidification of the solution after oxygen has been produced by the disproportionation of superoxide triggered by Ca^{2+} leads to CO_2 formation. The protonation of carbonates is believed to be the source of the CO_2 evolution [116]. Therefore we would also conclude the presence of carbonates after the disproportionation of superoxide in the presence of Ca^{2+}. We also observe a parallel O_2 evolution to the CO_2 evolution. A possible reason could be that the generated carbonates are deposited on the KO_2 surface and are therefore hindering a further disproportionation reaction. By adding H_2SO_4 to the solution the carbonates are consumed and the disproportionation can start again.

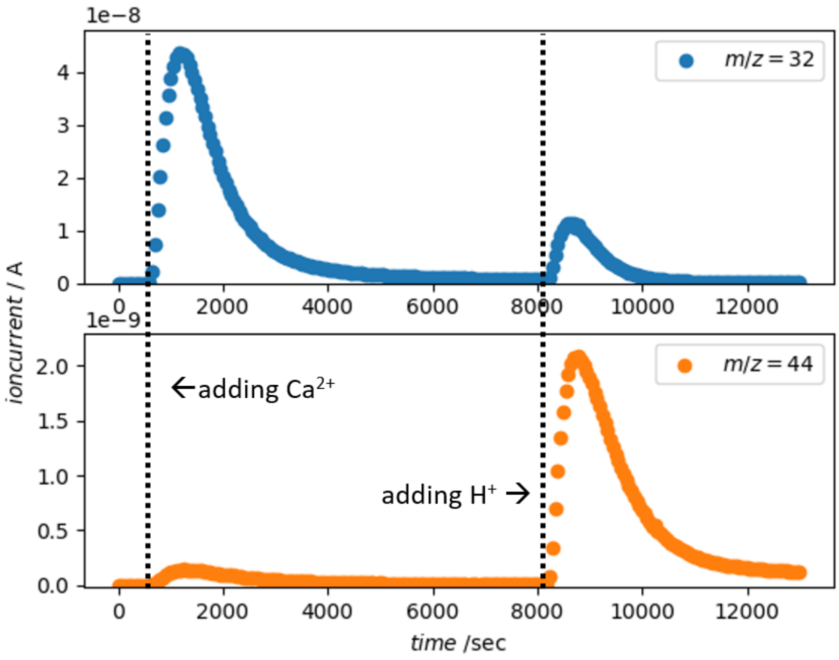

Figure 7.13: Ionic current of O_2 (blue, m/z=32) and CO_2 (orange, m/z=44) as a function of time. The gas phase over a stirred solution containing 0.1 g KO_2 in 25 mL DMSO was analyzed by MS after adding 3 mL of 1 M $Ca(ClO_4)_2$ in DMSO and 0.5 M H_2SO_4 in H_2O. The time at which the Ca^{2+} and H^+ containing solutions were added, are indicated as dashed line in the graphs.

Preparation of the XPS electrodes

To investigate the precipitation of solid products on Pt and Au electrodes during the ORR in Ca^{2+} containing DMSO XPS studies were carried out. As we showed in a previous study [97] and in the beginning of this paper (see Figure 7.2 and Figure 7.3 in the paper), the ORR in Ca^{2+} containing DMSO is mainly resulting in soluble products. Therefore, to accumulate species on Au and Pt surfaces the ORR was performed by holding the potential at -1.5 V vs. Ag^+| Ag for 60 min in 0.2 M $Ca(ClO_4)_2$ in DMSO. The resulting current transients are displayed in Figure 7.14.

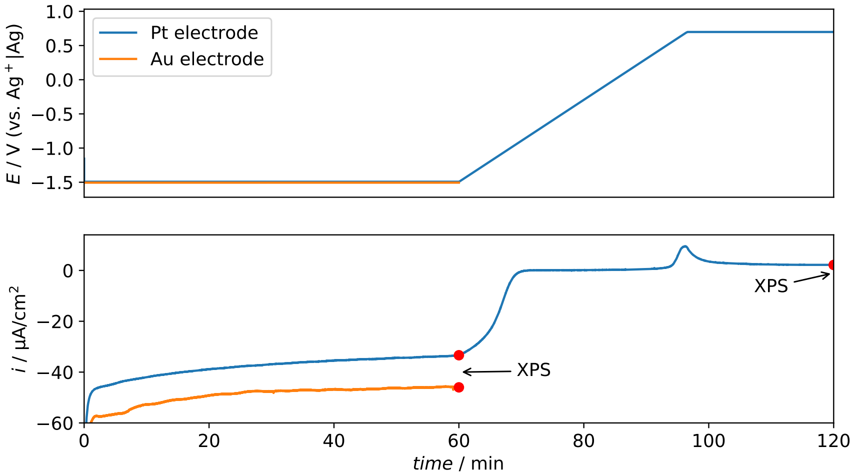

Figure 7.14: Potential versus time (top figure) and resulting current transient (bottom) in a 0.2 M $Ca(ClO_4)_2$ electrolyte in DMSO. As working electrode, Pt and Au were used (figure caption). All experiments were performed in a glovebox. The electrolyte was saturated with a 20% O_2 mixture in Ar. The red circles are indicating at which time the samples were transferred to the XP analysis chamber.

After an initial decrease of the current due to double-layer charging, the current reaches a slightly decreasing plateau within the first 100 s. This plateau, which most probably refers to a two-electron transfer, is followed by an abrupt decrease in current probably due to a transition of the two- to a one-electron process (compare with the RRDE results in the beginning of this paper). It is interesting to note that the current during the first plateau does not follow the behavior predicted by the Cottrell-equation, which implies that the reaction is not simply limited by mass-transfer in the bulk but maybe by the rate of precipitation in analogy to the findings in the Li^+-containing system. After that, the current decreases only slightly over time indicating a diffusion-limited process. In the time scale of the experiment no complete blocking of the electrode surface was observed, as we would expect in a similar experiment in a Li^+ containing system [202]. This again shows that in the Ca^{2+} system mainly soluble species are generated or that the species are not blocking the electrode/preventing the reaction from happening. After 60 min holding the potential in the ORR region the electrodes were transferred to the UHV chamber to record the XP spectra. With the Pt electrode an additional experiment was performed: After holding the potential at -1.5 V vs $Ag^+|$ Ag the potential was swept with 1 mV/s to 0.7 V vs $Ag^+|$ Ag, where the potential was held again. At positive electrode potentials the current transient is showing an oxidation peak. This suggests that species, which are deposited on the electrode surface during the ORR, are oxidized. The overall minor oxidative charge compared to the reductive charge is again implying that the main products of the ORR are soluble and are not deposited on the electrode surface. The oxidation of soluble ORR products is in our case not likely to be visible due to the large electrolyte excess of 35 mL in the electrochemical cell. After a total time of 120 min the experiment was stopped and the electrode was again transferred into the XP spectrometer.

Additional XP spectra

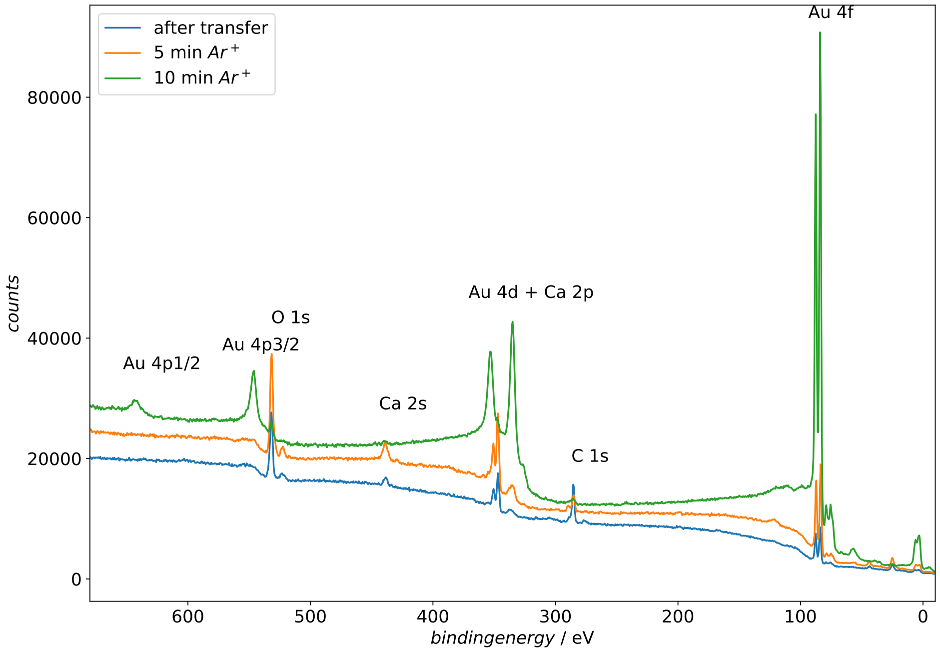

Figure 7.15: Survey XP Spectra of a Au electrode after performing the ORR in 0.2 M $Ca(ClO_4)_2$ in DMSO for 60 min.

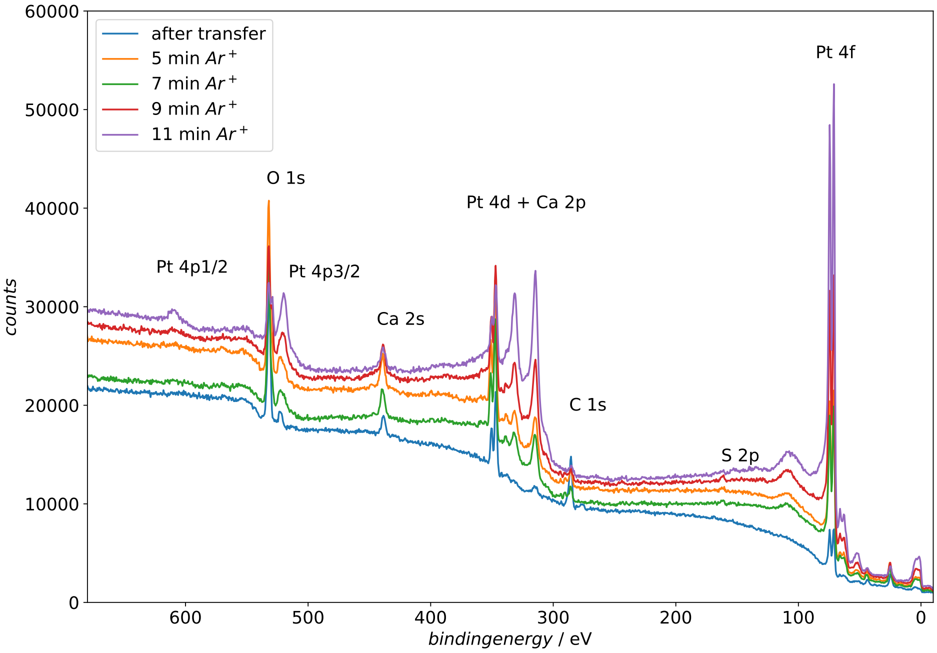

Figure 7.16: Survey XP Spectra of a Pt electrode after performing the ORR in 0.2 M $Ca(ClO_4)_2$ in DMSO for 60 min.

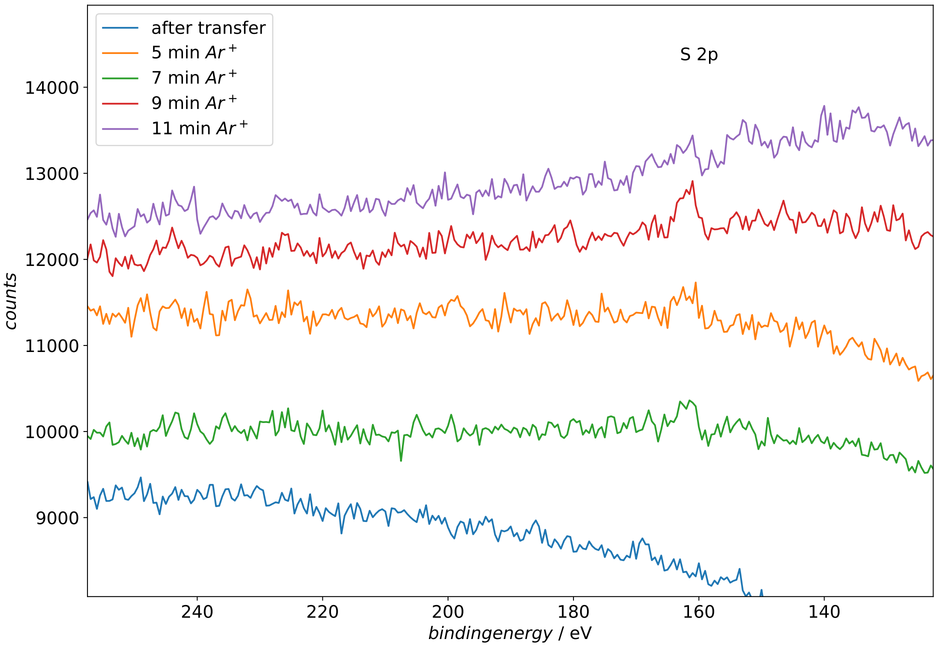

Figure 7.17: Magnification of the S 2p region out of Figure 7.16.

Deconvolution of the C1s region after the ORR on a Pt electrode

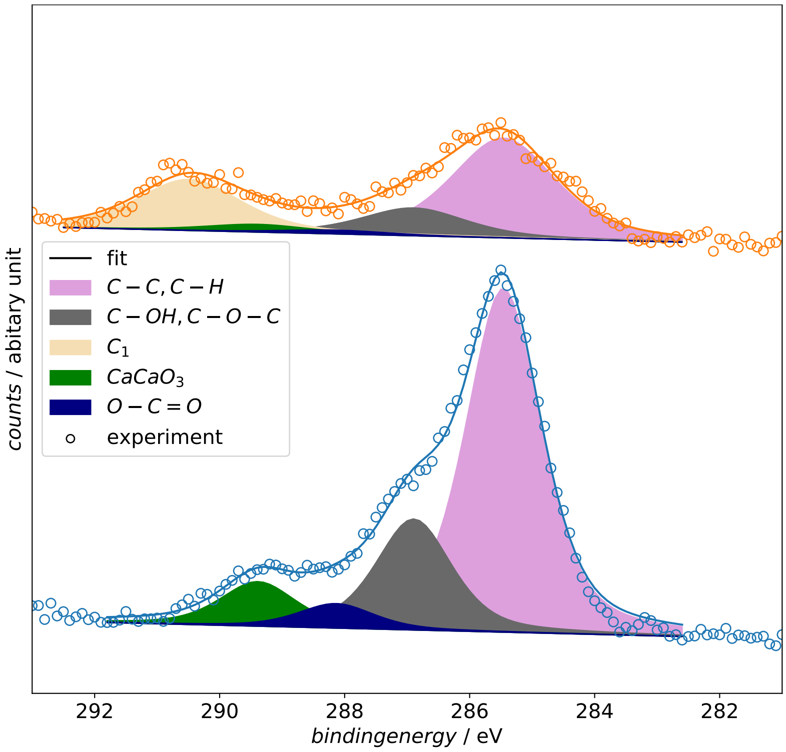

Figure 7.18: Deconvolution of the C 1s region of the spectra collected from the Pt electrode after transfer (blue) and 5 min Ar^+ treatment). The experimental data is shown as circles and the resulting fit is plotted as line. The different deconvoluted species are plotted as filled curves under the experimental data.

Figure 7.18 is showing the deconvolution of the C 1s region into different chemical compounds (see labels and the discussion in the paper). We also observed a peak at 291 eV binding energy (see deconvoluted peak C1 in Figure 7.18). A clear assignment of a species to this peak cannot be made, due to the high binding energy that is usually expected for fluorinated carbon compounds. In our case, no F 1s core level excitation was observed therefore a C–F compound is unplausible.

Literature research for binding energies of calcium oxygen compounds

Calcium carbonate

Table 7.3: Reported binding energies of the Ca $2p_{3/2}$, O 1s and C 1s core level excitation of calcium carbonate.

BE(Ca $2p_{3/2}$) / eV	BE(O 1s) / eV	BE(C 1s) / eV	Reference
347	531.4	289.6	[300]
346.8	531.2	289.4	[301]
	531.3		[302]
347.4	531.7	289.8	[303]
346.8	531.2	289.2	[304]
347			[305]
346.7			[306]
347.7		290.1	[307]
347.3			[308]
		289.7	[309]

Calcium hydroxide

Table 7.4: Reported binding energies of the Ca $2p_{3/2}$ and O 1s core level excitation of calcium hydroxide.

BE(Ca $2p_{3/2}$) / eV	BE(O 1s) / eV	Reference
346.9	531.4	[310]
	533.2	[311]
	532.2	[312]
	530.8	[290]

Calcium oxide

Table 7.5: Reported binding energies of the Ca $2p_{3/2}$ and O 1s core level excitation of calcium oxide.

BE(Ca $2p_{3/2}$) / eV	BE(O 1s) / eV	Reference
	531.3	[302]
346.1	529.4	[313]
347.3	530.1	[314]
346.1	529.0	[303]
347	531.5	[315]
346.8	531.4	[304]
346.65		[316]
346.1		[317]

XPS investigation of the ORR products of the by DBBQ mediated ORR in Ca^{2+} containing DMSO

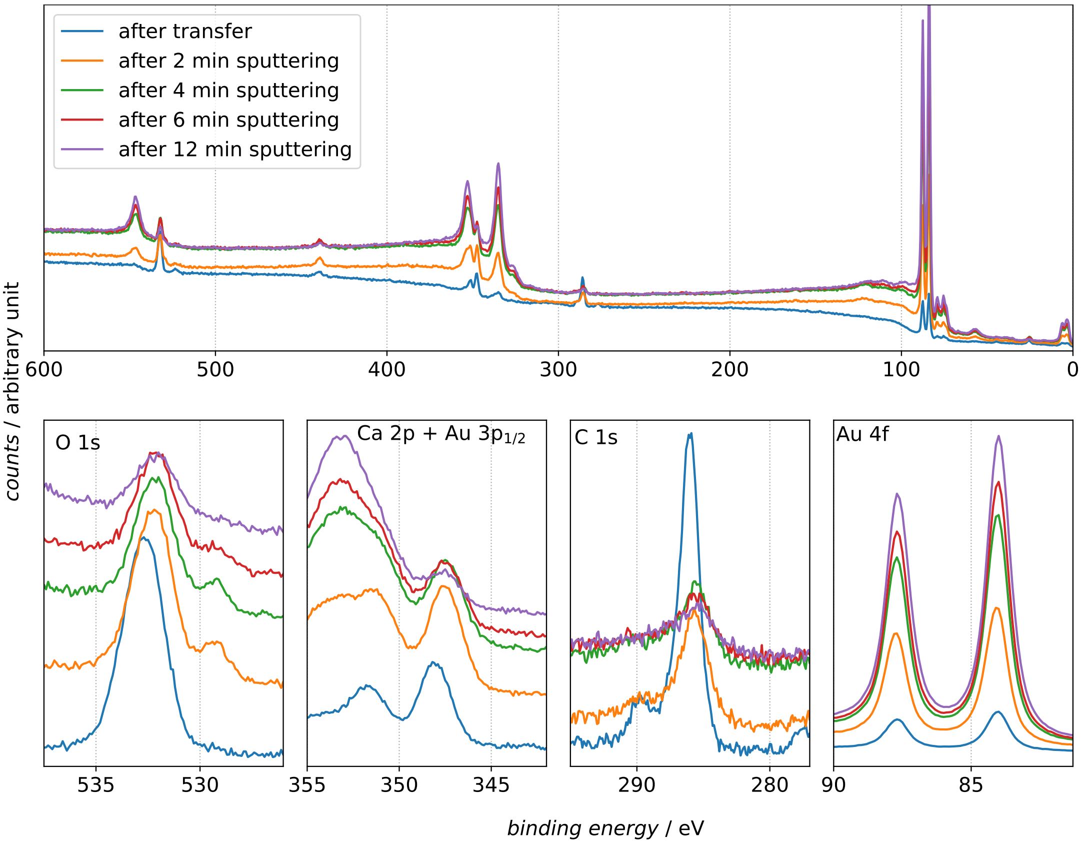

Figure 7.19: Survey and high resolution XP spectra of an Au electrode after performing the ORR in a 0.2 M $Ca(ClO_4)_2$ in DMSO with 5 mM DBBQ. Ar^+ etching accompanies the XP measurements. For the Ar^+ etching times see the figure caption.

Procedure to determine the stoichiometry of the calcium-oxygen compound with XPS

To determine the stoichiometry of the oxygen-compound the contribution of CaO has to be subtracted first from the total Ca 2p intensity (Figure 7.6 main paper). The evaluation is performed as follows. First the area of the peak corrected for the atomic sensitivity factor (ASF) and the CaO contribution $W(\text{Ca 2p}_{\text{corr}})$ is calculated. The amount of CaO can be determined by the respective deconvoluted peak area $A(\text{O 1s}_{\text{CaO}})$ in Figure 7.8 in the main manuscript. The following equation results for $W(\text{Ca 2p}_{\text{corr}})$.

$$W(\text{Ca 2p}_{\text{corr}}) = \frac{A(\text{Ca 2p})}{ASF_{\text{Ca 2p}}} - \frac{A(\text{O 1s}_{\text{CaO}})}{ASF_{\text{O 1s}}} \tag{7.7}$$

In equation 7.7 $A(\text{Ca 2p})$ is the overall integral of the Ca 2p core level excitation and $ASF_{\text{Ca 2p}}$ and $ASF_{\text{O 1s}}$ are the atomic sensitivity factors for the Ca 2p and O 1s core level excitation respectively. To subsequently get insights into the stoichiometry of the calcium-oxygen compound one can now calculate the area ratio of the remaining O 1s contribution (without the contribution of the O 1s core level excitation from CaO):

$$W(\text{O 1s}) = \frac{A(\text{O 1s}_{\text{Ca(O}_2)_2}) + A(\text{O 1s}_{\text{CaO}_2})}{ASF_{\text{O 1s}}} \tag{7.8}$$

$A(\text{O 1s}_{\text{Ca(O}_2)_2})$ and $A(\text{O 1s}_{\text{CaO}_2})$ are the integrals of the respective deconvoluted $Ca(O_2)_2$ and CaO_2 peaks in Figure 7.8 in the main manuscript. It may be confusing that the areas of the deconvoluted peaks are already assigned to the different species in equation 7.8, since the calculation described here should make the assignment possible in the first place. Therefore, we would like to point out that we did not make the assignment until after the evaluation described here was performed. By calculating the ratio $\frac{W(\text{O 1s})}{W(\text{Ca 2p}_{\text{corr}})}$ the stoichiometry of the Calcium oxygen compound was determined. The results are shown in the underlying paper.

The effect of Mg^{2+} on the reduction of DBBQ in DMSO based electrolyte

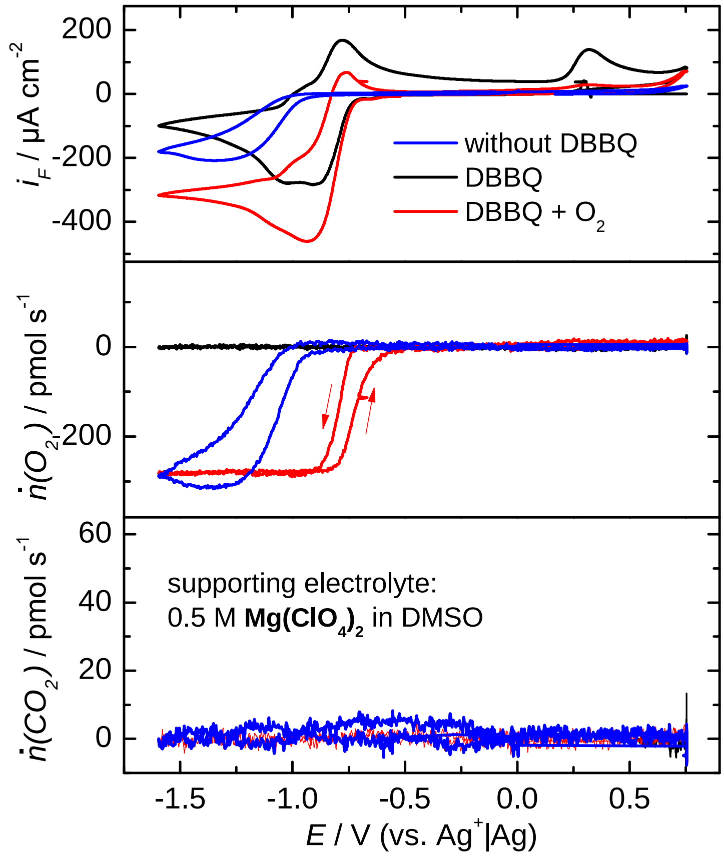

Figure 7.20: CVs, O_2 flux and CO_2 flux in a 0.5 M $Mg(ClO_4)_2$ solution in DMSO. The blue traced measurements were recorded in the absence of DBBQ. In the black traced measurements (deoxygenated solution) and in the red traced measurements (solution saturated with 700 mbar O_2) 7.5 mM DBBQ was added to the supporting electrolyte. The applied sweep rate was 10 mVs^{-1}. We used a porous Teflon membrane sputtered with Au as working electrode.

Excluding CaO as an XPS analysis artefact

In general, it is conceivable that CaO can form as an artefact of radiation damage from carbonates or peroxides. We can rule this out for the following reasons:

- The CaO peak can be recognized as a shoulder in the measurements immediately after the transfer (see Figure 7.7 in the paper). At this stage in the experiment a radiation damage is not reasonable.
- Carbonates were detected on the electrode surface after the transfer. The following reaction is assumed for the formation of oxides from carbonates: $CaCO_3 \longrightarrow CaO + CO_2$. A quantification of the amount of carbonate on the electrode surface shows that there is an insufficient small amount of ${CO_3}^{2-}$ to explain the amount of CaO on the surface.
- For the formation of CaO from CaO_2 the following reaction is assumed: $2CaO_2 \longrightarrow CaO + O_2$. This reaction can be excluded for the following reasons:
  - The formation of CaO from CaO2 by sputtering or excitation with X-rays was not observed before [292].
  - The reported temperature of 380 °C which is needed for the formation of CaO from CaO_2 [318], is probably not reached in the experiment. However, it is probable that this reaction is favored at lower temperatures in the UHV. But theoretical calculations show that CaO_2 is a stable compound at lower pressures [319].

8

XPS studies on the Mg deposition and insertion in MACC electrolyte

The studies summarized in this chapter are based on the electrochemical studies conducted by my colleague Da Xing. He investigated the electrochemical insertion of Mg into Sb modified Au electrodes. A characterization of the electrodes using XPS was of interest. Therefore, I repeated the electrochemical experiments and characterized the electrodes at different stages of preparation using XPS. The studies presented here are part of a planned publication [320].

8.1 | Abstract

In this study the deposition of Mg on Pt as well as the insertion into a Sb electrode is investigated using CV and XPS. The deposition is performed from a MACC/TEGDME based electrolyte. In both systems the irreversible Al co-deposition is observed. In addition, decomposition products of the electrolyte are present on the surface. With the help of Ar^+ etching, depth profiles of the electrodes are generated. Thus it can be shown that the decomposition products of the electrolyte, Al and Cl are surface species. Especially the presence of a surface enriched with Cl species shows the importance of Cl in the insertion process of Mg and fits into the similar observations in the literature on Mg deposition. Mg(0) and Al(0) can be detected after Ar^+ etching. The Sb electrodes used were produced by electrochemical deposition of Sb on Au. A characterization with XPS is also performed: It is shown that the generated Sb electrodes are oxidized by air contact. The detected Sb (+III) is reduced during the Mg insertion process.

8.2 | Introduction

In order to satisfy the future demand for storage media for electrical energy, research is being conducted on various electrochemical storage technologies. For example, due to its high volumetric capacity, the Mg battery has been proposed as an alternative for the Li-Ion technology [321]. The problem is that the Mg anode has a tendency to build up an insulating layer. This phenomenon is also known from the Li technology, but there these layers are Li^+-conducting and are therefore called solid electrolyte interphase SEI [322]. Therefore, a focus in Mg battery research is the formulation of a suitable electrolyte that does not have a tendency to form an insulating layer on the Mg anode. Different electrolyte systems such as Grignard-Based Electrolytes, Organoborate-Based Electrolytes and Borohydride-Based Electrolytes have been proposed for use in the Mg battery [321, 323]. Another class of electrolyte is based on Magnesium Aluminate Chloride Complex Solutions. Already in 2005 a simple synthesis of a fully inorganic salt in tetrahydrofuran THF for magnesium deposition was described [324]. This is produced from the salts $MgCl_2$ and $AlCl_3$ and is abbreviated with MACC (magnesium aluminium chloro complex). The first electrochemical tests showed a poor reversibility of the flowing charges in the Mg dissolution to the Mg deposition. However, it has been shown that repeated cycling between Mg deposition and Mg dissolution (about 50 cycles) can increase the reversibility to $> 98\%$ [325]. This procedure is called "conditioning". Experimental studies [326–328] and theoretical calculations [329, 330] have shown that this conditioning effect is due to the formation of the electrochemically active species for Mg deposition $[Mg_2(\mu - Cl)_3 \cdot 6THF]^+$. Another active species for the deposition of Mg from MACC is $[MgCl(THF)_5]^+$, which is only present in smaller concentrations in the electrolyte and is therefore not significantly responsible for Mg deposition [328, 331]. At the same time an irreversible Al deposition from the MACC electrolyte was observed [326–328]. Based on these observations the following reaction equations were postulated, which describe the formation of the active species $[\mathrm{Mg_2}(\mu-\mathrm{Cl})_3\cdot 6\mathrm{THF}]^+$ and the irreversible deposition of Al:

$$\mathrm{AlCl_3{\cdot}2THF} + 2\,\mathrm{MgCl_2} + 4\,\mathrm{THF} \rightleftharpoons \mathrm{AlCl_4}^- + [\mathrm{Mg_2}(\mu-\mathrm{Cl})_3\cdot 6\mathrm{THF}]^+ \tag{8.1}$$

$$4\,\mathrm{AlCl_4}^- + 6\,\mathrm{Mg(s)} + 6\,\mathrm{THF} \longrightarrow 4\,\mathrm{Al(s)} + [\mathrm{Mg_2}(\mu-\mathrm{Cl})_3\cdot 6\mathrm{THF}]^+ + \mathrm{Cl}^- \tag{8.2}$$

It has been shown that according to equation 8.2 the ratio of dissolved Mg to dissolved Al must be increased from 2 to 2.6 until reversible Mg deposition can be observed. Furthermore, alternative ways to promote the formation of the active complex of Mg deposition from MACC were found. It has been shown that increasing the $MgCl_2$ and $AlCl_3$ concentration shifts the equilibrium of equation 8.1 to the formation of $[\mathrm{Mg_2}(\mu-\mathrm{Cl})_3\cdot 6\mathrm{THF}]^+$ [328]. In general it is also advantageous to increase the Mg concentration by adding magnesium bis(trifluoromethanesulfonimide) ($Mg(TFSI)_2$) [332] and by electrochemcial dissolution of Mg metal by $CrCl_3$. This chemical conditioning shows that electrochemical conditioning is not required. It was also shown that electrochemical conditioning removes residual water from the electrolyte and that Mg deposition/dissolution only works at low water contents [333]. However, in experiments where $Mg(TFSI)_2$ was added to the electrolyte, the Mg deposition could also be performed with higher H_2O contents in the electrolyte [332]. To the best of our knowledge, there is only one report about XPS-measurements of Mg deposition from MACC using $Mg(TFSI)_2$ reported [332]. There, besides the Mg signals, signals for Al, Cl and C are observed. Decomposition products of TFSI were widely observed (F and S signal). Especially the signals of Mg and Al show that they are almost exclusively present in oxidized form.

Due to the reactivity of the Mg anode and the resulting formation of non-Mg^{2+} conducting insulating layers, alternative anode materials for the Mg anode are being investigated. For example, Sb-based electrodes as anode material were investigated for their suitability as electrode material in electrolyte mixture of ethylmagnesium chloride and diethylaluminum chloride in anhydrous THF [334]. The electrodes, consisting of pure Sb, showed a poor capacity retention. In a recent study from our group on the use of Sb as an electrode in a MACC tetraglyme (TEGDME) electrolyte it was shown that a capacity retention of 99.8% can be achieved [335].

In this study, first the electrochemically produced Sb electrodes are examined using XPS. Then a comparative study of Mg deposition on Pt and Mg insertion into Sb from MACC-TEGDME electrolytes is performed. In both cases the characterization of the electrode surfaces is performed by XPS.

8.3 | Experimental

Electrochemical Experiments

The aqueous electroytes were prepared with 18.2 MΩ MilliQ water with 0.5 M H_2SO_4. Prior to all electrochemical experiments shown in this study, the electrocatalysts were cycled in 0.5 M H_2SO_4 until the well known oxide formation regions and H-adsorption region (for Pt) were observed. This was a check for the cleanness of the system. The Sb deposition was performed form 0.5 M H_2SO_4 with 0.25 mM Sb_2O_3 via a 90 min potential hold at 0.05 V vs RHE. The transfer to the XP spectrometer was conducted through air.

The Mg deposition/insertion experiments were performed in an Ar filled glovebox. As electrolyte a mixture TEGDME (20.5 mL), $MgCl_2$ (0.966 g) and $AlCl_3$ (1.368 g), the MACC electrolyte. The All salts were dried in a Büchi Oven. The TEGDME was distilled with Na under reflux and stored over 3 Å molecular sieve. The deposition of Mg on Pt as well as the insertion of Mg into the prepared Sb layer is investigated via CV. Afterwards a potential step is preformed to deposit/insert Mg 820 min at 0.25 V vs Mg^{2+} | Mg for the insertion of Mg into Sb and 30 min at -0.75 V vs Mg^{2+} | Mg for the deposition of Mg on Pt. Already during the electrochemical experiments the sample electrodes are mounted on a crystal holder manufactured out of steel for the UHV chamber. All experiments were performed in glass cells with an 3 electrode arrangement.

XPS characterization

To investigate the chemical state of sample surfaces X-ray Photoelectron Spectroscopy (XPS) was used. In general the samples Au electrodes (d=10mm) which were modified in an electrochemical experiment are used. After the electrochemical experiment, the sample is washed with dry THF (Mg deposition experiments) or and mounted into a homemade sample transfer system. This transfer system allows the transfer of a sample between the glovebox and the UHV chamber without contact to air. The XP Spectrometer is part of a homemade UHV chamber with a base pressure of $5 \cdot 10^{-10}$ mbar. In the measurements in which the Sb electrode was examined without an insertion of magnesium, the transfer to the XP spectrometer was carried out via the laboratory atmosphere. The used X-ray source is a non-monochromatized Mg K_α (1253.6 eV) source. As electron energy analyzer a hemispherical electron analyzer (Omnicron NanoTechnology EA 125) is used. Survey spectra were recorded with a pass energy of 50 eV and an energy resolution of 0.5 eV. High-resolution spectra were recorded with different pass energies (the pass energies are noted in the captions of the spectra) and an energy resolution of 0.1 eV. To increase the signal to noise ratio, the high-resolution spectra are an average of 6 spectra. The binding energy was calibrated using the Au $4f_{7/2}$ peak at 83.95 eV binding energy or the Pt $4f_{7/2}$ at 71.09 eV binding energy [278], which is present in all measurements after a certain Ar^+ etching time. The XPS measurements were accompanied by Ar^+-etching (Physical Electronics Model 04-191, 3 kV, $I_{emission}$=25 mA, I_{sample}=1 µA).

8.4 | Results and discussion

8.4.1 | Electrochemical studies

The electrochemical deposition of Sb on Au is performed from a 0.25 mM Sb_2O_3 in 0.5 M H_2SO_4.Solution. A CV of this system on a polycrystalline Au electrode is shown in Figure 8.1. This shows two current fronts for cathodic current. The first is the under potential deposition (UPD) of Sb on the Au surface. Then, from 0.1 V vs. RHE, the bulk deposition is starting. In the anodic return, first the bulk Sb is dissolved (from 0.2 V vs. RHE) and then the UPD-Sb layer is dissolved. The UPD deposition of Sb on Au has already been investigated using in situ STM [335–337]. Hara *et al.* and Yan *et al.* were able to characterize an irreversible Sb adsorption before the Sb UPD adsorption. This is due to the irreversible adsorption of SbO^+ species. Furthermore, Zan *et al.* were able to characterize the UPD layers of Sb on Au(111) using in situ EC-STM, and thus determined the coverage to be 0.44 [335]. For the further intercalation studies the Sb electrode is prepared by a 90 min potential stop at 0.05 V vs. RHE.

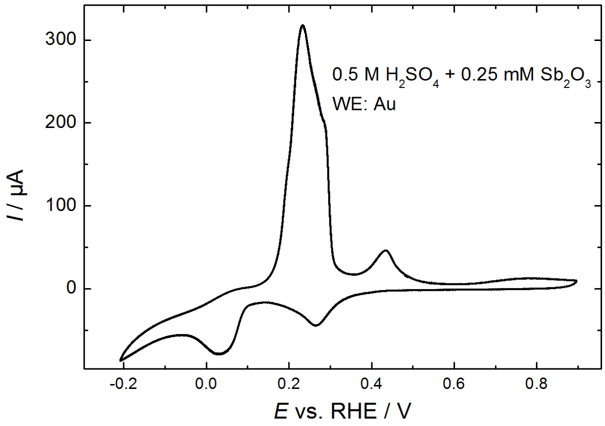

Figure 8.1: CV of the Sb deposition from 0.25 mM Sb_2O_3 in 0.5 M H_2SO_4 with a sweep rate of 10 mV s^{-1}.

Furthermore, the electrochemical studies on Mg deposition and Mg insertion into Sb are shown in Figure 8.2. The left figure in Figure 8.2 shows the time evolution of the CVs for Mg deposition and dissolution on Pt by cycling. After 30 cycles a steady state and a reversible Mg deposition/resolution is observed. This process was already described in chapter 8.2 and is due to the formation of the electrochemically active $[\mathrm{Mg_2}(\mu - \mathrm{Cl})_3]^+$ species. The right figure in Figure 8.2 shows the second CV cycle recorded in MACC/TEGDME on an Sb modified electrode. The insertion of Mg into Sb is indicated by a reduction peak that is 400 mV more positive than the start of Mg deposition. The anodic sweep shows first the bulk-Mg dissolution and then the deinsertion of Mg from Sb. It should also be mentioned that in this CV the conditioning process is not yet finished. This can be seen in the fact that the transition from Mg deposition to Mg dissolution is marked by an overvoltage of 200 mV. For the XPS investigations, potential stops were performed for Mg deposition and Mg insertion. For Mg deposition, a potential stop is performed for 30 min at -0.75 V vs $\mathrm{Mg^{2+}}$ | Mg. For Mg insertion in Sb, a potential stop is performed for 820 min at -0.25 V vs $\mathrm{Mg^{2+}}$ | Mg.

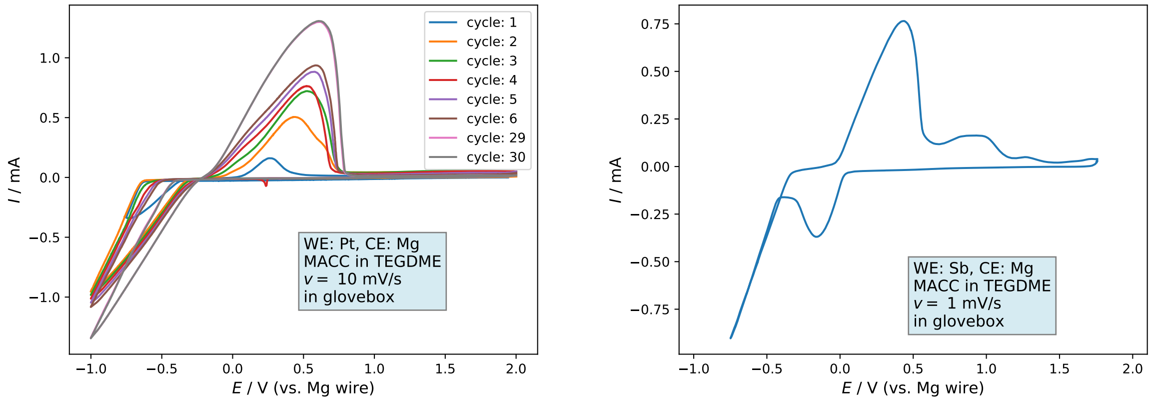

Figure 8.2: Left: CVs of te Mg deposition out of MACC in TEGDME. The CVs are showing the electrochemical conditioning process until a stable CV is reached (cycle 30). Right: CV for the Mg insertion and deposition into/on a Sb modified Au electrode. Shown is the 2nd cylce. Therefore the conditioning process is not yet finished.

8.4.2 | XPS characterization of the electrodeposited antimony

Figure 8.3 shows the Sb 3d region for the deposited Sb layer, after transfer for different $\mathrm{Ar^+}$ etch times. A total of 4 peaks can be observed. The peaks at 528.4 eV binding energy and 537.7 eV binding energy can be assigned to the elemental antimony [338]. Next to each of these peaks there is a second peak which is shifted to higher binding energies. Here an assignment of an antimony oxide species can be made. The O 1s peak of the antimony oxide is not directly measurable because it is hidden by the Sb 3d transitions. With the help of the Auger transition of oxygen from the survey spectrum, however, the existence of oxygen on the electrode surface could thereby verified. Furthermore the surface was etched with $\mathrm{Ar^+}$ ions. The etching times are shown in Figure 8.3. The combination of $\mathrm{Ar^+}$ etching and XPS shows that the proportion of antimony oxide to antimony decreases for longer etching times. However, we could not experimentally observe a pure Sb(0) surface. There are several possible reasons for this: The short contact of the electrochemically deposited antimony with the laboratory air is sufficient to partially oxidize the antimony even in deeper atomic layers. On the other hand, it is also conceivable that the deposited antimony surface has a high roughness, which means that the Ar^+ beam does not hit and remove the entire surface. Different etching rates of the different species of the surface are also conceivable. As a result, the elemental antimony, for example, could be removed more quickly than the antimony oxide, resulting in a distorted depth profile.

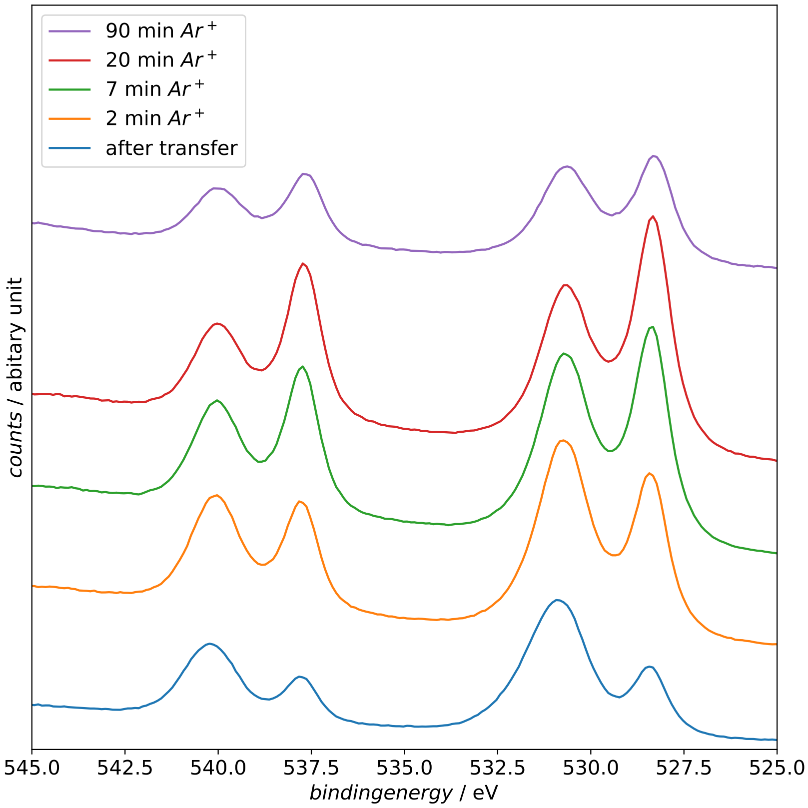

Figure 8.3: XP spectra of the Sb 3d region for different Ar^+ etching times. Recorded with a pass energy of 15 eV and a step width of 0.1 eV.

Finally, this measurement shows that the deposited antimony film is oxidized by contact with air. This is especially relevant for thin antimony films. This finding is not surprising when the different redox potentials of antimony and oxygen are considered ($O_2 + 4\,H^+ + 4\,e^- \rightleftharpoons 2\,H_2O$ $E^0 = 1.229\,V$ vs. NHE [339], $Sb_2O_3 + 6\,H^+ + 6\,e^- \rightleftharpoons 2\,Sb + 3\,H_2O$ $E^0 = 0.152\,V$ vs. NHE [339]).

8.4.3 | XPS characterization of the Pt electrode after magnesium deposition

Figure 8.4 shows the XP survey spectrum of a Pt electrode after Mg was deposited from MACC in TEGDME for 30 min. The first spectrum was recorded immediately after the transfer and the second after 30 min Ar^+ etching. After the transfer it can be seen that the Pt surface is buried by an electrochemically deposited layer because the Pt 4f core level excitation around 75 eV binding energy is hardly visible. The deposited layer consists mainly of C, O, Al and Cl (see assignment in Figure 8.4). The position of the C and Al signals shows that they are in oxidized chemical state. Regarding the C signal and the O signal, decomposition products of the electrolyte can be concluded. The deposited Al was probably oxidized in the transfer process by small impurities of O_2 and H_2O in the Ar atmosphere. The signal for the Mg 2s core level excitation (around 50 eV binding energy) is only visible after Ar^+ etching. It can be concluded that the deposited Mg was hidden by a layer of the above mentioned products after the transfer and could not be detected due to the surface sensitivity of the XPS experiment. Also, the Pt signals can be detected after Ar^+ etching. In general, the same elements were detected by XPS in this experiment as in the studies of He *et al.* [332]. In the XPS measurements concerning the Mg insertion in Sb it was possible to obtain a larger data set, therefore a more detailed analysis of the chemical environment of the elements can be performed in the following chapter.

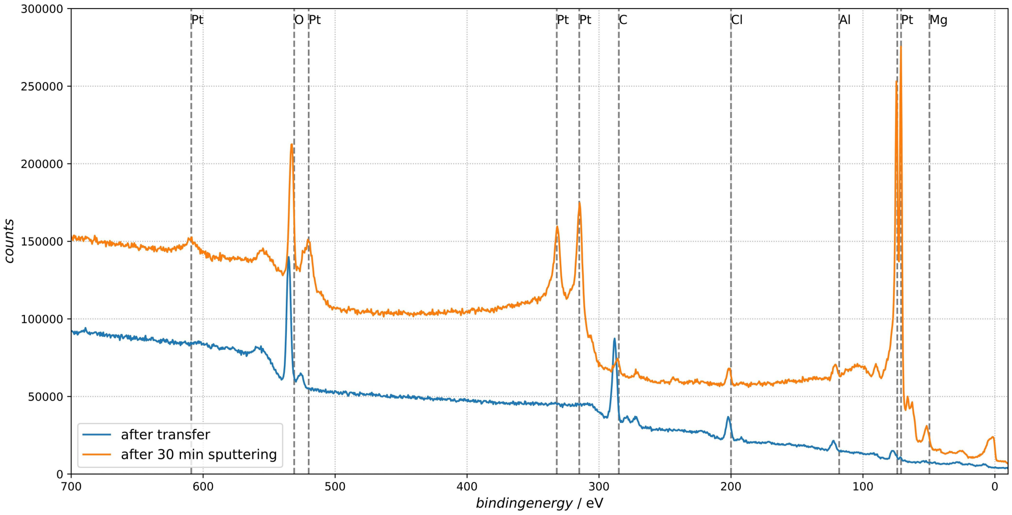

Figure 8.4: XP survey spectra of the Pt electrode after the Mg deposition. The blue traced spectrum is taken after the transfer. The orange traced spectrum was recorded after 30 min Ar^+ treatment. In addition the dashed lines are indicating the assignment of the observes peaks towards elements (in oxidation state 0).

8.4.4 | XPS characterization of the Sb electrode after magnesium insertion

Figure 8.5 shows the transient of the magnesium insertion into the Sb modified Au electrode. Magnesium was inserted by a potential jump to 0.25 V vs. Mg^{2+}| Mg and then holding this potential for 820 min. The experimental intention was to create a chemical equilibrium of the Mg-Sb phase due to the long duration of the experiment. Due to the diffusion inhibition of Mg in the Sb layer, the current drops after a short time, but it was observed that even after 820 min the current did not completely drop to the baseline (see magnification in Figure 8.5). This indicates side reactions (besides the Mg insertion) or an unachieved state of equilibrium.

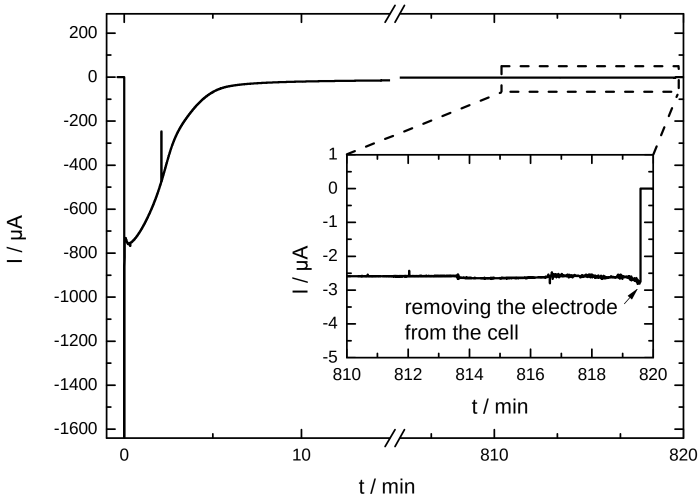

Figure 8.5: Current transient for a potential jump into the magnesium insertion into antimony (-0.25 V vs Mg^{2+}| Mg). The potential was held for 820 min. The inset is showing a magnification of the transient just before removing the working electrode from the electrochemical cell.

After the electrochemical experiment in Figure 8.5, the electrode was removed from the cell and washed with 5 mL THF. The electrode was then transferred under Ar atmosphere to the UHV of the XP spectrometer. The recorded XP Survey spectra are shown in Figure 8.6.

The XP spectra could be assigned the specific core electron excitation of Mg, Al, Cl, C, Sb, O and of the substrate Au. With the help of Ar^+ etching a depth profile is also obtained. After a total duration of 270 min of Ar^+ etching the XP spectrum shows almost only the core level excitations of the Au substrate. This shows that the chemical composition of the total deposited Sb film, together with the modification by Mg insertion, is examined in the following. The first spectrum after the transfer shows that the electrode consists mainly of carbon (50%). The chemical environment of carbon can be evaluated from the high resolution C 1s region (see Figure 8.7).

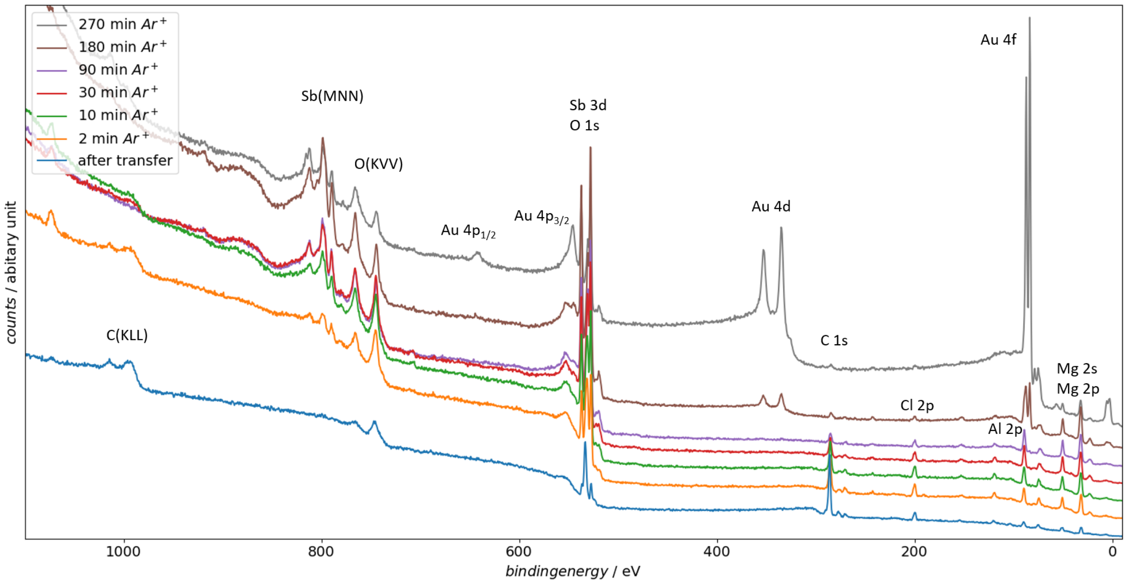

Figure 8.6: XP survey spectra of the Sb modified Au electrode after the Mg insertion shown in Figure 8.5. The XP spectra are taken after the transfer and for different Ar^+ etching times.

Figure 8.7 clearly shows that the detected carbon is a species on the electrode surface: During the Ar^+ etching process the signal is hardly detectable. In addition, the broadening of the signal to higher binding energies shows that the carbon present is oxidized in the first spectrum (after the transfer). There is a shoulder particularly noticeable at 290 eV binding energy [338]. This indicates a proportion of carbonates on the surface. In general, the oxidized state of the carbon fits well with the observed binding energy of the O1s core level excitation. It is known that the negative potentials and the reactivity of the inserted Mg can lead to side reactions at the interface electrode/electrolyte [340–342]. This can lead to the accumulation of decomposition products of the electrolyte on the electrode surface.

The atomic ratios in the individual XP spectra were calculated using the atomic sensitivity factors of the core level excitation of the different peaks [282]. In Figure 8.8 these are shown in a bar chart. For a better overview, the influence of carbon was not included. The values shown are the atomic proportion in relation to the sum of all elements shown. It is noticeable that the value for oxygen is very high and does not decay even after longer sputtering times. It can be assumed that the oxygen is transferred into the XP spectrometer. The oxidation of Mg and Al also takes place in the used Ar atmosphere. The contamination of O_2 and H_2O in the used Ar gas is 2 ppm/mol. From the concepts of surface science it is known that the dose of

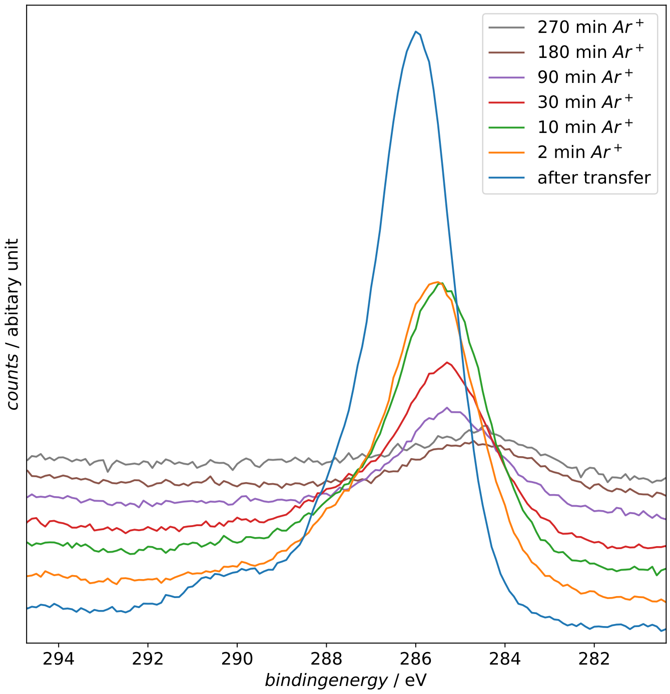

Figure 8.7: High resolution XP spectrum of the C 1s region for different Ar^+ etching times. Recorded with a pass energy of 50 eV and a step width of 0.1 eV.

1 L (1 L=$1.33 \cdot 10^{-6}$ mbar s) H_2O and O_2 is sufficient to create a monolayer of oxidation products. For the mentioned contaminations of O_2 and H_2O this corresponds to a time of 0.7 ms, which is sufficient to expose the surface to the glovebox atmosphere to trigger the oxidation process.[1] It is therefore conclusive that during the duration of the transfer (about 5 min), the deposited layers oxidize, which explains the high oxygen signal. The products of this oxidation reaction are hydroxides and oxides. In fact, the deconvoluted O 1s signal indicates the presence of these products. The binding energy of the deconvoluted O 1s region 1 (see red shaded area in Figure 8.9) indicates hydroxides, whereas the deconvoluted region 2 (see orange shaded area in Figure 8.9) indicates oxides in the XP spectra.

In general, this oxidation process limits the significance of the chemical shift of the binding energies, since oxidation is an artifact of the transfer process. Nevertheless, the XP spectra unravel some important information about the electrochemical reactions during the insertion.

An important observation is the dependence of the Cl signal as a function of the Ar^+ etch time. It can be seen that the Cl signal decreases with increasing Ar^+ etch time and therefore it

---

[1] The time of 0.7 ms was calculated assuming molecular flow (low pressure). To get a more accurate time for the problem presented here, the transport of O_2 and H_2O under higher pressure and thus a stronger interaction of the gas molecules with each other has to be considered.

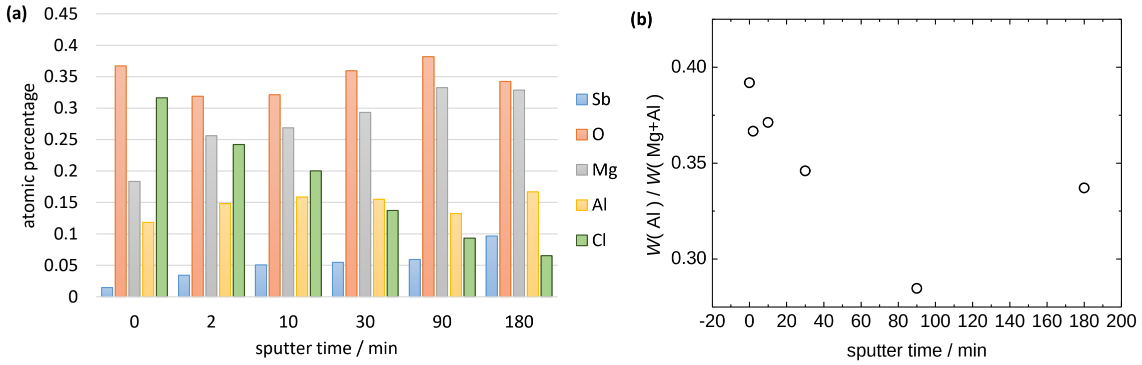

Figure 8.8: (a) Atomic ratios of Sb, O, Mg, Al and Cl to the sum of the displayed elements. The ratios were calculated out of the XP spectra taking the atomic sensitivity factors of the core level excitations into account (corresponding element and symmetry of the atomic orbital) [282]. Regarding the oxygen signal, this evaluation is more complex and the O 1s signal had to be deconvoluted from the overlap between the O 1s and Sb 3d signal (see Figure 8.9). (b) Ratio from the atomic sensitivity factor corrected Al 2p signal to the Mg 2s signal as a function of the Ar^+ etching time.

is a species that can be found on the surface. It was all ready shown, that in the presence of Cl^- ions in the electrolyte a magnesium surface decorated with Cl^- could be formed. This was postulated in the MACC/THF system and is due to the underlying exothermic process [329]. In general, it has been observed that the addition of chloride to the electrolytes is essential for the success of Mg deposition. It has been postulated that the Cl- decorated Mg surfaces are more stable against the formation of passivation layers [343]. Furthermore, the addition of $MgCl_2$ to the electrolyte appears to produce important electrochemically active species for Mg deposition [323, 344]. In addition to the deposited Mg, Al is also observed in the XP spectra. In Figure 8.8 (b) it is shown that the ratio of Al to Mg decreases with increasing Ar^+ etch time. Thus the Al signal is also originated from the electrode surface. Similar observations were made by Gewirth and coworkers in the case of bulk magnesium deposition from MACC in THF based electrolyte [326]. After 180 min Ar^+ etch time the Al/Mg ratio increases again. The reason for this is that most of the electrochemically deposited material has already been removed. This is visible in Figure 8.6 by the increasing signal for the Au substrate. Therefore, at this stage of the experiment, different rates of etching by the Ar^+ etching of the deposited material play a more important role.

The Sb signal increases with increasing Ar^+ etch time. Thus, it can be concluded that the electrochemically deposited layer of Sb is covered by a layer consisting mainly of C, Al, Cl as well as the O introduced by the transfer. Comparing the high resolution spectrum of the Sb 3d region after Mg insertion (see Figure 8.9) with the spectrum after the deposition of Sb from an aqueous electrolyte (see Figure 8.3), the spectrum after insertion shows no detectable amount of Sb in the oxidized state. The Sb 3d dubblet is observed at a binding energy that can be assigned to Sb(0). Bhardwaj *et al.* report a 0.6 eV shift to lower binding energies of the Sb 3 $d_{5/2}$ core level excitation of Mg_3Sb_2 compared to Sb(0) [345]. The reason that we cannot observe this shift is again due to oxidation by the transfer. Nevertheless, we do not observe any antimony oxide after the insertion of Mg. In general, the antimony oxide could be reduced due to the negative potential in the subsequent insertion experiment, or it could be reduced in a chemical pathway through the inserted Mg. A precise mechanism is still unknown here. However, it can be emphasized that the insertion material is elemental antimony and not antimony oxide.

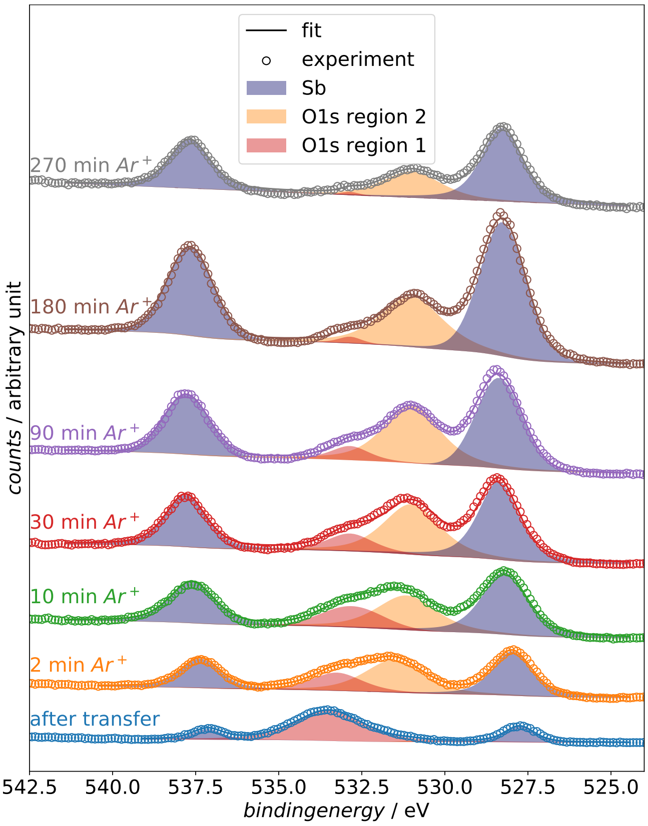

Figure 8.9: XP spectra showing the deconvoluted Sb 3d O 1s region. The experimental data is shown as circles. The different deconvoluted species are shown as hatched areas and the resulting fit as a line. The different spectra are originated from different Ar^+ etch times (see image labeling). In general, the O 1s region 1 can be assigned to hydroxides and the O 1s region 2 to oxides. However, the spectrum in the C 1s region immediately after the transfer also shows carbonates and other carbon-oxygen species. Therefore a uniform assignment is not valid here. Recorded with a pass energy of 15 eV and a step width of 0.1 eV.

When looking at the ratio of Mg to Sb (see Figure 8.8 (a)), it is striking that the experimentally determined amount of Mg is greater than the formulation of an insertion compound with the molecular formula Mg_3Sb_2 suggests. This finding could have several reasons. For one, it is conceivable that the antimony oxide present is chemically reduced by the inserted Mg, which would presumably result in the formation of magnesium oxide. Furthermore, the formation of a Mg-Al alloy is conceivable [346]. It is also conceivable that different etching rates of the Sb compounds and Mg compounds by Ar^+-etching will result in an enrichment of the Mg compound. The reasons listed above would explain the larger amount of Mg.

The high resolution spectrum of the Mg 2p core level excitation in Figure 8.10 (a) shows a relatively broad peak, which shifts to low binding energies for longer Ar^+ etch times. A deconvolution of these peaks into different Mg species does not seem to give reliable results. However, the width of the peak indicates that $MgCl_2$, $Mg(OH)_2$, MgO and Mg are likely to contribute. As an orientation, the common binding energies for the Mg species are indicated. After the transfer and for short Ar^+ treatment times, Mg-Cl species appear to be present on the surface, which is consistent with the observed Cl signal. The shift of the peak to lower binding energies indicates a higher proportion of Mg(0) in the investigated layer for longer Ar^+ etch times.

By means of the deconvolution of the Al 2p core level excitation (see Figure 8.10 (b)) it can be shown that elemental aluminium is present within the deposited layer at a binding energy of 72.8 eV [347]. In the deconvolutions routine, Al(0) and Al(+III) were each fitted with a doublet of gaussian-lorentz peaks. The area ratio corresponds to the expected ratio for a 2p core level excitation and the peak generation was fixed at 0.42 eV [338]. Thus it can be shown that a side reaction during Mg insertion in Sb is the deposition of elemental aluminium. Most of the Al(+III) on the electrode surface is probably due to the transfer of the electrode into the XP spectrometer, as discussed above. The deposition of Al(0) from MACC could not be detected by XPS so far [332].

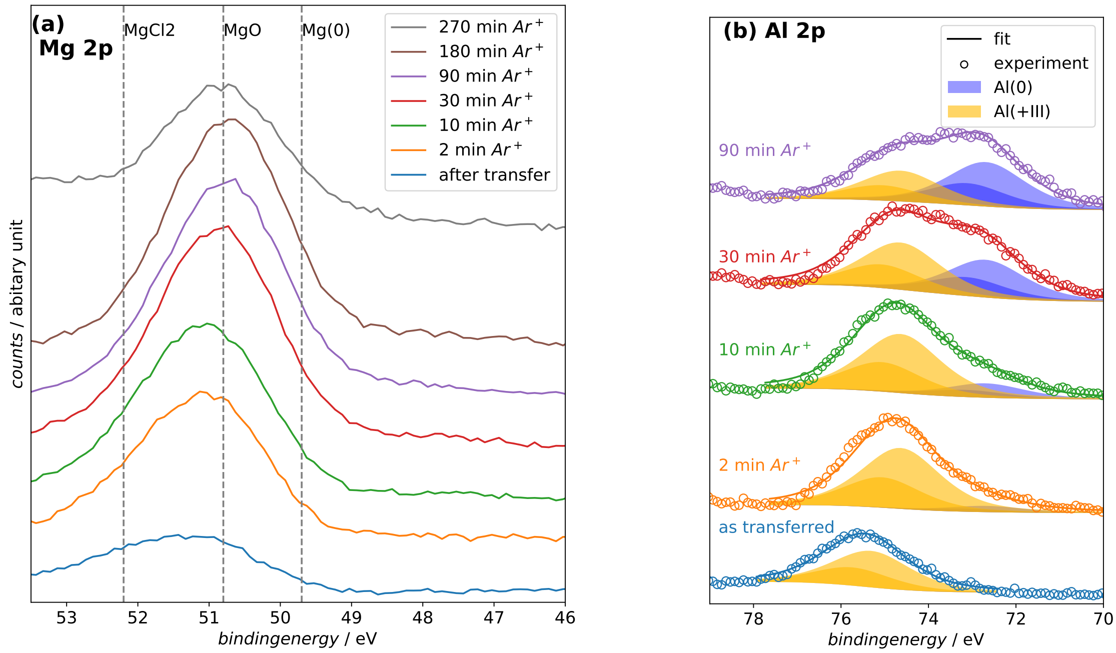

Figure 8.10: (a) High resolution XP spectra showing the Mg 2p core level excitation. As a guide, the common binding energies for $MgCl_2$ are also given. MgO and Mg(0) are also shown. (b) High resolution XP spectra showing the Al 2p core level excitation. Here a deconvolution of the experimental data is performed. Thereby two species Al(0) and Al(+III) each with a p excitation doublet with an binding energy difference of 0.42 eV were used [338]. Both sets of spectra were recorded with a pass energy of 50 eV and a step width of 0.1 eV.

8.5 | Conclusion

This work shows XPS studies of Sb deposition from a sulfuric acid electrolyte, the deposition of Mg from the MACC electrolyte on a Pt electrode and the insertion of Mg into a Sb electrode from the MACC electrolyte. The following observations could be made:

- After the deposition of Sb and transfer through the laboratory air, oxidation of the Sb surface occurs. In XPS both Sb(0) and Sb(+III) species could be detected. In the Mg insertion process the Sb(+III) species are reduced.
- The surface of the electrodes after Mg deposition and Mg insertion consists mainly of decomposition products of the electrolyte (CO_3^{2-} and other O containing C species). With the help of Ar^+ etching these species were removed to get an insight into the electrode surface.

- In general Mg and Al were found in an oxidized state. This can be mainly explained by the reaction with impurities of O_2 and H_2O in the Ar atmosphere of the glovebox.

- Both after Mg deposition and Mg insertion, Al was detected on the surface, which has already been described as the product of the conditioning process of Mg deposition [326–328]. By Ar^+ etching of the Sb insertion electrode Al(0) could be detected. The binding energy of the Mg 2s core level excitation also shows a higher proportion of Mg(0) after Ar^+ etching.

- The deposition of Cl species on the surface already known from Mg deposition from MACC was also observed for the insertion process. This again shows the importance of the Cl species during Mg deposition which could prevent the formation of a passivisation layer on the Mg surface.

- The Al and Cl concentrations decrease by Ar^+ etching, which proves that these are surface species. For the Sb signal the opposite trend was observed, which shows that Sb is buried by Al-, Cl- and C-containing species.

- The expected stoichiometry of the insertion compound (Mg_3Sb_2) could not be confirmed from the XPS data. The evaluated Mg content is higher than expected. The reason for this is probably the proportion of side reactions that lead to further Mg compounds.

9

Summary and Outlook

This dissertation deals with different questions from the current research on metal-O_2 batteries. In the following, the new findings will be summarized by topic.

Contributions to experimental methods

First, the contributions will be summarized to experimental methods. Within this study a new DEMS cell was developed. This cell has a small electrolyte volume with a larger electrode surface area and therefore the measurements can be compared with the conditions in a battery. In addition, the cell was optimized for fundamental research in a three electrode arrangement. Furthermore, the transport of oxygen to the electrode surface is well defined in this cell and stationary concentration profiles of oxygen in the cell (for example in the ORR) are quickly established. These conditions are also valuable for the investigation of the ORR under different aspects. The well defined transport conditions of this electrochemical DEMS cell were used to construct another cell for the determination of the solubility of gases in liquids and the diffusion coefficient of the gas in the liquid using a mass spectrometer. A major advantage of this cell is that only small electrolyte volumes are required and the experiments can be performed quickly. This data concerning O_2 in different electrolyte systems are essential for the development of a metal O_2 battery. For example, the product distribution of different reduced oxygen species can be calculated from diffusion limit currents in RRDE experiments or peak heights in CVs of the ORR using this data [109, 111]. Furthermore, this data is essential to gain deeper insights into the metal-air battery by numerical simulation and to validate reaction mechanisms [190, 348]. A first publication with solubilities and diffusion coefficients of O_2 in different DMSO based electrolytes has therefore already been published with this cell [128]. This experiment is still frequently used in the electrochemistry laboratory of the University of Bonn. Furthermore, we could use this cell to construct another experiment to evaluate the homogeneous chemical kinetics of ORR by a redox mediator using defined transport conditions of O_2 in combination with numerical simulations (see chapter 6).

Another part of this work deals with the characterization of ORR products in Ca^{2+} containing DMSO as well as the products of the Mg deposition from MACC in TEGDME and the insertion of Mg into Sb by XPS. For this purpose a transfer device was constructed, which allows the transfer of samples from the electrochemical experiment which are performed in an Ar filled glovebox to the spectrometer without exposing the samples to laboratory air (see chapter 2.4.2).

Redox Mediators for the ORR and OER

Redox mediators have attracted much attention in the Li-O_2 community [198, 211]. It could be shown that the charging voltage of the Li-O_2 battery is reduced by OER mediators and that the discharge voltage and the discharage capacity of the Li-O_2 battery can be increased by ORR mediators. However impressive these studies may be, in order to keep up with Li-ion technology, Li-O_2 batteries must have comparable cycle counts and for this the mediators must have a high resistance to the reactive oxygen species formed in the Li-O_2 battery. Therefore, one object of investigation in this study was to examine the stability of redox mediators for the OER within the Li-O_2 cell. For this purpose the mediators TMPD and TTF known from the literature were examined. Thus it was possible to prove the instability of these molecules in situ in the OER by evaluation of the e^-/O_2 number. The instability of the redox mediators is further indicated by a CO_2 development in the MSCV. At the same time as we published these results, a study from the Aurbach group appeared which confirmed our observations [349]. However, the instability of these mediators was demonstrated by a long-term measurement and not in situ. We have already postulated, using TTF as an example, that one reason for instability is the formation of $^1O_2$ and the associated [2+2]-cycloaddition (see chapter 4. This was experimentally confirmed one year by Kwak *et al* [120]. Using the mediators TTF, TMPD, Fc and TEMPO, the kinetic of Li_2O_2 oxidation was studied. By combining a Nernst behavior for the oxidation of the mediator and assuming the Marcus theory for the oxidation of Li_2O_2 by the oxidized mediator, we were able to derive a model which we could confirm experimentally. From this study we could deduce that the oxidation of Li_2O_2 by RM^+ is conducted through an outer sphere electron transfer. The kinetics of the oxidation of Li_2O_2 by RM^+ is a topic of current research and discussion. Thus, in the same year in which we published our results Chen *et al.* published an opposing finding [60]. In 2019, however, Ko *et al.* published a study on this topic that confirms our findings [59].

Furthermore, we investigated the molecule DBBQ as a mediator for the ORR. DBBQ shows a strong interaction with the cations of the supporting electrolyte. Our investigations have shown that the ORR kinetics increases when the association between the cation and DBBQ increases. The reaction rates could be quantified by us (see 6). An increasing association between the cation in the supporting electrolyte and DBBQ also results in a shift of the ORR potential to higher potentials. This finding is of practical relevance, because the discharge voltage of a metal-O_2 battery could be increased, resulting in an increase of the energy density of the battery. To the best of our knowledge, our study on ORR kinetics by DBBQ is the only one so far.

Insights into the ORR and OER in Ca^{2+} containing DMSO

In recent years research on electrochemical Ca deposition / dissolution has grown and first promising results have been published [350]. Therefore, research on the ORR and the OER in Ca^{2+} containing electrolyte is of interest for the development of a Ca-O_2 battery. At the beginning of the work for this thesis only a few studies on ORR in Ca^{2+} containing electrolyte were available in the literature [351, 352]. The first basic research on this topic was published at the beginning of the work for this by Reinsberg and Baltuschat *et al.* [97]. The results showed promising findings concerning the ORR in Ca^{2+} containing DMSO. In the present study, based on this initial work, further experiments were performed to complete the mechanistic picture of the ORR in Ca^{2+} containing DMSO. It could be shown that Ca-superoxide, which was previously described as the main product of ORR in Ca^{2+} containing DMSO, disproportionates. This is of application-related relevance, because the Ca-peroxide thus formed would represent a Ca-O_2 cell with a considerably higher energy density. Furthermore, it could be shown that the formed Ca-peroxide is soluble in DMSO. Especially in comparison to Li-O_2 cell, it has a big advantage as the insolubility of Li_2O_2 is an issue in this technology. Using XPS Au and Pt surfaces could be characterized after the ORR in Ca^{2+} containing DMSO. It has been shown that the same ORR products can be detected on Au and Pt. These are decomposition products of the electrolyte in the top layer, followed by $Ca(O_2)_2$ and CaO_2. CaO was found close to the electrode surface. Based on this analysis we postulated that the observed transition from 2 e^- process to 1 e^- process is due to the formation of an adsorbed monolayer of CaO (or strongly adsorbed peroxide). Due to this irreversibly adsorbed layer, the active centers on the electrocatlyst necessary for the 2 e^- process are blocked and a transition to the 1 e^- process occurs. RDE measurements have shown that applying a potential of 0.4 V vs. $Ag^+ | Ag$ is necessary to regenerate the electrocatalyst. We were also able to confirm the functioning of DBBQ as ORR mediator in DMSO containing Ca^{2+} using DEMS.

XPS studies on the Mg deposition and insertion

In addition to the investigations on the insertion of Mg from MACC/TEGDME in Sb, which were already carried out in the Baltruschat working group, the electrodes are characterized at different preparation steps using XPS (see chapter 8). It could be shown that the electrochemically produced Sb electrodes are oxidized by the transfer through the laboratory air. The Sb 3d region showed a splitting of the Sb 3d doublet into two doublets, which could be assigned to Sb(0) and Sb(+III). The insertion of Mg from MACC/TEGDME reduces the Sb(+III) species. In general, a characterization of the electrode surface after insertion showed similar products as already known from Mg deposition on Pt from MACC/TEGDME [326–328]. Thus an irreversible Al deposition takes place. The Al accumulates on the surface and loses intensity in deeper layers. Another surface species is Cl, which is known in literature as an important additive for Mg deposition [323, 344]. The accumulation of Cl species on the surface is likely to be important for inhibiting surface passivation [343]. Al and Mg were detected on the surface mainly in the oxidized state. This is due to oxidation by contamination of O_2 and H_2O in the transfer system (even when filled with highly pure Ar) and the reactivity of these metal surfaces. By Ar^+ ethching, however, Mg(0) and Al(0) could be detected.

Outlook

The research field of metal-O_2 batteries is experiencing a strong participation due to the need for new electrochemical energy storage devices with energy densities greater than the Li-ion technology. This dissertation addresses kinetic investigations on redox mediators, the determination of solubility and transport properties of O_2 in the electrolyte, the characterization of the reaction in the Ca-O_2 cell and the Mg insertion in Sb. It has been shown that it is absolutely necessary to understand the side reactions by reactive oxygen species in the battery in order to optimize them. Some studies, which were carried out before the beginning the work for this thesis, have already pointed out the problem concerning the reactivity of the $O_2^{\cdot -}$ formed in the ORR [82–87, 106, 107]. Studies by other workgroups published duiring the work on this dissertation indicate $^1O_2$ as a main reason for the parasitic reactions in the metal O_2 battery [115–119, 122]. This species is the main reason for the decomposition of redox mediators. Therefore, the search for mediators that are stable in the metal-O_2 cell is of relevance. A recent study shows that possibly corrole-chelated metal complexes are stable redox mediators for the OER [353]. In general it is advisable to prevent the formation of $^1O_2$. A first approach is to use $^1O_2$ quencher [121]. In the future, however, redox mediators can also be tested for their suitability in reducing $^1O_2$ in the metal-O_2 battery. For example, a mediator can be used to reduce the OER potential below the formation of $^1O_2$. However, the formation of $^1O_2$ in the disproportionation of $O_2^{\cdot -}$ is problematic. But even here, a redox mediator that produces a 2 e^- reduction could inhibit the disproportionation reaction. To a large extent it is necessary to investigate the use of dual mediator systems in detail. There are already some publications on this topic [64], but there is a lack of detailed research on the reaction mechanism. Appendix B shows studies for the system DBBQ/I^-.

In summary, the development of a metal O_2 battery is currently slowed down mainly by the problems with side reactions. Therefore it is even more important to characterize the chemical reactions on the anode and cathode in detail. In this way it is possible to suppress the side reactions. This work provides some important contributions towards side reactions and a characterization of the reactions in the Li-O_2 cell with redox mediators as additive, the Ca-O_2 cell and the Mg insertion in Sb is given. If one additionally considers the developments in research on metal-O_2 batteries, approaches to solve some problems have already been found. These developments make the construction of the metal O_2 battery look promising.

A

Fabrication of Super P Carbon DEMS membranes

Furthermore, iodide should be investigated as a redox mediator for the OER with the new DEMS cell described in chapter 4. The porous PTFE membranes in the Baltruschat lab, on which Pt and Au were deposited, are not suitable for these experiments. This is due to the fact that Iodo-Pt and Iodo-Au complexes have a high stability constant, which shifts the Au and Pt dissolution to lower potentials (into the potential range of I_2 formation). Therefore the development of carbon-DEMS membranes was necessary. For this purpose, a recipe that has already been tested by project partners from the "Zentrum für Sonnenenergie- und Wasserstoff-Forschung Baden-Württemberg" for the application in Li ion batteries and Li-O_2 cells was used [93]. This recipe was optimized for DEMS application:

A suspension of 80% Super P Carbon[1] (*Alfa Aesar*, 99%) and 20% polyvinylidene fluoride (PVDF, *Sigma Aldrich*) in N-methyl-2-pyrrolidone (NMP, Sigma Aldrich, $\geq$99.0%) is produced. The concentration of Super P carbon and PVDF in NMP is $5.4\,\mathrm{g\,L^{-1}}$. The suspension is stirred for 24 hours. In the next step, the porous PTFE DEMS membrane with a thickness of 50 µm and a porosity of 50% is placed in a petri dish. A sharp-edged stainless steel tube is pressed onto the membrane. This serves to limit a defined area. The suspension is then added to this area so that a loading of $0.2\,\mathrm{mg\,cm^{-2}}$ is achieved. The surface is filled with NMP until it is completely wetted. The Petri dish is then placed on a heating plate and the solvent is evaporated in a fume cupboard at 60°C. A photo of the resulting membrane is shown in Figure A.1. The electrodes can now be stamped out of this membrane.

In order to ensure a complete electrical contact of the Super P carbon surface, one of the PTFE spacers used in the DEMS cell (see chapter 4) is replaced by an Au coated spacer. This spacer is pressed onto the Super P electrode and contacted with the potentiostat using an Au

---

[1] Super P Carbon is obtained by oxidation products from the petroleum industry. It is known for its high surface area and good electrical conductivity. The high proportion of sp^2-hypritized carbon is responsible for the good electrical conductivity (sp^3/sp^2=2.44) [354].

wire. This method increases the contact area between carbon and gold. The assembly described here is also sketched in Figure A.1.

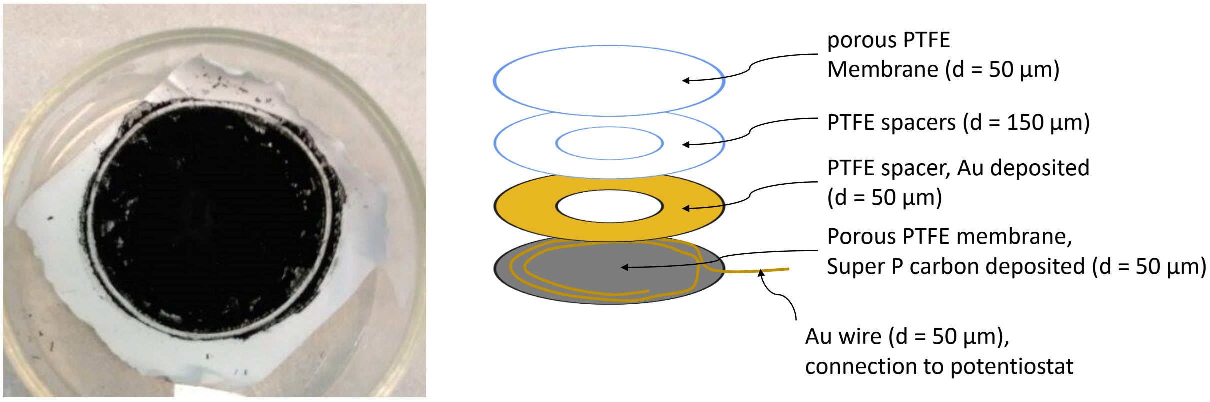

Figure A.1: Picture of the Super P Carbon DEMS membrane (left) as well as an illustration of the assembling of the cell components (right). Here the thickness *d* of the diffrent components is included.

Due to the high surface area, higher double layer currents have been observed for the experiments with the Super P carbon electrode than with the Au electrodes. In addition, these electrodes were cycled in oxygen-free electrolytes before starting the measurement with the mediator until a stable CV was obtained (see A.2).

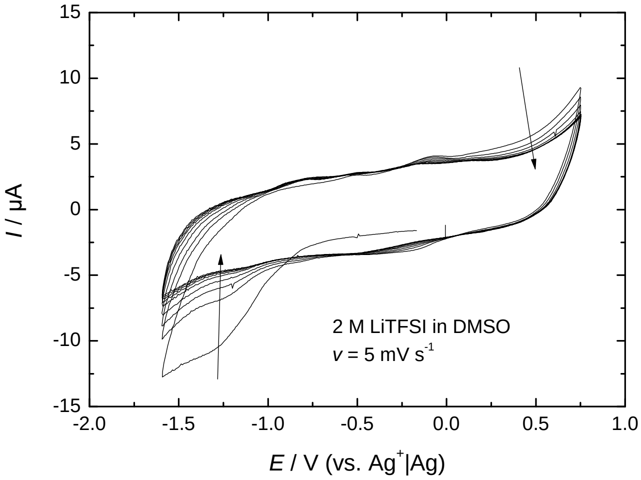

Figure A.2: Time evolution of the double layer current of the Super P Carbon DEMS electrode.

B

Dual mediator system for the Li-O_2 cell

The suitability of LiI as a mediator for the OER is investigated. In a second step DBBQ will be added as a mediator for the ORR to construct a dual-mediator Li-O_2 cell. DBBQ was already examined as mediator for the ORR in chapter6. The measurements are performed in 2 M LiTFSI in DMSO (see Figure B.1 and in TEGDME (see Figure B.2) based electrolytes. The Figures B.1 show (a) and B.2 (a) are showing the DEMS measurements in the supporting electrolyte without addition of the mediators. As DEMS cell the previously described thin layer DEMS cell (see chapter 4) was used. The working electrode is a porous PTFE membrane on which Super P Carbon was deposited. The reversibility *Rev* from OER charge to ORR charge, determined from the MSCV data for $\dot{n}_{32}$ as well as the average electron numbers for ORR z_{ORR} and OER z_{OER} are calculated for the shown measurements. The results are listed in the tables B.1 and B.2. It is noticeable here that the measurements without mediator show $z_{ORR} > 2$. This is probably due to the use of Super P carbon as electrode material, since it is known that carbon based electrodes can be attacked by reactive oxygen species [241].

I^- is oxidized to I_2 during a positive sweep in a two-stage process:

$$3\,I^- \longrightarrow {I_3}^- + 2\,e^- \tag{B.1}$$

$$2\,{I_3}^- \longrightarrow 3\,I_2 + 2\,e^- \tag{B.2}$$

These two processes occur at different potentials and are represented by two peaks in the CVs in O_2 free solution in Figure B.1 (b) and Figure B.2 (b). In these figures the potential range of ${I_3}^-$ formation was highlighted in blue (region I) and the potential range of I_2 formation was highlighted in green (region II). It is noticeable that a comparison of the $\dot{n}_{32}$ in Figure B.1 (a) and (b) shows that ${I_3}^-$ acts as a mediator for the OER. The same comparison for measurements in the TEGDME based electrolyte (see Figure B.2 (a) and (b)) only shows here I_2 as a redox mediator for the OER. In general, the *Rev* values increase in both DMSO and TEGDME electrolytes when LiI is added to the supporting electrolyte. In TEGDME based electrolyte the kinetics for the OER by I_2 is slow, which means that the OER is not completed in a sweep. Therefore a potential stop in the OER was performed here until $\dot{n}_{32}$ drops to the baseline to determine *Rev*. However, this procedure makes an evaluation of z_{OER} no longer possible (this is why the entries in table B.2 are missing).

The addition of DBBQ to the DMSO and TEGDME based electrolyte significantly lowers the *Rev* value. This trend does not correspond to the expectation, since it is assumed that the Li_2O_2 formed by the DBBQ within the electrolyte volume should be oxidized by I_3^- or I_2 and should lead to a similar reversibility as only with LiI in the electrolyte. For the DMSO based electrolyte, additional measurements were made with a 2 M LiTFSI with 10 mM DBBQ. The measurements are not shown here, but table B.1 shows the relevant values. It can be seen that the addition of LiI increases the reversibility from 12% (only DBBQ) to 28% (DBBQ and LiI), which underlines the mediation effect of LiI. A further observation is that the electron number of ORR z_{ORR} in the double mediator system is lower in both cases than the expected value of 2 e^-/O_2. This could be an indication that the two mediators have influenced each other. It was also observed that the measurements in the double-mediator system shows higher CO_2 signals. Therefore, it can be assumed that in the presence of DBBQ the proportion of side reactions that produce CO_2 releasing species is higher.

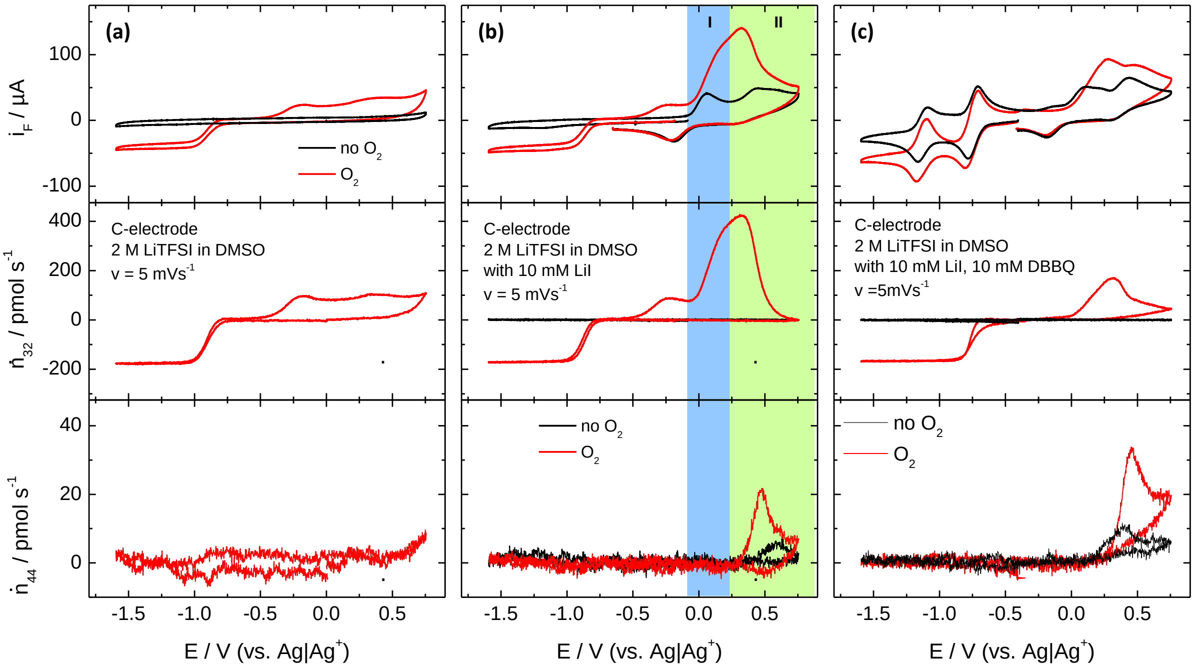

Figure B.1: CVs, oxygen flows $\dot{n}_{32}$ and carbon dioxide flows $\dot{n}_{44}$ for different electrolytes: (a) 2 M LiTFSI in DMSO, (b) 2 M LiTFSI in DMSO with 10 mM LiI and (c) 2 M LiTFSI in DMSO with 10 mM LiI and 10 mM DBBQ.

Table B.1: Summary of the results in 2 M LiTFSI in DMSO based electrolytes with different combinations of the redox mediators DBBQ and LiI. The reversibilities with respect to the oxygen signal in mass spectrometry *Rev* were calculated. Furthermore the electron numbers of the ORR z_{ORR} and the OER z_{OER} have been calculated.

Electrolyte	*Rev*	z_{ORR}	z_{OER}
without mediator	47%	2.13	2.61
10 mM LiI	79%	2.14	2.46
10 mM DBBQ	12%	2.14	2.82
10 mM LiI and 10 mM DBBQ	28%	1.73	2.56

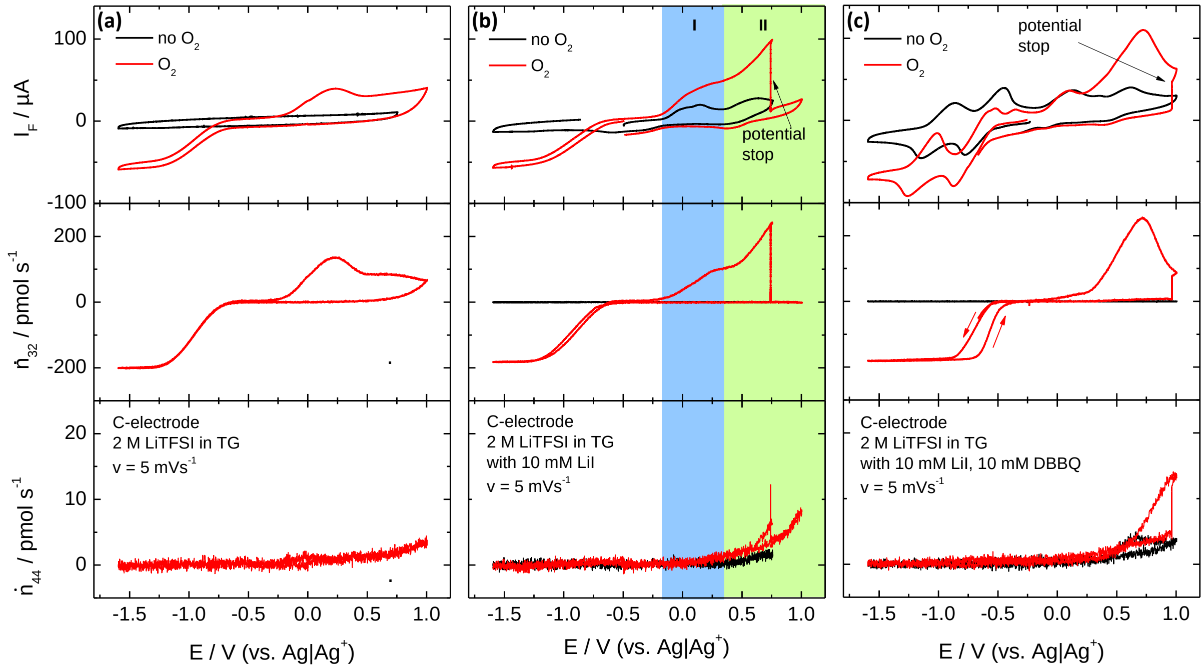

Figure B.2: CVs, oxygen flows $\dot{n}_{32}$ and carbon dioxide flows $\dot{n}_{44}$ for different electrolytes: (a) 2 M LiTFSI in TEGDME, (b) 2 M LiTFSI in TEGDME with 10 mM LiI and (c) 2 M LiTFSI in TEGDME with 10 mM LiI and 10 mM DBBQ.

Table B.2: Summary of the results in 2 M LiTFSI in TEGDME based electrolytes with different combinations of the redox mediators DBBQ and LiI. The reversibilities with respect to the oxygen signal in mass spectrometry *Rev* were calculated. Furthermore, the electron numbers of ORR z_{ORR} and OER z_{OER} have been calculated.

Electrolyte	*Rev*	z_{ORR}	z_{OER}
without mediator	39%	2.58	2.45
10 mM LiI	76%	2.14	-
10 mM LiI and 10 mM DBBQ	44%	1.12	-

Iodid mediation of the OER in Ca^{2+} containing DMSO

Iodide was investigated as a redox mediator for the OER in DMSO containing Ca^{2+}, since it had been shown that iodide can increase the reversibility of a Li-O_2 cell (see Appendix B). This mediator is mainly known from studies on the Li-O_2 battery [53, 55]. DEMS measurements were carried out with the cell described in [58] using a porous PTFE membrane coated with SuperP Carbon as electrode. Figure C.1 shows the DEMS measurements without iodide (a) and with iodide (b).

In particular, a comparison of the MSCVs of O_2 in Figure C.1 shows that the kinetics of the OER are faster in the presence of iodide in the electrolyte. This is also shown by the fact that at the upper potential limit of the CV the OER in the iodide containing electrolyte is allready finished. This effect is even more obvious in Figure C.2. There the MSCVs of O_2 from Figure C.1 were normalized to the diffusion limited current of the ORR. In this figure, the MSCV in the iodide-containing electrolyte shows higher currents in the OER. In the presence of iodide in the electrolyte the CO_2 development is shifted by 250 mV to more negative electrode potentials. Thus the onset of CO_2 development correlates here with that of the formation of I_2 (second redox peak in the CV at anodic sweep). It is conceivable here that the oxidation of decomposition products of the electrolyte is favoured by I_2. With regard to the reversibility of the OER charge to the ORR charge, only a small improvement can be observed with the addition of iodide (from 41 % to 50 %).

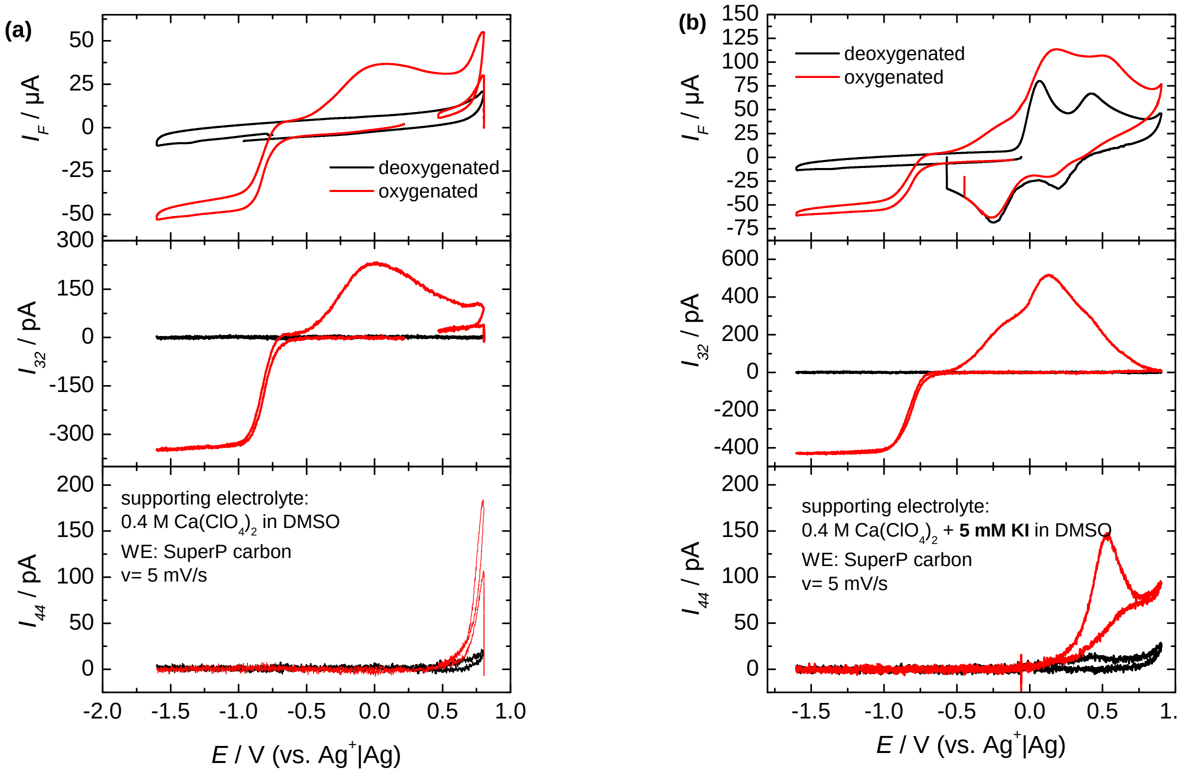

Figure C.1: (a) DEMS measurement in 0.4 M $Ca(ClO_4)_2$ in DMSO. (b) DEMS measurement in 0.4 M $Ca(ClO_4)_2$ +5 mM KI in DMSO. In the measurements shown in red, the electrolyte was saturated with 800 mbar O_2. Different diffusion limiting currents result from different electrolyte layer thicknesses, which result from the assembly of the cell (compare [58]). In the measurements shown in black there is no O_2 in the electrolyte.

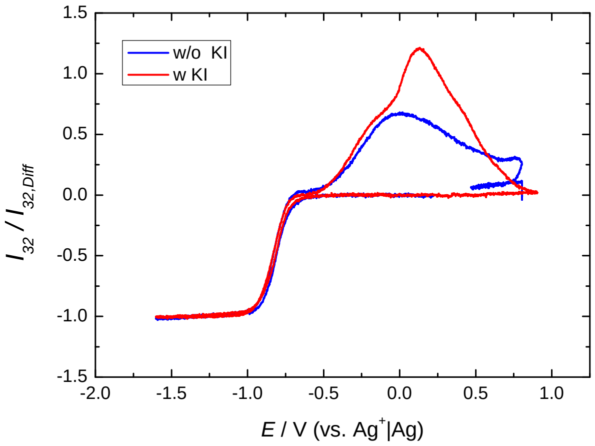

Figure C.2: MSCVs normalized to the diffusion limit current of the ORR of the ion current of O_2 from Figure C.1.

D

Finite diffrence RRDE simulations

The algorithm for simulating RRDE experiments already described in chapter 3.3 can be used to validate the experimental data. For example, Figure D.1 shows transients of the ring current of the reduction of the decamethylferrocene cation. The decamethylferrocene cation was previously formed by a sudden potential jump in the oxidation of decamethylferrocene at the disc electrode. This experiment was already illustrated in chapter 2.2. Figure D.1 shows a comparison between the experimental data (circles) and the simulated transients (lines). It can be seen that the finite difference algorithm reproduces the experimental data excellently.

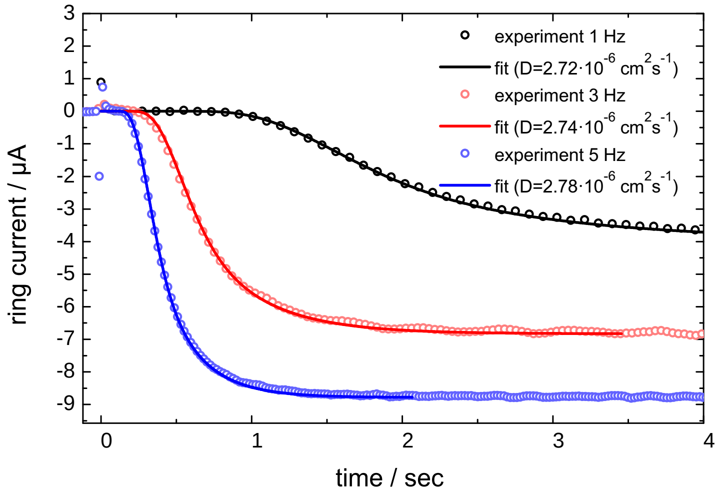

Figure D.1: A comparison between the experimental ring current and the simulated ring current for the reduction of the decamethylferrocene cation. This was previously formed in a potential jump at the disc electrode. The adjusted diffusion coefficients are shown in the figure.

RRDE simulations can also be used to illustrate the consequences of the simplifications made when deriving the common formulas for RRDE. In chapter 2.2, the expression for the collection efficiency of the RRDE is already given (see equation 2.12). In the derivation of this expression the series expansion for the description of the velocity field of the electrolyte in front of the RRDE (see also chapter 2.2 after the first element was stopped. Figure D.2 shows that the calculated values for the collection efficiency according to equation 2.12 as well as the simulated values for the collection efficiency, if only the first Kraman-Crohan-coefficient is used in the simulation. In this case an excellent agreement between those two values is produced. However, if the simulation uses the entirety of the published Kraman-Crohan coefficients (up to the ninth element of the series expansion) [177], a clear deviation from the previously calculated values for the collection efficiency can be seen (see red line in Figure D.2). This shows that it is possible to achieve more precise results with the numerical RRDE simulations than it is possible with the usual formula for the RRDE. If particularly complex kinetic models, such as those used in ORR, are to investigated, a fit of the experimental data using the RRDE simulations should provide more accurate results.

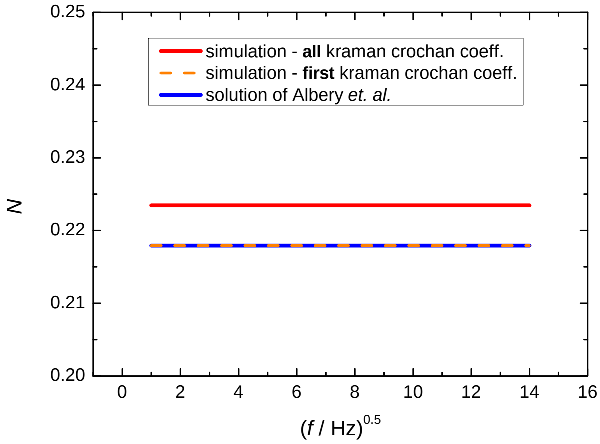

Figure D.2: A comparison of the collection efficiencies of RRDE with different precise velocity fields (simulation) to the calculated value for the collection efficiency using the published asymptotic expression.

For the further RRDE simulations, we have cooperated with Dr. Jürgen Fuhrmann, René Kehl and Dr. Christian Merdon of the Weierstrass Institute for Applied Analysis and Stochastics in Berlin (WIAS) . A new RRDE code was developed at WIAS. This new code could be benchmarked against the finite difference code. The simulation times of both codes and the simulated results were compared. Figure D.3 shows the simulation times for a linear sweep experiment for different rotation frequencies. The required simulation time increases with the rotation frequency.

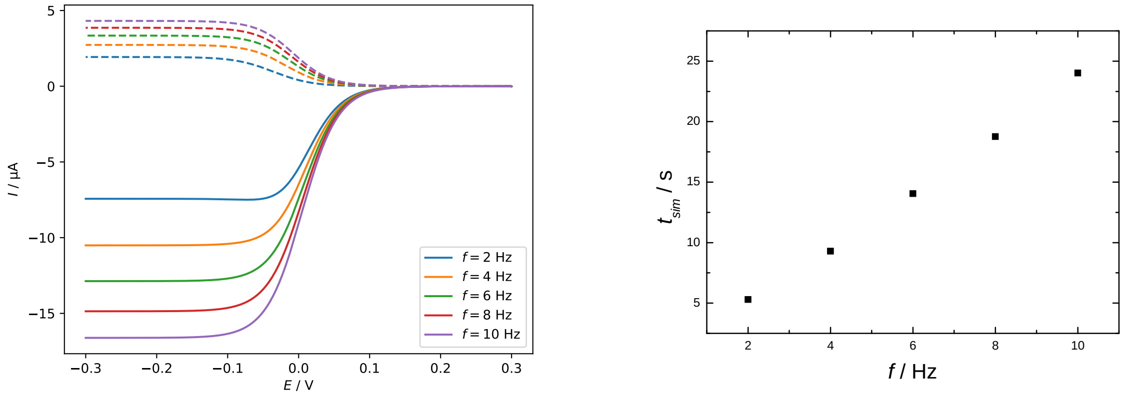

Figure D.3: Simulated linear sweep voltammery for an RRDE for different rotation frequencies (left) and required simulation time (right). The sweep rate was 10 mV s^{-1}. A redox system was simulated, which shows a Nernst behavior. This is reduced at the disc electrode (solid line) and oxidized at the ring electrode (dashed line).

Furthermore, Figure D.4 shows the collection efficiencies N in the steady state for different refined grids. The grid is refined by increasing k_0 and decreasing $\bar{\beta}$ (see chapter 3.3). Also shown is the N value that was calculated for the same RRDE geometry with the WIAS code. It can be seen that when refining the grid, the finite difference value for N follows that produced with the WIAS code. At the same time, the simulation time required increases significantly (see the numbers in Figure D.4). For comparison: The WIAS code needs 2 s to calculate the N value, whereas the calculation with the finite difference code needs 233.33 s for the finest grid used. This comparison shows that using the WIAS code, it is possible to make a time effective adjustment of experimental RRDE data using numerical simulations. At the time of writing this thesis this comparison is still ongoing research between the University of Bonn and WIAS.

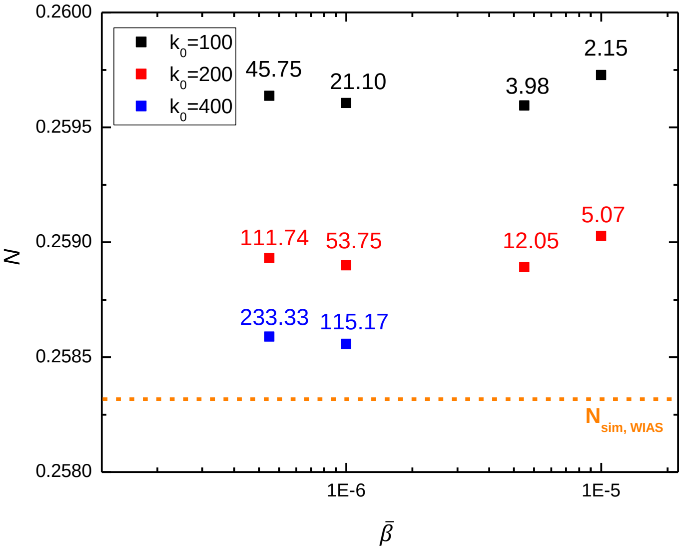

Figure D.4: Calculated collection efficencies for different fine grids for the finite difference algorithm. In addition, the calculated N value with the WIAS code is shown as well as the required simulation times in seconds.

Bibliography

[1] FFF, Fridays for future - what we do, `https://fridaysforfuture.org/what-we-do/who-we-are/`, (accessed: 23.04.2020).

[2] United Nations - The Paris Agreement, `https://unfccc.int/process-and-meetings/the-paris-agreement/the-paris-agreement`, (accessed: 23.04.2020).

[3] J. Hansen, M. Sato, P. Kharecha, D. Beerling, R. Berner, V. Masson-Delmotte, M. Pagani, M. Raymo, D. L. Royer, J. C. Zachos, *The Open Atmospheric Science Journal* **2008**, *2*, 217–231.

[4] J. Hansen, R. Ruedy, M. Sato, K. Lo, *Reviews of Geophysics* **2010**, *48*, DOI `10.1029/2010rg000345`.

[5] M. Sterner, I. Stadler, *Energiespeicher - Bedarf, Technologien, Integration*, Springer Berlin Heidelberg, **2014**.

[6] A. Energiewende, Agora Energiewende, `https://www.agora-energiewende.de/presse/neuigkeiten-archiv/corona-krise-und-milder-winter-lassen-deutschland-klimaziel-fuer-2020-erreichen-1/`, (accessed: 15.04.2020).

[7] Y. Nishi, *The Chemical Record* **2001**, *1*, 406–413.

[8] M. S. WHITTINGHAM, *Science* **1976**, *192*, 1126–1127.

[9] K. Mizushima, P. Jones, P. Wiseman, J. Goodenough, *Materials Research Bulletin* **1980**, *15*, 783–789.

[10] T. W. Post, The cobalt pipeline, `https://www.washingtonpost.com/graphics/business/batteries/congo-cobalt-mining-for-lithium-ion-battery/`, (accessed: 15.04.2020).

[11] E. Corcoran, *Sick water?: the central role of wastewater management in sustainable development: a rapid response assessment*, UNEP/Earthprint, **2010**.

[12] W. Liu, D. B. Agusdinata, *Journal of Cleaner Production* **2020**, *260*, 120838.

[13] G. Leclanché, "une pile à oxyde insoluble" [an insoluble oxide battery], French patent no. 71 865, **1866**.

[14] L. David, B. R. Thomas, Handbook of batteries, **2001**.

[15] G. W. Heise, Air-depolarized primary battery, US Patent 1 899 615, **1933**.

[16] A. M. Colclasure, K. A. Smith, R. J. Kee, *Electrochimica Acta* **2011**, *58*, 33–43.

[17] P. Lu, S. J. Harris, *Electrochemistry Communications* **2011**, *13*, 1035–1037.

[18] Süddeutsche Zeitung, Nur Tesla kann das E-Auto aus der Nische holen, `https://www.sueddeutsche.de/auto/zukunftsplaene-des-herstellers-nur-tesla-kann-das-e-auto-aus-der-nische-holen-1.3114836`, (accessed: 16.04.2020).

[19] A. Eftekhari, *ACS Sustainable Chemistry & Engineering* **2018**, *7*, 3684–3687.

[20] G. E. Blomgren, *Journal of The Electrochemical Society* **2016**, *164*, A5019–A5025.

[21] N. Nitta, F. Wu, J. T. Lee, G. Yushin, *Materials Today* **2015**, *18*, 252–264.

[22] Batterie2020, LiBaLu: Suche nach dem besten Elektrolyt, `https://batterie-2020.de/projekte/forschungsfelder/zukuenftige-batteriesysteme/libalu-suche-nach-dem-besten-elektrolyt/`, (accessed: 20.04.2020).

[23] C. Wang, Y. Yu, J. Niu, Y. Liu, D. Bridges, X. Liu, J. Pooran, Y. Zhang, A. Hu, *Applied Sciences* **2019**, *9*, 2787.

[24] Y. Zhang, L. Wang, Z. Guo, Y. Xu, Y. Wang, H. Peng, *Angewandte Chemie International Edition* **2016**, *55*, 4487–4491.

[25] V. Viswanathan, K. S. Thygesen, J. S. Hummelshøj, J. K. Nørskov, G. Girishkumar, B. D. McCloskey, A. C. Luntz, *The Journal of Chemical Physics* **2011**, *135*, 214704.

[26] C. Bondue, P Reinsberg, A. Abd-El-Latif, H Baltruschat, *Physical Chemistry Chemical Physics* **2015**, *17*, 25593–25606.

[27] B. D. McCloskey, C. M. Burke, J. E. Nichols, S. E. Renfrew, *Chemical Communications* **2015**, *51*, 12701–12715.

[28] A. C. Luntz, V. Viswanathan, J. Voss, J. B. Varley, J. K. Nørskov, R. Scheffler, A. Speidel, *The Journal of Physical Chemistry Letters* **2013**, *4*, 3494–3499.

[29] O. Gerbig, R. Merkle, J. Maier, *Advanced Materials* **2013**, *25*, 3129–3133.

[30] J. B. Varley, V. Viswanathan, J. K. Nørskov, A. C. Luntz, *Energy Environ. Sci.* **2014**, *7*, 720–727.

[31] W. Li, H. Yao, K. Yan, G. Zheng, Z. Liang, Y.-M. Chiang, Y. Cui, *Nature Communications* **2015**, *6*, DOI `10.1038/ncomms8436`.

[32] Here's why Samsung Note 7 phones are catching fire, `https://www.cnet.com/news/why-is-samsung-galaxy-note-7-exploding-overheating/`, (accessed: 22.04.2020).

[33] W. Yin, A. Grimaud, F. Lepoivre, C. Yang, J. M. Tarascon, *The Journal of Physical Chemistry Letters* **2016**, *8*, 214–222.

[34] X. Gao, Z. P. Jovanov, Y. Chen, L. R. Johnson, P. G. Bruce, *Angewandte Chemie International Edition* **2017**, *56*, 6539–6543.

[35] D. G. Kwabi, T. P. Batcho, S. Feng, L. Giordano, C. V. Thompson, Y. Shao-Horn, *Physical Chemistry Chemical Physics* **2016**, *18*, 24944–24953.

[36] N. B. Aetukuri, B. D. McCloskey, J. M. García, L. E. Krupp, V. Viswanathan, A. C. Luntz, *Nature Chemistry* **2014**, *7*, 50–56.

[37] R. R. Mitchell, B. M. Gallant, Y. Shao-Horn, C. V. Thompson, *The Journal of Physical Chemistry Letters* **2013**, *4*, 1060–1064.

[38] C. Xia, R. Black, R. Fernandes, B. Adams, L. F. Nazar, *Nature Chemistry* **2015**, *7*, 496–501.

[39] K. U. Schwenke, M. Metzger, T. Restle, M. Piana, H. A. Gasteiger, *Journal of The Electrochemical Society* **2015**, *162*, A573–A584.

[40] D. Zhai, H.-H. Wang, J. Yang, K. C. Lau, K. Li, K. Amine, L. A. Curtiss, *Journal of the American Chemical Society* **2013**, *135*, 15364–15372.

[41] M. J. Lacey, J. T. Frith, J. R. Owen, *Electrochemistry Communications* **2013**, *26*, 74–76.

[42] L. Yang, J. T. Frith, N. Garcia-Araez, J. R. Owen, *Chemical Communications* **2015**, *51*, 1705–1708.

[43] W. R. Torres, F. Davia, M. del Pozo, A. Y. Tesio, E. J. Calvo, *Journal of The Electrochemical Society* **2017**, *164*, A3785–A3792.

[44] T. Homewood, J. T. Frith, J. P. Vivek, N. Casañ-Pastor, D. Tonti, J. R. Owen, N. Garcia-Araez, *Chemical Communications* **2018**, *54*, 9599–9602.

[45] S. Matsuda, K. Hashimoto, S. Nakanishi, *The Journal of Physical Chemistry C* **2014**, *118*, 18397–18400.

[46] X. Gao, Y. Chen, L. Johnson, P. G. Bruce, *Nature Materials* **2016**, *15*, 882–888.

[47] T. Liu, J. T. Frith, G. Kim, R. N. Kerber, N. Dubouis, Y. Shao, Z. Liu, P. C. M. M. Magusin, M. T. L. Casford, N. Garcia-Araez, C. P. Grey, *Journal of the American Chemical Society* **2018**, *140*, 1428–1437.

[48] J. P. Vivek, T. Homewood, N. Garcia-Araez, *The Journal of Physical Chemistry C* **2019**, *123*, 20241–20250.

[49] Y.-C. Lu, Y. Shao-Horn, *The Journal of Physical Chemistry Letters* **2012**, *4*, 93–99.

[50] Y. Chen, S. A. Freunberger, Z. Peng, O. Fontaine, P. G. Bruce, *Nature chemistry* **2013**, *5*, 489.

[51] Y. Qiao, S. Ye, *The Journal of Physical Chemistry C* **2016**, *120*, 15830–15845.

[52] B. J. Bergner, A. Schürmann, K. Peppler, A. Garsuch, J. Janek, *Journal of the American Chemical Society* **2014**, *136*, 15054–15064.

[53] H.-D. Lim, H. Song, J. Kim, H. Gwon, Y. Bae, K.-Y. Park, J. Hong, H. Kim, T. Kim, Y. H. Kim, et al., *Angewandte Chemie International Edition* **2014**, *53*, 3926–3931.

[54] W.-J. Kwak, D. Hirshberg, D. Sharon, H.-J. Shin, M. Afri, J.-B. Park, A. Garsuch, F. F. Chesneau, A. A. Frimer, D. Aurbach, Y.-K. Sun, *Journal of Materials Chemistry A* **2015**, *3*, 8855–8864.

[55] T. Liu, M. Leskes, W. Yu, A. J. Moore, L. Zhou, P. M. Bayley, G. Kim, C. P. Grey, *Science* **2015**, *350*, 530–533.

[56] W.-J. Kwak, D. Hirshberg, D. Sharon, M. Afri, A. A. Frimer, H.-G. Jung, D. Aurbach, Y.-K. Sun, *Energy & Environmental Science* **2016**, *9*, 2334–2345.

[57] Z. Liang, Y.-C. Lu, *Journal of the American Chemical Society* **2016**, *138*, 7574–7583.

[58] P. P. Bawol, P. Reinsberg, C. J. Bondue, A. A. Abd-El-Latif, P. Königshoven, H. Baltruschat, *Physical Chemistry Chemical Physics* **2018**, *20*, 21447–21456.

[59] Y. Ko, H. Park, B. Lee, Y. Bae, S. K. Park, K. Kang, *Journal of Materials Chemistry A* **2019**, *7*, 6491–6498.

[60] Y. Chen, X. Gao, L. R. Johnson, P. G. Bruce, *Nature communications* **2018**, *9*, 767.

[61] T. H. Yoon, Y. J. Park, *RSC Advances* **2014**, *4*, 17434.

[62] W. Zhang, Y. Shen, D. Sun, Z. Huang, J. Zhou, H. Yan, Y. Huang, *Nano Energy* **2016**, *30*, 43–51.

[63] T. Liu, J. P. Vivek, E. W. Zhao, J. Lei, N. Garcia-Araez, C. P. Grey, *Chemical Reviews* **2020**, DOI `10.1021/acs.chemrev.9b00545`.

[64] X. Gao, Y. Chen, L. R. Johnson, Z. P. Jovanov, P. G. Bruce, *Nature Energy* **2017**, *2*, DOI `10.1038/nenergy.2017.118`.

[65] W.-J. Kwak, S. H. Ha, D. H. Kim, K. H. Shin, Y.-K. Sun, Y. J. Lee, *ACS Catalysis* **2017**, *7*, 8192–8199.

[66] Z. Liang, Y. Zhou, Y.-C. Lu, *Energy & Environmental Science* **2018**, *11*, 3500–3510.

[67] K. Abraham, Z Jiang, *Journal of The Electrochemical Society* **1996**, *143*, 1–5.

[68] D Aurbach, B Markovsky, I Weissman, E Levi, Y Ein-Eli, *Electrochimica Acta* **1999**, *45*, 67–86.

[69] G. Gachot, S. Grugeon, M. Armand, S. Pilard, P. Guenot, J.-M. Tarascon, S. Laruelle, *Journal of Power Sources* **2008**, *178*, 409–421.

[70] T. Ogasawara, A. Débart, M. Holzapfel, P. Novák, P. G. Bruce, *Journal of the American Chemical Society* **2006**, *128*, 1390–1393.

[71] A. Débart, J. Bao, G. Armstrong, P. G. Bruce, *Journal of Power Sources* **2007**, *174*, 1177–1182.

[72] A. Débart, A. Paterson, J. Bao, P. Bruce, *Angewandte Chemie International Edition* **2008**, *47*, 4521–4524.

[73] G. Girishkumar, B. McCloskey, A. C. Luntz, S. Swanson, W. Wilcke, *The Journal of Physical Chemistry Letters* **2010**, *1*, 2193–2203.

[74] A. K. Thapa, T. Ishihara, *Journal of Power Sources* **2011**, *196*, 7016–7020.

[75] A. K. Thapa, T. H. Shin, S. Ida, G. U. Sumanasekera, M. K. Sunkara, T. Ishihara, *Journal of Power Sources* **2012**, *220*, 211–216.

[76] Y.-C. Lu, Z. Xu, H. A. Gasteiger, S. Chen, K. Hamad-Schifferli, Y. Shao-Horn, *Journal of the American Chemical Society* **2010**, *132*, 12170–12171.

[77] J. Read, *Journal of The Electrochemical Society* **2002**, *149*, A1190.

[78] X. Ren, S. S. Zhang, D. T. Tran, J. Read, *Journal of Materials Chemistry* **2011**, *21*, 10118.

[79] D. Zhang, Z. Fu, Z. Wei, T. Huang, A. Yu, *Journal of The Electrochemical Society* **2010**, *157*, A362.

[80] H. Cheng, K. Scott, *Applied Catalysis B: Environmental* **2011**, *108-109*, 140–151.

[81] S. R. Younesi, S. Urbonaite, F. Björefors, K. Edström, *Journal of Power Sources* **2011**, *196*, 9835–9838.

[82] B. D. McCloskey, D. S. Bethune, R. M. Shelby, G. Girishkumar, A. C. Luntz, *The Journal of Physical Chemistry Letters* **2011**, *2*, 1161–1166.

[83] G. M. Veith, N. J. Dudney, J. Howe, J. Nanda, *The Journal of Physical Chemistry C* **2011**, *115*, 14325–14333.

[84] S. A. Freunberger, Y. Chen, Z. Peng, J. M. Griffin, L. J. Hardwick, F. Bardé, P. Novák, P. G. Bruce, *Journal of the American Chemical Society* **2011**, *133*, 8040–8047.

[85] J. Xiao, J. Hu, D. Wang, D. Hu, W. Xu, G. L. Graff, Z. Nie, J. Liu, J.-G. Zhang, *Journal of Power Sources* **2011**, *196*, 5674–5678.

[86] W. Xu, V. V. Viswanathan, D. Wang, S. A. Towne, J. Xiao, Z. Nie, D. Hu, J.-G. Zhang, *Journal of Power Sources* **2011**, *196*, 3894–3899.

[87] W. Xu, K. Xu, V. V. Viswanathan, S. A. Towne, J. S. Hardy, J. Xiao, Z. Nie, D. Hu, D. Wang, J.-G. Zhang, *Journal of Power Sources* **2011**, *196*, 9631–9639.

[88] D. Aurbach, M. Daroux, P. Faguy, E. Yeager, *Journal of Electroanalytical Chemistry and Interfacial Electrochemistry* **1991**, *297*, 225–244.

[89] S. Wu, Y. Qiao, S. Yang, J. Tang, P. He, H. Zhou, *ACS Catalysis* **2018**, *8*, 1082–1089.

[90] C. Bondue, A. Abd-El-Latif, P Hegemann, H Baltruschat, *Journal of The Electrochemical Society* **2015**, *162*, A479–A487.

[91] C. O. Laoire, S. Mukerjee, K. M. Abraham, E. J. Plichta, M. A. Hendrickson, *The Journal of Physical Chemistry C* **2009**, *113*, 20127–20134.

[92] C. O. Laoire, S. Mukerjee, K. M. Abraham, E. J. Plichta, M. A. Hendrickson, *The Journal of Physical Chemistry C* **2010**, *114*, 9178–9186.

[93] M. Marinaro, S. K. E. Moorthy, J. Bernhard, L. Jörissen, M. Wohlfahrt-Mehrens, U. Kaiser, *Beilstein Journal of Nanotechnology* **2013**, *4*, 665–670.

[94] F. D. Giorgio, F. Soavi, M. Mastragostino, *Electrochemistry Communications* **2011**, *13*, 1090–1093.

[95] J. Herranz, A. Garsuch, H. A. Gasteiger, *The Journal of Physical Chemistry C* **2012**, *116*, 19084–19094.

[96] P. H. Reinsberg, PhD thesis, Universitäts-und Landesbibliothek Bonn, **2019**.

[97] P. Reinsberg, C. J. Bondue, H. Baltruschat, *The Journal of Physical Chemistry C* **2016**, *120*, 22179–22185.

[98] P. Reinsberg, C. Bondue, H. Baltruschat, *Electrochimica Acta* **2016**, *200*, 214–221.

[99] P. Hartmann, C. L. Bender, M. Vračar, A. K. Dürr, A. Garsuch, J. Janek, P. Adelhelm, *Nature Materials* **2012**, *12*, 228–232.

[100] N. Xiao, R. T. Rooney, A. A. Gewirth, Y. Wu, *Angewandte Chemie* **2018**, *130*, 1241–1245.

[101] X. Ren, K. C. Lau, M. Yu, X. Bi, E. Kreidler, L. A. Curtiss, Y. Wu, *ACS Applied Materials & Interfaces* **2014**, *6*, 19299–19307.

[102] L. Lutz, W. Yin, A. Grimaud, D. A. D. Corte, M. Tang, L. Johnson, E. Azaceta, V. Sarou-Kanian, A. J. Naylor, S. Hamad, J. A. Anta, E. Salager, R. Tena-Zaera, P. G. Bruce, J.-M. Tarascon, *The Journal of Physical Chemistry C* **2016**, *120*, 20068–20076.

[103] W.-J. Kwak, Rosy, D. Sharon, C. Xia, H. Kim, L. R. Johnson, P. G. Bruce, L. F. Nazar, Y.-K. Sun, A. A. Frimer, M. Noked, S. A. Freunberger, D. Aurbach, *Chemical Reviews* **2020**, DOI `10.1021/acs.chemrev.9b00609`.

[104] R. S. Assary, K. C. Lau, K. Amine, Y.-K. Sun, L. A. Curtiss, *The Journal of Physical Chemistry C* **2013**, *117*, 8041–8049.

[105] V. S. Bryantsev, V. Giordani, W. Walker, M. Blanco, S. Zecevic, K. Sasaki, J. Uddin, D. Addison, G. V. Chase, *The Journal of Physical Chemistry A* **2011**, *115*, 12399–12409.

[106] V. S. Bryantsev, M. Blanco, *The Journal of Physical Chemistry Letters* **2011**, *2*, 379–383.

[107] V. S. Bryantsev, F. Faglioni, *The Journal of Physical Chemistry A* **2012**, *116*, 7128–7138.

[108] V. S. Bryantsev, J. Uddin, V. Giordani, W. Walker, D. Addison, G. V. Chase, *Journal of The Electrochemical Society* **2012**, *160*, A160–A171.

[109] P. H. Reinsberg, A. Koellisch, P. P. Bawol, H. Baltruschat, *Physical Chemistry Chemical Physics* **2019**, *21*, 4286–4294.

[110] Q. Yu, S. Ye, *The Journal of Physical Chemistry C* **2015**, *119*, 12236–12250.

[111] P. Reinsberg, A. Weiß, P. P. Bawol, H. Baltruschat, *The Journal of Physical Chemistry C* **2017**, *121*, 7677–7688.

[112] J. Hassoun, F. Croce, M. Armand, B. Scrosati, *Angewandte Chemie International Edition* **2011**, *50*, 2999–3002.

[113] M. Scholz, PhD thesis, Charles University in Prague, **2011**.

[114] D. G. Bradley, D. B. Min, *Critical Reviews in Food Science and Nutrition* **1992**, *31*, 211–236.

[115] J. Wandt, P. Jakes, J. Granwehr, H. A. Gasteiger, R. Eichel, *Angewandte Chemie International Edition* **2016**, *55*, 6892–6895.

[116] N. Mahne, B. Schafzahl, C. Leypold, M. Leypold, S. Grumm, A. Leitgeb, G. A. Strohmeier, M. Wilkening, O. Fontaine, D. Kramer, et al., *Nature Energy* **2017**, *2*, 17036.

[117] N. Mahne, S. E. Renfrew, B. D. McCloskey, S. A. Freunberger, *Angewandte Chemie International Edition* **2018**, *57*, 5529–5533.

[118] E. Mourad, Y. K. Petit, R. Spezia, A. Samojlov, F. F. Summa, C. Prehal, C. Leypold, N. Mahne, C. Slugovc, O. Fontaine, S. Brutti, S. A. Freunberger, *Energy & Environmental Science* **2019**, *12*, 2559–2568.

[119] L. Schafzahl, N. Mahne, B. Schafzahl, M. Wilkening, C. Slugovc, S. M. Borisov, S. A. Freunberger, *Angewandte Chemie International Edition* **2017**, *56*, 15728–15732.

[120] W.-J. Kwak, H. Kim, Y. K. Petit, C. Leypold, T. T. Nguyen, N. Mahne, P. Redfern, L. A. Curtiss, H.-G. Jung, S. M. Borisov, S. A. Freunberger, Y.-K. Sun, *Nature Communications* **2019**, *10*, DOI `10.1038/s41467-019-09399-0`.

[121] Y. K. Petit, C. Leypold, N. Mahne, E. Mourad, L. Schafzahl, C. Slugovc, S. M. Borisov, S. A. Freunberger, *Angewandte Chemie International Edition* **2019**, *58*, 6535–6539.

[122] D. Córdoba, H. B. Rodriguez, E. J. Calvo, *ChemistrySelect* **2019**, *4*, 12304–12307.

[123] D. Aurbach, B. D. McCloskey, L. F. Nazar, P. G. Bruce, *Nature Energy* **2016**, *1*, 16128.

[124] Y. Zhang, X. Zhang, J. Wang, W. C. McKee, Y. Xu, Z. Peng, *The Journal of Physical Chemistry C* **2016**, *120*, 3690–3698.

[125] E. L. Clennan, A. Pace, *Tetrahedron* **2005**, *61*, 6665–6691.

[126] X. Zhang, F. Lin, C. S. Foote, *The Journal of Organic Chemistry* **1995**, *60*, 1333–1338.

[127] P. P. Bawol, MA thesis, University of Bonn, **2016**.

[128] P. H. Reinsberg, P. P. Bawol, E. Thome, H. Baltruschat, *Analytical Chemistry* **2018**, *90*, 14150–14155.

[129] A. J. Bard, L. R. Faulkner, J. Leddy, C. G. Zoski, *Electrochemical methods: fundamentals and applications*, *Vol. 2*, wiley New York, **1980**.

[130] D. Pletcher, R Greff, R Peat, L. Peter, J Robinson, *Instrumental methods in electrochemistry*, Elsevier, **2001**.

[131] L. Zan, PhD thesis, University of Bonn, **2017**.

[132] G. Gritzner, *Journal of Molecular Liquids* **2010**, *156*, 103–108.

[133] V. G. Levich, *Physicochemical hydrodynamics*, Prentice-Hall Inc., **1962**.

[134] T. V. Kármán, *ZAMM - Journal of Applied Mathematics and Mechanics / Zeitschrift für Angewandte Mathematik und Mechanik* **1921**, *1*, 233–252.

[135] W. G. Cochran, *Mathematical Proceedings of the Cambridge Philosophical Society* **1934**, *30*, 365–375.

[136] J. Newman, *The Journal of Physical Chemistry* **1966**, *70*, 1327–1328.

[137] F. Dalton, *Electrochemical Society Interface* **2016**, *25*, 50.

[138] S. Bruckenstein, G. A. Feldman, *Journal of Electroanalytical Chemistry (1959)* **1965**, *9*, 395–399.

[139] W. J. Albery, *Trans. Faraday Soc.* **1966**, *62*, 1915–1919.

[140] W. J. Albery, S. Bruckenstein, *Trans. Faraday Soc.* **1966**, *62*, 1920–1931.

[141] S. Bruckenstein, R. R. Gadde, *Journal of the American Chemical Society* **1971**, *93*, 793–794.

[142] O Wolter, J Heitbaum, *Berichte der Bunsengesellschaft für physikalische Chemie* **1984**, *88*, 2–6.

[143] E. Mostafa, A.-E.-A. A. Abd-El-Latif, H. Baltruschat, *ChemPhysChem* **2014**, *15*, 2029–2043.

[144] U Schmiemann, U Müller, H Baltruschat, *Electrochimica Acta* **1995**, *40*, 99–107.

[145] F. Vidal-Iglesias, J. Solla-Gullón, J. Feliu, H. Baltruschat, A. Aldaz, *Journal of Electroanalytical Chemistry* **2006**, *588*, 331–338.

[146] C. Bondue, P. Königshoven, H. Baltruschat, *Electrochimica Acta* **2016**, *214*, 241 –252.

[147] Z. Jusys, H. Massong, H. Baltruschat, *Journal of The Electrochemical Society* **1999**, *146*, 1093.

[148] M. Heinen, Y. Chen, Z. Jusys, R. Behm, *Electrochimica Acta* **2007**, *53*, 1279–1289.

[149] Z. Jusys, J. Schnaidt, R. J. Behm, *The Journal of Chemical Physics* **2019**, *150*, 041724.

[150] Z. Jusys, M. Binder, J. Schnaidt, R. J. Behm, *Electrochimica Acta* **2019**, *314*, 188–201.

[151] G. Eggert, J. Heitbaum, *Electrochimica Acta* **1986**, *31*, 1443–1448.

[152] R. Imhof, P. Novák, *Journal of The Electrochemical Society* **1998**, *145*, 1081–1087.

[153] H. Baltruschat, *Journal of the American Society for Mass Spectrometry* **2004**, *15*, 1693–1706.

[154] A. Wexler et al., *J. Res. Natl. Bur. Stand. A* **1976**, *80*, 775–785.

[155] C. Bondue, M Hegemann, C Molls, E Thome, H Baltruschat, *Journal of The Electrochemical Society* **2016**, *163*, A1765–A1775.

[156] R. Arrigo, M. Hävecker, M. E. Schuster, C. Ranjan, E. Stotz, A. Knop-Gericke, R. Schlögl, *Angewandte Chemie International Edition* **2013**, *52*, 11660–11664.

[157] V. Streibel, M. Hävecker, Y. Yi, J. J. V. Vélez, K. Skorupska, E. Stotz, A. Knop-Gericke, R. Schlögl, R. Arrigo, *Topics in Catalysis* **2018**, *61*, 2064–2084.

[158] H. Hertz, *Annalen der Physik* **1887**, *267*, 983–1000.

[159] W. Hallwachs, *Annalen der Physik* **1888**, *269*, 301–312.

[160] P. Lenard, *Annalen der Physik* **1900**, *307*, 359–375.

[161] A. Einstein, *Annalen der Physik* **1905**, *322*, 132–148.

[162] T. N. Prize, Nobel Prize Facts: Manne Siegbahn, `https://www.nobelprize.org/prizes/physics/1924/siegbahn/facts/`, (accessed: 24.03.2020).

[163] K. Siegbahn, *Reviews of Modern Physics* **1982**, *54*, 709–728.

[164] M. P. Seah, W. A. Dench, *Surface and Interface Analysis* **1979**, *1*, 2–11.

[165] G. Attard, C. Barnes, *Oxford chemistry primers* **1998**, *59*, ALL–ALL.

[166] D. A. Shirley, *Physical Review B* **1972**, *5*, 4709–4714.

[167] S. Tougaard, *Surface and Interface Analysis* **1988**, *11*, 453–472.

[168] S. Tougaard, *Surface Science* **1989**, *216*, 343–360.

[169] M. Seah, *Surface Science* **1999**, *420*, 285–294.

[170] C. Wagner, W. Riggs, L. Davis, J. Moulder, G. Muilenberg, *Eden Prairie MN* **1979**, 38.

[171] C. Wagner, *Journal of Electron Spectroscopy and Related Phenomena* **1983**, *32*, 99–102.

[172] G. Samjeské, H. Wang, T. Löffler, H. Baltruschat, *Electrochimica Acta* **2002**, *47*, 3681–3692.

[173] S. Tillmann, G. Samjeské, K. Friedrich, H. Baltruschat, *Electrochimica Acta* **2003**, *49*, 73–83.

[174] H. M. Amin, C. J. Bondue, S. Eswara, U. Kaiser, H. Baltruschat, *Electrocatalysis* **2017**, *8*, 540–553.

[175] G. Samjeské, PhD thesis, University of Bonn, **2013**.

[176] N. L. W. Bogolowski, PhD thesis, University of Bonn, **2020**.

[177] S. W. Feldberg, M. L. Bowers, F. C. Anson, *Journal of Electroanalytical Chemistry and Interfacial Electrochemistry* **1986**, *215*, 11–28.

[178] S. W. Feldberg, *Electroanalytical chemistry* **1969**, *3*, 199–296.

[179] D. Britz, J. Strutwolf, *Digital simulation in electrochemistry*, *Vol. 666*, Springer, **2005**.

[180] J. Bezanson, A. Edelman, S. Karpinski, V. B. Shah, *SIAM Review* **2017**, *59*, 65–98.

[181] B. D. McCloskey, R. Scheffler, A. Speidel, D. S. Bethune, R. M. Shelby, A. C. Luntz, *Journal of the American Chemical Society* **2011**, *133*, 18038–18041.

[182] B. McCloskey, A Speidel, R Scheffler, D. Miller, V Viswanathan, J. Hummelshøj, J. Nørskov, A. Luntz, *The journal of physical chemistry letters* **2012**, *3*, 997–1001.

[183] K. P. Yao, J. T. Frith, S. Y. Sayed, F. Barde, J. R. Owen, Y. Shao-Horn, N. Garcia-Araez, *The Journal of Physical Chemistry C* **2016**, *120*, 16290–16297.

[184] J. R. Harding, PhD thesis, Massachusetts Institute of Technology, **2015**.

[185] J. Staszak-Jirkovsky, R. Subbaraman, D. Strmcnik, K. L. Harrison, C. E. Diesendruck, R. Assary, O. Frank, L. Kobr, G. K. Wiberg, B. Genorio, et al., *ACS catalysis* **2015**, *5*, 6600–6607.

[186] C. Liu, S. Ye, *The Journal of Physical Chemistry C* **2016**, *120*, 25246–25255.

[187] N. Mozhzhukhina, L. P. Mendez De Leo, E. J. Calvo, *The Journal of Physical Chemistry C* **2013**, *117*, 18375–18380.

[188] M. Chase, NIST-JANAF Thermochemical Tables (J. Phys. Chem. Ref. Data Monogr. 9), **1998**.

[189] B. J. Bergner, C. Hofmann, A. Schürmann, D. Schröder, K. Peppler, P. R. Schreiner, J. Janek, *Physical Chemistry Chemical Physics* **2015**, *17*, 31769–31779.

[190] D. Grübl, B. Bergner, D. Schröder, J. Janek, W. G. Bessler, *The Journal of Physical Chemistry C* **2016**, *120*, 24623–24636.

[191] D. S. Kim, Y. J. Park, *Journal of Alloys and Compounds* **2014**, *591*, 164–169.

[192] C. M. Burke, R. Black, I. R. Kochetkov, V. Giordani, D. Addison, L. F. Nazar, B. D. McCloskey, *ACS Energy Letters* **2016**, *1*, 747–756.

[193] D. Sun, Y. Shen, W. Zhang, L. Yu, Z. Yi, W. Yin, D. Wang, Y. Huang, J. Wang, D. Wang, et al., *Journal of the American Chemical Society* **2014**, *136*, 8941–8946.

[194] D. Sharon, M. Afri, M. Noked, A. Garsuch, A. A. Frimer, D. Aurbach, *The Journal of physical chemistry letters* **2013**, *4*, 3115–3119.

[195] A. Khetan, H. Pitsch, V. Viswanathan, *The journal of physical chemistry letters* **2014**, *5*, 2419–2424.

[196] J. M. Garcia, H. W. Horn, J. E. Rice, *The journal of physical chemistry letters* **2015**, *6*, 1795–1799.

[197] B. D. Adams, R. Black, Z. Williams, R. Fernandes, M. Cuisinier, E. J. Berg, P. Novak, G. K. Murphy, L. F. Nazar, *Advanced Energy Materials* **2015**, *5*, 1400867.

[198] B. D. McCloskey, D. Addison, A viewpoint on heterogeneous electrocatalysis and redox mediation in nonaqueous Li-O2 batteries, **2016**.

[199] B. INSTRUMENTS, Gas analysis system and software.

[200] T. Hartung, H. Baltruschat, *Langmuir* **1990**, *6*, 953–957.

[201] B. D. McCloskey, D. Bethune, R. Shelby, T Mori, R Scheffler, A Speidel, M Sherwood, A. Luntz, *The journal of physical chemistry letters* **2012**, *3*, 3043–3047.

[202] C. Bondue, P Reinsberg, H Baltruschat, *Electrochimica Acta* **2017**, *245*, 1035–1047.

[203] Z. Peng, S. A. Freunberger, Y. Chen, P. G. Bruce, *Science* **2012**, *337*, 563–566.

[204] S. Meini, N. Tsiouvaras, K. U. Schwenke, M. Piana, H. Beyer, L. Lange, H. A. Gasteiger, *Physical Chemistry Chemical Physics* **2013**, *15*, 11478–11493.

[205] J. Hurvois, C Moinet, *Journal of Organometallic Chemistry* **2005**, *690*, 1829–1839.

[206] P. D. Bartlett, A. P. Schaap, *Journal of the American Chemical Society* **1970**, *92*, 3223–3225.

[207] W. Adam, J.-C. Liu, *Journal of the American Chemical Society* **1972**, *94*, 1206–1209.

[208] W. Ando, T. Saiki, T. Migita, *Journal of the American Chemical Society* **1975**, *97*, 5028–5029.

[209] B. Zhuang, Z.-G. Wang, *The Journal of Physical Chemistry B* **2016**, *120*, 6373–6382.

[210] S Trasatti, O. Petrii, *Journal of Electroanalytical Chemistry* **1992**, *327*, 353–376.

[211] J.-B. Park, S. H. Lee, H.-G. Jung, D. Aurbach, Y.-K. Sun, *Advanced Materials* **2017**, *30*, 1704162.

[212] C.-S. Li, Y. Sun, F. Gebert, S.-L. Chou, *Advanced Energy Materials* **2017**, *7*, 1700869.

[213] M. J. Trahan, S. Mukerjee, E. J. Plichta, M. A. Hendrickson, K. M. Abraham, *Journal of The Electrochemical Society* **2012**, *160*, A259–A267.

[214] C. M. Burke, V. Pande, A. Khetan, V. Viswanathan, B. D. McCloskey, *Proceedings of the National Academy of Sciences* **2015**, *112*, 9293–9298.

[215] D. Sharon, P. Sharon, D. Hirshberg, M. Salama, M. Afri, L. J. W. Shimon, W.-J. Kwak, Y.-K. Sun, A. A. Frimer, D. Aurbach, *Journal of the American Chemical Society* **2017**, *139*, 11690–11693.

[216] M. Olivares-Marín, A. Sorrentino, E. Pereiro, D. Tonti, *Journal of Power Sources* **2017**, *359*, 234–241.

[217] Y. Law, J. Schnaidt, S. Brimaud, R. Behm, *Journal of Power Sources* **2016**, *333*, 173–183.

[218] M. Kar, T. J. Simons, M. Forsyth, D. R. MacFarlane, *Phys. Chem. Chem. Phys.* **2014**, *16*, 18658–18674.

[219] J. L. Anthony, E. J. Maginn, J. F. Brennecke, *The Journal of Physical Chemistry B* **2001**, *105*, 10942–10949.

[220] J. Read, K. Mutolo, M. Ervin, W. Behl, J. Wolfenstine, A. Driedger, D. Foster, *Journal of The Electrochemical Society* **2003**, *150*, A1351.

[221] J. Read, *Journal of The Electrochemical Society* **2006**, *153*, A96.

[222] J. Lindberg, B. Wickman, M. Behm, A. Cornell, G. Lindbergh, *Journal of Electroanalytical Chemistry* **2017**, *797*, 1–7.

[223] F. Messaggi, I. Ruggeri, D. Genovese, N. Zaccheroni, C. Arbizzani, F. Soavi, *Electrochimica Acta* **2017**, *245*, 296–302.

[224] M. Khodayari, P. Reinsberg, A.-E.-A. A. Abd-El-Latif, C. Merdon, J. Fuhrmann, H. Baltruschat, *ChemPhysChem* **2016**, *17*, 1647–1655.

[225] J. Lindberg, B. Endrődi, G. Åvall, P. Johansson, A. Cornell, G. Lindbergh, *The Journal of Physical Chemistry C* **2018**, *122*, 1913–1920.

[226] D. Camper, C. Becker, C. Koval, R. Noble, *Industrial & Engineering Chemistry Research* **2006**, *45*, 445–450.

[227] O. Wijaya, P. Hartmann, R. Younesi, I. I. E. Markovits, A. Rinaldi, J. Janek, R. Yazami, *Journal of Materials Chemistry A* **2015**, *3*, 19061–19067.

[228] P. Hartmann, D. Grübl, H. Sommer, J. Janek, W. G. Bessler, P. Adelhelm, *The Journal of Physical Chemistry C* **2014**, *118*, 1461–1471.

[229] F. S. Gittleson, R. E. Jones, D. K. Ward, M. E. Foster, *Energy & Environmental Science* **2017**, *10*, 1167–1179.

[230] I. Gunasekara, S. Mukerjee, E. J. Plichta, M. A. Hendrickson, K. M. Abraham, *Journal of The Electrochemical Society* **2015**, *162*, A1055–A1066.

[231] A. R. Neale, P. Li, J. Jacquemin, P. Goodrich, S. C. Ball, R. G. Compton, C. Hardacre, *Physical Chemistry Chemical Physics* **2016**, *18*, 11251–11262.

[232] T. Hartung, U. Schmiemann, I. Kamphausen, H. Baltruschat, *Analytical Chemistry* **1991**, *63*, 44–48.

[233] R. Battino, T. R. Rettich, T. Tominaga, *Journal of Physical and Chemical Reference Data* **1983**, *12*, 163–178.

[234] B. B. Benson, D. Krause, M. A. Peterson, *Journal of Solution Chemistry* **1979**, *8*, 655–690.

[235] R. T. Ferrell, D. M. Himmelblau, *Journal of Chemical & Engineering Data* **1967**, *12*, 111–115.

[236] D. M. Himmelblau, *Chemical Reviews* **1964**, *64*, 527–550.

[237] H. S. Carslaw, J. C. Jaeger, *Oxford: Clarendon Press 1959 2nd ed.* **1959**.

[238] S. Aiba, M. Ohashi, S. Y. Huang, *Industrial & Engineering Chemistry Fundamentals* **1968**, *7*, 497–502.

[239] J. Wichterlová, K. Wichterle, J. Michálek, *Polymer* **2005**, *46*, 9974–9986.

[240] M. Carboni, A. G. Marrani, R. Spezia, S. Brutti, *Journal of The Electrochemical Society* **2018**, *165*, A118–A125.

[241] Z. Zhao, J. Huang, Z. Peng, *Angewandte Chemie International Edition* **2018**, *57*, 3874–3886.

[242] S. K. Das, S. Lau, L. A. Archer, *Journal of Materials Chemistry A* **2014**, *2*, 12623.

[243] D. Schröder, C. L. Bender, M. Osenberg, A. Hilger, I. Manke, J. Janek, *Scientific Reports* **2016**, *6*, DOI `10.1038/srep24288`.

[244] I. Landa-Medrano, M. Olivares-Marín, B. Bergner, R. Pinedo, A. Sorrentino, E. Pereiro, I. R. de Larramendi, J. Janek, T. Rojo, D. Tonti, *The Journal of Physical Chemistry C* **2017**, *121*, 3822–3829.

[245] C. J. Bondue, P. P. Bawol, A. A. Abd-El-Latif, P. Reinsberg, H. Baltruschat, *The Journal of Physical Chemistry C* **2017**, *121*, 8864–8872.

[246] X. Ren, Y. Wu, *Journal of the American Chemical Society* **2013**, *135*, 2923–2926.

[247] P. Fischer, P. Reinsberg, R. M. Schwarz, M. Marinaro, M. Wachtler, T. Diemant, R. J. Behm, H. Baltruschat, L. Jörissen, *Journal of The Electrochemical Society* **2018**, *165*, A2037–A2046.

[248] M. Peover, J. Davies, *Journal of Electroanalytical Chemistry (1959)* **1963**, *6*, 46–53.

[249] M. Oyama, T. Hoshino, S. Okazaki, *Journal of Electroanalytical Chemistry* **1996**, *401*, 243–246.

[250] T. Hoshino, M. Oyama, S. Okazaki, *Journal of Electroanalytical Chemistry* **1999**, *472*, 91–98.

[251] J.-M. Savéant, *The Journal of Physical Chemistry B* **2001**, *105*, 8995–9001.

[252] Y. Wang, N.-C. Lai, Y.-R. Lu, Y. Zhou, C.-L. Dong, Y.-C. Lu, *Joule* **2018**, *2*, 2364–2380.

[253] K. B. Prater, A. J. Bard, *Journal of The Electrochemical Society* **1970**, *117*, 207.

[254] A. Pal, Y. P. Singh, *Journal of Chemical & Engineering Data* **1996**, *41*, 1008–1011.

[255] P. P. Bawol, P. H. Reinsberg, H. Baltruschat, *Analytical Chemistry* **2018**, *90*, 14145–14149.

[256] W. J. Albery, S. Bruckenstein, *Trans. Faraday Soc.* **1966**, *62*, 1946–1954.

[257] W. Wang, N.-C. Lai, Z. Liang, Y. Wang, Y.-C. Lu, *Angewandte Chemie International Edition* **2018**, *57*, 5042–5046.

[258] R. Tatara, D. G. Kwabi, T. P. Batcho, M. Tulodziecki, K. Watanabe, H.-M. Kwon, M. L. Thomas, K. Ueno, C. V. Thompson, K. Dokko, Y. Shao-Horn, M. Watanabe, *The Journal of Physical Chemistry C* **2017**, *121*, 9162–9172.

[259] G. E. McManis, M. N. Golovin, M. J. Weaver, *The Journal of Physical Chemistry* **1986**, *90*, 6563–6570.

[260] C. Riadigos, R. Iglesias, M. Rivas, T. Iglesias, *The Journal of Chemical Thermodynamics* **2011**, *43*, 275–283.

[261] N. Bjerrum, *Untersuchungen über Ionenassoziation*, AF Høst, **1926**.

[262] V. Gutmann, *Electrochimica Acta* **1976**, *21*, 661–670.

[263] G. Gritzner, *The Journal of Physical Chemistry* **1986**, *90*, 5478–5485.

[264] D. G. Kwabi, V. S. Bryantsev, T. P. Batcho, D. M. Itkis, C. V. Thompson, Y. Shao-Horn, *Angewandte Chemie International Edition* **2016**, *55*, 3129–3134.

[265] D. Lindsay, W. Kerr, *Nature Chemistry* **2011**, *3*, 494–494.

[266] N. Tsurukawa, S. Prakash, A. Manhart, *Öko-Institut eV Freiburg* **2011**.

[267] D. Wang, X. Gao, Y. Chen, L. Jin, C. Kuss, P. G. Bruce, *Nature Materials* **2017**, *17*, 16–20.

[268] A. Shyamsunder, L. E. Blanc, A. Assoud, L. F. Nazar, *ACS Energy Letters* **2019**, *4*, 2271–2276.

[269] D Aurbach, R Skaletsky, Y Gofer, *Journal of The Electrochemical Society* **1991**, *138*, 3536–3545.

[270] A. Ponrouch, C. Frontera, F. Bardé, M. R. Palacín, *Nature Materials* **2015**, *15*, 169–172.

[271] Z. Li, O. Fuhr, M. Fichtner, Z. Zhao-Karger, *Energy & Environmental Science* **2019**, *12*, 3496–3501.

[272] D. Sharon, D. Hirshberg, M. Afri, A. A. Frimer, M. Noked, D. Aurbach, *Journal of Solid State Electrochemistry* **2017**, *21*, 1861–1878.

[273] S. Zhao, B. Qin, K.-Y. Chan, C.-Y. V. Li, F. Li, *Batteries & Supercaps* **2019**, *2*, 725–742.

[274] K. Song, D. A. Agyeman, M. Park, J. Yang, Y.-M. Kang, *Advanced Materials* **2017**, *29*, 1606572.

[275] N. Imanishi, A. C. Luntz, P. Bruce, *The lithium air battery: fundamentals*, Springer, **2014**.

[276] P. Reinsberg, A.-E.-A. A. Abd-El-Latif, H. Baltruschat, *Electrochimica Acta* **2018**, *273*, 424–431.

[277] P. H. Reinsberg, A. Koellisch, H. Baltruschat, *Electrochimica Acta* **2019**, *313*, 223–234.

[278] C. Powell, *Journal of Electron Spectroscopy and Related Phenomena* **2012**, *185*, 1–3.

[279] Koellisch-Mirbach, I. Park, H. Baltruschat, "Electrochemical reduction of O2 in Ca2+ containing DMSO - Role of roughness and single crystal structure", in preperation.

[280] C. Sheng, F. Yu, Y. Wu, Z. Peng, Y. Chen, *Angewandte Chemie* **2018**, *130*, 10054–10058.

[281] S. Tougaard, *Surface and Interface Analysis* **2018**, *50*, 657–666.

[282] C. D. Wagner, L. E. Davis, M. V. Zeller, J. A. Taylor, R. H. Raymond, L. H. Gale, *Surface and Interface Analysis* **1981**, *3*, 211–225.

[283] R. Younesi, P. Norby, T. Vegge, *ECS Electrochemistry Letters* **2014**, *3*, A15–A18.

[284] F. Marchini, S. Herrera, W. Torres, A. Tesio, F. Williams, E. Calvo, *Langmuir* **2015**, *31*, 9236–9245.

[285] N. Mozhzhukhina, F. Marchini, W. R. Torres, A. Y. Tesio, L. P. M. D. Leo, F. J. Williams, E. J. Calvo, *Electrochemistry Communications* **2017**, *80*, 16–19.

[286] F. S. Gittleson, W.-H. Ryu, M. Schwab, X. Tong, A. D. Taylor, *Chemical Communications* **2016**, *52*, 6605–6608.

[287] B. Sexton, N. Avery, T. Turney, *Surface Science* **1983**, *124*, 162–174.

[288] J. Y. Katekaru, G. A. Garwood, J. F. Hershberger, A. T. Hubbard, *Surface Science* **1982**, *121*, 396–410.

[289] J. Sobkowski, M. Szklarczyk, *Electrochimica Acta* **1980**, *25*, 383–389.

[290] J.-C. Dupin, D. Gonbeau, P. Vinatier, A. Levasseur, *Physical Chemistry Chemical Physics* **2000**, *2*, 1319–1324.

[291] Y.-C. Lu, E. J. Crumlin, T. J. Carney, L. Baggetto, G. M. Veith, N. J. Dudney, Z. Liu, Y. Shao-Horn, *The Journal of Physical Chemistry C* **2013**, *117*, 25948–25954.

[292] K. Zhou, B. Wu, L. Su, X. Gao, X. Chai, X. Dai, *Chemical Engineering Journal* **2017**, *328*, 35–43.

[293] D. G. Kwabi, T. P. Batcho, C. V. Amanchukwu, N. Ortiz-Vitoriano, P. Hammond, C. V. Thompson, Y. Shao-Horn, *The Journal of Physical Chemistry Letters* **2014**, *5*, 2850–2856.

[294] M. A. Schroeder, N. Kumar, A. J. Pearse, C. Liu, S. B. Lee, G. W. Rubloff, K. Leung, M. Noked, *ACS Applied Materials & Interfaces* **2015**, *7*, 11402–11411.

[295] M. Binnewies, E. Milke, *Thermochemical data of elements and compounds*, Wiley-VCH, **1999**.

[296] C. BROSSET, N.-G. VANNERBERG, *Nature* **1956**, *177*, 238–238.

[297] E. V. Ballou, P. C. Wood, L. A. Spitze, T. Wydeven, *Industrial & Engineering Chemistry Product Research and Development* **1977**, *16*, 180–186.

[298] P. P. Bawol, J. H. Thimm, H. Baltruschat, *ChemElectroChem* **2019**, *6*, 6038–6049.

[299] Z.-Z. Shen, S.-Y. Lang, Y. Shi, J.-M. Ma, R. Wen, L.-J. Wan, *Journal of the American Chemical Society* **2019**, *141*, 6900–6905.

[300] A. Christie, J. Lee, I. Sutherland, J. Walls, *Applications of Surface Science* **1983**, *15*, 224–237.

[301] W. J. Landis, J. R. Martin, *Journal of Vacuum Science & Technology A: Vacuum Surfaces and Films* **1984**, *2*, 1108–1111.

[302] C. D. Wagner, D. A. Zatko, R. H. Raymond, *Analytical Chemistry* **1980**, *52*, 1445–1451.

[303] M. Sosulnikov, Y. A. Teterin, *Doklady Akademii Nauk SSSR* **1991**, *317*, 418–421.

[304] B. Demri, D. Muster, *Journal of Materials Processing Technology* **1995**, *55*, 311–314.

[305] J. F. Moulder, *Physical electronics* **1995**, 230–232.

[306] D. Briggs, *Handbook of X-ray and ultraviolet photoelectron spectroscopy*, Heyden, **1977**.

[307] S. L. Stipp, M. F. Hochella, *Geochimica et Cosmochimica Acta* **1991**, *55*, 1723–1736.

[308] Q. Liu, J. Laskowski, Y. Li, D. Wang, *International Journal of Mineral Processing* **1994**, *42*, 251–266.

[309] E. Z. Kurmaev, V. V. Fedorenko, V. R. Galakhov, S. Bartkowski, S. Uhlenbrock, M. Neumann, P. R. Slater, C. Greaves, Y. Miyazaki, *Journal of Superconductivity* **1996**, *9*, 97–100.

[310] T. Sugama, L. Kukacka, N. Carciello, N. Hocker, *Cement and Concrete Research* **1989**, *19*, 857–867.

[311] G. Chiarello, A. Lumachi, F. Parmigiani, P. Ghetti, G. de Michele, *Journal of Electron Spectroscopy and Related Phenomena* **1990**, *50*, 229–237.

[312] B.-S. Lee, Y.-C. Lin, S.-F. Chen, S.-Y. Chen, C.-C. Chang, *Clinical Oral Investigations* **2013**, *18*, 489–498.

[313] Y. Inoue, I. Yasumori, *Bulletin of the Chemical Society of Japan* **1981**, *54*, 1505–1510.

[314] H. v. Doveren, J. T. Verhoeven, *Journal of Electron Spectroscopy and Related Phenomena* **1980**, *21*, 265–273.

[315] T. Hanawa, M. Ota, *Biomaterials* **1991**, *12*, 767–774.

[316] H. Franzen, J. Merrick, M. Umaña, A. Khan, D. Peterson, J. McCreary, R. Thorn, *Journal of Electron Spectroscopy and Related Phenomena* **1977**, *11*, 439–443.

[317] H. Seyama, M. Soma, *Journal of the Chemical Society Faraday Transactions 1: Physical Chemistry in Condensed Phases* **1984**, *80*, 237.

[318] W HESSE, M JANSEN, W SCHNICK, *Progress in Solid State Chemistry* **1989**, *19*, 47–110.

[319] J. R. Nelson, R. J. Needs, C. J. Pickard, *Physical Chemistry Chemical Physics* **2015**, *17*, 6889–6895.

[320] D. Xing, P. P. Bawol, A. A. Abd-El-Latif, L. X. Zan, H. Baltruschat, **in preparation**.

[321] J. Muldoon, C. B. Bucur, T. Gregory, *Chemical Reviews* **2014**, *114*, 11683–11720.

[322] G. Zampardi, F. L. Mantia, *Batteries & Supercaps* **2020**, DOI `10.1002/batt.201900177`.

[323] R. Attias, M. Salama, B. Hirsch, Y. Goffer, D. Aurbach, *Joule* **2019**, *3*, 27–52.

[324] Y. Viestfrid, M. Levi, Y. Gofer, D. Aurbach, *Journal of Electroanalytical Chemistry* **2005**, *576*, 183–195.

[325] R. E. Doe, R. Han, J. Hwang, A. J. Gmitter, I. Shterenberg, H. D. Yoo, N. Pour, D. Aurbach, *Chem. Commun.* **2014**, *50*, 243–245.

[326] C. J. Barile, E. C. Barile, K. R. Zavadil, R. G. Nuzzo, A. A. Gewirth, *The Journal of Physical Chemistry C* **2014**, *118*, 27623–27630.

[327] K. A. See, K. W. Chapman, L. Zhu, K. M. Wiaderek, O. J. Borkiewicz, C. J. Barile, P. J. Chupas, A. A. Gewirth, *Journal of the American Chemical Society* **2015**, *138*, 328–337.

[328] K. A. See, Y.-M. Liu, Y. Ha, C. J. Barile, A. A. Gewirth, *ACS Applied Materials & Interfaces* **2017**, *9*, 35729–35739.

[329] P. Canepa, G. S. Gautam, R. Malik, S. Jayaraman, Z. Rong, K. R. Zavadil, K. Persson, G. Ceder, *Chemistry of Materials* **2015**, *27*, 3317–3325.

[330] P. Canepa, S. Jayaraman, L. Cheng, N. N. Rajput, W. D. Richards, G. S. Gautam, L. A. Curtiss, K. A. Persson, G. Ceder, *Energy & Environmental Science* **2015**, *8*, 3718–3730.

[331] J. B. Moss, L. Zhang, K. V. Nielson, Y. Bi, C. Wu, S. Scheiner, T. L. Liu, *Batteries & Supercaps* **2019**, *2*, 792–800.

[332] Y. He, Q. Li, L. Yang, C. Yang, D. Xu, *Angewandte Chemie* **2019**, *131*, 7697–7701.

[333] S. He, J. Luo, T. L. Liu, *Journal of Materials Chemistry A* **2017**, *5*, 12718–12722.

[334] T. S. Arthur, N. Singh, M. Matsui, *Electrochemistry Communications* **2012**, *16*, 103–106.

[335] L. Zan, D. Xing, A. A. Abd-El-Latif, H. Baltruschat, *Beilstein Journal of Nanotechnology* **2019**, *10*, 2541–2552.

[336] M. Hara, J. Inukai, S. Yoshimoto, K. Itaya, *The Journal of Physical Chemistry B* **2004**, *108*, 17441–17447.

[337] J. Yan, Q Wu, W. Shang, B. Mao, *Electrochemistry Communications* **2004**, *6*, 843–848.

[338] X Nist, Xray Photoelectron Spectroscopy Database, Version 4.1 (National Institute of Standards and Technology, Gaithersburg, 2012), **2012**.

[339] W. Haynes, D. Lide, T. Bruno, CRC Handbook of Chemistry and Physics, 97th edn, Vol. 2016–2017, **2017**.

[340] Y. Gofer, R. Turgeman, H. Cohen, D. Aurbach, *Langmuir* **2003**, *19*, 2344–2348.

[341] H. Kuwata, M. Matsui, N. Imanishi, *Journal of The Electrochemical Society* **2017**, *164*, A3229–A3236.

[342] T. J. Seguin, N. T. Hahn, K. R. Zavadil, K. A. Persson, *Frontiers in Chemistry* **2019**, *7*, DOI `10.3389/fchem.2019.00175`.

[343] J. G. Connell, B. Genorio, P. P. Lopes, D. Strmcnik, V. R. Stamenkovic, N. M. Markovic, *Chemistry of Materials* **2016**, *28*, 8268–8277.

[344] M. Salama, I. Shterenberg, L. J. Shimon, K. Keinan-Adamsky, M. Afri, Y. Gofer, D. Aurbach, *The Journal of Physical Chemistry C* **2017**, *121*, 24909–24918.

[345] A. Bhardwaj, A. Rajput, A. K. Shukla, J. J. Pulikkotil, A. K. Srivastava, A. Dhar, G. Gupta, S. Auluck, D. K. Misra, R. C. Budhani, *RSC Advances* **2013**, *3*, 8504.

[346] A. Shukla, A. D. Pelton, *Journal of Phase Equilibria and Diffusion* **2008**, *30*, 28–39.

[347] C. Hinnen, D. Imbert, J. Siffre, P. Marcus, *Applied Surface Science* **1994**, *78*, 219–231.

[348] Y. Yin, C. Gaya, A. Torayev, V. Thangavel, A. A. Franco, *The Journal of Physical Chemistry Letters* **2016**, *7*, 3897–3902.

[349] W.-J. Kwak, H. Kim, H.-G. Jung, D. Aurbach, Y.-K. Sun, *Journal of The Electrochemical Society* **2018**, *165*, A2274–A2293.

[350] M. E. A. de Dompablo, A. Ponrouch, P. Johansson, M. R. Palacín, *Chemical Reviews* **2019**, DOI `10.1021/acs.chemrev.9b00339`.

[351] N. U. Pujare, *Journal of The Electrochemical Society* **1988**, *135*, 260.

[352] T. Shiga, Y. Kato, Y. Hase, *Journal of Materials Chemistry A* **2017**, *5*, 13212–13219.

[353] W.-J. Kwak, A. Mahammed, H. Kim, T. T. Nguyen, Z. Gross, D. Aurbach, Y.-K. Sun, *Materials Horizons* **2020**, *7*, 214–222.

[354] V. Palomares, A. Goñi, I. G. de Muro, I. de Meatza, M. Bengoechea, I. Cantero, T. Rojo, *Journal of Power Sources* **2010**, *195*, 7661–7668.